



**HAL**  
open science

# Towards ultra-compact inertial platforms based on piezoresistive nanogauges : focus on co-integration issues

Yannick Deimerly

## ► To cite this version:

Yannick Deimerly. Towards ultra-compact inertial platforms based on piezoresistive nanogauges : focus on co-integration issues. Electronics. Université Paris-Est, 2013. English. NNT : 2013PEST1082 . tel-01327172

**HAL Id: tel-01327172**

**<https://theses.hal.science/tel-01327172v1>**

Submitted on 6 Jun 2016

**HAL** is a multi-disciplinary open access archive for the deposit and dissemination of scientific research documents, whether they are published or not. The documents may come from teaching and research institutions in France or abroad, or from public or private research centers.

L'archive ouverte pluridisciplinaire **HAL**, est destinée au dépôt et à la diffusion de documents scientifiques de niveau recherche, publiés ou non, émanant des établissements d'enseignement et de recherche français ou étrangers, des laboratoires publics ou privés.

# UNIVERSITÉ — — PARIS-EST

Ecole Doctorale  
Mathématiques, Science de l'Information et de la Communication (MSTIC)

THÈSE  
pour obtenir le grade de  
Docteur de l'Université Paris-Est

Spécialité : Electronique, Optronique et Systèmes

Présenté et soutenu publiquement par  
Yannick DEIMERLY

Soutenue le 08/10/2013

Vers des centrales inertielle compactes basées sur des nanojauges  
piezoresistives : Problématique de co-intégration

Towards compact inertial platform based on piezoresistive nanogauges :  
Focus on co-integration issues

Thèse dirigée par  
Tarik BOUROUINA  
et suivie par  
Patrice REY  
Guillaume JOURDAN

**Jury :**

Skandar BASROUR, Professeur, TIMA, Grenoble  
Antonio Longoni, Professeur, Politecnico di Milano, Milan  
Alain Bosseboeuf, Professeur, IEF, Orsay  
Stéphane RENARD, CTO, TRONICS, Crolles  
Tarik BOUROUINA, Professeur, ESIEE, Paris  
Patrice REY, CEA-LETI, Grenoble  
Guillaume JOURDAN, CEA-LETI, Grenoble

Rapporteur  
Rapporteur  
Examineur  
Examineur  
Directeur  
Examineur  
Examineur

# Acknowledgements

Tout d'abord j'aimerais adresser ma sincère reconnaissance aux personnes sans qui cette thèse n'aurait jamais pu être ce qu'elle est aujourd'hui. Merci à toi *Guillaume Jourdan*, pour ces longues discussions toujours utiles et tes conseils toujours probant. Merci *Patrice Rey* pour ton encadrement et ta patience. *Arnaud Walther* je te remercie pour tes explications claires et concises ainsi que ta vision technique. Vous avez su vous rendre disponible. Je tiens à dire que j'ai trouvé extrêmement agréable le temps passé à travailler avec vous.

Merci à toi *Tarik Bourouina*, qui a pris le temps de diriger cette thèse. Ton soutien, tes suggestions et ton encadrement furent appréciés.

Je tiens à remercier messieurs *Skandar Basrour* et *Antonio Longoni* d'avoir accepté de rapporter cette thèse. Je veux également remercier monsieur *Stéphane Renard* et monsieur *Alain Bosseboeuf* pour leur participation à l'évaluation de ce travail en tant qu'examineur.

*Philippe Robert*, je te remercie de m'avoir accueilli dans au sein du LCMC (Laboratoire Composant Micro-Capteur), ainsi que pour les discussions constructives que nous avons eu.

Merci à l'équipe 'M&NEMS' sans qui cette thèse ne comporterait aucun résultat. Merci à vous *Fanny Delaguillaumie*, *Carine Dumas*, *Audrey Berthelot* et *Marie-Hélène Vaudaine*.

*Omar Said Ali*, merci pour le temps que tu as bien voulu consacrer avec moi aux dessins de ces accéléromètres.

Merci à vous *Véronique Lheveder* et *Bernard Diem* pour ces multiples discussions fructueuses, et la mise au point de ces textes au combien tortueux.

Je voulais également te remercier *Sebastien Hentz* pour les riches discussions que nous avons eues.

Je remercie *Frédéric Souchon*, *Patrick Brunet-Manquat* et *Denis Mercier* du LCFC (Laboratoire Caractérisation et Fiabilité des Composants) pour leur aide aux travaux de caractérisation.

Merci à vous *Fabrice Terry*, *Guillaume Dodane*, *Lucas Dudon* et *Nicolas Bertin* pour le travail apprécié que vous avez fourni afin de faire avancer, courir ces capteurs.

Je voudrais ensuite remercier mes collègues de bureau, *Dirk Ettelt*, *Antoine Niel*, *Henri Blanc*, *Jean-Sebastien Moulet* et bien sur *Eric Sage* collègue et ami depuis bien longtemps.

A l'équipe des 'jeunes', *Remi Dejaeger*, *Czarny Jaroslaw*, *Jeremie Ruellan*, *Nils Rambal* et *Benoit Savornin*, merci pour la bonne ambiance et le rire qui ont éclairé ces trois années.

Merci *Pierre-Patrick Lassagne*, *Sophie Giroud*, *Amy N'Hari*, *Nicolas Bertolami* ainsi que tous les membres du SCMS (Service Composants Microsystèmes) pour les bons moments passés à discuter et déguster de succulentes gourmandises.

Et bien sur je ne pouvais pas conclure sans remercier *Christine Courtois* qui réduit tous les problèmes à néant en deux temps trois mouvements.

Acknowledgements.....	2
Chapter 1: Introduction .....	4
1.1 Organisation of the manuscript.....	4
1.2 Market analysis .....	4
1.3 Specifications.....	6
1.4 State-of-the-art for MEMS accelerometers.....	7
1.5 State-of-the-art of MEMS Coriolis based gyroscopes.....	9
1.7 The M&NEMS concept as a technological platform for inertial sensor .....	12
1.6 Pro and cons of suspended piezoresistive transduction versus capacitive transduction.....	13
1.8 Motivation and scope of this thesis.....	14
Chapter 2: Model of the piezoresistive nanogauge.....	19
2.1 Piezoresistive detection based on suspended nanogauges .....	19
2.2 Mechanical limits of piezoresistivity in silicon .....	20
2.3 Thermo-electro-mechanical behavior of the detection mean.....	23
2.4 Self-heating and gauge burn-out.....	29
2.5 Noise model of the nanogauge.....	32
2.6 Doping influence on performances of piezoresistive nanogauge .....	37
2.7 Consumption-noise strategy of piezoresistive readout systems.....	37
Chapter 3: Design of springs.....	39
3.1 Fabrication limitations .....	39
3.2 Single parallelepiped beam .....	39
3.3 Association rules of springs .....	41
3.4 Mechanical function of springs.....	42
Chapter 4: Non resonant structure .....	52
4.1 Single-axis accelerometers.....	52
4.2 Pressure sensor.....	66
4.3 Two-axis accelerometers .....	74
4.4 Prospects of three-axis accelerometers .....	78
Chapter 5: Resonant structures .....	81
5.1 Dual-mass gyroscopes with piezoresistive detection.....	81
5.2 Design of a two-axis gyroscope.....	93
5.3 Dynamic accelerometer .....	98
5.4 Design of a coupled accelerometer-gyroscope .....	103
5.5 Conclusion .....	112
Chapter 6: Electromechanical damping.....	113
6.1 Motivation towards co-integration of gyroscopes with non resonant accelerometers.....	113
6.2 Theory of RC coupling .....	113
6.3 Experimental results.....	117
6.4 Vacuum packaged low Q accelerometers sensors .....	123
Conclusions and prospects:.....	126
Appendix.....	128
References:.....	132

# Chapter 1: Introduction

## 1.1 Organisation of the manuscript

- The first chapter introduces the state-of-the-art concerning accelerometers and gyroscopes *MEMS sensors*. In this chapter, the *M&NEMS concept* is introduced. The scope and motivation of this thesis is presented.
- The second chapter focuses on the detection mean used during this thesis work to transform mechanical signal into the electrical domain. A model of the *piezoresistive nanogauge* backed by experiments is presented. Mechanical and thermal limitations are described. These limitations fix some of the sensor performances.
- Chapter three discusses the *design of springs* used in this thesis. Simple stiffness calculations along with the different mechanical functions of springs are included in this chapter.
- Chapter four presents the different *quasi-static* sensors designed during this thesis. The analytical models of the different sensors are discussed. Experimental results obtained on in-plane, out-of-plane accelerometers along with pressure sensors are presented.
- Chapter five describes the *resonant* structures characterized during this thesis. Gyroscopes, dynamic accelerometer and coupled accelerometer-gyroscopes are presented.
- An *electrically controllable source of damping* is reported in chapter six, intended to facilitate the co-integration of resonant gyroscopes and quasi-static accelerometers. Structures specifically designed to increase this electromechanical coupling are presented along with the experimental results obtained.

## 1.2 Market analysis

Inertial sensors are used in a very wide range of applications. In general the application of a sensor can be deduced from its bias stability specification. Figure 2 shows the different bias stability requirements for accelerometers and gyroscopes depending on the military application.

Strategic grade inertial measurement units (IMU) represent the best positioning systems available (except the GPS, which is not applicable in many cases). They can be used for long range (nuclear or conventional) missiles guidance and submarines positioning systems. Strategic grade inertial measurement units can cost up to 1M\$. Because of performance issues, MEMS inertial sensors have not been able to enter this market yet

Tactical grade systems also concerns military applications. They address low range military applications such as bomb guidance or Unmanned Aerial Vehicles (UAVs) positioning. High performances MEMS inertial sensors have begun to compete with macro sensors for this market.

Navigation grade systems concern non military applications where human life could be at risks. They can be found in airplanes or automated guidance systems.

Consumer grade systems represent sensors with low stability. They are used for other functions than positioning (i.e shocks detection). This consumer market represents the largest market both in terms of units sold and market revenue. Examples of application from the consumer market are airbags, gaming, camcorders and smartphones.

Medical applications require very high performance sensors with different requirements with respect to tactical or strategic grades systems. For instance, long term autonomy is critical whereas the temperature behaviour of the sensor is not (The body stays at a very constant temperature). Figure 1 shows a graph which depicts the size of the different markets concerning accelerometer applications. The major market is the automotive and the consumer market.

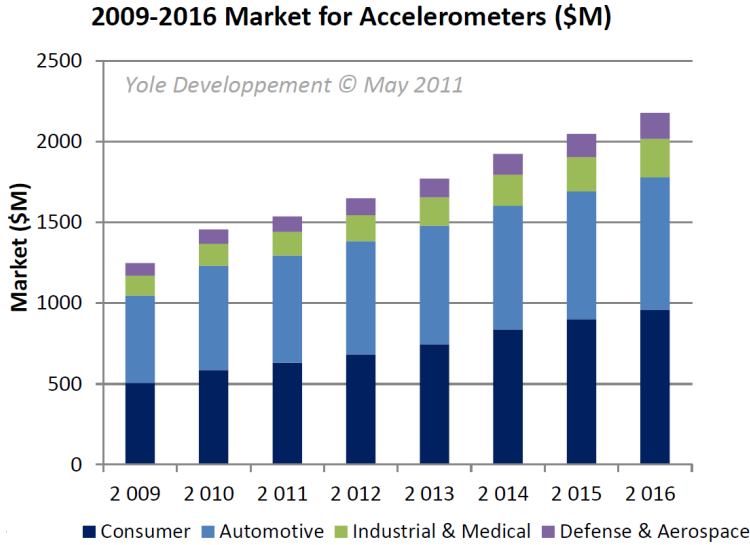


Figure 1: Size of the different market concerning accelerometers application [Yole11]

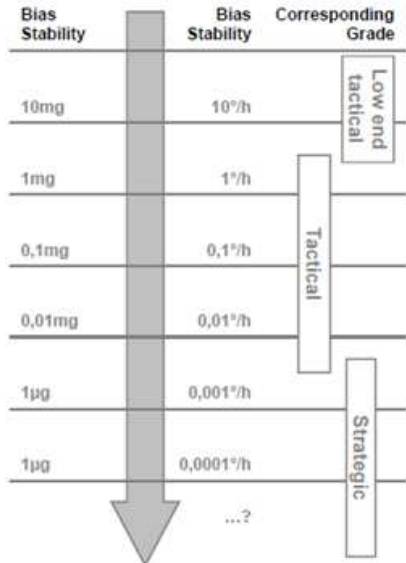


Figure 2: Bias stability requirements for accelerometer and gyroscopes depending on the application

The markets addressed by gyroscopes are identical to the market described for accelerometer in 1.2.2. MEMS gyroscope is a complex device. Its development has been delayed with respect to accelerometers. The introduction of MEMS gyroscopes in mobile phones drives the expansion of the market revenue predicted by Yole [Yole11].

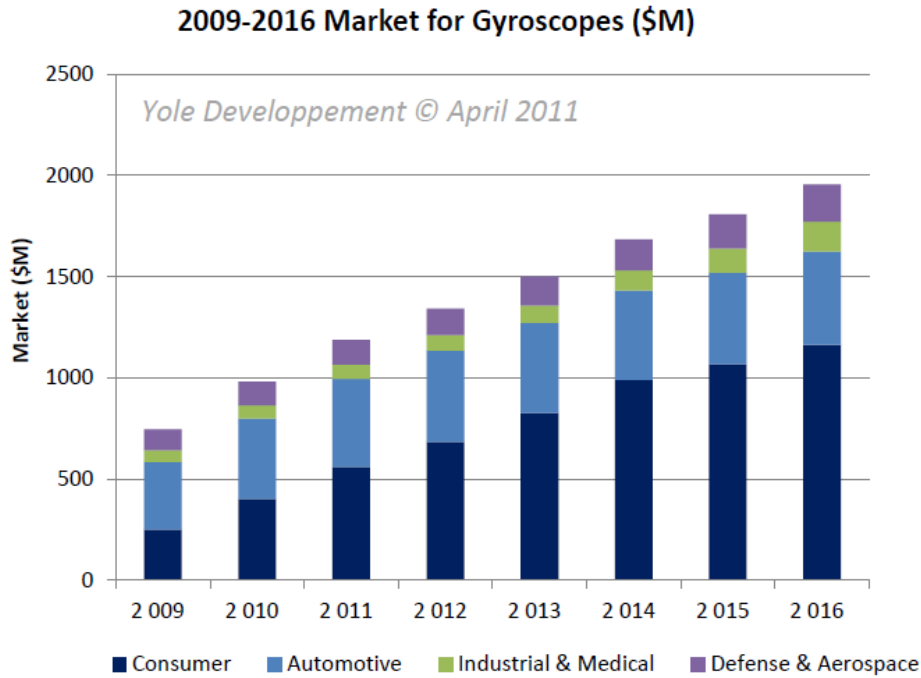


Figure 3: Size of the different markets concerning gyroscopes applications [Yole11]

## 1.3 Specifications

### 1.3.1 Accelerometer specifications for consumer applications

In this thesis, we will focus on accelerometers for the consumer market. Specifications for consumer applications have been extracted from industrial accelerometers datasheet and partly based on the specification used for the NIRVANA (*Nine-Axis Inertial Sensor Based On Piezoresistive Nano-Gauge Detection*) European project supported by the FP7 program.

Parameters	Specification	Units
Full Scale	+/-10 to +/-20g	g
Sensitivity	100	mV/g
Resolution	1	mg
Acceleration noise density	50	$\mu\text{g} / \sqrt{(\text{Hz})}$
Temperature sensitivity	0.01	%/°C
Non-linearity	<1	%
Cross-axis sensitivity	<2%	%
Bandwidth	100	Hz
Operating temperature range	[-40, +85]	°C
Shock resistance	10000g/0.1ms; 3000g/0.5ms	
Package dimensions	1*1*1	mm <sup>3</sup>
Power consumption	<1	mW

*Table 1 : Three-axis accelerometers specification chosen for consumer applications*

The last generation of commercialized devices is driven by cost reduction. Reducing the size of inertial sensors is of utmost importance from the industrial point of view. The main technical parameters to take into account when designing accelerometers are the mechanical footprint, and the number of integrated axis.

### 1.3.2 Gyroscopes specifications for consumer applications

The gyroscopes designed in this thesis aims for the consumer market. Like the accelerometer specifications, the gyroscopes specifications have been extracted from industrial datasheets and partly based on the specifications used for the NIRVANA European project supported by the FP7 program.

Parameters	Specification	Units
Full Scale	+/- 2000	°/s
Sensitivity	2	mV/°/s
Resolution	30	mdps
Rate Noise density	0.05	°/s/√(Hz)
Temperature sensitivity	0.02	%/°C
Non-linearity	0.2	%
Cross-axis sensitivity	<2%	%
Bandwidth	500	Hz
Operating temperature range	[-40, +85]	°C
Shock resistance	10000g/0.1ms 3000g/0.5ms	
Package dimensions	2*2*1	mm <sup>3</sup>
Power consumption	<25	mW

Table 2 : Three-axis gyroscopes specification chosen for consumer applications

The main issues of gyroscopes for consumer applications are the power consumption and the mechanical footprint. The power consumption required by the control loop of the driving section requires most of the power of a whole 6-axis sensor. The proposed specifications intend to build a complete IMU (*Inertial Measurement Unit*) on a single die whose area would be around 5mm<sup>2</sup>.

### 1.4 State-of-the-art for MEMS accelerometers

Most MEMS accelerometers are based on a suspended mass that moves when acceleration occurs [Wei01]. More often than not, the mass-spring system is linked to an electrostatic transducer; the capacitance formed by one side of the suspended mass and the anchor at the corresponding side varies because of the displacement of the suspended mass. Multi-axes capacitive sensing can be achieved by using several electrodes with a single suspended mass [Min96]. Capacitances arranged in comb fingers enable an improvement in the linearity of the transduction from displacement to capacitance [Mat98]. Figure 4 shows an example of three-axis capacitive accelerometer implementation.

On the other hand, piezoresistive accelerometers are based on stress detection (probed on a deformable structure) rather than displacement detection. Large stress can be obtained on the suspension beam of the inertial mass as depicted in figure 5 [Pat00]. Three-axis detection can be implemented using this suspension beam approaches [Zha07]. Figure 5 shows an accelerometer based on implanted piezoresistor.



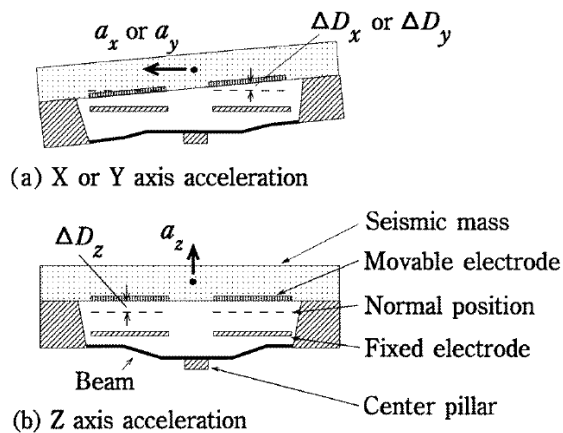


Figure 4: Implementation of capacitive three-axis accelerometer by [Min96]

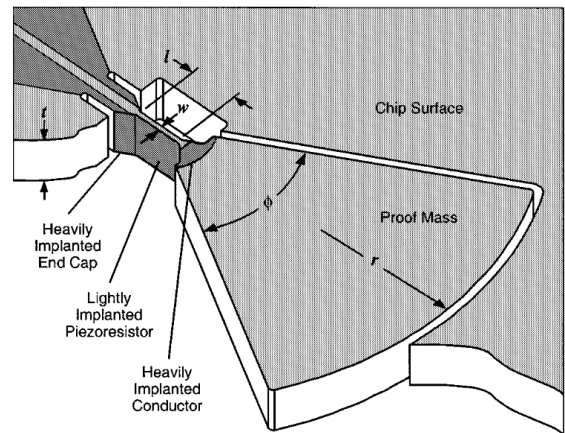


Figure 5: Implementation of piezoresistive based accelerometer by [Pat00]

It is worth mentioning that this rough benchmark does not take into account the piezoresistive accelerometers developed at the early times of the MEMS era, since the 70's, and which are based on piezoresistors implemented on the top surface of a silicon substrate following a doping step. It is important to highlight at this stage that the piezoresistors considered in this work are formed from bulk silicon shaping by micromachining, and therefore, they can be seen as suspended piezoresistors. Most of the time those suspended piezoresistors are arranged in a vertical fashion (as in figure 2) rather than the conventional horizontal one.

Other detection mean have been reported in the literature. Piezoelectric detection is very similar to the implanted piezoresistive detection. The stress induced by an inertial mass displacement on the deposited PZT elements induces a voltage drop that can be directly measured by the readout electronic [Kunz01] see figure 7.

Accelerometers using thermal convection have been proposed using Porous Silicon Thermal Accelerometer (PTSA). Temperature is measured at both side of a heater. Acceleration can be extracted from these two measurements [Gou04]. Thermal accelerometers have the advantage that they do not require inertial mass. Better shock resistance and robustness is expected from this detection mean. Figure 6 shows the top view of the thermal accelerometer reported in [Gou04].

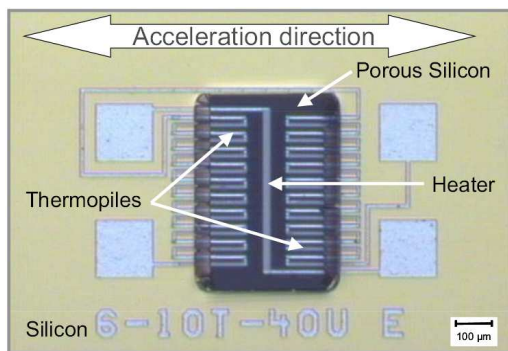


Figure 6: Thermal accelerometer based on PSTA detection [Gou04]

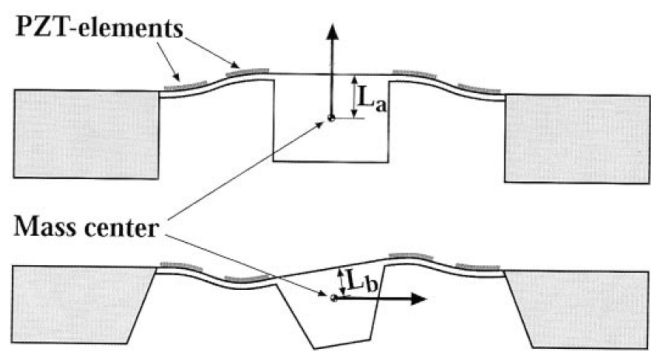


Figure 7: Three-axis accelerometer based on PZT detection [Kunz01]

Accelerometers are quasi-static sensors. Ideally they should have an overdamped behavior. Electronic filtering can be used to obtain overdamped response.

## 1.5 State-of-the-art of MEMS Coriolis based gyroscopes

### Single-mass gyroscopes

Most MEMS gyroscopes are based on Coriolis force detection in order to provide the user with a measure of the rotation speed. Coriolis forces are proportional to the translational speed, to the inertial mass and to the rotation speed as shown in equation (1).

$$\vec{F}_Y = -2.m_i.\vec{v}_X \wedge \vec{\Omega}_Z \quad (1)$$

$m_i$  is the inertial mass,  $v_x$  the speed along the x-axis,  $\Omega_z$  is the rotation speed along the z-axis and  $F_Y$  is the resulting Coriolis force along the y-axis. We see from equation (1) that gyroscopes need an actuation to induce a controlled speed. The direction of the resulting Coriolis force is perpendicular to the excitation direction. This defines the two main perpendicular directions of Coriolis-based gyroscopes, the **drive** direction (excitation) and the **sense** direction (detection). The cinematic model of such a structure is shown in figure 1 below:

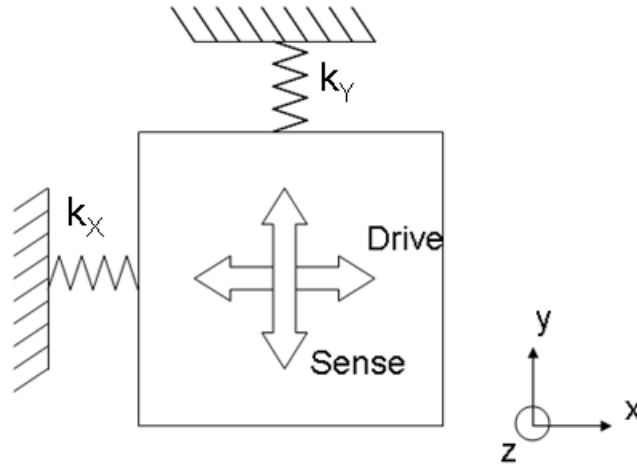


Figure 8: Simple analytical model of a Coriolis-based vibratory gyroscope

Excitation is done by electrostatic force through electrodes. In order to create large displacement, the electrostatic force is actuated at the drive resonance frequency. The resulting amplitude corresponds to the quasi-static displacement multiplied by the quality factor. In vacuum, quality factor of MEMS structures can easily go up to  $10^4$ . The detection of the sense mode can be done either through capacitive or piezoresistive transduction. In capacitive transduction, the displacement due to the Coriolis force is measured through gap variation. In piezoresistive transduction, the Coriolis force is monitored through the resulting stress inside the detecting piezoresistive nano-gauges [Wal12]. The equation of motion of the system shown in figure 1 along the x and y axis are described below.

$$m \ddot{x} + c_X \dot{x} + k_X x = F_d \quad (2)$$

$$m \ddot{y} + c_Y \dot{y} + k_Y y = -2m \dot{x} \Omega \quad (3)$$

Here  $F_d$  corresponds to the drive excitation force along x.  $m$  corresponds to the inertial mass.  $k_X$  and  $k_Y$  corresponds to the stiffness along the x-axis and y-axis, respectively.  $c_X$  and  $c_Y$  corresponds to the damping along x and y direction respectively. The Coriolis force  $F_C$  is defined by equation (3).

This simple system has several limitations:

- Parasitic vibrations will influence the sense mode depending on the excitation frequency of the sensor. Since acceleration is orders of magnitude larger than Coriolis forces in terms of amplitude, acceleration compensation is mandatory. Sensitivity to acceleration can be corrected by using differential measurement.

- The springs  $k_x$  and  $k_y$  are not perfect. Their stiffness matrix exhibit cross-components. A force along the x-axis (i.e drive electrostatic force) will induce a movement along the x-axis but also a smaller parasitic movement in the y-direction [Wal13]. This parasitic movement occurs at the drive frequency. Such bias effect can be orders of magnitude more important than the Coriolis signal. Decoupling between the drive and the sense mechanical parts reduces this parasitic bias.

### Dual-mass gyroscopes

A second generation of gyroscopes was built [Acar03], [Che09]. This new generation is called dual-mass gyroscopes because of the two identical masses that are excited in opposite directions. Drive and sense mechanical functions are also decoupled by transmitting springs. Transmitting springs possess a high stiffness in one direction i.e the drive direction and a very low stiffness in the other direction i.e the sense direction. Use of such springs reduces the parasitic influence of the bias. The two driving masses of a dual-mass gyroscope are coupled by a coupling spring in order to keep at all time an opposite displacement amplitude. Figure 9 shows the cinematic scheme of a dual-mass gyroscope.

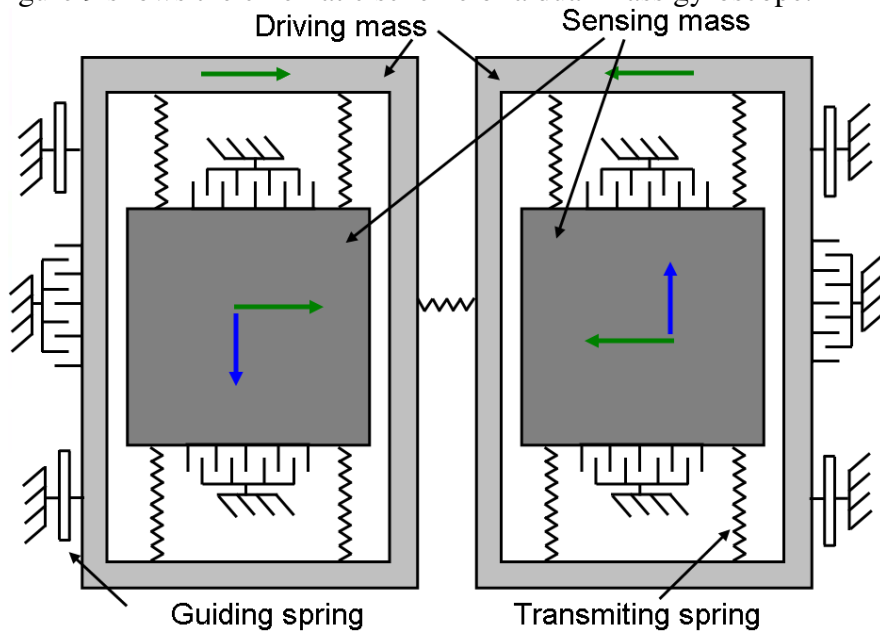


Figure 9: Cinematic scheme of a dual-mass gyroscope

The green arrows represent the displacements in the drive direction. The blue arrows represent the displacements in the sense direction. Additionally differential measurement of the two sensing mass displacements allows common mode rejection in order to suppress acceleration sensitivity. Two modes are present along the drive direction, the drive mode and a parasitic in-phase mode. Additionally, in the sense direction, the sense mode and a parasitic in-phase sense mode also exists.

## Improved mode ordering for dual-mass gyroscopes

A third mass has been added to **increase the decoupling** between the drive and the sense mode. The sensing mass is divided into an inertial mass and a detection arm. Additionally the detection arm is directly anchored to the substrate via an anchored spring.

In order to improve the mechanical rejection of acceleration, improvements of the coupling spring have been proposed [Wal12], [Trusov09]. The objective is to fix the parasitic in-phase mode of the drive direction far and after the drive mode. Keeping the parasitic mode after the drive mode provides a  $-40\text{dB/dec}$  rejection rate, thanks to the transfer function of the 2DoF spring-mass system.

Figure 10 depicts the cinematic scheme of a piezoresistive dual-mass gyroscope with improved mode ordering. The drive part of the device (in green) will be actuated along the x-direction and is mechanically coupled to the inertial mass (in red) by transmitting springs. The movement of the inertial mass along the sense direction will be monitored by the detection arm (in blue). Decoupling springs (in black) are dimensioned in order to transmit the movement in only one direction (see Chapter 2: Design of springs).

Figure 11 show the scheme of a dual-mass gyroscope with a levered anti-phase drive-mode and linearly coupled anti-phase sense-mode. The rejection of the in-phase drive mode is done by the anchor of the lever mechanism. On the contrary to figure 10 the sensing mass is not anchored.

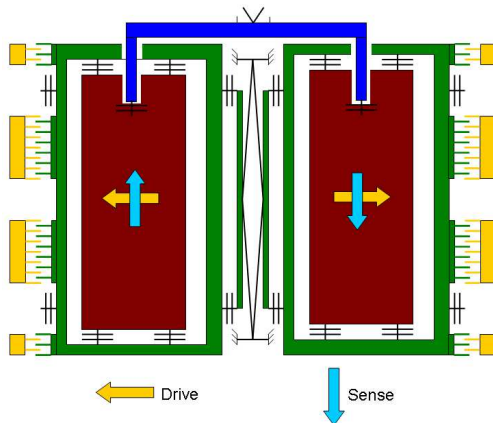


Figure 10: Cinematic scheme of an improved mode ordering piezoresistive dual-mass gyroscope [Wal12]

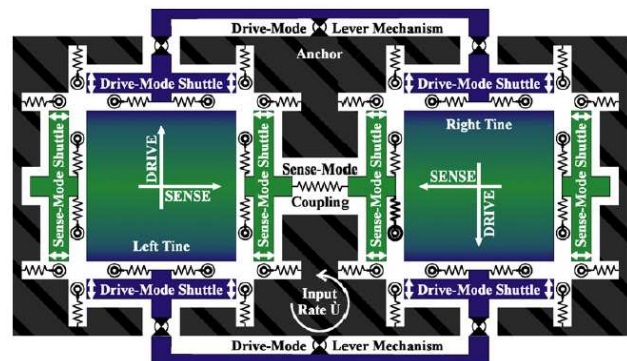


Figure 11: Cinematic scheme of an improved mode ordering dual-mass gyroscope with balanced sense mode [Trusov09]

The quality factor of gyroscopes is maximized in order to create large drive velocities. To obtain large quality factor, all sources of losses should be removed. Vacuum packaging enables the reduction of viscous losses which enables quality factor up to  $10^5$ . Energy transfer to the substrate represents also a source of losses. To reduce them, balanced design should be implemented. Thanks to dual-mass implementation, the drive mode is already balanced. By balancing the sense mode the quality factor can go as high as  $0.86\text{M}$  [Trusov11]. Thermo-Elastic Damping (TED) becomes more and more important for these high quality factors [LeFoulgoc06].

## Multi-axis gyroscopes

Designs of multi-axis sensing have been proposed [Tsai06], [EP2339293]. Each drive part requires an electronics control loop. Using circular designs, the drive part of the gyroscopes can be shared by several axes. This architecture allows large reduction of the power consumption and in electronic size. Two main approaches exist.

In circular approaches as shown in figure 12 the drive displacement is a rotation. This allows two modes of operation where the sense rotation occurs around the x- or y-axis.

Figure 13 shows another mode of drive actuation. In this structure, the drive mode beats like a heart, inducing common displacement of the four inertial masses to the center of mass and then away from it.

The objective of these architectures is to create a displacement in both in-plane directions. However the architecture chosen in figure 13 is balanced whereas the architecture shown in figure 12 is not. The drive quality factor of figure 13 will probably be higher than in figure 12.

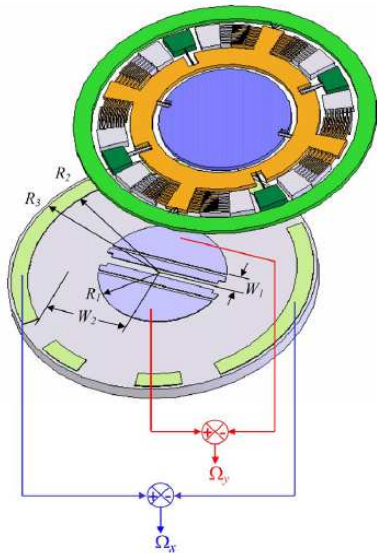


Figure 12: Two-axis circular gyroscope [Tsai06]

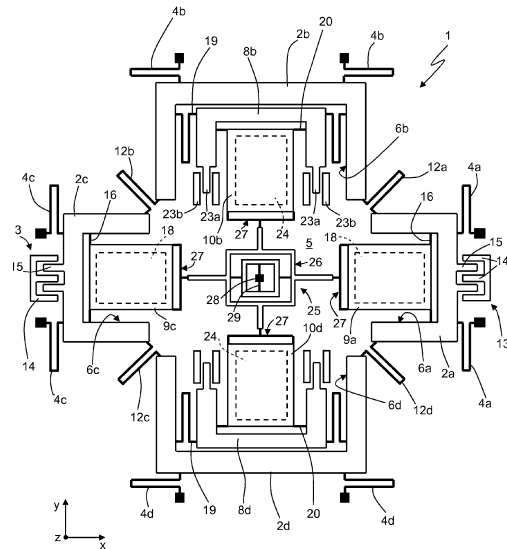


Figure 13: Three-axis gyroscope with common drive mode [EP2339293]

## 1.7 The M&NEMS concept as a technological platform for inertial sensor

All sensors designed in this thesis are based on the ‘M&NEMS’ concept. This approach has already been presented as new solution for low-cost inertial sensor in 2009 [Rob09]. The concept is to create a sensor with mechanical parts of very different dimensions. The concept is based on two different thicknesses:

- A thin layer is used for the detecting elements (i.e the piezoresistive nanogauge).
- A thick layer defines the inertial mass and the deformable springs.

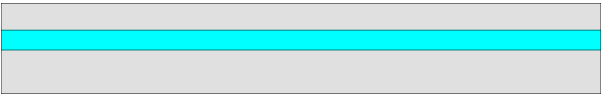
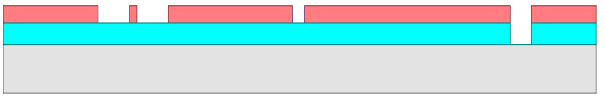
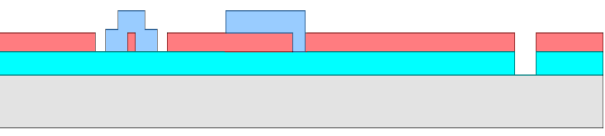
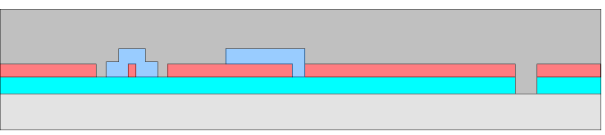
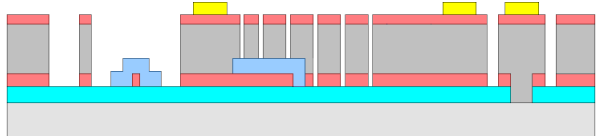
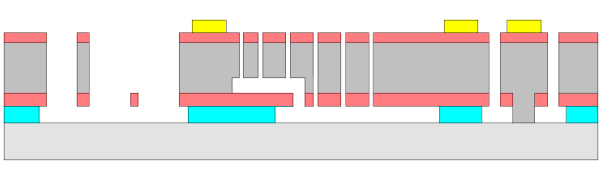
The nanogauge allows a large constraint concentration. The sensitivity of piezoresistive detection increases with a decreasing cross-section of the nanogauges. Hence the concept enables high sensitivity sensor with low mechanical footprint. This concept fits well with industrial needs for low-cost inertial sensors. Downscaling limits of piezoresistive accelerometers have already been studied in [Eng09]. By considering silicon fracture and buckling, the minimum mechanical footprint of a one-axis piezoresistive accelerometer has been evaluated around  $150*150*10\mu\text{m}^3$ .

MEMS inertial sensors are based on two major fabrication steps. A critical fabrication step is the release step. Oxides present inside the MEMS are selectively etched through vapor hydrofluoric acid etching. Selective isotropic etching allows the creation of movable parts.

The fabrication steps which allowed a dramatic expansion of the inertial sensor development is the so-called ‘‘Bosch process’’ the most popular form of DRIE, which stands for *Deep Reactive Ion Etching* [Bosch96]. This process consists in loops of isotropic etching and passivation in order to create almost vertical walls. This fabrication step allows structures



with very high aspect ratio. Table 3 present the main fabrication steps of the ‘M&NEMS’ process flow (without packaging).

Starting from an SOI wafer. (Si Top typical thickness: 250nm, BOX:1μm)	
Doping, annealing and DUV lithography step on the NEMS layer.	
A protecting layer (SiO2) is placed on critical NEMS parts (i.e nanogauges, electrodes).	
Silicon epitaxy in order to form the MEMS layer. Planarization of the layer at a thickness of some tens of microns.	
Deep Reactive Ion Etching. Definition of the MEMS structure (i.e inertial mass, decoupling springs, comb drive). Metallization (contact pads, electric lines)	
Release step through vapor hydrofluoric acid etching.	
<i>Table 3 : Description of the main steps of the ‘M&amp;NEMS’ process flow</i>	

This process flow creates suspended piezoresistive nanogauges with a thickness much smaller than the one of the MEMS layer. To keep a low cost process e-beam lithography was avoided. The minimum lateral dimension of the NEMS layer is fixed by Deep UV lithography limitation (i.e 250nm). The fact that the gauges are suspended suppresses the current leakage issues. Using mechanical fulcrum described in chapter 3, both in-plane and out-of-plane inertial force can be converted into compressive/tensile stress within the nanogauge. Additionally the process flow described in table 3 is compatible with both accelerometers and gyroscope structures. Through minor adjustment magnetometer and pressure sensor can also be co-integrated to this monolithic fabrication process. The need for an SOI wafer reduces somehow the attractiveness of the overall process flow for low-cost application.

Concerning the Wafer Level Packaging (WLP), Au-Si eutectic bonding has been chosen for its good hermetic and conductive behavior. Additionally the temperature process (363°C) is compatible with the getter developed at CEA-LETI.

## 1.6 Pro and cons of suspended piezoresistive transduction versus capacitive transduction

Capacitive transduction is the prevailing transduction scheme in recent inertial MEMS sensors [Zeng11]. In-plane capacitances are generally defined through DRIE (Deep Reactive Ion Etching). Starting from an SOI wafer, out-of-plane capacitance only requires a metal deposition and a release step. Capacitive transduction is based on gap variation of the

capacitance. The readout signal is proportional to the **capacitance surface**. Gap variation induces nonlinear capacitance change. To reduce this intrinsic nonlinearity, specific comb drive electrodes have been designed. Using identical capacitance both detection and actuation can be done. Conversion from capacitance to voltage requires relatively complex electronics. The simplicity of fabrication and the flexibility of variable capacitance are largely responsible for the spread of this transduction mean.

Piezoresistive detection has been widely used for pressure sensor applications. In a piezoresistive material, the mechanical stress induces change in the material electrical resistivity. Piezoresistive effect is very linear. Silicon is among the best piezoresistive materials. More importantly the sensitivity of piezoresistive detection increases with **decreasing cross-section**.













Implanted piezoresistor isolation is based on a pn-junction. This isolation exhibits a leakage current increasing exponentially with temperature.

On the other hand, suspended piezoresistance isolation is achieved thanks to the permittivity of air. Current leakage is hence extremely small for suspended piezoresistance. Additionally all the stress is applied to the piezoresistor which leads to higher efficiency.

However piezoresistive detection exhibit major drawbacks. Piezoresistive detection shows large sensitivity to temperature. Moreover, vertical nanowires that might act as suspended piezoresistors are not easy to fabricate even using DRIE processes. This makes out-of-plane detection difficult. Piezoresistive readout is based on resistance change. Intrinsically the resistance needs to be biased which increase the electrical consumption.

A fair comparison of the power consumption of piezoresistive readout with respect to capacitive readout is difficult to evaluate. The readout strategy will dictate the power consumption required. For instance thanks to the low capacitance of piezoresistive readout, small duty cycle can be achieved which can reduce the biasing by orders of magnitude. Additionally conversion from capacitance to voltage also requires power.

It is also worth mentioning that actuation of a piezoresistance can be done through self-heating and thermal extension [Ste11]. Table 4 shows a comparison between the capacitive and piezoresistive transduction.

	Piezoresistive transduction	Capacitive transduction
Linearity		
Output signal		
Size reduction		
Fabrication complexity		
Actuation possibility		
Out-of plane measurement		
Power consumption	-	-

*Table 4 : Comparison of piezoresistive and capacitive transduction mean*

The main advantage of piezoresistive transduction with respect to capacitive transduction in the recent development of low cost inertial sensor is the more favourable scaling law. Indeed, a reduction of the size of the detection means increases the sensitivity of the piezoresistance whereas it decreases the capacitance variation.

## 1.8 Motivation and scope of this thesis

The main motivation of this thesis is to provide efficient solution for the co-integration of inertial sensors, in particular accelerometers and gyroscopes. Coriolis based dual-mass

gyroscope is the prevailing MEMS structure to measure rotation speed. These structures are usually packaged under **vacuum** to provide high quality factor to *resonant* MEMS. On the other hand, accelerometers are *quasi-static* sensors. ASIC designers expect a transient response of the MEMS in accordance with the acceleration. To obtain overdamped structures, accelerometers are generally packaged at **atmospheric pressure**.

From these packaging constraints, it appears that accelerometers and gyroscopes seem to have an opposite working point in terms of pressure environment. The first step of this thesis has been to validate this apparent issue.

### 1.8.1- Gyroscopes constraints on quality factor

The minimum quality factor for gyroscopes has been assessed through the following set of assumptions. The maximum AC actuation voltage is set to 1.7V because it is the half of the maximum voltage allowed in the ASIC (i.e 3.3V and no charging pump is considered). The resonance frequency is set around 20 kHz and the silicon inertial mass to  $400 \times 400 \times 10 \mu\text{m}^3$ . The maximum displacement that can be safely obtained without encountering nonlinear problems is considered to be around  $2 \mu\text{m}$  [Kaa04]. Assuming a reasonable geometry of the comb drive electrodes ( $N=120$  and  $g=1 \mu\text{m}$ ), the gyroscopes should have a quality factor of at least  $Q > 2.10^3$  to obtain a drive displacement of  $2 \mu\text{m}$ . Equations (4) and (5) gives the formula used to obtain this rough estimation.

$$u_{MAX} = \frac{Q_{exc} \cdot F_{exc}}{k_x} \quad \text{with,} \quad (4)$$

$$k_x = (2\pi \cdot f_d)^2 m_{exc} \quad \text{and} \quad F_{exc} = \frac{N \cdot \epsilon_0 \cdot t \cdot V^2}{g} \quad (5)$$

With  $u_{MAX}$  the displacement obtained,  $k_x$  the spring stiffness in the drive direction,  $t$  the MEMS thickness,  $V$  the voltage applied and  $g$  the comb drive gap.  $f_d$  corresponds to the drive frequency and  $m_{exc}$  to the excitation mass. A lower quality factor will imply either use of larger voltages, more comb drives or a reduced sensitivity.

### 1.8.2- Accelerometers constraints on quality factor

The maximum quality factor of accelerometers is more difficult to assess. The main constraint is the response time of the system. Saturation of the Analog to Digital Converter (ADC) occurs when the analog input is larger than the largest analog value the ADC can transform into a digital value. Depending on the chosen architecture, the saturation will occur more or less easily. During shocks the inertial mass will hit the stoppers and induce a high stress into the gauges. Measurements indicate that the stress induced by shocks is about 3 times the full scale of the considered accelerometer for stoppers present at  $1 \mu\text{m}$  of the inertial mass.

Considering a bandwidth of 100Hz from table 1, the system should have recovered from any shock before the next measurement (i.e in less than 10 msec). The relationship between the relaxation time  $\tau$  and the quality factor  $Q$  is given in equation (6) below.

$$\tau = \frac{Q}{\pi \cdot f} \quad (6)$$

$f$  is the natural frequency of the accelerometer. Assuming a resonance frequency around 3.5 kHz and a relaxation time equal to  $5\tau$ , equation (6) gives a maximum quality factor around  $Q < 20$  for accelerometers. If the quality factor is larger than 20, the response time will increase. For quality factor higher than 1, the main parasitic mode is at the natural



frequency. Electronic filters can be implemented to reduce the response time but the efficiency of filtering will be limited by the frequency difference between the natural frequency and the bandwidth. The main risk linked to the quality factor of accelerometers is a large response time.

### 1.8.3- Evolution of the quality factor with pressure

The damping of a mechanical system  $\gamma$  is related to both the quality factor  $Q$  and the relaxation time  $\tau$  through equation (7).

$$Q = \frac{\tau \cdot \omega}{2} = \frac{\omega}{\gamma} \quad (7)$$

$\omega$  stands for the natural pulsation. A mechanical system can be modelled by a system of the second order. Its transient response depends on its damping coefficient  $\gamma$ . Figure 14 shows the different possible transient responses to a step input.

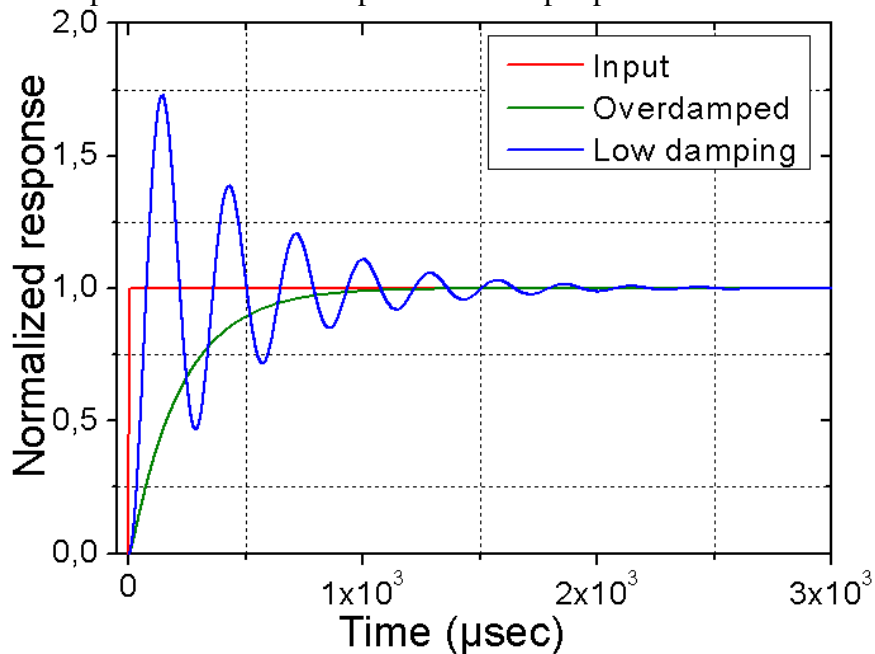


Figure 14: Different types of transient response with respect to the damping factor

The resonance frequency of the mechanical system is fixed at 3.5 kHz. The ‘low damping’, respectively ‘overdamped’ curves correspond to an arbitrary quality factor of 5, respectively 0.2. The transient response expected from an accelerometer corresponds to the ‘green’ curve.

Figure 15 shows the evolution of the quality factor of MEMS inertial sensors with respect to pressure. The gyroscope used in this measurement has already been reported in [Wal12]. The accelerometer measured has already been described in [Rob09]. The green and blue zone corresponds respectively to the pressure environment which is compatible with the quality factor constraints required by gyroscope and accelerometers respectively.

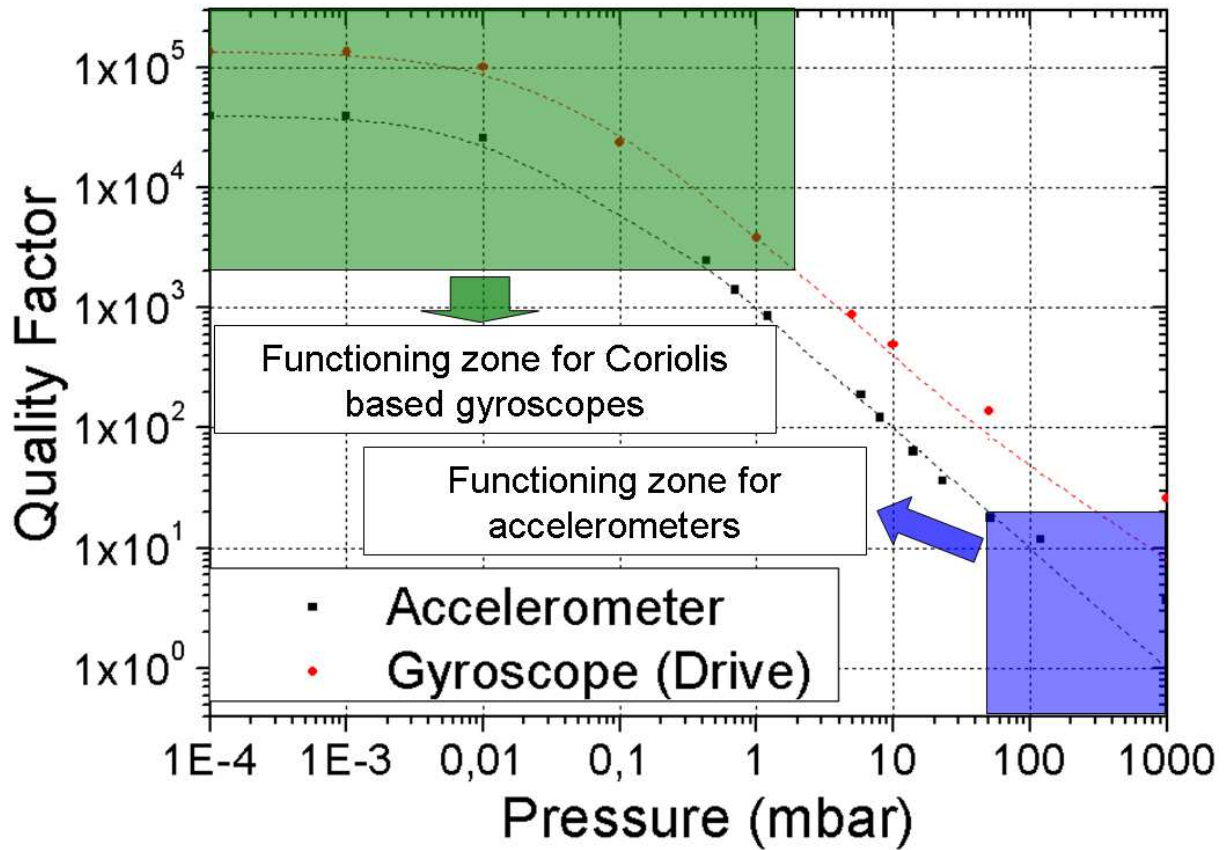


Figure 15: Evolution of the quality factor of MEMS inertial sensor with pressure

Assuming a viscous behavior of the sensor the experimental points have been fitted (dash line) using the law given in equation (8) [Ten11PhD]:

$$Q = \frac{1}{A.P + K_i} \quad (8)$$

$P$  is the external pressure,  $A$  and  $K_i$  the fitting parameters. The behaviour of the two sensors is identical. Both of them behave in a viscous way for pressures down to 0.1mbar. Because the drive mode of the gyroscope is balanced the dual-mass gyroscopes possesses a higher quality factor than the accelerometer. Table 5 gives the fitting parameters used for in figure 15.

Accelerometer	$A=10^{-3} \text{mbar}^{-1}$ and $K_i=25 \cdot 10^{-6}$
Gyroscope (drive mode)	$A=25 \cdot 10^{-5} \text{mbar}^{-1}$ and $K_i=7 \cdot 10^{-6}$

*Table 5 : Fitting parameters for inertial MEMS sensor*

These rough calculations show that using only one cavity to package both accelerometers and gyroscopes is risky. The constraints on quality factor extrapolated in this section show no pressure window com with both sensors. Therefore, other approaches need to be developed in order to authorize easy monolithic co-integration of accelerometer and gyroscopes with a standard Wafer Level Packaging (WLP).

In this thesis we will focus on two different strategies. In chapter 5, the development of resonant accelerometer will be described. Dynamic accelerometers are resonant sensors. They provide a co-integration solution because they function in vacuum, like the Coriolis based gyroscopes.

In chapter 6, a controllable source of damping is proposed. Such control can be applied on the accelerometer in order to selectively decrease the quality of the sensor whatever its pressure environment.

But before any advanced development of co-integrated inertial sensors, the sensing element should be studied. Since all sensors described in this thesis use the same detecting elements, it is critical that its behavior is well known and modeled. A mechanical and thermal model of the nanogauge is described in the next chapter along with a noise evaluation of the sensor. Consumption issue and their influence on self-heating and on dynamic range are also studied.

## Chapter 2: Model of the piezoresistive nanogauge

The detection mean of all the sensors described in this thesis is a half Wheatstone bridge made of two piezoresistive Silicon nanogauges. In order to understand the behavior of the sensor, a model of the detection mean has to be built. In the following section we will describe the response of a single nanogauge to the main external parameters. Then the Wheatstone bridge influence on the model will be evaluated. Finally the model limitations will be extracted from experiments.

### 2.1 Piezoresistive detection based on suspended nanogauges

Figure 16 shows a SEM view of a nanogauge used as detection mean. On the picture, we clearly see the thickness difference of the MEMS part of the device etched by DRIE (Deep Reactive Ion Etching) with respect to the small NEMS part in which the nanogauge is formed. On this picture, the MEMS part is 10 $\mu$ m thick and the NEMS part is 250nm thick.

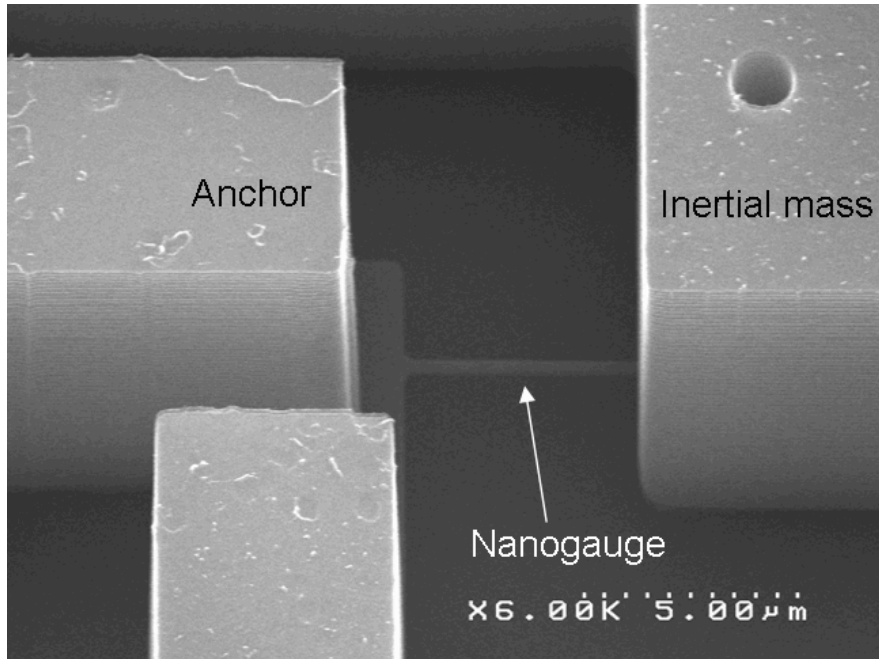


Figure 16: SEM view of a typical suspended nano-gauge

The electromechanical transduction is done through the piezoresistive effect. All nanogauges are p-type and [110] oriented in order to maximize the piezoresistive coefficient [Kan91]. The nanogauges are suspended and we will consider that they are submitted to compressive/tensile stress only. Given the mechanical configuration, the piezoresistive coefficient to be considered is the longitudinal piezoresistive coefficient  $\pi_l$  described by Kanda in [Kan91]. The efficiency of the piezoresistive transduction can be assessed through the gauge factor  $G$ . Equation (9) gives the gauge factor relationship with the longitudinal piezoresistive coefficient  $\pi_l$  and the relative resistance change  $\Delta R/R$ .

$$\frac{\Delta R}{R} = \varepsilon.G \quad \text{with} \quad G = E.\pi_l \quad \text{and} \quad \varepsilon = \frac{\Delta L}{L} \quad (9)$$

Here  $E$  is the Young modulus of silicon (whose value is 169 GPa) and  $\varepsilon$  the relative elongation. Considering a doping of  $5 \cdot 10^{19} \text{ cm}^{-3}$  the piezoresistive coefficient can be evaluated to  $23 \cdot 10^{-11} \text{ Pa}^{-1}$  from [Kan82]. The gauge factor has therefore a theoretical value of 37.

It is worth mentioning that this evaluation is based on the assumption that the values of both Young's modulus and piezoresistive coefficient are not affected by confinement or surface effects in the sub-micrometer thin suspended nanogauge. Hence we assumed the same value as in a bulk material of single-crystalline material.

## 2.2 Mechanical limits of piezoresistivity in silicon

### 2.2.1 Mechanical limitation

#### 2.2.1.a Buckling conditions

The piezoresistive effect describes the relative resistance change due to the mechanical stress applied to the material i.e silicon. Compressing a mono-crystal material can result in its destruction if the stress applied is too important. Several limits reduce the maximum stress that can be applied to a silicon nanogauge. First of all, the gauge should not buckle. Buckling calculation [Roarks12] leads to equation (10) for the critical stress of buckling.

$$\sigma_C = \frac{\pi^2}{3} \cdot \frac{t_j^2}{l_j^2} \cdot E \quad (10)$$

$t_j$  is the gauge thickness and  $l_j$  the gauge length. With a gauge thickness  $t_j = 250 \text{ nm}$  and a length  $l_j = 5 \text{ }\mu\text{m}$ , the critical stress for buckling condition is evaluated in this case at  $\sigma_C = 1.4 \text{ GPa}$ .

#### 2.2.1.b Fracture deformation limit

In order to measure the fracture limit on the nanogauges, structures authorizing large displacement were measured. The available structure which authorizes the largest gauge constraints is an in-plane gyroscope structure embedding nanogauges and electrostatic actuators. In-plane movement has been created in this structure through AC electrostatic actuation. A frequency sweep has been carried out around the resonance frequency of the sense mode so as to maximize the displacement amplitude. In order to create the largest displacement, the experiment has been carried out in vacuum, which allowed a significant amplification of the displacement obtained through the quality factor of the sense mode of the gyroscope ( $Q \sim 4 \cdot 10^4$ ). The induced stress has been followed by the piezoresistive signal measurement. Figure 17 shows the piezoresistive signal measured at resonance with respect to the actuation voltage.

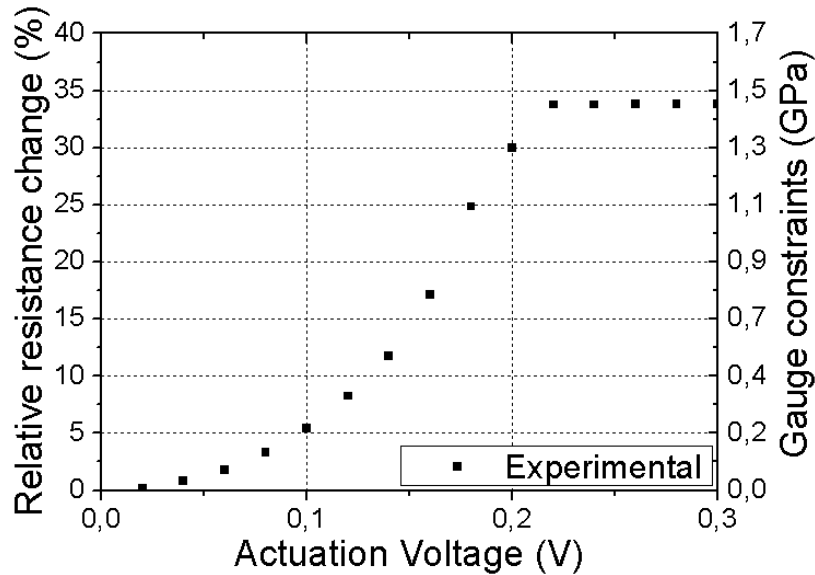


Figure 17: Piezoresistive signal obtained for in-plane displacement

The piezoresistive signal initially increases with the applied voltage following a quadratic dependence. The lever arm reaches the mechanical stoppers at an amplitude corresponding to 33% of relative resistance change. Assuming a piezoresistive coefficient of  $23 \cdot 10^{-11} \text{ Pa}^{-1}$ , the mean gauge stress is estimated to be around 1.4 GPa when the lever arm reaches the stoppers, which are at  $0.75 \mu\text{m}$  from the inertial mass. The geometrical dimensions allow an evaluation of the relative displacement (that is the strain)  $\varepsilon$  of 3.8 %, (corresponding to a stress level of 6,4 GPa) which is in the order of magnitude (even with a larger value here) of the fracture limit, which is usually given as 1 GPa for high quality single-crystal silicon having very low level of dislocations. From these values, a numerical estimation of the gauge factor around 10 can be given. However, the estimation of the relative displacement and hence the stress level and gauge factor is submitted here to a large uncertainty. Indeed, due to the initial inertial mass deformation and the technological variations on the MEMS etching, the uncertainty on the distance from the lever arm to the stops is quite large. It is worth mentioning that the 6,4 GPa is an extremely large stress level, which is difficult to reach without breaking the structure due to fracture. Therefore, it is much better to define a safety margin for the operation of silicon nanogauges. Hence, the maximum allowable stress level is fixed at 100 MPa..

Repetitive measurements were carried out on the same structure. The relative change of resonance frequency induced by this measurement is about 50 ppm (1 Hz out of 20 kHz) which is below our uncertainty level (due to temperature among others). This experiment shows that the nanogauges can provide a relative resistance change up to 33 % without observing fracture and gauge destruction. The linear range of the piezoresistive effect is probably much higher than the 100 MPa limit chosen in our design rules. However precise dedicated test structures are needed to be assertive on that subject.

### 2.2.2 Piezoresistive limitation

Another limitation, possibly more restrictive, is the linearity limit of the piezoresistive coefficient. Stress up to 150 MPa induces nonlinearities below 0.1% from [Bar09]. Simultaneous displacement and electrical measurements allowed an evaluation of the linearity of the piezoresistive response. An AC actuation voltage has been applied to the actuation electrode of an out-of-plane accelerometer. The corresponding displacement has been monitored through optical Doppler measurement. On the other hand, the electrical signal read

from the piezoresistive nanogauges has been measured at the same time. Figure 18 shows the setup used for this measurement.

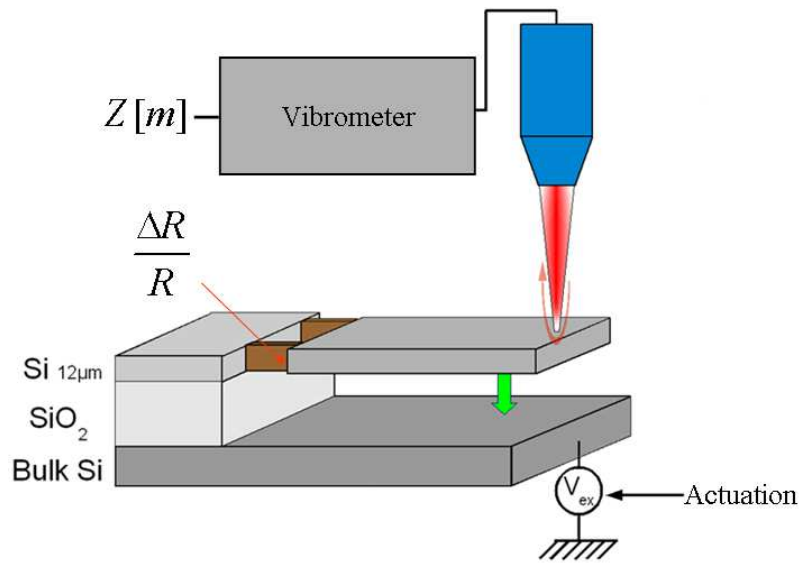


Figure 18: Experimental implementation of coupled vibrometer and electrical measurement

Figure 19 shows the piezoresistive response with respect to the inertial mass displacement. The discrepancy with respect to the linear fit is shown on the top.

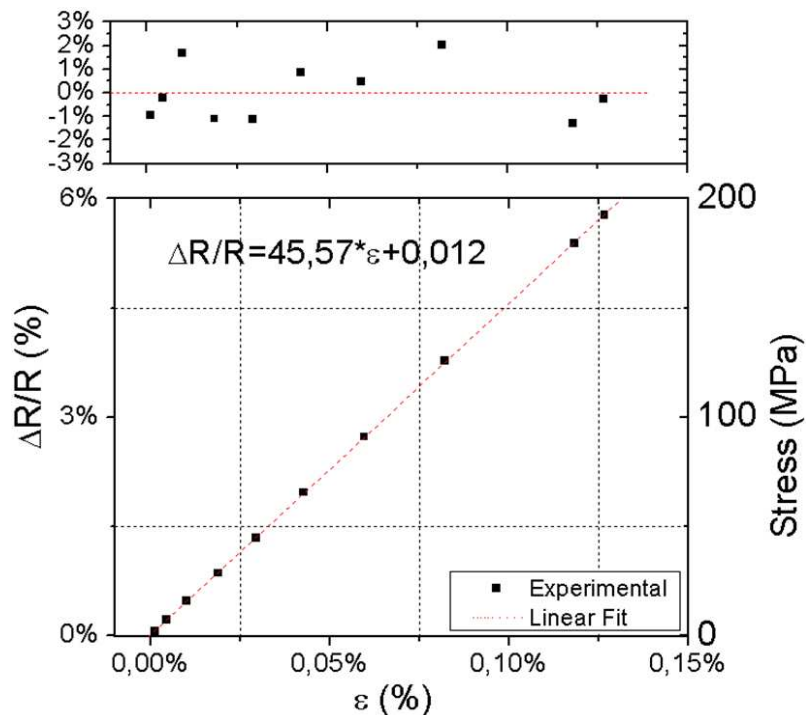


Figure 19: Linearity evaluation of the piezoresistive effect

Larger ranges are inaccessible because of geometric and material limitations. The linearity of the piezoresistive response is better than 0.3% up to  $\epsilon = 0,13 \%$  ( $\sigma = 220 \text{ MPa}$ ). In order to keep a safeguard, sensors have been designed with a full scale of 100MPa.

## 2.3 Thermo-electro-mechanical behavior of the detection mean

### 2.3.1 Model of a piezoresistive nanogauge

In this section, we will model the behavior of the piezoresistive nanogauge used as detection mean. The thermal, electrical and piezoresistive parameters defined in the model will be validated experimentally. The model objectives are to provide simple analytical formulas able to predict the nanogauge behavior for standard environment. The model needs to be valid for a temperature range extending from  $-45^{\circ}\text{C}$  to  $85^{\circ}\text{C}$ . The stress applied to the nanogauge should stay below the linear range of 200 MPa as defined in section 2.2.

While submitted to heating, the nanogauge is guided at both ends i.e displacement can occur only along the longitudinal direction (due to the compression induced by thermal expansion). The temperature of the anchors is considered as constant and equal to  $T_{EXT}$ . The behavior of the piezoresistive nanogauge has been modeled by considering that only two parameters can influence the resistance of the nanogauge: stress  $\sigma$  and temperature  $T$ . If we consider that the electrical resistance is influenced only by these parameters, the resistance value of the nanogauge can be modeled at the first order by equation (11):

$$R(T, \sigma) = R_0 + \frac{\partial R}{\partial T}_{\sigma=\sigma_0} \cdot \Delta T + \frac{\partial R}{\partial \sigma}_{T=T_0} \cdot \Delta \sigma + \frac{\partial^2 R}{\partial \sigma \partial T} \cdot \Delta \sigma \cdot \Delta T \quad (11)$$

$R_0$  defines the reference working point at  $T=T_0=300\text{K}$ ,  $\sigma=\sigma_0$ .  $\sigma_0$  is the residual constraint applied to the gauge by the fabrication process. We can define the first order coefficients, the Temperature Coefficient of Resistance (TCR), the Piezoresistive Coefficient ( $\pi$ ) and the second order coefficient, the Temperature Coefficient of piezoresistivity (TC $\pi$ ) as:

$$TCR = \frac{1}{R_0} \cdot \frac{\partial R}{\partial T}, \quad \pi = \frac{1}{R_0} \cdot \frac{\partial R}{\partial \sigma} \quad \text{and} \quad TC\pi = \frac{1}{\pi_0} \cdot \frac{\partial \pi}{\partial T} \quad (12)$$

$\pi_0$  defines the reference piezoresistive coefficient at  $T=T_0=300\text{K}$ . Using equation (11) we can express the resistance as has a function of the different coefficients already defined:

$$R(T, \sigma) = R_0 \left[ 1 + TCR \cdot \Delta T + \Delta \sigma \cdot \pi_0 (1 + \Delta T (TCR + TC\pi)) \right] \quad (13)$$

In order to predict the behavior of the piezoresistive nanogauge, evaluation of the four coefficients ( $R_0$ ,  $\pi_0$ , TCR, TC $\pi$ ) are required.

### 2.3.2 Experimental measurement

#### Setup limitation

The setup used for nanogauge measurement is described in this section. The polarization source used is a 2600a from Keithley Instrument. The voltage measurement and switching is done through the System Switch/Multimeter 3700a. Figure 20 shows a picture of the measurement bench.



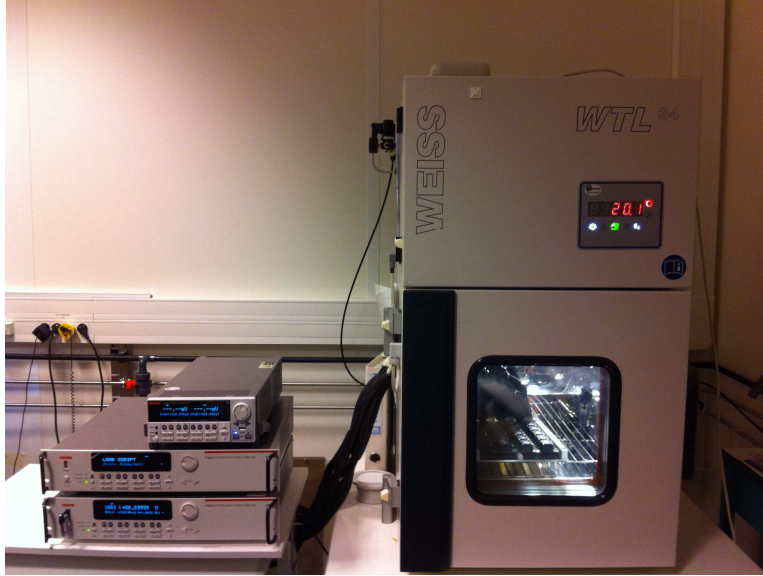


Figure 20: Experimental setup using temperature controlled chamber

Using the datasheet, the resistance measurement uncertainty has been calculated in equation (14). For this calculation, we consider a bias current around  $100 \mu A$ , with an uncertainty of  $90 nA$ . A nanogauge resistance of  $2 k\Omega$ . A fullscale range of  $1 V$  and an uncertainty of  $5 \mu V$  for the 3700a.

$$\frac{\Delta R}{R} = \frac{\Delta V}{V} + \frac{\Delta I}{I} = 925 ppm \quad \text{Or } \sim 2\Omega \text{ for a } 2k\Omega \text{ nanogauge} \quad (14)$$

The main source of uncertainty is the sourcemeter with a relative uncertainty of  $900 ppm$ .

The temperature is extracted from five platinum resistance ( $Pt100$ ) mounted at the center and at the four corners of the PCB. The same instruments follow their resistance change with temperature. Therefore, knowing that  $TCR = 3906 ppm/^\circ C$  for Platinum resistance, equation (15) gives the uncertainty obtained concerning the temperature measurement.

$$\Delta T = \frac{1}{TCR} \cdot \frac{\Delta R}{R} = 0.23^\circ C \quad (15)$$

All resistance measurements are done in a temperature-controlled chamber and they have been performed following the same measurement protocol using four-point measurement and offset compensation. For more details about the measurement protocol please refer to Appendix 1.

#### *R<sub>0</sub> estimation*

The value of  $R_0$  can be measured at room temperature through standard four-point measurement. For a doping of  $5 \cdot 10^{19} \text{ cm}^{-3}$ , typical nanogauges values gives  $R_0 \sim 1950 \Omega$  (with a standard deviation of 4% at the wafer level). This value is an agreement with the value  $R = 1840 \Omega$  that one can calculate directly from the resistor dimensions ( $L = 5 \mu m$ ,  $w = 250 \text{ nm}$ ,  $t = 250 \text{ nm}$ ) and the resistivity  $\rho = 2.3 \cdot 10^{-5} \Omega \cdot \text{cm}$  related to p-type silicon at a doping level of  $5 \cdot 10^{19} \text{ atoms/cm}^3$ .

#### *$\pi_0$ estimation*

The experiment done in section 2.2 allowed an evaluation of the efficiency of the piezoresistive transduction. The electrical measurement allows an evaluation of the relative resistance change. Using geometrical values, the optical measurement of the vibrations allows an extraction of the relative elongation of the nanogauges. Using both measurements, the

gauge factor has been evaluated to **43**. It corresponds to a longitudinal piezoresistive coefficient  $\pi_0$  of  $23.10^{-11} \text{ Pa}^{-1}$ . The value extracted from the measurement corresponds well with the theoretical value considering a doping of  $5.10^{19} \text{ cm}^{-3}$ .

*TCR estimation*

Measurement in temperature controlled room has been performed. Using a packaged accelerometer, the resistance of the nanogauge has been measured while taken up to  $80^\circ\text{C}$  by steps of  $20^\circ\text{C}$ . Figure 22 shows the evolution of two nanogauges for different temperature steps.

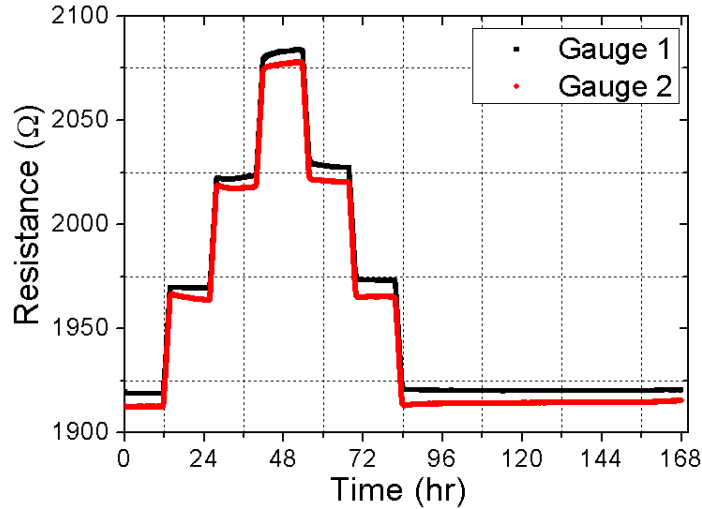


Figure 21: Nanogauge resistance for different temperature steps

The resistance values of the two nanogauges stay close to each other and follow the temperature profile of the chamber. The temperature has been recorded using platinum resistances (Pt100) placed on the PCB chip. Using this temperature measurement it is possible to extract the TCR value for these nanogauges. Figure 22 shows the evolution of the nanogauges resistance with respect to temperature.

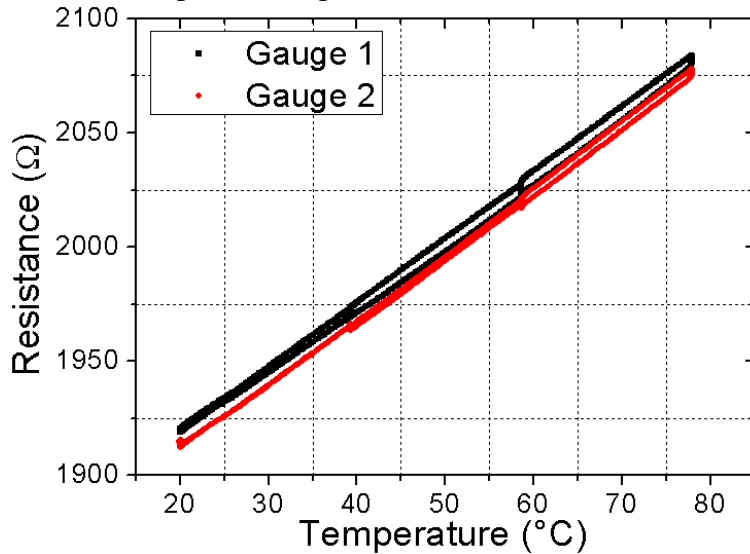


Figure 22: Resistance variation with respect to temperature

The assumption of first order correlation between resistance and temperature seems acceptable. Using definition provided by equation (12) the TCR of the nanogauges has been calculated. The mean **TCR** of nanogauges for this batch has been evaluated around **1433 ppm/°C** with a standard deviation of 186 ppm/°C. Considering gauges from the same bridge,

the TCR difference between those nanogauges falls to 103 ppm/°C with a standard deviation of 161 ppm/°C. These statistical values are given using a population of 30 different bridges.

*TC $\pi$  estimation*

While in the temperature-controlled chamber, a controlled actuation has been applied to a functional accelerometer, the temperature of the chamber followed a repetitive cycles of 8 hours at 10°C and 8 hours at 70°C. Every minute a measurement cycle occurred. The nanogauges were measured in two positions. In a first position when no actuation voltage was applied and when a 10V actuation voltage was applied to the actuation electrode.

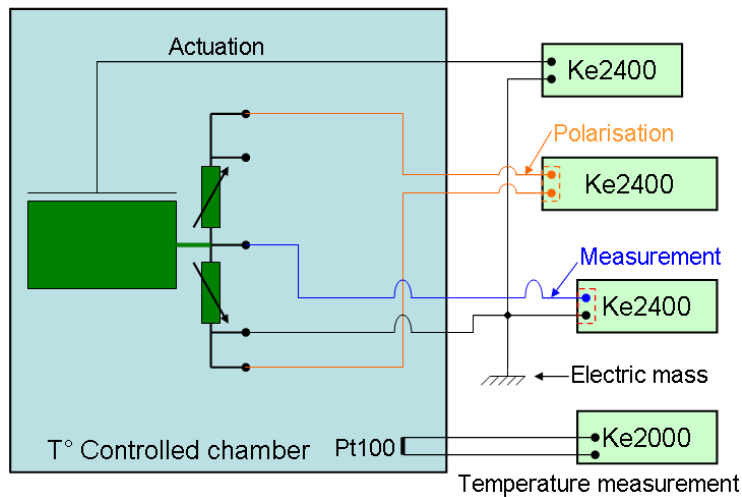


Figure 23: Electrical setup of the experiment for piezoresistive coefficient measurement

Using the device sensitivity measured in chapter 4.1.1 and equation (12), the piezoresistive coefficient can be calculated under the assumption of a linear trend between 10°C and 70°C. Figure 24 shows the variation of the piezoresistive coefficient with temperature.

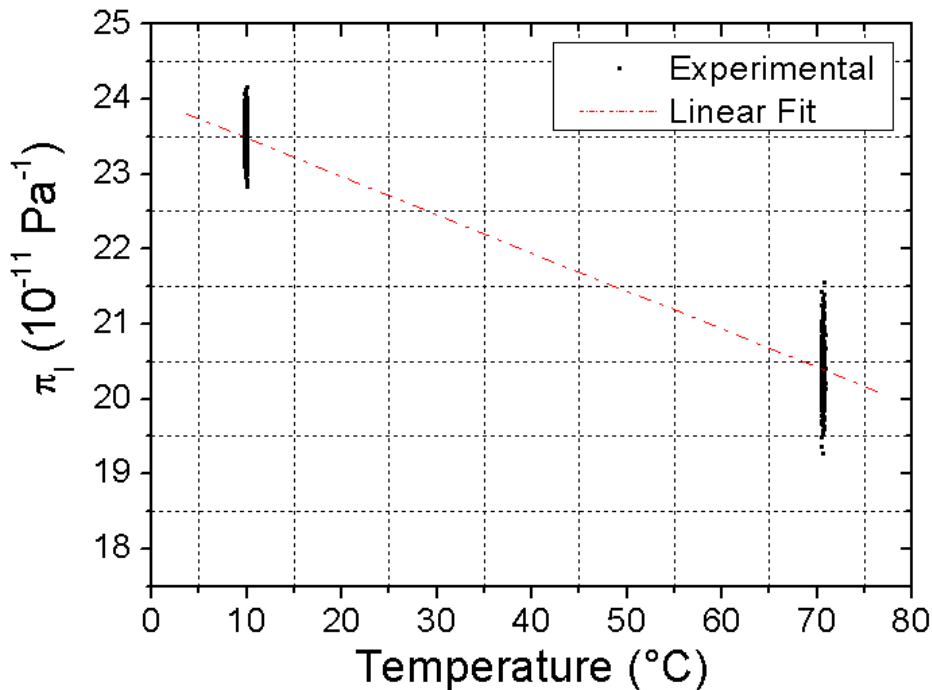


Figure 24: Piezoresistive coefficient for different temperatures

In equation (13) a linear variation of the piezoresistive coefficient has been assumed. The linear variation coefficient  $TC\pi$  can be evaluated around **-2060 ppm/°C**. Figure 25 shows a study from [Kan91] which depicts the variation of the piezoresistive coefficient with respect to doping. With a doping around  $5.10^{19} \text{cm}^{-3}$  our measurement fits well with this study (even if it relates to the  $\pi_{44}$  coefficient) .

$$P \equiv \text{corrective factor on } \pi_{44} \quad \pi_{44} = \pi_{44}(300K)P(N, T)$$

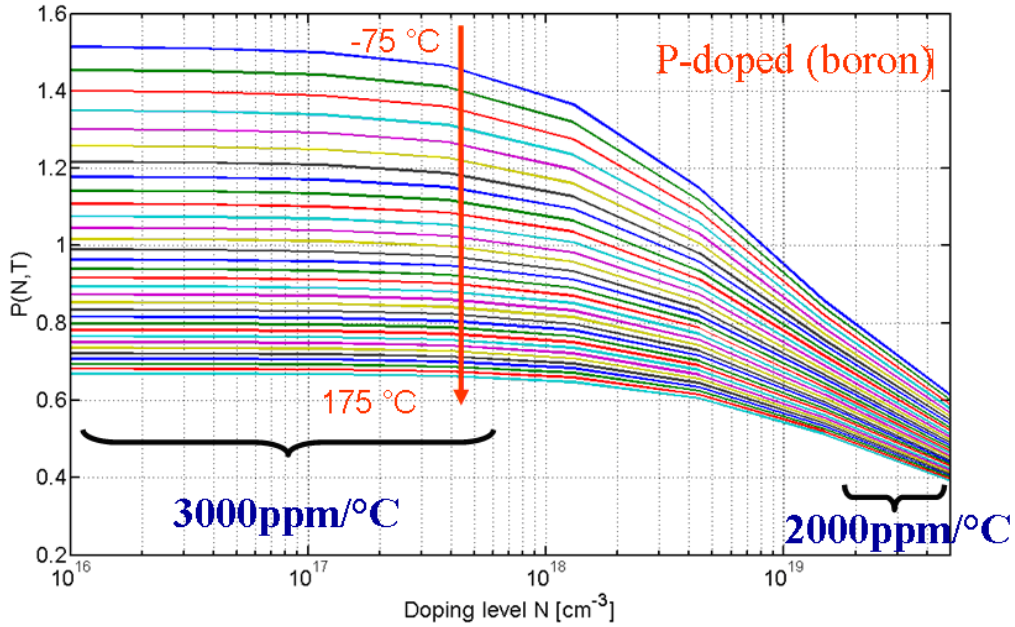


Figure 25: Piezoresistive coefficient variation with doping

Using the previous results of this section, a summary table has been built that gives the different modeling parameters obtained for the model of the single nanogauge. Table 6 shows a summary of the different modeling parameters found for these fabricated nanogauges.

Nanogauge Parameters	Mean value	Standard deviation	Relative Standard deviation
$R_0$	1950Ω	80 Ω	4%
TCR	1440 ppm/°C	110ppm/°C	7.6%
$\pi_0$	$23.10^{-11} \text{ Pa}^{-1}$	-	-
$TC\pi$	-2060ppm/°C	2 Samples	N.A

Table 6 : Modelling parameters of a piezoresistive nanogauge

### 2.3.3 Model of a half Wheatstone bridge based on nanogauges

The thermal behavior of the sensor output strongly depends on the polarization scheme. In the previous section we have assumed that two parameters  $T$  and  $\sigma$  can influence the nanogauge resistance. The temperature tends to increase the resistance of all nanogauges in the same way. On the other hand, stress is applied specifically on each nanogauge depending on the mechanical architecture.

We can therefore define a common mode where the nanogauges will vary identically mainly due to temperature variation. A differential mode can also be defined where the nanogauges will vary in opposite way through the opposite mechanical stress submitted to each nanogauge. In a Wheatstone bridge configuration the stress applied to each of the nanogauge are indeed opposite. With this organization, the influence of temperature on the sensor output can be minimized.

In this section we will consider only the polarization scheme shown in figure 26 corresponding to a half-bridge configuration with four-probe read-out. Other temperature parameters can be obtained using different polarization schemes. Figure 26 shows a schematic of the considered readout circuit. The two nanogauges submitted to an opposite stress forms a half Wheatstone bridge.  $V_{POL}$  is the polarization voltage along one nanogauche.

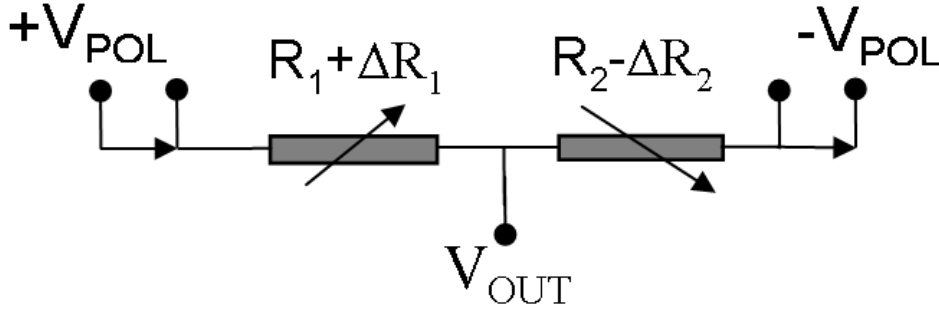


Figure 26: Schematic of the half Wheatstone bridge used for detection

Considering equation (13) the theoretical behavior of the two resistances can be written:

$$R_1(T, \sigma) = R_{10} [1 + TCR_1 \cdot \Delta T + \Delta \sigma \cdot \pi_1 (1 + \Delta T (TCR_1 + TC \pi_1))] \quad (16)$$

$$R_2(T, \sigma) = R_{20} [1 + TCR_2 \cdot \Delta T - \Delta \sigma \cdot \pi_2 (1 + \Delta T (TCR_2 + TC \pi_2))] \quad (17)$$

The output voltage for the polarization scheme considered is expressed in equation (18).

$$V_{OUT}(T, \sigma) = \frac{R_2(T, \sigma) - R_1(T, \sigma)}{R_1(T, \sigma) + R_2(T, \sigma)} \cdot V_{POL} \quad (18)$$

The output voltage of the half Wheatstone bridge can be described in function of the temperature and stress at the first order.

$$V_{OUT}(T, \sigma) = V_{OUT_0} + \frac{\partial V_{OUT}}{\partial T} \Delta T + \frac{\partial V_{OUT}}{\partial \sigma} \Delta \sigma + \frac{\partial^2 V_{OUT}}{\partial \sigma \partial T} \Delta \sigma \Delta T \quad (19)$$

The Temperature Coefficient Offset (TCO), is defined as:

$$TCO = \frac{1}{V_{POL}} \cdot \frac{\partial V_{OUT}}{\partial T_{a=0}} \quad (20)$$

The Sensitivity (S) and the Temperature Coefficient of Sensitivity (TCS) are defined as:

$$S = \frac{1}{V_{POL}} \frac{\partial V_{OUT}}{\partial \sigma} \quad \text{and} \quad TCS = \frac{1}{S_0} \cdot \frac{\partial S}{\partial T_{\sigma=\sigma_0}} \quad (21)$$

$S_0$  is the sensitivity at temperature at  $T=T_0=300K$  and  $\sigma=\sigma_0$ . Using (21) we can derive the expression of the output voltage using the sensor thermal parameters.

$$V_{OUT}(T, \sigma) = V_{POL} \cdot (A_0 + TCO \cdot \Delta T + \Delta \sigma \cdot (S_0 + (TCS + TCO) \cdot \Delta T)) \quad (22)$$

The expression of  $A_0$  the output reference offset can be easily extracted from (18):

$$A_0 = \frac{R_{20} - R_{10}}{R_{10} + R_{20}} \quad (23)$$

Using equation (16), (17) and (19) the expression of the TCO can be expressed using the temperature parameters of the nanogauges. Equation (24) shows the first order term approximation of the Temperature Coefficient Offset.

$$TCO = \frac{R_{10}TCR_1 - R_{20}TCR_2}{R_{20} + R_{10}} \quad (24)$$

Let's assume that the stress applied on the two nanogauges possess the exact same intensity but opposite value. Using the equations (16) and (17) the reference sensitivity  $S_0$  can be extracted:

$$S_0 = \frac{R_{10}\pi_1 + R_{20}\pi_2}{R_{20} + R_{10}} \quad (25)$$

The expression of the TCS can also be extracted using the temperature parameters of the nanogauge. Equation (26) gives the **first order term** of the Temperature Coefficient of Sensitivity respectively.

$$TCS = \frac{R_{10}\pi_1(TCR_1 + TC\pi_1) + R_{20}\pi_2(TCR_2 + TC\pi_2)}{R_{10}\pi_1 + R_{20}\pi_2} \quad (26)$$

Equations (23) to (26) show that the thermal performances of the sensors can be extracted using the behavior a single nanogauge. Table 7 shows a summary of the thermal parameters extracted for the half Wheatstone bridge configuration described in figure 26.

Nanogauge Parameters	Mean value	Standard deviation (STD)	Datasheet parameters (Assuming $V_{POL}=0.1V$ )
$A_0$	300ppm	8000ppm (30 Samples)	30 $\mu V$ STD(800 $\mu V$ )
$TCO$	30ppm/ $^{\circ}C$	70ppm/ $^{\circ}C$ (30 Samples)	3 $\mu V/^{\circ}C$ or 0.1%F.S / $^{\circ}C$ or 10mg/ $^{\circ}C$ for a10g accelerometer
$S_0$	23.10 $^{-11}V/V/Pa$	-	2mV/V/g or 200 $\mu V/g$ for an accelerometer
$TCS$	-2080ppm/ $^{\circ}C$	1 Sample	4.2 $\mu V/g/^{\circ}C$ for an accelerometer

*Table 7 : Modelling parameters of a half Wheatstone bridge based on piezoresistive nanogauge*

Thanks to the half Wheastone bridge configuration all the common mode influence can be drastically reduced with respect to the differential mode. The common mode rejection can be defined as the ratio between the influence of temperature on a single nanogauge and the same influence on a half wheatstone bridge (i.e TCR/TCO). The common mode rejection has been evaluated to 30dB.

## 2.4 Self-heating and gauge burn-out

There are two ways to measure the resistance change induced through piezoresistive effect. One can either polarize the gauge through a constant current and measure the voltage across the gauge or one can fix the voltage and measure the current going through it. The characterization methods used to accurately measure resistances are defined in Appendix.1. Read-out electronics will usually measure a voltage drop. If the electronics measure a voltage,

the signal can be artificially amplified by increasing the polarization current. This is however limited by power consumption and self heating issues. Evidence of gauge fusion has been found on several devices. Figure 27 shows an almost melted nanogauge due to misuse of the polarization instruments.

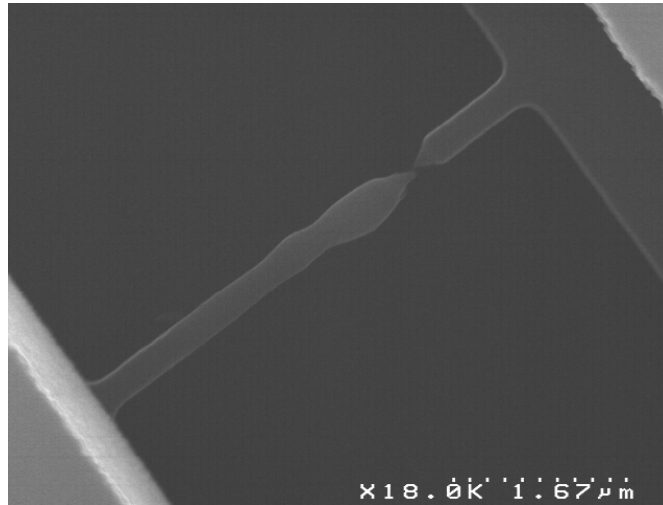


Figure 27: Almost melted nanogauge

#### 2.4.1 Self-Heating model

The thermal model for nanogauge developed in [Ett11] takes into account the temperature increase due to the Joule effect occurring on the resistance increase due to the TCR. The exact influence of self-heating has been derived using the second order differential equations shown in equation (27), where heat loss is considered to be mainly driven by heat conduction across the nanogauge (conduction, convection and emission through the surrounding air are neglected in this model).

$$\frac{\partial^2 T}{\partial x^2} + J^2 \rho_{el} \cdot TCR \cdot \rho_{th} \cdot T = \lambda_{Si} \cdot J^2 \rho_{th} (1 - TCR \cdot T_0) \quad (27)$$

$J$  is the current density,  $\rho_{th}$  the thermal resistivity of silicon and  $\rho_{el}$  the electrical resistivity of silicon. The temperature profile is parabolic and it is maximal at the middle of the gauge. Figure 28 shows the theoretical temperature distribution across the gauge for a polarization current of 400  $\mu\text{A}$ . The nanogauge considered has dimensions of  $5 \times 0.25 \times 0.25 \mu\text{m}^3$ .

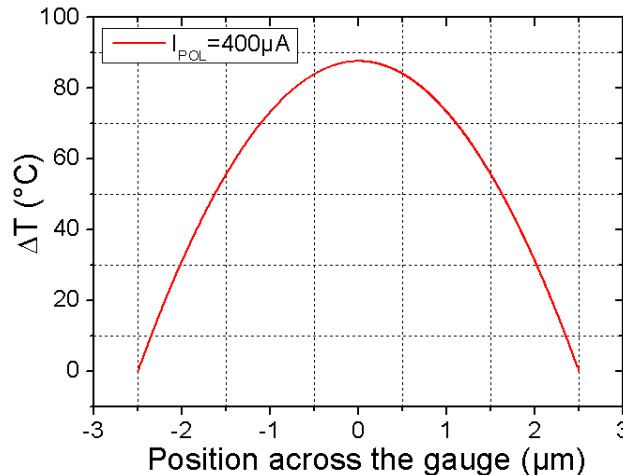


Figure 28: Temperature profile across the nanogauge ( $I_{POL}=400\mu\text{A}$ )



In this section we will investigate the current behavior of the gauge of standard dimension ( $5 \times 0.25 \times 0.25 \mu\text{m}^3$ ). The objective is to extract the critical current at which irreversible degradations appears due to excessive heating. The polarization current induces a differential voltage along the gauge. Power is dissipated through Joule effect. This power dissipation will increase the gauge temperature. It will additionally increase the nanogauge resistance through the positive TCR. If the current is too strong the gauge will finally act as a fuse; it will deteriorate and eventually melt. The I-V curve of the nanogauge has been measured for large currents (black curve). Figure 29 shows the evolution of the voltage drop across the gauge for different polarization currents. The current starts from  $0 \mu\text{A}$  and ramps up to a maximum current  $I_{MAX}$  (here  $900 \mu\text{A}$ ), then decreases to  $-I_{MAX}$  and then finishes the loop by coming down to  $0 \mu\text{A}$ .

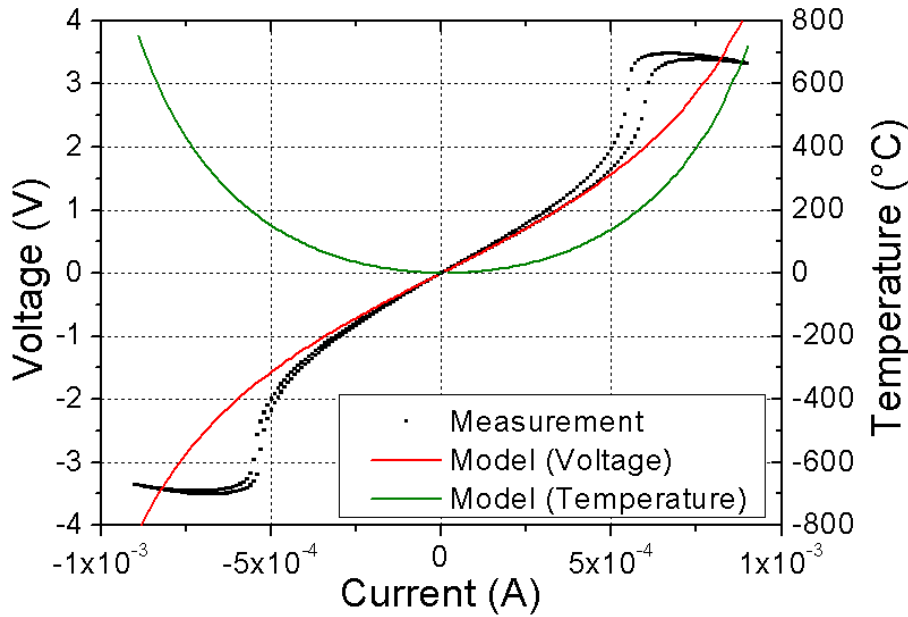


Figure 29: I/V behavior of the nanogauge for high currents

The red curves represent the model taking into account the measured TCR of the nanogauge and the self-heating effect that has been set up by [Ett11]. The green curve represents the theoretical temperature at the hottest point i.e the middle of the gauge. The model follows the measurement up to  $\sim 500 \mu\text{A}$ . We observe a maximum of polarization voltage for a current around  $600 \mu\text{A}$ . For higher currents the voltage across the nanogauge decreases. This behavior has been consistently observed. A destructive measurement of the same nanogauge shows a destructive current around  $1\text{mA}$ .

#### 2.4.2 Measurement of irreversible degradation

In order to extract the current at which irreversible degradation begins a non-destructive protocol has been set up. A standard polarization current was defined at  $50 \mu\text{A}$ . Preliminary experiments showed no observable evolution of the voltage drop for that polarization current. Identical measurements to the experiment shown in figure 29 were done in loops with increasing, for each loop cycle, the value of the maximum polarization current  $I_{MAX}$ . For each loop cycle, the voltages measured at the standard polarization (i.e  $50 \mu\text{A}$ ) were recorded. Figure 30 shows the evolution of that voltage measured across the nanogauge for an increasing maximum polarization current  $I_{MAX}$ . The voltage change have been normalized by  $V_0$ , the voltage measured on the 1<sup>st</sup> loop with  $I_{MAX} = 50 \mu\text{A}$ .



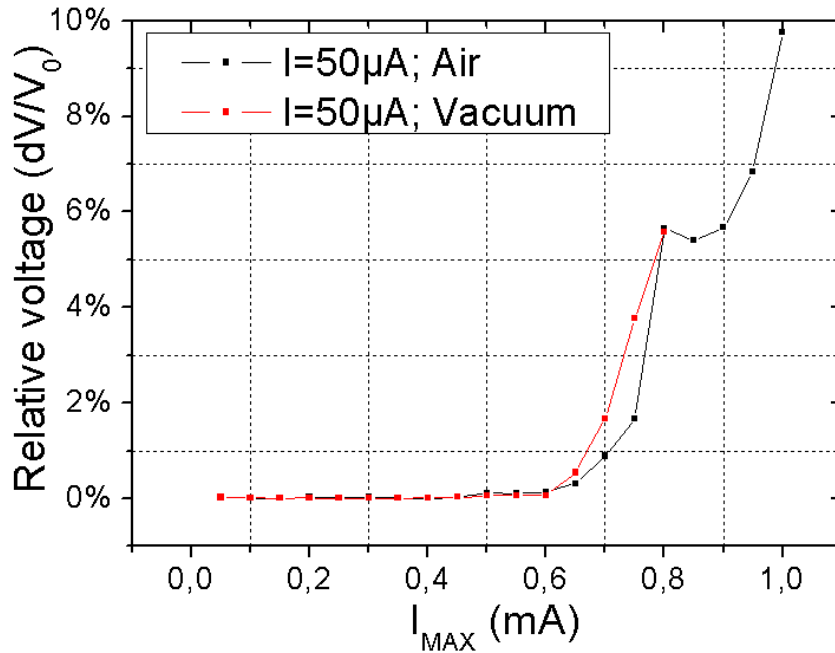


Figure 30: Voltage measured for different  $I_{MAX}$  and identical polarization ( $I=50\mu A$ )

Any evolution of the voltage drop for an identical polarization voltage will be due to the previous cycle. This graph shows that irreversible degradation begins when the maximum polarization current reaches **600 $\mu A$**  for both vacuum and air environments. This current also corresponds to the current at which the behavior of degradation has been observed in figure 29. This irreversible behavior could come from irreversible geometrical change of the nanogauge (See an exemple figure 27). The analytical thermal model is therefore suitable to predict the behavior of the nanogauge for polarization current up to 600 $\mu A$ . For higher currents, the nanogauge supports irreversible electric changes and such changes will be very difficult to model. It is even more reasonable to consider that the described model is able to predict the gauge behavior for current up to 500  $\mu A$ . The analytical model is convenient for a rough expression of the temperature behavior inside the nanogauge. In order to suppress any irreversible degradation and to limit self-heating, an additional safety margin is chosen and the maximum current in the gauge has been set to 300 $\mu A$ . This corresponds to a polarization voltage of 0.4V on standard 5\*0.25\*0.25 $\mu m^3$  nanogauge.

## 2.5 Noise model of the nanogauge

Different sources of noise generate parasitic signals which superimpose with the sensor output signal and limit its resolution. These randomly generated signals will define the Signal to Noise Ratio (SNR) that can be reached by the sensor. Considering the nanogauges only, there are mainly three types of noise to consider: the electronics noise on one hand and the thermal (Johnson) noise and the flicker noise within the nanogauge, in the other hand. The thermo-mechanical noise present in the gauge (NEMS dimensions) is considered negligible with respect to the thermo-mechanical noise of the inertial mass (MEMS dimensions). Generally, noise contributions to the sensor are considered in terms of Power Spectral Density (PSD) expressed in  $V^2/Hz$ . It represents the amount of power randomly generated for each frequency.

### 2.5.1 Electronics noise

The electronics noise comes from the readout electronics circuit which is necessary to extract and amplify a signal from the MEMS. Considering piezoresistive nanogauge, two types of electronic noise will superimpose. Due to readout noise the voltage read by the electronics will vary with time around the actual value of the MEMS. Due to the polarization noise, the current (assuming a current polarization) will vary with time and change the voltage measured across the resistance. These two types of noise add. Together they are considered as a white noise of amplitude of the order of  $10nV/\sqrt{Hz}$ . If the polarization source is linked to the electrical supply, 50 Hz parasitic peak can also appear.

### 2.5.2 Johnson noise

The Johnson noise is the fundamental noise limit of a resistor [Har00]. This white noise is due to the thermally activated electrons in the gauge whose movement causes voltage fluctuations. Its spectral density is proportional to the resistance of the gauge and to its temperature. Equation (28) depicts the expression of its Power Spectral Density.

$$S_J = 4.k_B.T.R \quad (28)$$

Here  $S_J$  is the Johnson noise spectral density,  $k_B$  is the Boltzmann constant,  $T$  is the temperature (in K) and  $R$  the resistance (in  $\Omega$ ).

### 2.5.3 Flicker Noise

When considering noise of quasi-static sensors, flicker noise is the predominant issue. It is also called the  $1/f$  noise because its power spectral density decreases with increasing frequency (with a  $1/f$  slope). Some theoretical explanation points out electron-phonon scattering in the crystal. They would induce mobility fluctuation with an occurring probability in  $1/f$ . Hooge [Hoo78] sets an empirical relation to evaluate such noise (29).

$$S_{1/f} = \frac{\alpha.V_{POL}^2}{N.f} \quad (29)$$

$V_{POL}$  is the voltage polarization across the gauge,  $N$  the number of carriers in the gauge and  $f$  the frequency.  $\alpha$  is the Hooge factor. This factor is an empirical parameter related to the material. Less crystal defects or better mobility could reduce the flicker noise. The Hooge factor could possibly be modified by surface preparation and annealing [Van86]. For silicon value,  $\alpha$  is estimated in the range from  $10^{-7}$  to  $10^{-3}$  [Har00].

### 2.5.4 Experimental evaluation of the Hooge Factor

The  $1/f$  noise is the predominant noise for quasi-static sensors. Evaluation of the Hooge factor obtained for this batch is critical in order to assess the resolution of the fabricated inertial sensors. A specific setup has been used for this measurement. Figure 31 shows the setup along with the instrumentation used.

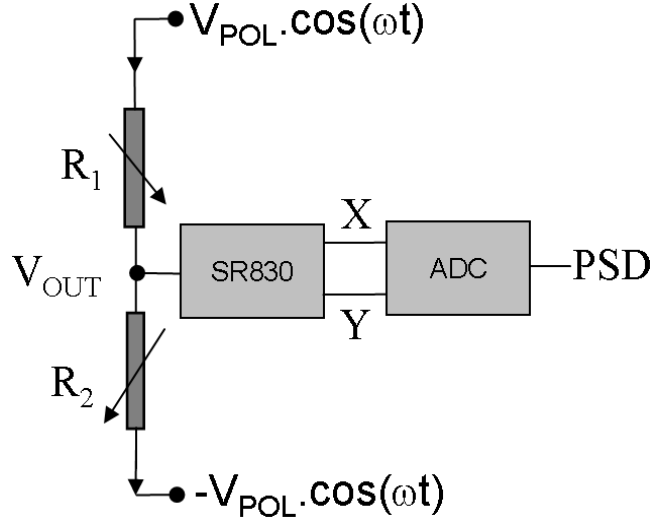


Figure 31: Experimental setup for 1/f noise measurement

A FG120 Yokogawa polarizes the nanogauge with an AC voltage at relatively high frequency (here 12.205 kHz). The Lock-in Amplifier SR830 is used as a low noise amplifier and a demodulator. The analog amplified signal is transmitted to an Analog Digital Converter. The data from the ADC allows the computer to calculate the Power Spectral Density. The main advantage of using an AC modulated polarization voltage with respect to the DC polarization is the intrinsic insensitivity to external low parasitic frequencies, such as temperature change. This insensitivity to low frequency parasitics is important for long measurements. The noise coming from the electricity supply (50Hz) and its harmonics are also avoided. The observation of the 1/f noise is easier at low frequency. Hence the setup fits well with the objectives needs. If we consider that the 1/f noise induces resistance change in the nanogauge in the form:

$$R_1 = R_{TOT1} + \delta R_1 \quad \text{and} \quad R_2 = R_{TOT2} + \delta R_2 \quad (30)$$

then, the intrinsic offset due to the nanogauge mismatch  $R_{TOT1}-R_{TOT2}$  is compensated by a slight adaptation of the polarization voltage  $V_{POL}$  at one end of the half bridge. The expression of the output voltage  $V_{OUT}$  is described in equation (31):

$$V_{OUT} = \frac{\delta R_1 + \delta R_2}{R_{TOT1} + R_{TOT2}} \cdot V_{POL} \cdot \cos(\omega t) \quad (31)$$

Assuming that  $\delta R_1$  and  $\delta R_2$  are decorrelated and similar, we will write  $\delta R$  for  $\delta R_1$  and  $\delta R_2$  independently. Identically  $R_{TOT}$  represents the mean value of  $R_{TOT1}$  and  $R_{TOT2}$ . Expressions of the power spectral density of  $X$  and  $Y$  after amplification and demodulation of the signal gives:

$$S_X = \frac{\delta R}{R_{TOT}} \cdot \left( \frac{V_{POL} \cdot G \cdot \cos(\varphi)}{2} \right)^2 \quad \text{and} \quad S_Y = \frac{\delta R}{R_{TOT}} \cdot \left( \frac{V_{POL} \cdot G \cdot \sin(\varphi)}{2} \right)^2 \quad (32)$$

With  $G$  the amplification provided by the Lock-in Amplifier.  $\varphi$  represents the phase with respect to the polarization signal. The power spectral density of the relative resistance change can be reconstructed using equation (33):

$$\frac{\delta R}{R_J} = (S_X + S_Y) \cdot \frac{4}{V_{POL}^2 \cdot G^2} \cdot \frac{R_J}{R_{TOT}} \quad (33)$$

The polarization scheme corresponds to a 2-point measurement. An additional measurement is needed in order to evaluate the parasitic resistance between the polarization

source and the nanogauge. The Power Spectral Density of the relative resistance change can then be corrected using the ratio  $R_{TOT} / R_J$  used in equation (33).  $R_{TOT}$  is the total resistance (including parasitic resistance) and  $R_J$  is the resistance of the gauges.

The Flicker noise of the nanogauge has been measured for low frequency. The dimensions of the nanogauge measured in figure 32 are  $5 \times 0.25 \times 0.25 \mu\text{m}^3$  with a doping level around  $5 \cdot 10^{19} \text{cm}^{-3}$ . The setup limitation has been evaluated by measuring the noise coming from a ceramic resistance. Using equations (29) and (33), the measurement could be correlated to the model. A Hooge factor of  $4 \cdot 10^{-6}$  could be extracted from the different measurements for a frequency range of  $[10^{-3}, 1\text{Hz}]$ . The integration time used in this measurement was  $100 \mu\text{s}$ .

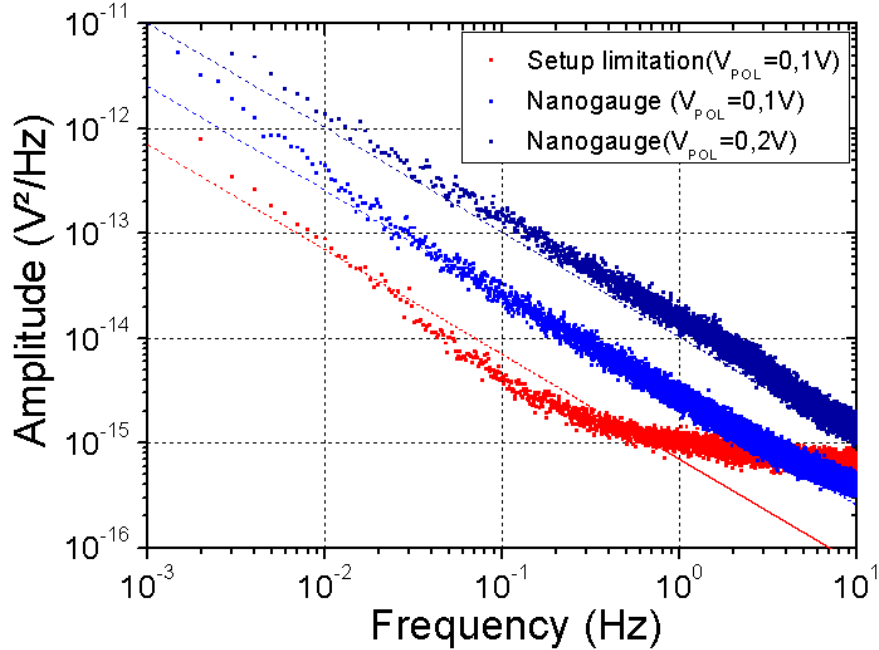


Figure 32: Measurement of the flicker noise on piezoresistive nanogauge

The white noise limitation of the setup corresponds to an electronics noise level around  $20 \text{ nV}/\sqrt{\text{Hz}}$ . The  $1/f$  slope measured on the **setup limitation** corresponds to an  $\alpha/N$  value around  $7 \cdot 10^{-14}$ . With this measurement setup no  $1/f$  with a PSD lower than the red curve can be measured. This limitation can be explained by a phase noise appearing during the demodulation step and/or from the AC source.

### 2.5.5 Influence of the different sources of noise on the output voltage

The output voltage is submitted to the different types of noise described in the previous sections and which are intrinsic to the nanogauge itself or to its readout electronics. Figure 33 shows the theoretical power spectral density of the different noise. The Brownian noise is introduced in this graph as an additional contribution. The Brownian noise is a white force noise proportional to the inertial mass. It does not depend on the nanogauges. A force noise will be transformed into voltage noise through the transfer function of the mechanical system. Its spectral density is therefore shaped by this transfer function. Here we will consider a mechanical system with a resonance frequency around  $3.5 \text{ kHz}$  and a quality factor of  $4 \cdot 10^4$ . The inertial mass considered is around  $1 \text{ ng}$ . The graph shown in figure 33 is done considering nanogauge with standard dimensions and a doping level of  $5 \cdot 10^{19} \text{cm}^{-3}$  and a polarization voltage of  $0.1 \text{ V}$ .

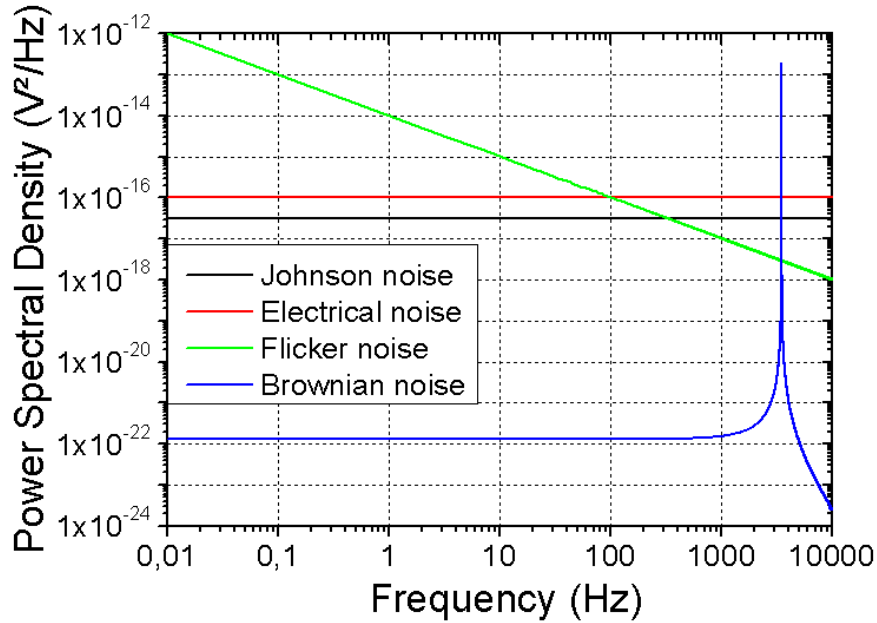


Figure 33: Theoretical Power Spectral Density of the different noise contributions in a nanogauge

The accelerometer specifications defined in chapter 1 led to a frequency bandwidth from DC to 100 Hz. Given this specification, the Brownian noise can be considered negligible. Additionally the Flicker noise is the dominant noise. Because the Flicker noise possess a square dependence to the polarization, the consumption choices made for the system and its readout electronics will be important. By reducing the polarization, the Flicker noise can be reduced along with the nanogauge consumption. This will increase the need for amplification i.e the consumption of the Low Noise Amplifier (LNA). Additionally, the amplitude of the nanogauge signal will be reduced. Hence the electronics noise influence will be increased.

### 2.5.6 Dynamic range of quasi-static sensors

All sensors in this thesis were produced on the same wafer. They were subjected to the same process flow. We have assumed that the Hooge factor is constant for the different nanogauge geometries and over a large bandwidth. Considering a bandwidth of [ $10^{-8}$ ;  $10^2$  Hz] for quasi-static sensors, the integrated noise due to both the Flicker noise and the theoretical Johnson noise were calculated. Table 8 gives the expected noise from the different quasi-static sensors along with their respective dynamic range. These estimations were done considering a maximum stress of 100 MPa. An electronics white noise of 100 nV was included for the calculation of the total noise (not shown in the table). Johnson noise has also been taken into account in the total noise evaluation; however its influence is completely negligible with respect to flicker noise.

	Nanogauge dimension	Johnson Noise	Flicker Noise	Total noise	Dynamic range
Small nanogauge ( $V_{POL}=0.1V$ )	$5 \times 0.25 \times 0.25 \mu m^3$	78.1 $\eta V$	343.4 $\eta V$	366 $\eta V$	$8,2 \cdot 10^3$
Large nanogauge ( $V_{POL}=1V$ )	$5 \times 25 \times 0.25 \mu m^3$	7.8 $\eta V$	343.4 $\eta V$	357.7 $\eta V$	$8,4 \cdot 10^4$

Table 8 : Noise evaluation of different types of gauge and sensors

For quasi-static sensors, the flicker noise is the predominant noise. The flicker noise is proportional to the polarization voltage. The other noises such as the electronics and the Johnson noise do not depend on the polarization. At the same time, the maximum output voltage (which corresponds to  $\Delta R/R=3\%$ ) is also proportional to the polarization voltage. Large gauges benefits from a large dynamic range (One order of magnitude improvement with respect to small nanogauges). However the consumption of the small nanogauges is  $5 \mu\text{W}/\text{gauge}$ , whereas it is  $54 \text{ mW}/\text{gauge}$  for the large nanogauge. The gauges **dimensions** and **doping** will set both the **dynamic range** of the sensor and the MEMS **consumption**.

## 2.6 Doping influence on performances of piezoresistive nanogauge

Thermal, mechanical and stability behavior of the nanogauge has been studied in this chapter. The doping of the nanogauge is a transverse parameter that influences many of the nanogauge performances. Table 9 shows a summary of the doping influence on the different aspects of the sensor performances.

	Sheet resistance ( $\Omega/\square$ )	Flicker Noise	Johnson Noise	$\pi_0$	$\text{TC}\pi$	TCR
If the doping increase	$\searrow$ ( $\text{N}^{-1}$ )	$\searrow$ ( $\text{N}^{-1}$ )	$\searrow$ ( $\text{N}^{-1}$ )	$\searrow$ (Low)	$\searrow$ (Low)	$\searrow$ (Low)

*Table 9 : Influence of doping on performance of piezoresistive nanogauge*

According to table 9, one can deduce that the sensitivity of the sensor will decrease with increasing doping through  $\pi_0$ . However the dynamic range and the thermal stability will increase faster. The maximum gauge stress is limited to  $100 \text{ MPa}$  due to linearity reason. The sensitivity will intrinsically be limited by this nonlinearity. A relatively high doping of  $5.10^{19} \text{ cm}^{-3}$  has been used in order to limit the influence of temperature and keep a large dynamic range.

## 2.7 Consumption-noise strategy of piezoresistive readout systems

The polarization strategy used in a piezoresistive MEMS non resonant sensor is important for the performances of the sensor. The polarization voltage has limitations:

- In section 2.4 the experimental evaluation of the degradation current exhibits the **maximum polarization** voltage that can be used for a standard nanogauge.
- If the polarization voltage is reduced, the readout signal will be also reduced. If the polarization voltage is tends to 0 the dominant noise will be the electronics noise. The **electronics consumption** will increase in order to obtain large amplification. At some point the total consumption will tend to increase because of the electronics consumption. At the same time the Signal to Noise Ratio will be reduced because of the small polarization voltage. An optimal polarization voltage can be found depending on the performances of the readout electronics (noise & consumption), and on the specifications of the whole system.

The consumption-noise relationship will be modified by the introduction of a duty cycle. Because of the **small capacitance** found in piezoresistive detection, **high duty cycle** can be applied in order to divide the gauge consumption by orders of magnitude:

Introduction of high duty cycle will influence the resolution of the device. Assuming a bandwidth of  $100 \text{ Hz}$ , each measurement point is integrated for  $10 \text{ msec}$ . Assuming a duty cycle of  $10\%$  with a modulation period of  $100 \mu\text{sec}$ , the nanogauge consumption will be

divided by 10. Additionally the measurement time for one measurement will decrease from 10 msec to 1 msec. To extract the correct SNR the noise of the device corresponds to the sum of the noise of every measurement of 10  $\mu$ sec-long i.e with a bandwidth of 100 kHz. From figure 33 we can see that the noise considering a bandwidth of 100 kHz is much larger than when considering a bandwidth of 100 Hz. In case of a dominant white noise, this technique reduces critically the SNR. In case of a dominant 1/f noise, considering a larger bandwidth of 100 kHz, the reduction is smaller.

Again, depending on the specification, different SNR-consumption tradeoffs can be made for identical MEMS.

The next chapter will focus on stiffness issues. Complex mechanical function needs to be implemented using the fabrication technology described in chapter 1. Simple analytical formulas and rules are provided to extract the stiffness of complex structures. Additionally the main mechanical functions used in chapter 4 and 5 are described and analyzed in this chapter.

## Chapter 3: Design of springs

Except very rare demonstrations of MEMS levitation [Ter12], only springs provide mobility to the MEMS structure through a structural link. A spring is usually defined as a deformable part, specifically designed so that it exhibits a predefined stiffness, which fixes the relative displacement of the two parts attached to it, when submitted to a given force. Assuming a linear behavior, the stiffness can be seen as the proportionality factor between the applied force and the resulting relative displacement. This statement holds for the different axes, leading to different values of the stiffness for each axis. In a more general formalism, the stiffness matrix of a spring is a mathematical view of the mechanical function provided by the spring. The quality of a mechanical function can be assessed through two performance parameter, the **maximum displacement amplitude** and the **directionality** of the induced displacement.

In this chapter we will begin by describing the fabrication possibilities provided by the clean room facilities. A short introduction of the spring stiffness is then given. Simple association rules are provided. They are needed to assess the stiffness of more complex structures. The most important part of the chapter is the description of specific mechanical functions such as coupling springs, decoupling springs and pivots. The geometry of the springs that realize these functions are given along with their respective advantages and limitations.

### 3.1 Fabrication limitations

In this section we will consider that the plane of the wafer surface is the X-Y plane. The geometrical dimensions of the spring all possess the same importance in terms of stiffness. The M&NEMS fabrication process flow possesses limitations on all three directions.

The springs are fabricated through successive epitaxy and photo-lithography steps. Hence they have the major drawback to possess only a very limited number of different thicknesses. The thickness of the spring is therefore limited to either the NEMS thickness (i.e 250nm) or the MEMS thickness (i.e ~10 $\mu$ m). Table 10 gives a summary of the different limitation along the three directions of space.

	In-plane directions (X, Y)	Out-of-plane direction (Z)
Dimension	<b>Continuum</b>	<b>Discretized</b> (250nm and 10 $\mu$ m)
Uncertainty	100nm (or 1:20 aspect ratio)	Respectively 10nm and 1 $\mu$ m

*Table 10 : Limitation of the fabrication process along the main directions of the wafer*

Due to this difference between the in-plane directions and the out-of-plane directions, In-plane springs will exhibit better properties than out-of-plane springs.

### 3.2 Single parallelepiped beam

In this first section, we will study a simple beam model. Using Euler-Bernoulli equation, the deformation of the beam can be calculated for different applied forces. Figure 34 shows a parallelepiped beam. The nanogauges possess an identical geometry.



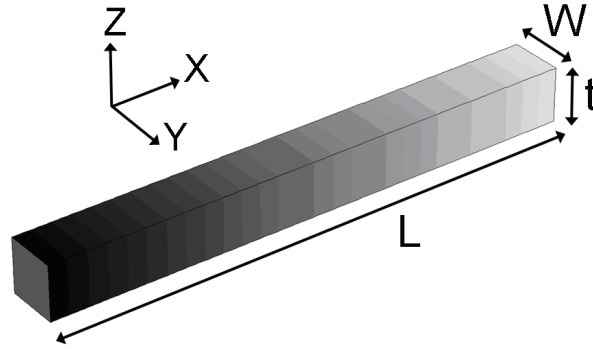


Figure 34: Dimension of a parallelepiped beam

$T$  is the thickness,  $W$  the width and  $L$  the length of the cantilever. From [Fedder94] the expression of the cantilever stiffness has been evaluated. Assuming Hooke's law and Euler-Bernoulli theory, the beam deformation has been computed for different configurations. From the force and the induced displacement, the **translational stiffness** is defined through equation (34).

$$k_i = \frac{F_i}{u_i} \quad (34)$$

$k_i$  is the translational stiffness in the  $i$  direction.  $F_i$  is the force applied on the spring in the same direction and  $u_i$  is the elongation of the spring obtained in the  $i$  direction. The **rotational stiffness** is defined through equation (35).

$$C_i = \frac{M_i}{\vartheta_i} \quad (35)$$

$C_i$  is the rotational stiffness in the  $i$  direction. Identically  $M_i$  and  $\theta_i$  are respectively the torque applied on the spring and the deformation angle induced on the spring. A summary of the beam stiffness formulas along the different translation directions and rotation directions is given in table 11 [Roark7].

$k_X = k_C = \frac{E.t.W}{L}$		$C_{MX} = \frac{2}{3} \cdot \frac{E.W^3.t}{L}$
Tensile/Compressive		Torsion
$k_Y = k_{FY} = \frac{1}{4} \cdot \frac{E.t.W^3}{L^3}$	$k_Z = k_{FZ} = \frac{1}{4} \cdot \frac{E.W.t^3}{L^3}$	$\frac{M_Y}{z} = \frac{1}{6} \cdot \frac{E.W.t^3}{L^2} \text{ and } \frac{M_Y}{\vartheta} = \frac{1}{12} \cdot \frac{E.W^3.t}{L}$
Bending	Bending	Bending

Table 11: Stiffness of a parallelepiped beam in different direction

$k_x$ ,  $k_y$  and  $k_z$  corresponds to the stiffness in the compressive, and bending directions.  $C_{MX}$  corresponds to the rotational stiffness around x. In the following section of the chapter the compressive stiffness will be noted  $k_C$ , the in-plane bending  $k_{FY}$  and the out-of-plane bending  $k_{FZ}$ . The effect of a moment  $M_Y$  inducing bending along the z-axis is also given in terms of deflection  $z$  and angle  $\theta$ . The stiffness given in table 11 are derived from differential equation assuming small deflection and rotation angle. In this chapter, the small deflection range for a cantilever beam deformed in **bending** is defined by relation (36) from [Roarks8]:

$$\frac{R_C}{10.W} \gg 1 \quad (36)$$

$W$  is the width of the beam.  $R_C$  is the maximum radius of curvature found on the beam. The definition of small deflection in **compressive/tensile** state is linked to the chosen material, here silicon. A maximum constraints  $\sigma_{MAX}$  of 100 MPa in compression has been defined in the specification for the detection mean. Considering a standard nanogauge of 5  $\mu\text{m}$  long, the maximum elongation is then given in equation (37).

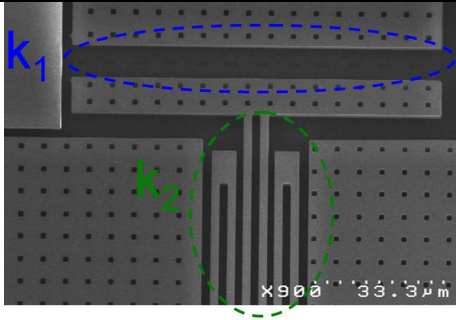
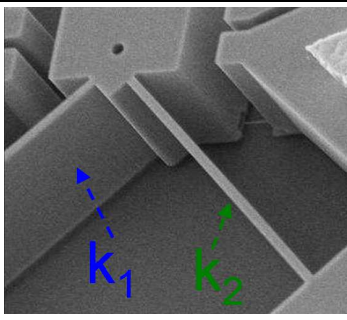
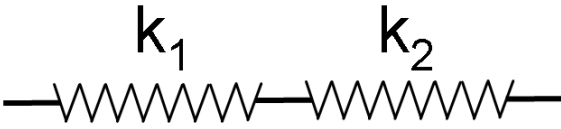
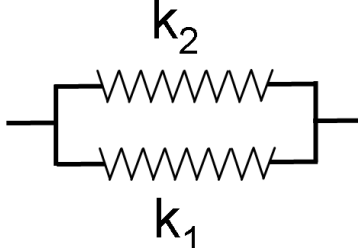
$$x_C = L. \frac{\sigma_{MAX}}{E} \approx 3nm \quad (37)$$

$E$  is the Young's modulus of silicon. However concerning springs beam, the maximum constraints can rise up to 1 GPa.

### 3.3 Association rules of springs

#### 3.3.1 Spring in parallel and in series

In order to better construct complex mechanical functions or to improve the performance of already existing functions, several identical springs are often placed symmetrically around the seismic mass. The total equivalent stiffness corresponding to the addition in series or in parallel of several identical springs can be calculated using figure 35 and 36 below.

	
	
$k_{TOT} = k_1 // k_2 = \frac{k_1.k_2}{k_1 + k_2}$	$k_{TOT} = k_1 + k_2$
<p>Figure 35: Scheme of two springs in series</p>	<p>Figure 36: Scheme of two springs in parallel</p>

The formulas given here are simple approximated analytical formulas, which can be used to obtain a rough evaluation of the stiffness. Additionally, these formulas are valid only along one direction. No global matrix operation can be done using these guidelines. Spring in series and in parallel are not the only architecture possible.  $\Delta$  and Y spring architecture can also be found. The  $\Delta$ -Y transformation in case of spring stiffness is demonstrated in Appendix 3.

### 3.4 Mechanical function of springs

In this section, we will now elaborate some key mechanical parts used in various sensor architectures, which will be presented in the next chapters. Various limitations will be applied to the MEMS degree of freedom. Different mechanical functions will be described in terms of stiffness limitations and geometrical implementations.

#### 3.4.1 Importance of geometrical dimension and architecture

Figure 37 shows the kinematic scheme of a spring of stiffness  $k_i$  placed at a distance  $L$  from its center of rotation.

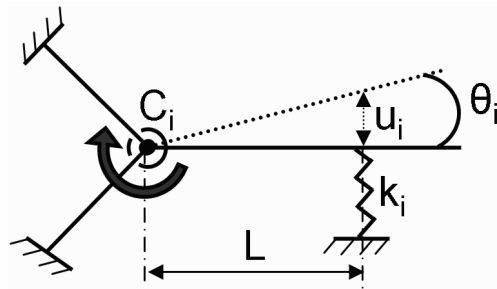


Figure 37: Kinetic scheme of a rotational stiffness of a spring

Assuming small deflections, the equivalent rotational stiffness of the spring  $k_i$  is calculated in equation (38).

$$C_i = \frac{M_i}{\vartheta_i} = \frac{F_i \cdot L}{u_i / L} = \frac{F_i}{u_i} \cdot L^2 = k_i \cdot L^2 \quad (38)$$

$L$  is the distance from the spring to the rotation axis of the structure. From (38) we see that the rotational stiffness of a spring largely depends on its **position** inside the mechanical system. In general mechanical functions can be deduced only from the whole mechanical system.

#### 3.4.2 Fulcrum

A fulcrum defines the rotation point of the mechanical structure. In order to forbid translational displacements, their stiffness along the in-plane directions should be higher than any other stiffness present in the mechanical structure. Only through this condition can these springs fix the rotation point.

##### 3.4.2.b Out-of-plane fulcrum

**Torsion bars** properly anchored can act as out-of-plane fulcrum. In this case all stiffness but the  $C_X$  or  $C_Y$  stiffness should be high. Figure 38 shows a SEM top view of a fabricated out-of-plane pivot. Figure 39 shows the mechanical function fulfilled by the spring.

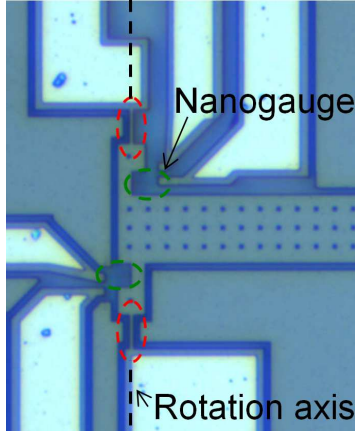


Figure 38: SEM image of an out-of-plane fulcrum

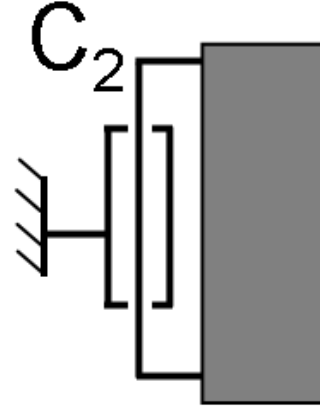


Figure 39: Mechanical function realized by the out-of-plane pivot

The mechanical model of an out-of-plane pivot/gauge assembly is shown in figure 40.  $k_f$  is the bending stiffness of the torsion beam and  $k_J$  is the compressive stiffness of the nanogauge.  $C_1$  and  $C_2$  are respectively the rotational stiffness of the torsion beam and of the gauges.  $L_0$  is the distance from the center of rotation to the center of mass. The two springs will deform by  $x_1$  and  $x_2$  respectively.  $t/2$  is the distance between the two springs.

The scheme shows that the torsion beam and the nanogauge are not at the same height. The position of the rotation axis along the Z-axis is critical in order to evaluate the lever arm amplification.

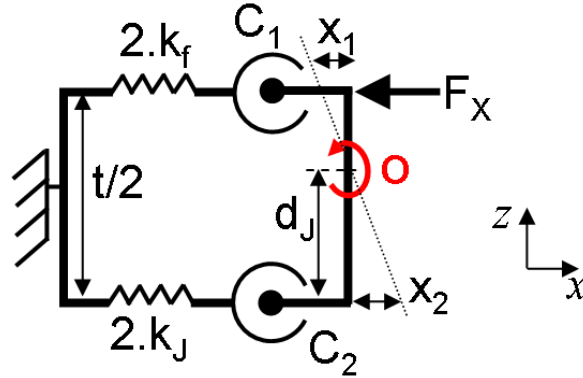


Figure 40: Kinematic model of the out-of-plane pivot/gauge assembly

Because the two springs possess a different position along the  $z$ -axis, the position of the center of rotation  $O$  is fixed through the competition of these two springs (i.e the bending stiffness of the torsion beam and the compression stiffness of the gauges). The spring with the dominant stiffness will force the whole sensor to rotate around it.

Considering a non-deformable transmission arm the geometrical relationship between the two deformations is:

$$\frac{x_1}{t/2 - d_J} = \frac{x_2}{d_J} \quad (39)$$

Writing Newton's 3<sup>rd</sup> law along the  $y$ -axis we obtain another equation:

$$M_Y = \left( \frac{t}{2} - d_J \right) k_p \cdot x_1 - d_J \cdot k_J \cdot x_2 = 0 \quad (40)$$

From equation (39) and (40) we can calculate the position of the center of rotation  $O$  through the  $d_J$  value. The variable parameters of the torsion beam are the width  $W$  and length

L. The graph 41 shows the simulated gauge stress for 1 g acceleration along the Z-direction considering different torsion beam geometries.

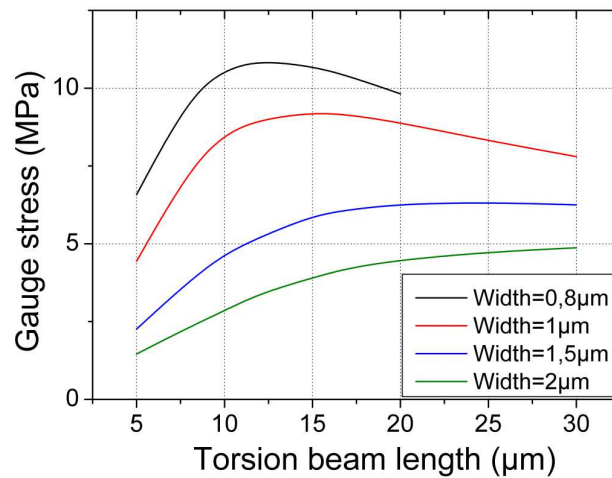


Figure 41: Pivot/gauge dimensioning model

Using lower and lower width, an optimum arises for beams of 10 to 15 µm long. Design rules drawn out of technological limitations forbids a torsion beam width lower than 1 µm. Dimensions of torsion beam with 10 µm length and 1 µm width were chosen.

### 3.4.2.a In-plane pivot

In order to obtain an in-plane pivot, all the stiffness but the *in-plane* rotational stiffness should be high in order to protect from shocks issues. The mechanical function is formed by **two perpendicular beams**. The idea is to take advantage of the compressive stiffness of each single beam in order to obtain large stiffness in the two in-plane directions while keeping the in-plane rotational stiffness low. Figures 42 and 43 are SEM pictures of fabricated in-plane fulcrum. Figure 44 shows the equivalent mechanical function of the in-plane pivot.

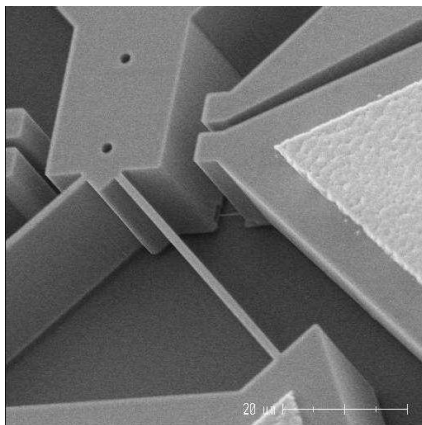


Figure 42: SEM image of an in-plane fulcrum

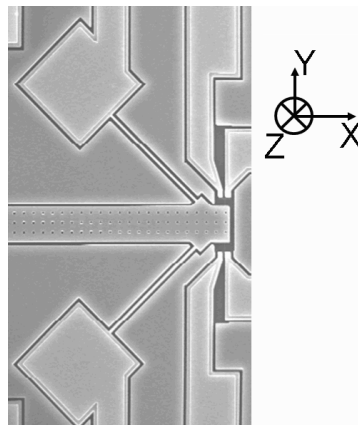


Figure 43: SEM top view of an in-plane fulcrum

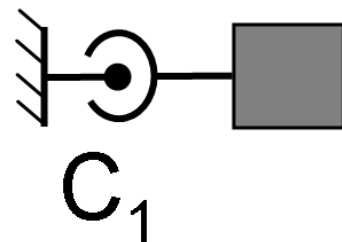


Figure 44: Mechanical function realized by the pivot

The mechanical structure will rotate around the point formed by the intersection of the two perpendicular beams. Finite Element Model (FEM) simulation has been carried out in order to find the optimum design considering the sensor geometry. Figure 45 shows the mean longitudinal stress inside the nanogauges obtained for different geometries.

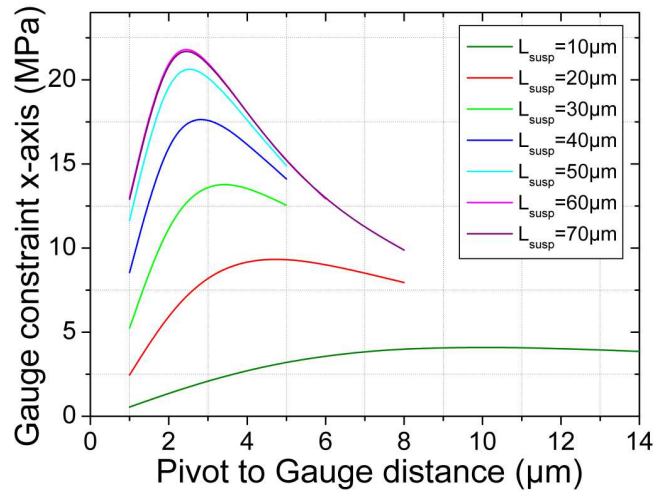


Figure 45: Parametric study of the gauge/fulcrum sensitivity

Fabrication point is set to  $d_J = 3 \mu\text{m}$  for a suspension beam length equal to  $70 \mu\text{m}$ . Shorter suspension beams reduce the sensitivity because of an increased stiffness. Longer suspension beam reduce the out-of-plane stiffness, decrease the out-of-plane frequency and increase the footprint of the sensor.

### 3.4.3 Guiding springs

The objective of guiding springs is to provide the inertial mass with a **unidirectional displacement of large amplitude**.

#### 3.4.3.a In-plane decoupling springs

##### *U-Shape spring*

In order to obtain large and directional amplitude, very long beam are fixed symmetrically in order to form several U [Wal13]. By placing several of these springs symmetrically around the inertial mass, a good directionality can be obtained. Figure 46 shows a SEM top view of a fabricated *U-shape* spring. The holed mass corresponds to the inertial mass. The top side of the spring corresponds to the anchorage. Figure 47 shows the corresponding mechanical function of the *U-shape* spring.

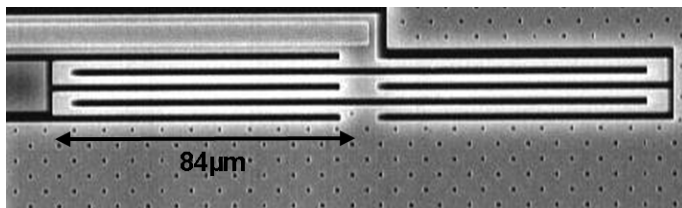


Figure 46: SEM image of an U-shaped guiding spring

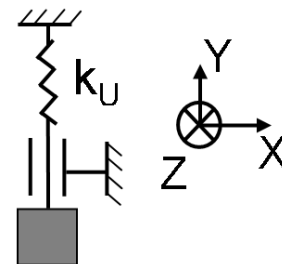


Figure 47: Mechanical function realized by 4 U-shape spring positioned symmetrically

In theory a single spring will induce a perfectly unidirectional displacement. In most of drive mode gyroscopes, the inertial mass is guided through 4 identical springs placed at each corner. According to [Wal13], due to technological dispersion one of the springs will possess slightly different dimensions. This technological dispersion will induce a non-diagonal coefficient  $k_{xy}$ .

### Folded spring

Another way to obtain a guiding function is to use another geometry also using long guided-clamped beams. This spring has good complementarities with the *U-shaped* spring because it possess the same mechanical function but the anchorage is at one side of the spring and the spring shape can be easily inserted into an inertial mass. Figure 48 shows a SEM image of the spring. The mechanical function realized by the spring is shown in figure 49.

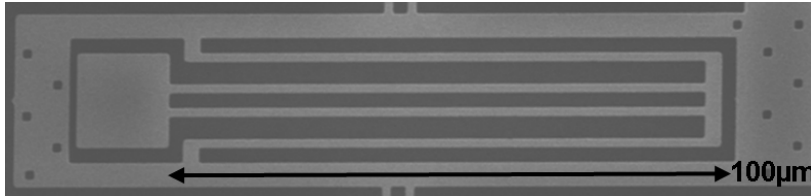


Figure 48: SEM image of a folded guiding spring

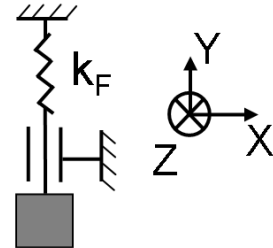


Figure 49: Mechanical function realized by the folded spring

According to [Wal13], using an inertial mass with one spring placed at a corner, when submitted to technological dispersion, U-Shaped springs exhibit a directionality two times better with respect to folded springs (which give a  $k_{xy}/k_x$  around 500 ppm for a 10 % over-etching on one of the springs). Since they possess a lower directionality than the U-Shape spring, folded spring will be used for in-plane decoupling purposes only.

### 3.4.3.b Out-of-plane decoupling springs

#### H-Shaped spring

Because of the thickness constraints induced by the lithographic process flow, efficient out-of-plane mechanical functions are difficult to realize. [Moch99] developed an *H-shaped* springs that allow a relatively low out-of-plane spring stiffness. Figure 50 shows a SEM image of the *H-shaped* spring. Figure 51 shows the mechanical function realized by the spring.

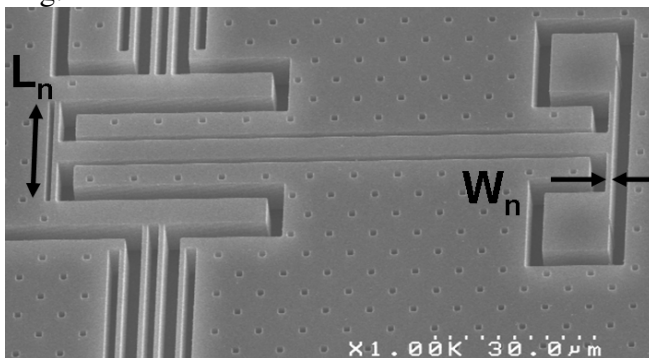


Figure 50: SEM image of a H-shape spring

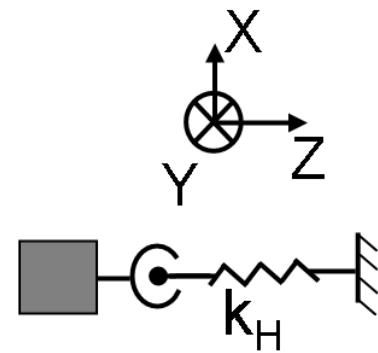


Figure 51: Mechanical function realized by the H-shaped spring

The translation out-of-plane stiffness is given in [Liu06]. The proposed model stays valid if  $L_n < 2.t$  and  $L_n < 2.W_n$ .  $t$  is the thickness of the spring. If these conditions are not met, the stress field inside the spring becomes completely 3D and stiffness differences between FEM simulations and the analytical formulas given by [Liu06] are larger than 20 %.



### 3.4.4 Coupling spring

Coupling springs provide a different kind of mechanical function with respect to the other springs already described.

#### 3.4.4.a Interest of coupling spring in inertial sensors

Dual-mass gyroscopes are based on the opposite drive displacement of the two inertial mass to obtain a differential measurement. Parasitic acceleration signal is proportional to the in-phase frequency and to the energy transferred from the in-phase mode to the drive mode (i.e inversely proportional to frequency separation [Sim13]). In order to obtain a good acceleration rejection, a **high in-phase frequency** should be obtained along with a **large frequency separation**. An **anti-phase spring coupling** is therefore required. Additionally frequency matching with the sense mode is also required (See chapter 5).

In order to force an opposite displacement on each of the inertial mass, a rhomb shape coupling spring is described. This shape has already been reported in [Wal12] among others. Figure 52 shows a SEM picture of the coupling spring. The coupling spring is linked to several *U-shape* springs in order to provide large displacement amplitude to the inertial mass.

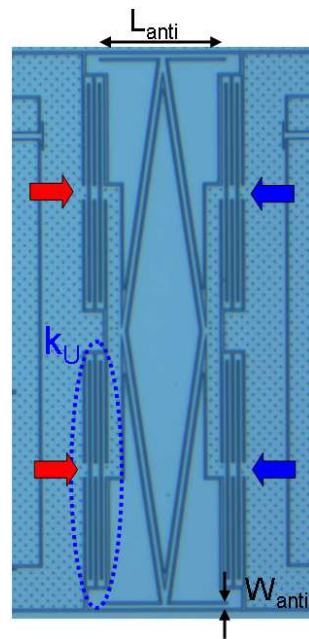


Figure 52: SEM Top view of a coupling spring

#### 3.4.4.b Anti-phase mode

The coupling spring is described cinematically in figure 53. The red and blue arrows represent the displacement occurring in the coupling spring for an anti-phase mode. The inset is a simulated view of the deformation induced by the anti-phase mode.



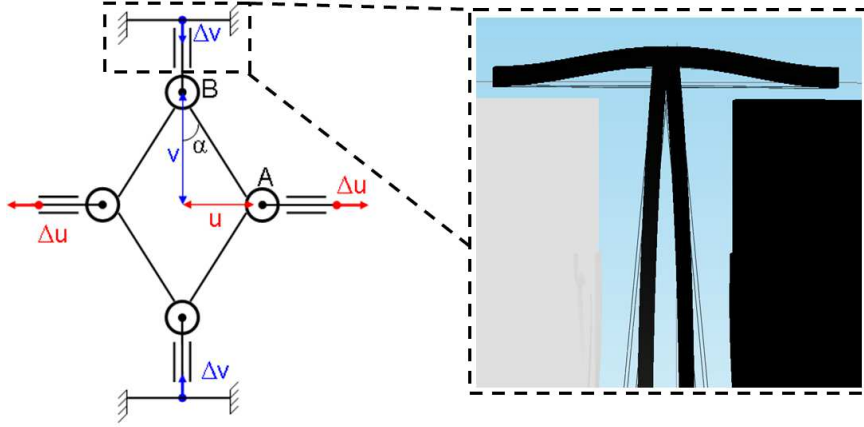


Figure 53: Modelling of the anti-phase mode

The deformation profile shows that **bending** is induced on the horizontal beam of length  $L_{anti}$ . The expression of the beam stiffness  $k_{bending}$  in the bending mode is given in equation (41).

$$k_{bending} = \frac{16.E.t.W_{anti}^3}{L_{anti}^3} \quad (41)$$

In case of an anti-phase movement, the rhomb shape tends to transmit the beam deformation to the two inertial mass. The stiffness amplification  $A_{rhomb}$  due to the rhomb is expressed with equation (42).

$$A_{rhomb} = \frac{k_X}{k_Y} = \frac{u^2}{v^2} \quad (42)$$

$u$  (30  $\mu\text{m}$ ) and  $v$  (200  $\mu\text{m}$ ) are respectively the vertical and horizontal dimensions of the rhomb shape.  $k_X$  is the horizontal stiffness at point A and  $k_Y$  is the vertical stiffness at point B, which in our case correspond to  $k_{bending}$ . Thanks to the rhomb shape stiffness amplification, the coupling spring stiffness  $k_C$  is directly proportional to the beam stiffness as shown in equation (43).

$$k_{C\_anti} = \frac{16.E.t.W_{anti}^3}{L_{anti}^3} \cdot \frac{u^2}{v^2} \quad (43)$$

### 3.4.4.c In-phase mode

The in-phase mode is modeled in figure 54. From the FEM simulation shown in the inset, the same beam is now submitted to a **torsion** deformation.

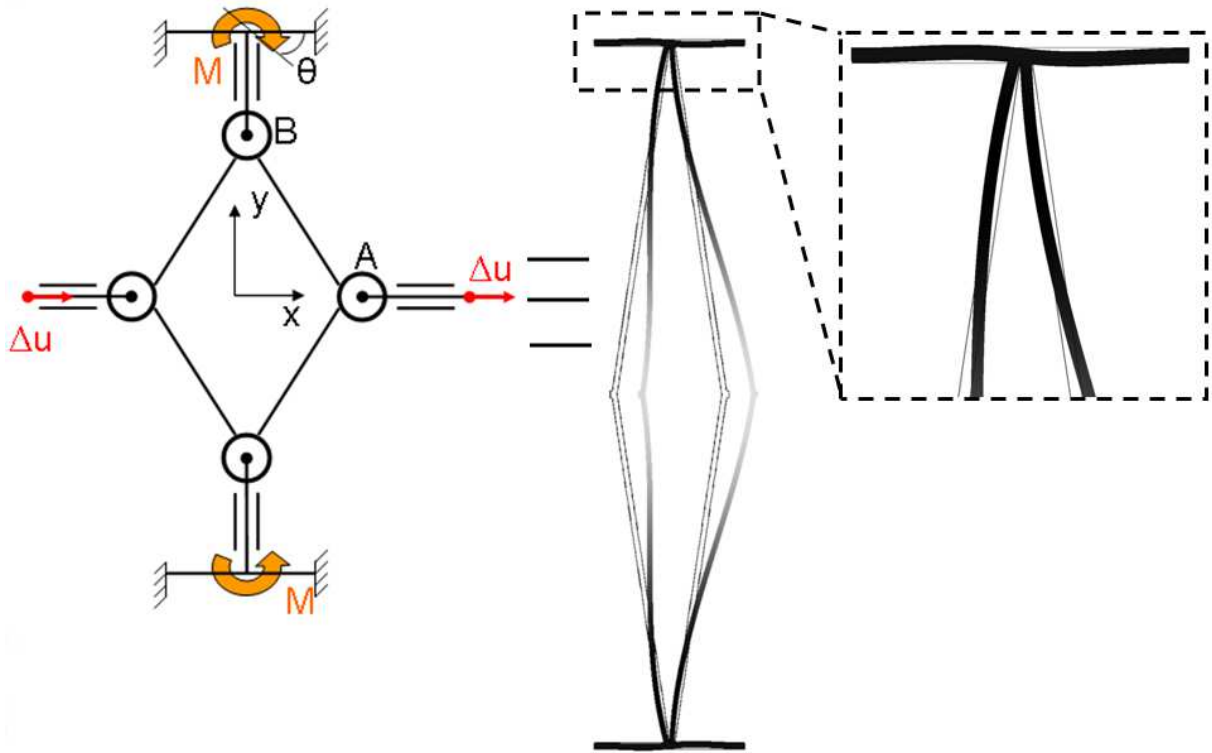


Figure 54: SEM Modeling of the in-phase mode

No flexion can occur in the in-phase deformation mode. The stiffness in compression and torsion of the beam of length  $L_{anti}$  gives respectively  $1.4 \cdot 10^5 \text{ N/m}$  and  $2.1 \cdot 10^{-7} \text{ N.m}$ . These stiffness correspond a high translation stiffness and a low rotational stiffness. These stiffness shows that a good model for the beam is a pivot. The scheme of figure 54 is modeled as shown in figure 55.

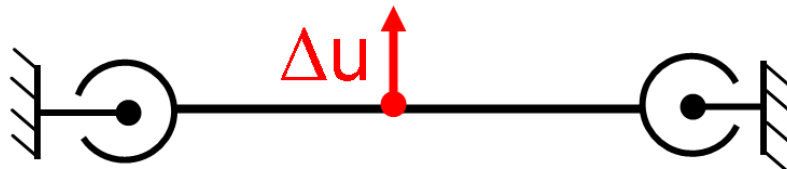


Figure 55: Beam model and cinematic issue

At the first order, a displacement  $\Delta u$  cannot occur in figure 55 because of the two pivots on opposite sides. In this model, we will consider the first order approximation case where the displacement at point B is null (including no rotation). Hence the displacement of the in-phase mode will be dominated by the stiffness of the rhomb shaped given in equation (44).

$$\text{with } k_{rhomb} = \cos(\alpha) \cdot \frac{E \cdot W_r^3 \cdot t_r}{4 \cdot L_r^3} + \sin(\alpha) \cdot \frac{E \cdot W_r \cdot t_r}{L_r} \quad (44)$$

$\alpha$  is the angle formed by the rhomb shape with respect to the vertical axis (see Figure 53).  $W_r$ ,  $t_r$  and  $L_r$  are respectively the width, thickness and length of the rhomb shape.  $k_{rhomb}$  is the stiffness of the rhomb shape which tends to deform due to the in-phase displacement. In first order approximation, we have  $k_{C\_phase} = k_{rhomb}$ . (Note that for very different dimensions, an influence of the length  $L_{anti}$  on the in-phase mode will occur)

### 3.4.4.d Frequency mode

This difference of mode of deformation allows the coupling spring to exhibit very different spring stiffness depending on the displacement of the inertial masses (i.e in anti-phase or in in-phase mode). Considering the environment of the coupling spring (i.e 2 U-Shape are placed at each side of the inertial mass). Figure 56 below shows the environment of the coupling spring along the drive direction for the two deformation mode. In the in-phase mode the coupling spring stiffness is considered to be  $k_{C\_phase}$ . In anti-phase mode the coupling spring stiffness is  $k_{C\_anti}$ .

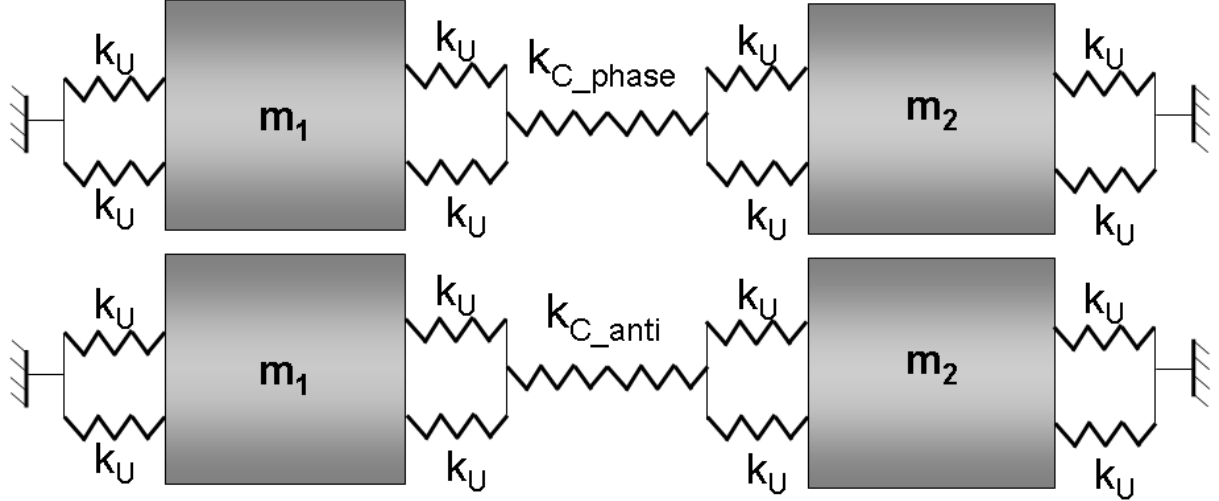


Figure 56: Schematic of the gyroscope in the drive direction (in-phase and anti-phase mode)

Based on figure 56, the resonant frequency of the different modes can be calculated analytically using equation (45).

$$\omega = \sqrt{\left(2.k_U + \frac{2.k_U.k_C}{2.k_U + k_C}\right) / m_i} = \sqrt{\left(4.k_U - \frac{4.k_U^2}{(2.k_U + k_C)}\right) / m_i} \quad (45)$$

$k_U$  is the stiffness of one U-shape spring.  $m_i$  corresponds to the mass of one inertial mass.  $k_C$  correspond to either  $k_{C\_anti}$  or  $k_{C\_phase}$  depending on the mode considered.

In anti-phase mode we have  $k_{C\_anti} \sim k_U$ . From equation (43) we can see that, the anti-phase mode frequency will change if the beam geometry changes. From equation (45) the frequency will ultimately vary from  $\sqrt{4.k_U / m_i}$  to  $\sqrt{2.k_U / m_i}$  if  $k_C$  goes from 0 to infinity. This translates into an ultimate relative frequency variation of  $\sqrt{2}-1$ .

In the in-phase mode  $k_{C\_phase}$  is equal to  $k_{rhomb}$  in first approximation. Hence the frequency of the in-phase mode deformation will stay identical whatever the beam dimensions.

In order to assure rough frequency matching by dimensioning, FEM simulations of the different modes frequencies of the drive part of the gyroscope have been performed. Figure 57 and 58 shows the resonant frequency variation of the in-phase and anti-phase modes with respect to geometry of the beam (through its length  $L_{anti}$  and its width  $W_{anti}$ ).

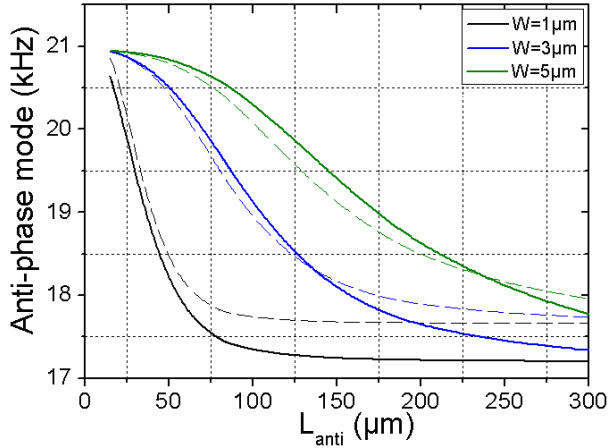


Figure 57: Anti-phase mode resonance frequency variation due to geometrical change in the coupling beam

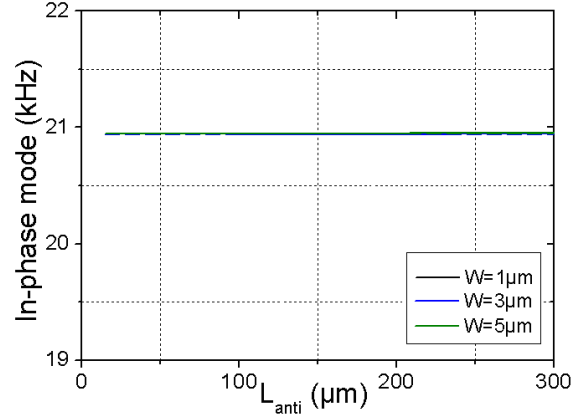


Figure 58: In-phase mode resonance frequency variation due to geometrical change in the coupling beam

We can see that the anti-phase mode tends to decrease. Hence the in-phase mode comes before the anti-phase mode, which fits with our requirements.

The large frequency difference (up to 3 kHz) between in-phase and anti-phase modes due to a simple beam length can be used to improve acceleration rejection (i.e frequency difference improves acceleration rejection by 40dB/dec) and frequency matching. Additionally the in-phase mode is after the anti-phase mode, which is better for acceleration rejection (i.e high in-phase frequency).

### 3.4.5 Conclusion

Within the limitation imposed by the fabrication techniques, the main mechanical functions have been described. We have seen that the position of a spring have a major influence on the system stiffness. Hence the optimization should be done at the system level (i.e pivot/gauge assembly). U-Shape springs with high directionality will be used in low quadrature bias gyroscopes. Additionally, the coupling spring described in 3.4.4 can be used in the drive mode of gyroscopes to obtain a good acceleration rejection for gyroscopes. Theses springs represent a basic but critical function of our sensors. Due to the limitation induced by epitaxial techniques, out-of-plane springs exhibit lower performances than in-plane springs. Now, as the critical mechanical functions have been validated, the leap to the system level is simple. Roughly, an accelerometer is a spring fixed to an inertial mass. In the next chapter, in-plane and out-of-plane accelerometers will be described along with a new strategy for shock protection.

# Chapter 4: Non resonant structure

In this chapter we will describe different inertial sensors all functioning in a quasi-static mode. Different designs of acceleration sensors along with a pressure sensor are described and characterized. In conclusion, a comparison between single mass and multiple-mass accelerometer approaches is given.

## 4.1 Single-axis accelerometers

Single-axis accelerometers are sensors that measure acceleration and for which the output signal is proportional to acceleration in one direction. Ideally, temperature, time, rotation speed or acceleration in another direction should not influence its output signal. Considering the given specifications (defined in chapter 1) accelerometers are supposed to respond for accelerations up to 100 Hz. However, the main sensor constraint is the 1 mm<sup>2</sup> packages that should include all 3-axis accelerometers. Accelerometers using the same concept with different specifications have already been designed in a previous project [Rey10].

### 4.1.1 In-plane-accelerometers

In-plane accelerometers refer to accelerometers that measure acceleration in the plane of the wafer. In this section, we will present a single axis in-plane accelerometer.

#### 4.1.1.a Concept of a single axis in-plane accelerometer

The different elements of the sensors are pointed out in figure 38. The inertial mass occupies most of the mechanical area however the non-mechanical area (i.e pads, electrical lines) occupies the remaining surface.

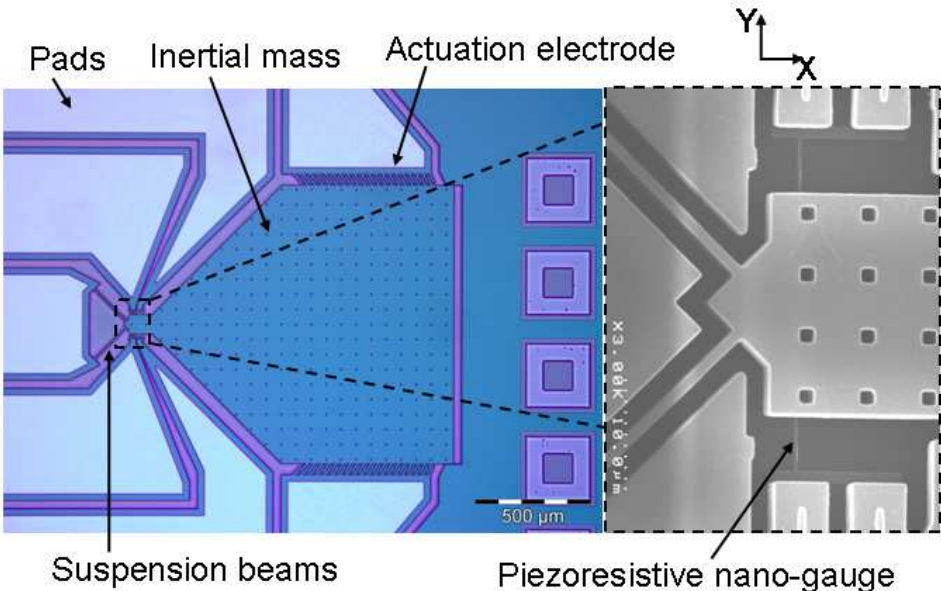


Figure 59: Top view of an in-plane accelerometer

The principle of operation of such sensor is the following: When submitted to acceleration along the y direction, an inertial force arises at the center of the inertial mass. The inertial force is amplified through an amplification arm (lever arm effect) and transmitted to

the piezoresistive nano-gauges. Two perpendicular suspension beams operates as a pivot. Due to the amplified inertial force, the piezoresistive gauges are compressed/tensed hence their electrical resistance changes. The differential resistance change is then monitored through 4-point measurements. The transduction chain of the sensor is given in figure 60.

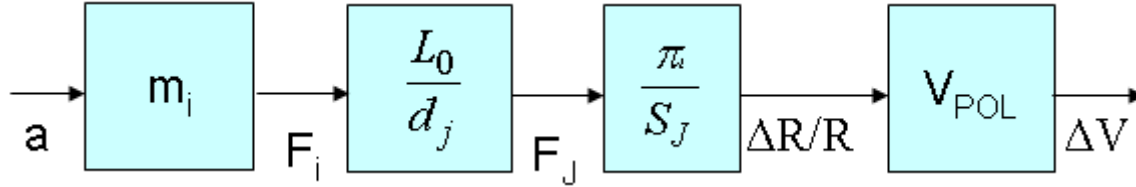


Figure 60: Rough transduction chain of the in-plane sensor

$a$  stands for acceleration along the  $y$ -direction.  $F_i$  is the inertial force,  $F_J$  the force applied on the gauges.  $\Delta R/R$  is the relative variation of the gauge resistance and  $\Delta V$  the difference of potential measured in the middle of the bridge.  $m_i$  stands for the inertial mass,  $L_0$  is the distance from the center of mass to the fulcrum.  $d_j$  is the distance from the fulcrum to the gauge.  $S_J$  is the gauge surface and  $\pi_l$  is the longitudinal piezoresistive factor.  $V_{POL}$  is the polarization voltage across the gauge. This definition of the different parameters will be kept for the upcoming parts of the thesis.

The first transduction box of figure 60 transforms the acceleration into the inertial force thanks to the inertial mass. The second transduction box assesses the mechanical amplification that is due to the gauge/fulcrum assembly. The third transduction box is the electro-mechanical transduction. The fourth box concerns the electric readout and polarization voltage.

#### 4.1.1.b In-plane-pivot/gauge assembly

The aim of the pivot/gauge assembly is to provide the system with a fixed point. This fixed point is mandatory in order to obtain a lever configuration. A way to create this fixed point is to fabricate two perpendicular suspension beams as already described in chapter 3. A large stiffness is obtained in both in-plane directions whereas the obtained rotational stiffness  $C_l$  is small. This configuration forms a mechanical pivot at the intersection of the suspension beams.

On figure 61, we can see the mechanical model corresponding to the fabricated structure (figure 38).  $d_j$  is the gauge to pivot distance and  $L_0$  is the distance from the center of mass to the pivot. In order to generate a complete model, a parasitic spring has been added with a distance  $L_a$  from the pivot and a spring constant of  $k_a$ . However this spring is not present in the accelerometer given in figure 38.  $C_l$  is the rotational stiffness of the fulcrum.  $k_j$  is the stiffness of a single gauge (there are 2 gauges).

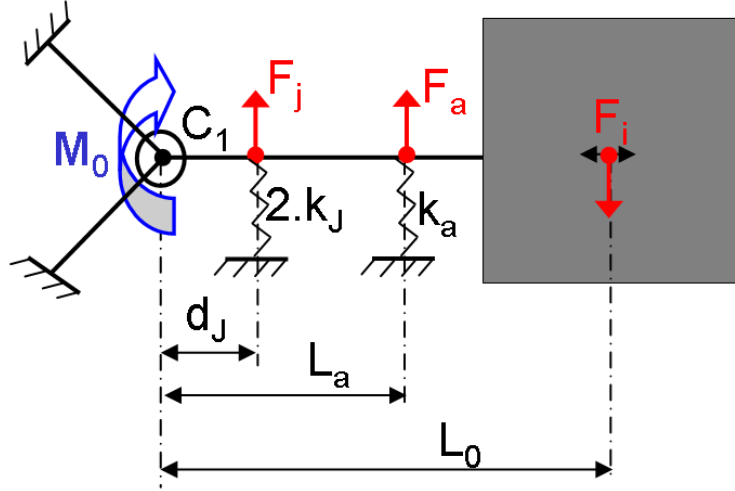


Figure 61 : Kinematic model of the pivot/gauge assembly

Considering a non deformable lever arm and using 3<sup>rd</sup> Newton's law, one obtains:

$$\sum M = J \ddot{\theta} = F_i L_0 + 2.F_j.d_J + F_a.L_a + C_1 \theta + \gamma_m \dot{\vartheta} \quad (46)$$

With  $J$  is the moment of inertia,  $\gamma_m$  the mechanical damping factor of the sensor. Considering a spring such as:

$$F_j = k_J.d_J \text{ and } F_a = k_a.L_a \quad (47)$$

And using equation (46) and (47), we can express all the spring influence through  $\theta$  as:

$$\sum M = J \ddot{\theta} = F_i L_0 + [C_1 + 2.k_J.d_J^2 + k_a.L_a^2] \theta + \gamma_m \dot{\vartheta} \quad (48)$$

For small displacements and considering Hooke's law, we obtain:

$$\tan \theta \approx \theta = \frac{\sigma.l_J}{E.d_J} \quad (49)$$

From Equation (48) and (49) we can express the transfer function of the piezoresistive accelerometer as:

$$\frac{\Delta R/R}{a_X} = m.\pi_l \cdot \frac{E.d_J.L_0}{l_J.(J\omega^2 + j\omega\gamma_m + C_1 + 2.k_J.d_J^2 + k_a.L_a^2)} \quad (50)$$

The sensitivity to a quasi-static acceleration  $S_{DC}$  (Computed using  $\omega=0$ ) can be deduced as the gain of the previous transfer function:

$$S_{DC} = m.\pi_l \cdot \frac{L_0}{d_J} \cdot \frac{1}{S_{EQ}} \text{ with } S_{EQ} = 2.S_J + (C_1 + k_a.L_a^2) \cdot \frac{l_J}{E.d_J^2} \quad (51)$$

From equation (51), the sensitivity is proportional to the inertial mass, the lever arm  $L_0/d_J$ , the piezoresistive factor and the constraint concentration  $1/S_{EQ}$ . Using Euler-Bernoulli equations for a clamped-clamped beam submitted to a torque, as described in chapter 3, Equation (52) below gives the rotational stiffness of the suspension beams.

$$C_1 = \frac{M}{\theta} = \frac{1}{6} \cdot \frac{E.W_s^3.t}{L_s} \quad (52)$$

where  $L_s$ ,  $W_s$  and  $t$  represent the length, width and thickness of the suspension beam respectively.

#### 4.1.1.c Frequency behavior of a pivot/gauge assembly

Using the mechanical model of figure 61 described through the transfer function (50) we can extract an estimation of the resonant frequency:

$$\omega_0 = \sqrt{\frac{C_1 + 2.k_J.d_J^2 + k_a.L_a^2}{J}} \quad (53)$$

From equation (53), we see that the distance from the center of rotation is of utmost importance when positioning springs. If one of the three terms is a lot larger than the other it will fix the resonant frequency.

Some structures have a constraint on resonant frequency rather than on sensitivity (i.e gyroscopes). Indeed, they have to match drive and sense frequency for optimum sensitivity and bandwidth considerations. In this case, a different trade-off can be found using equations (51) and (53). A parasitic spring  $k_a$  could be used to set the resonant frequency at the desired value at the cost of sensitivity reduction.

Concerning again the accelerometer case, the resonance frequency constraints is weak. The ideal configuration is to obtain all terms but the gauge terms negligible in order to maximize sensitivity. The expression of the quality factor can also be extracted from the transfer function of equation (50):

$$Q = \frac{\omega_0}{\gamma_m} = \sqrt{\frac{C_1 + 2.k_J.d_J^2 + k_a.L_a^2}{J.\gamma_m^2}} \quad (54)$$

#### 4.1.1.d Main source of uncertainty of the pivot/gauge assembly

In this section, we will study the influence of the process variation on the sensitivity of the sensor. There is no guiding spring  $k_a$  in the sensor studied. In order to evaluate the uncertainty due to technological fabrication, the following method was applied. First, the sensor characteristics are expressed directly as a function of the geometrical parameters of the sensor. Each dimension is then linked to its key fabrication process. Knowing each technological process standard variation, we can weight the influence of each dimension and find the most critical geometrical parameter. Ways to reduce sensitivity variation can then be drawn from such calculations. Such method will also give us the fabrication windows allowed for the different design parameters (i.e design rules).

The fabrication processes studied in this section are the **MEMS Etching** (which defines the structure of most springs), the **NEMS Etching** (which defines the gauges geometry), **the MEMS/NEMS mask alignment** (which defines the position of the gauge with respect to the MEMS structure) and the **MEMS thickness** defined by grinding. The typical parameters considered as variables in this study are:  $W_s$ ,  $d_J$ ,  $W_J$  and  $t_s$ . These parameters are considered to be the most subjected to technological variations.

Other parameters are defined by the same technological process (i.e same uncertainty) however their dimension are larger (i.e  $l_J$  or  $L_s$ ). The gauge thicknesses  $t_j$  is defined by thermal oxidation which is a well-controlled process thus not considered in this study.

##### Technological variation influence on Zero-g-Offset

First of all, we can evaluate the technological influence on the Zero-g-Offset output of the sensor. It corresponds to the output value when no acceleration is applied to the sensor.



Only the embedded constraints and geometry dissymmetry will affect the Zero-g-Offset. Figure 62 shows the polarization circuit used for gauge readout:

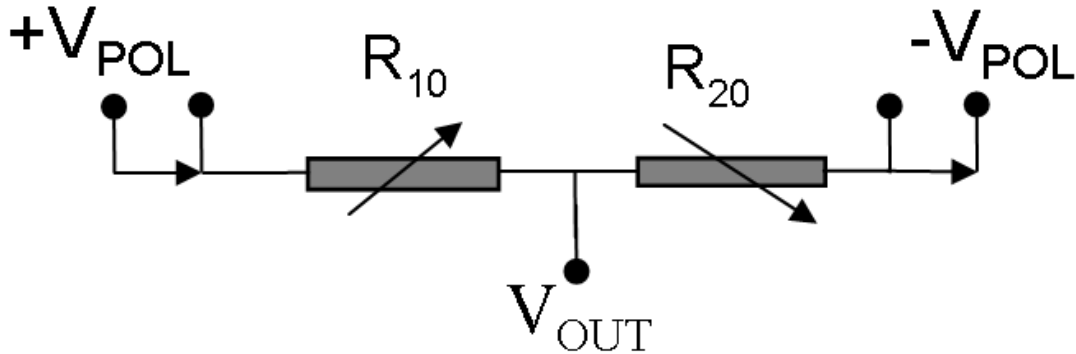


Figure 62: Equivalent readout electrical circuit

Using Millman's theorem, the output voltage  $V_{OUT}$  is extracted in Equation (55).

$$\frac{V_{OUT}}{V_{POL}} = \frac{R_{20} - R_{10}}{R_{10} + R_{20}} \quad (55)$$

Since  $l_J$  and  $t_J$  are considered constant. The offset existence and variation will be mainly due to the gauge width  $W_J$ .

$$V_{OUT}(a_X = 0) \approx V_{POL} \cdot \frac{W_2 - W_1}{W_1 + W_2} \quad (56)$$

Automatic measurement of Critical Dimensions (CD) gives a NEMS etching uncertainty of 10 nm, a numerical estimation of the offset gives 4 % offset. This estimated offset (based on the "3 sigma" variance method) is in the order of magnitude of the full range of the sensor. Gauge forming a half Wheatstone bridge are close from each other. Measurements of the resistance difference of gauges of the same bridge indicate a lower offset value of 2.4 % of the gauge resistance. Resistivity measurements confirm that resistivity variations can be neglected thanks to the thermal annealing and the proximity of the two nanogauges.

#### Technological variation influence on sensitivity

The second important sensor parameter which can be influenced by technological variation is the quasi-static sensitivity. Using equation (51), the sensitivity to acceleration can be expressed using only constant and geometrical parameters. Equation (57) shows the main geometrical parameter subjected to change.

$$S_{DC} = m \cdot \pi l \cdot \frac{L_0}{d_J} \cdot \frac{1}{\frac{2 \cdot E W_J t_J}{l_J} + \frac{E W_s^3 t_s}{6 L_s d_J^2}} \quad (57)$$

Here we will consider that variations on:

- $W_J$  can be reduced to the **NEMS etching** step influence,
- $d_J$  can be reduced to the **MEMS/NEMS misalignment** masks influence,
- $W_s$  can be reduced to the **MEMS etching** step,

- $t_s$  can be reduced to the **grinding** process.

Then we can evaluate the importance of each technological step and their influence in terms of uncertainty on the sensitivity of the accelerometer. The misalignment masks influence along the  $y$ -direction will change the gauge length by a negligible amount. The total uncertainty on the sensitivity ( $\Delta S_{DC}$ ) is considered to be:

$$\Delta S_{DC} = \frac{\partial S_{DC}}{\partial d_J} \cdot \Delta d_J + \frac{\partial S_{DC}}{\partial W_S} \cdot \Delta W_S + \frac{\partial S_{DC}}{\partial W_J} \cdot \Delta W_J + \frac{\partial S_{DC}}{\partial t_s} \cdot \Delta t_s \quad (58)$$

Using equation (57), the influence of the selected process step has been derived. Critical Dimension (CD) measurement has been performed on different technological steps. Technological variation has been measured for each of the four process steps considered. From these measurements, the standard deviation (3 sigma) for the MEMS Etching is estimated to 100 nm, 10 nm for the NEMS Etching and 500 nm for the MEMS/NEMS alignment masks and 500 nm for the grinding process. The contribution of each fabrication process should be weighted with typical dimension used for each dimension. Using absolute dimensions of 1  $\mu\text{m}$  for  $W_s$ , 250 nm for  $W_J$  and 3  $\mu\text{m}$  for  $d_J$ , the influence of the global technological uncertainty is given in table 12.

Technological process	Influence on sensitivity (3 sigma)	Nominal dimension / dispersion ( $\mu\text{m}$ )
Alignment mask ( $d_J$ )	<b>11.4 %</b>	3 / 0.5
Grinding ( $t_s$ )	1.8 %	10 / 1
MEMS Etching ( $W_s$ )	0.52 %	1 / 0.1
NEMS Etching ( $W_J$ )	3.4 %	0.25 / 0.01
Total uncertainty	12.08 %	-

*Table 12 : Influence of technological variation on sensitivity*

The accelerometers fabricated here have a standard variation (3 sigma) on sensitivity due to technological uncertainty of about 12%. We can see that the major uncertainty source comes from the **alignment mask error**, i.e the error on  $d_J$ . This uncertainty could be reduced by using larger suspension beams (increasing  $C_1$ ).

#### 4.1.1.e Design optimization

##### Pivot/gauge dimension

Finite Element Model (FEM) simulation has been carried out in order to find the optimum design considering the sensor geometry. Figure 45 shows the mean longitudinal stress inside the nanogauges obtained for different geometries. Fabrication point is set to  $d_J = 3 \mu\text{m}$  for a suspension beam length equal to 70  $\mu\text{m}$ . The sensitivity objective of 20 MPa/g is obtained, which correspond to a full scale of 5 g. Shorter suspension beam reduce the sensitivity because of an increased stiffness. Longer suspension beam reduce the out-of-plane stiffness, decrease the out-of-plane frequency and increase the footprint of the sensor.

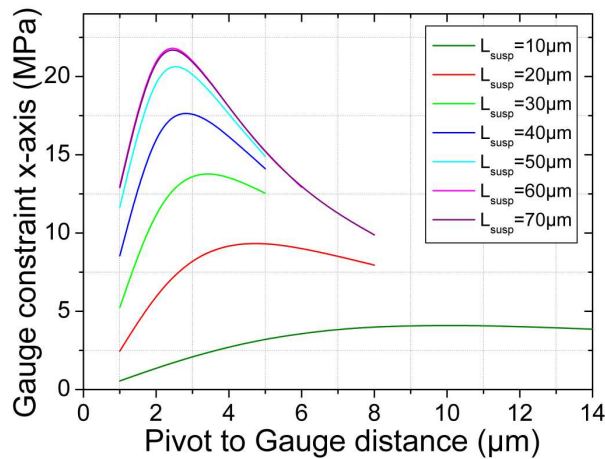


Figure 63: Parametric study of the gauge/fulcrum sensitivity

#### Self-test electrodes

In terms of test, electrical actuation is by far easier to implement than gravity. It allows frequency characterization and very flexible tests. Two angular comb drive electrodes have been implemented onto the in-plane accelerometer. Figure 64, 65 and 66 shows the different construction steps of the circular comb drives that have been designed. These comb drives aim at creating a torque compatible with the sensor's rotation movement. They should also exhibit the smallest possible negative spring stiffness.

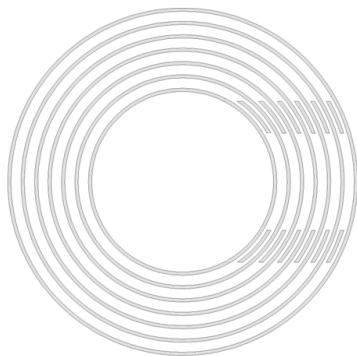


Figure 64: Top view of angular comb drive construction lines

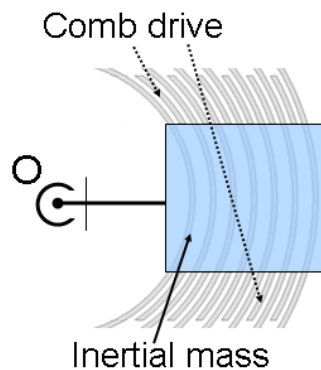


Figure 65: Top view of angular comb drive design

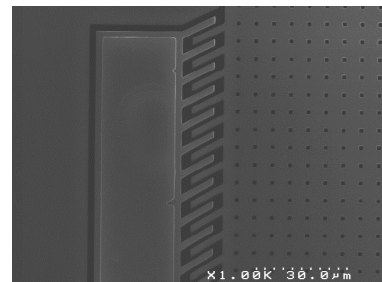


Figure 66: Angular comb drive implemented on the sensor

#### 4.1.1.f Mechanical characterization of in-plane accelerometers

Dynamic characterization by frequency sweeps:

Using frequency sweeps, it is straightforward to characterize the mechanical resonant frequency along with the quality factor of the sensor. Dynamic actuation was performed using the angular comb drives. Figure 67 and 68 show the piezoresistive response of the sensor in atmospheric pressure and in vacuum ( $\sim 10^{-5}$  mbar). The resonance frequency doesn't change too much with respect to pressure. However the quality factor changes by orders of magnitude due to the predominance of viscous damping.

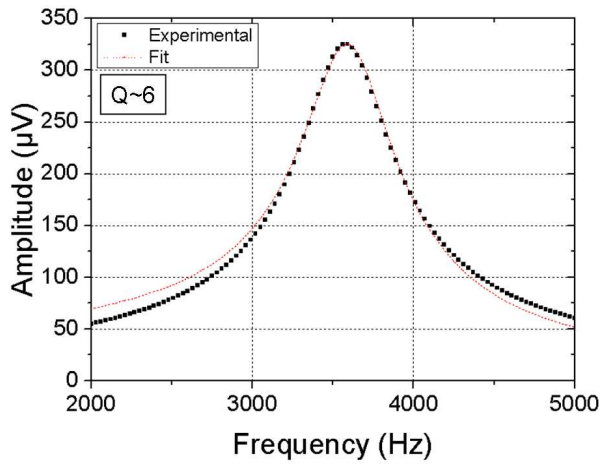


Figure 67: frequency response of an accelerometer in air

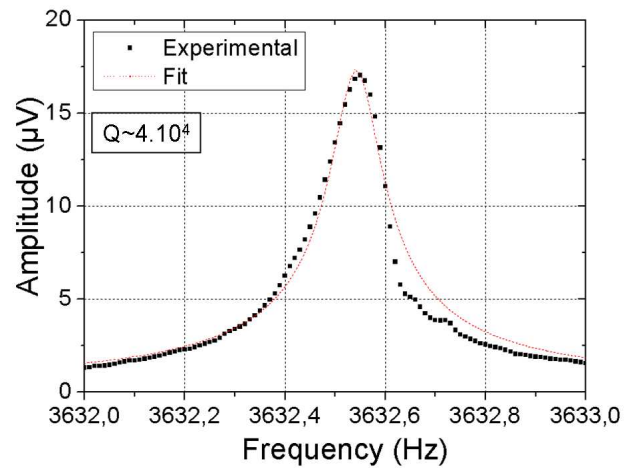


Figure 68: frequency response of an accelerometer in vacuum

Figure 69 shows the piezoresistive response of single-axis accelerometers in air for different dynamic excitation amplitudes. AC electrostatic actuation at different voltages simulates an acceleration which is detected by the sensor. Figure 69 allows an evaluation of the resonant frequency of this sensor around 3.6 kHz.

The curves seem limited around a piezoresistive response of 3 mV. This limitation corresponds to gauge stress of 160 MPa (Assuming  $\pi_l = 23 \cdot 10^{-11} \text{ Pa}^{-1}$ ). This limitation is due to mechanical stoppers placed at the maximum displacement areas. They are used to limit the displacement of the inertial mass and limit the stress in the gauges in case of shocks. Such measurement validates the effectiveness of stoppers as a way to ensure protection against shocks for the nanogauges. As long as the stoppers hold, the stress into the nanogauges should not exceed 160 MPa. The position of the stoppers depends on numerous technological processes. Hence the distances travelled by the inertial mass possess a large uncertainty.

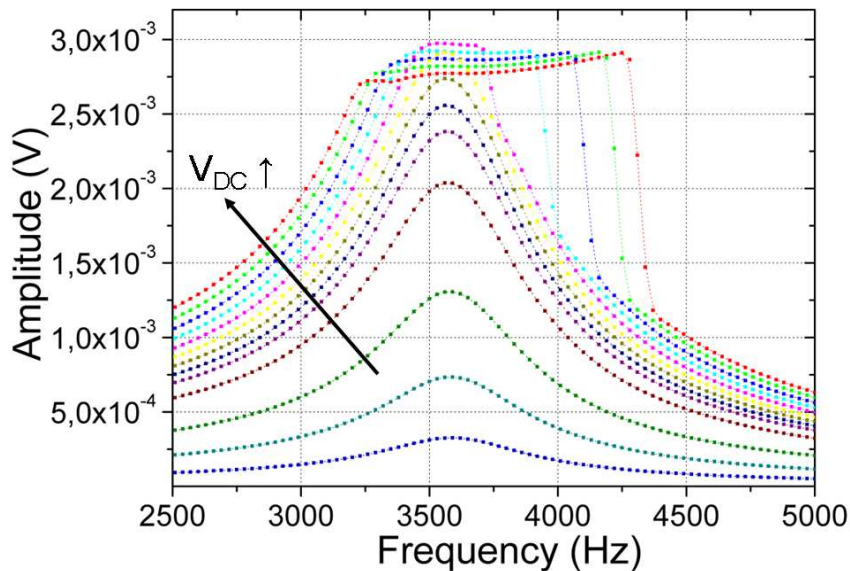


Figure 69: Effect of shocks stops on piezoresistive detection

Due to the obtained quality factor (i.e  $Q \sim 6$  in air), the amplitude response of the sensor is frequency dependent. Fitting the measurements done in figure 69 the sensitivity should vary by roughly 15 % from DC to 500 Hz. A frequency compensation algorithm can be a way to compensate this behavior. It is also worth mentioning that the frequency

responses recorded for the highest values of the DC voltage lead to a nonlinear behavior, which is clearly exhibited in the right side of the resonance peak.

Out-of-plane movement in in-plane accelerometers

The gauge/fulcrum assembly has been optimized for sensitivity. However from process fabrication, we know that the nanogauge and the suspension beam are not at the same height. Hence the influence of the gauge on the global stiffness of the system will deflect the rotation axis of the accelerometer from the vertical axis. Figure 70 is a deformed scheme (side view) of the accelerometer showing the difference between the rotation axis and the vertical angle ( $\theta$ ).

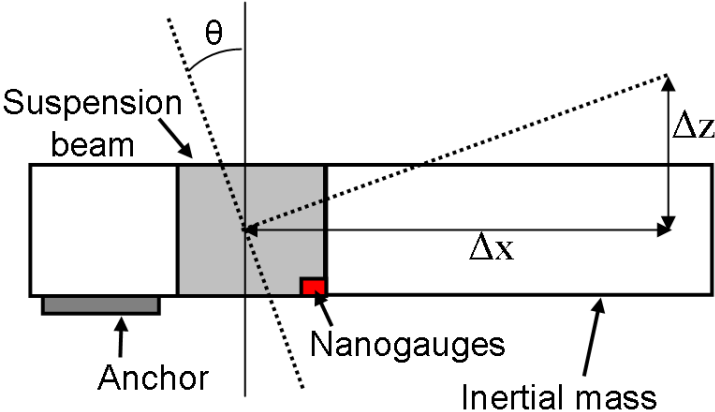


Figure 70: Scheme of the out-of-plane component of the rotation angle

The sensor was actuated in quasi-static mode, using the self-test electrode with a low frequency signal. The resulting vertical displacement of the in-plane accelerometer was monitored using a laser Doppler vibrometer (See figure 71). The measured out-of-plane movement is a periodic movement showing a small tilt of the inertial mass. Figure 72 shows the obtained displacement (arrows) of the inertial mass, depending on the position along the horizontal axis. The top view of the accelerometer (bottom part of figure 72) shows the used cut line.

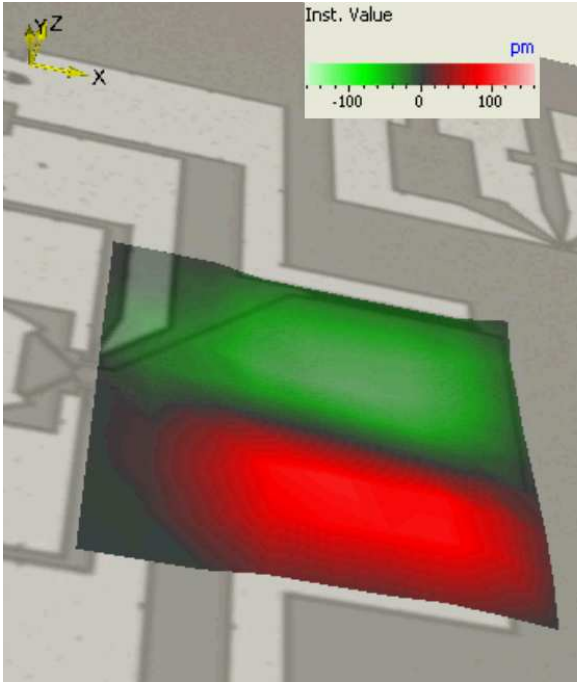


Figure 71: Measured out-of-plane displacement of an in-plane accelerometer

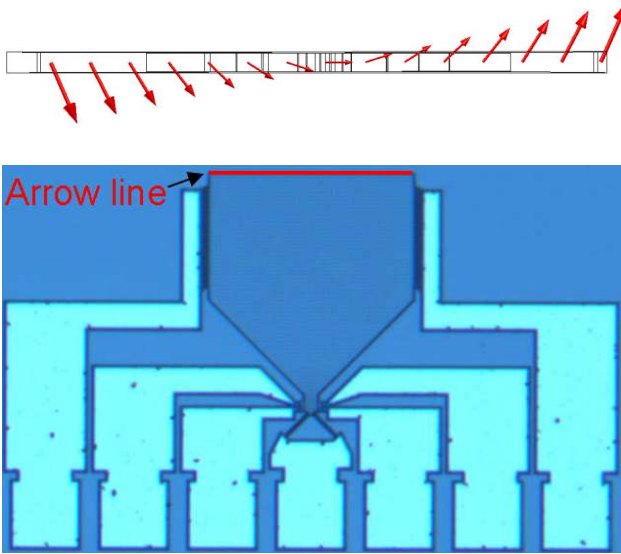


Figure 72: Simulated representation of the out-of-plane movement obtained



The amplitude of the out-of-plane movement is 140 pm. Using figure 71, the in-plane amplitude corresponding to the AC actuation has been evaluated around 100 nm. This results in an angle  $\theta = \Delta z/\Delta x$  around  $\sim 1.4 \cdot 10^{-3}$  rad. Equivalent FEM simulation gives an angle  $\theta = \Delta z/\Delta x$  of  $2 \cdot 10^{-2}$  rad. An additional out-of-plane torque of about  $10^{-15}$  N.m is needed to obtain matching of the FEM simulation with the experimental results. A torque of this amplitude can be easily obtained by electrostatic means. Indeed this amplitude corresponds to the actuation force used in this experiment when considering a directionality of  $10^{-3}$  rad (and a distance to the rotation axis of 150  $\mu\text{m}$ ).

The difference between the vertical axis and the rotation axis of the accelerometer is below the experimental limits of our setup and hence **cannot be evaluated** through electrostatic means. FEM simulations give an angle difference around 1 degree ( $2 \cdot 10^{-2}$  rad).

#### Sensitivity to earth gravity

The piezoresistive response of a single-axis in-plane accelerometer has been measured when submitted to earth acceleration through a rotating table (See picture figure 74). A angular tilt  $\theta$  of the table induces a modification of the acceleration seen by the accelerometer in ( $g \cdot \sin(\theta)$ ). The plus or minus 1 g acceleration provided by gravity ensures evaluation of the sensitivity with respect to a known reference. From figure 73 the sensitivity, extracted for these accelerometers is around 2 mV/V/g. Measurements and model agree within 5 to 10 %, depending on the sensor.

Repetitive cycles of +/- 1g were done in order to evaluate the stability of the sensor. A fast evolution of the offset follows the first cycles; however, the signal stabilizes itself after some tens of cycles. More detail about stability measurement can be found in 2.1.3 (Stability of the Piezoresistive nanogauge). This experiment validates the functionality of the in-plane accelerometers.

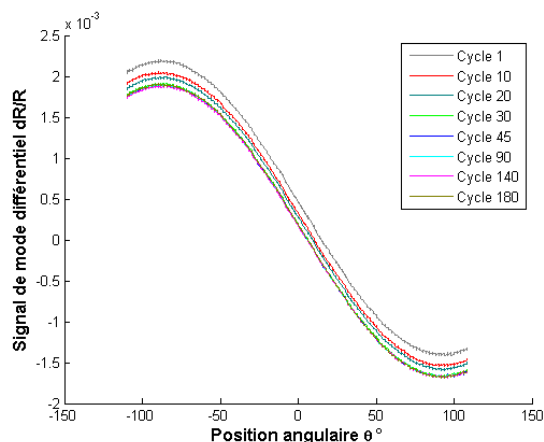


Figure 73: Acceleration response to angular position

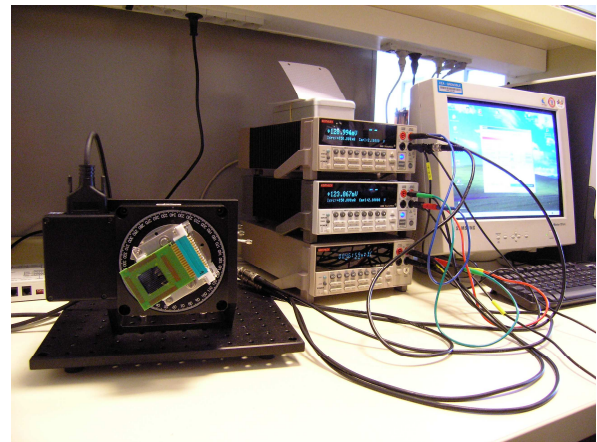


Figure 74: Picture of the experimental setup

### 4.1.2 Out-of-plane-accelerometers

Out of plane accelerometers generally have specific design and constraints with respect to their in-plane counterparts. The main difficulty is to measure an out-of-plane acceleration using an in-plane structure.

#### 4.1.2.a Concept and constraints

The out-of-plane accelerometer follows the same transduction process as the in-plane accelerometer (See figure 60). A pivot will transform vertical acceleration into mechanical stress within the piezoresistive nanogauges. The differential resistive change will be monitored through 4-point measurement.

The main objective of the out-of-plane pivot/gauge assembly is to optimize the longitudinal stress into the gauge obtained for a given vertical acceleration. However the gauge should also be protected from shocks up to 10.000 g in the 3 directions. In his PhD thesis, D.Ettelt [Ett11] showed that both flexural beams and torsion beams can be used to realize an out-of-plan pivot.

Shocks protection can be done by several means. Suspensions beam can act as protection in their compressive direction. As shown in the previous section (4.1.1.f) stoppers are a very good way to provide limitation of the gauge stress. The main limitation of stoppers is the minimum allowed displacement due to a technological limitation around 1  $\mu\text{m}$ .

A new strategy for protection against shocks has been implemented in the out-of-plane accelerometer. The out-of-plane architecture that has been chosen includes torsion beams along with a decoupling spring. The torsion beams act as an out-of-plane pivot and protect the nanogauges from shocks in the  $y$ -direction. The decoupling spring and the stoppers embedded in the design act as a new way to provide shocks protection in the  $x$ -direction. Figure 75 and 76 show top views of the designed out-of-plane accelerometer.

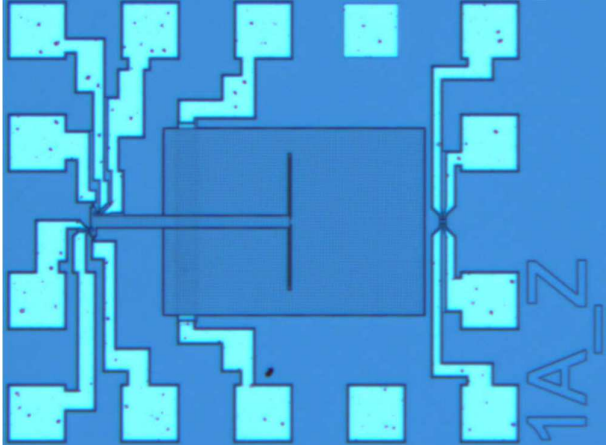


Figure 75: Top view the designed out-of-plane accelerometer

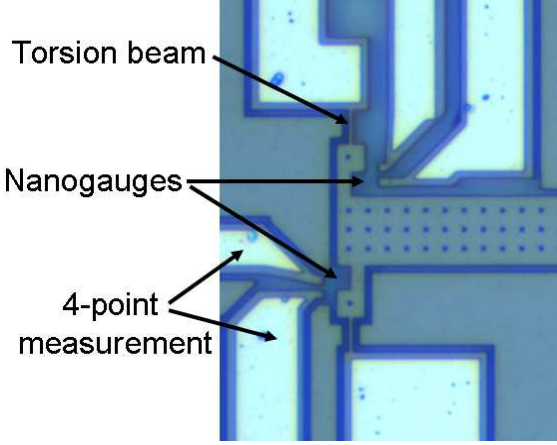


Figure 76 : Top view of the out-of-plane pivot/gauge assembly

**4.1.2.b Model of an out-of-plane pivot/gauge assembly**

The mechanical model of an out-of-plane pivot is shown in figure 40. The right part of the scheme corresponds to the model of an out-of-plane pivot-gauge assembly.  $k_f$  is the torsion beam stiffness in bending and  $k_j$  the compressive stiffness of the nanogauge.  $C_1$  and  $C_2$  are respectively the rotational stiffness of the torsion beam and of the gauges.  $L_0$  is the distance from the center of rotation to the center of mass.

The left part of the scheme corresponds to the inertial mass and the coupling spring.  $k_d$  corresponds to the stiffness of the decoupling spring and  $M$  the mass of the inertial mass.

The scheme shows that the torsion beam and the nanogauge are not at the same height. The position of the rotation axis along the  $Z$ -axis is critical in order to evaluate the lever arm amplification.

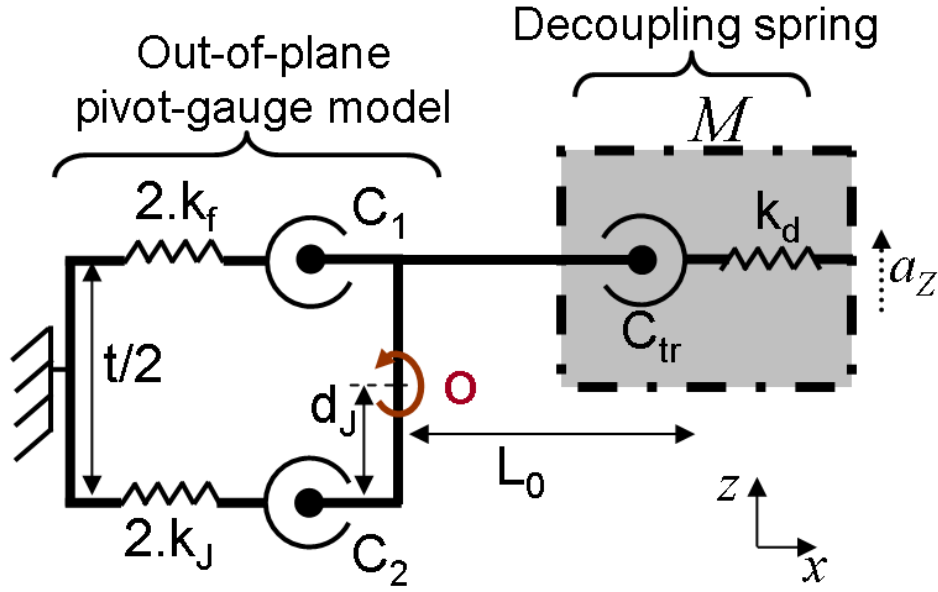


Figure 77: Kinematic model of the out-of-plane pivot/gauge

As already described in chapter 3, the position of the center of rotation O is fixed through the competition of two springs: the compression stiffness of the flexion beam and the compression stiffness of the gauges. The spring with the dominant stiffness will force the whole sensor to rotate around it. In our case  $d_J$  has been estimated to  $2.9 \mu\text{m}$ . Like in 4.1.1, we consider a non deformable lever arm. The sum of all torques is given in equation (59).

$$\sum M = J \ddot{\theta} = m \cdot a_z \cdot L_0 + \left( 2 \cdot k_J \cdot d_J^2 + 2 \cdot k_f \cdot \left( \frac{t}{2} - d_J \right)^2 + C_1 + C_2 \right) \cdot \theta + \gamma_m \dot{\theta} \quad (59)$$

The transfer function of the out-of-plane sensor can be extracted from equations (60) to (62):

$$\frac{\Delta R / R}{a_z} = \frac{G_0}{\sqrt{\left( 1 - \frac{\omega}{\omega_{res}} \right)^2 + \left( \frac{\omega}{\omega_{res} \cdot Q} \right)^2}} \quad (60)$$

$$G_0 = \pi_l \cdot m \cdot \frac{L_0}{d_J} \cdot \frac{1}{2 \cdot S_J + \left( C_1 + C_2 + k_f \cdot \left( \frac{t}{2} - d_J \right)^2 \right) \cdot \frac{l_J}{d_J^2}} \quad (61)$$

$$\omega_{res} = \sqrt{\frac{C_1 + C_2 + 2 \cdot k_J \cdot d_J^2 + k_f \cdot \left( \frac{t}{2} - d_J \right)^2}{J}} \quad (62)$$

Expressions for the quality factor and the resonance frequency can be extracted by the same process as in 4.1.1.c from equation (60). The value of  $\gamma_m$  is a lot larger with respect to the in-plane case because of the larger surface compressing the air gaps. Due to this increased  $\gamma_m$ , out-of-plane accelerometers are overdamped in atmospheric pressure.



Figure 78 shows a FEM simulation of the displacement of the sensor when subjected to a quasi-static out-of-plane acceleration. Color scale shows the intensity of the displacement, blue meaning no displacement and red the maximum amplitude. Such deformation allows us to understand why the transmitting spring stiffness  $k_{tr}$  did not appear in the transfer function calculation. Being placed at the center of mass of the inertial mass, the transmission spring has only the effect of a pivot when the sensor is subjected to an out-of-plane acceleration. On the other hand, when subjected to in-plane acceleration along the x-axis, the transmitting spring will deform itself. Hence the inertial mass will hit the stoppers and limit the stress applied to the nanogauges.

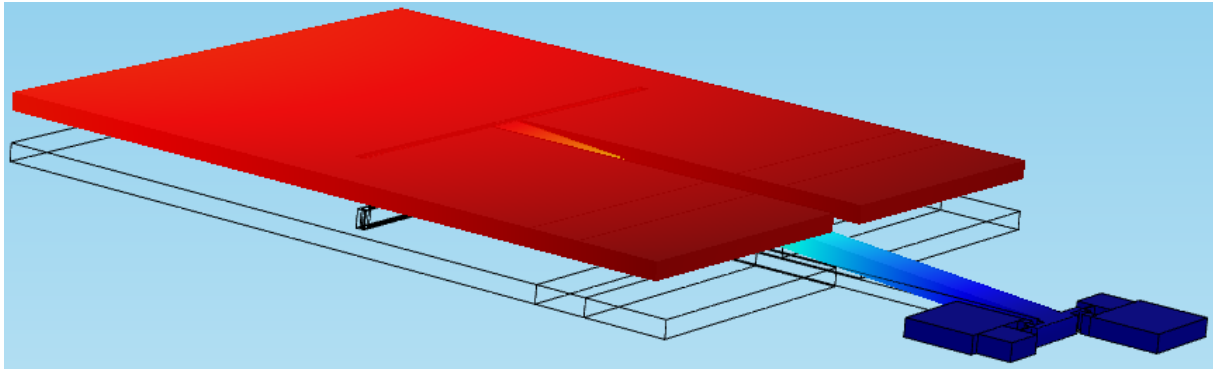


Figure 78: Expected deformation of the sensor when submitted to out-of-plane quasi-static acceleration

Figures 79 and 80 show the simulated Eigen frequencies, whose corresponding eigen modes possess an out-of-plane movement. Figure 79 shows a parasitic mode in which the inertial mass turns around the translation spring. No displacement occurs on the lever arm. The second figure 80 shows the detection mode that should detect quasi-static acceleration.

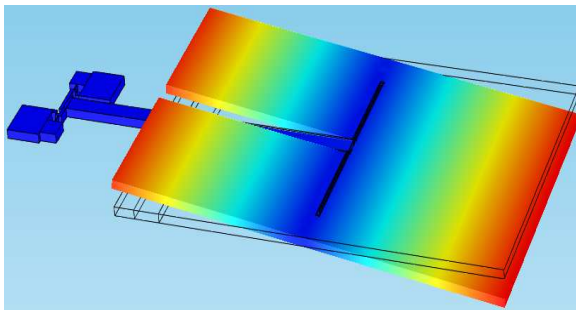


Figure 79 : Parasitic Eigen mode (displacement field - frequency~820Hz). In this case, no stress is induced inside the gauges

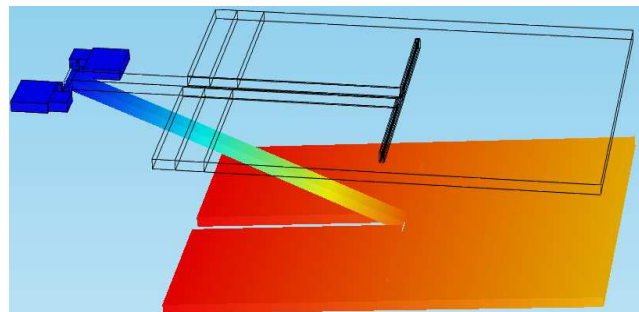


Figure 80: Detection Eigen mode (displacement field - frequency~2302Hz). In this case, a large stress is induced in the nanogauges

The existence of an out-of-plane parasitic mode exhibits a weakness in the design. Symmetric actuation electrodes have to be implemented in order to forbid such low frequency parasitic mode during electrical characterization.

#### Parametric optimization

The gauge geometry is fixed for noise considerations. The epitaxy thickness defining the structure thickness is also fixed to 10  $\mu\text{m}$ . The torsion beam geometry is left for sensitivity optimization. The Graphs in Figure 41 show the gauge stress for 1 g acceleration along Z-direction, considering different torsion beam dimensions. Design rules drawn out of technological limitations forbids a torsion beam width lower than 1  $\mu\text{m}$ . Dimensions of torsion beam with 10  $\mu\text{m}$  length and 1  $\mu\text{m}$  width were chosen.

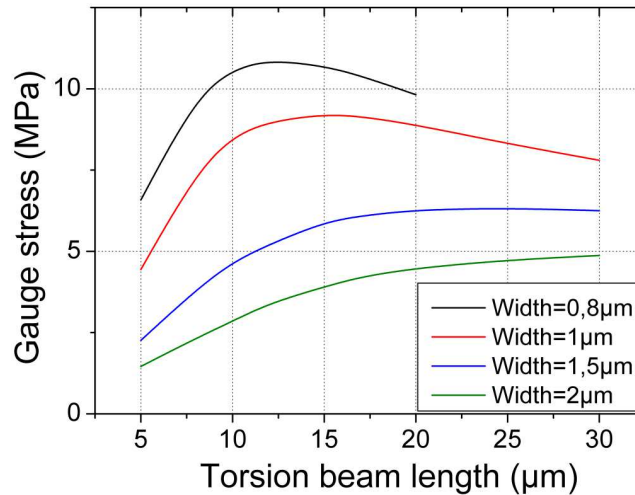


Figure 81: Pivot/gauge dimensioning model

#### 4.1.2.c Shocks protection

In order to protect the gauge from shocks, stoppers were placed at areas of maximum in-plane direction displacement. Their functionality has already been proven in Section 4.1.1.f.

Along the sensing direction  $z$ , the sensor is flexible enough to reach the stoppers when high acceleration occurs. Along the  $y$ -axis, the decoupling spring will increase the movement of the inertial mass with respect to the lever arm displacement. Hence the stoppers will be easily reached, limiting the stress into the gauge. Along the  $x$ -axis, the torsion beams are in compression. Hence they forbid any displacement in the gauge region but they also forbid any displacement of the inertial mass.

FEM simulations showing the expected gauge stress when the inertial mass hits the stoppers under  $x$ ,  $y$  and  $z$  directions is given in table 13. Gauge stress for acceleration in the  $z$ -direction corresponds to the sensitivity of the sensor. Unfortunately, the process flow does not present packaging. Hence no stoppers are present in the upper part of the sensor (i.e  $z$ -direction).

Acceleration	Displacement of the inertial mass (nm)	Stress into the gauge for 1 g acceleration (MPa)	Stress in the gauge (assuming stops at 1 μm)
1 g along $X$	9	1.67	<b>180 MPa</b>
1 g along $Y$	33	0.12	<b>4 MPa</b>
1 g along $Z$	95	6.1 ( <i>Sensitivity</i> )	<b>64 MPa</b>

*Table 13: Influence of shocks for out-of-plane accelerometers*

From table 13 the maximum stress that will occur in the gauge is given in the last column. Assuming that stress up to 1 GPa induce elastic deformation, the gauges are efficiently protected from shocks. The decoupling spring seems to be more efficient than the suspension beam to prevent stress inside the gauge. Provided it does not impact sensitivity or weaken the design, the use of decoupling spring could be enlarged to provide shocks protection.

#### 4.1.2.d Mechanical characterization

##### Dynamic characterization

The actuation electrodes have to be symmetrical with respect to the transmitting spring. If it is not the case, the electrode will excite preferentially the parasitic mode. The parasitic mode induces a deformation of the inertial mass as it turns around the decoupling spring. No constraint is seen by the nanogauges. Dynamic characterization done in vacuum ( $P^{\circ} < 10^{-5}$  mbar) allows a mechanical validation of the sensor. The resonance frequency measured in figure 82 corresponds well with the simulated frequency of the detection mode.

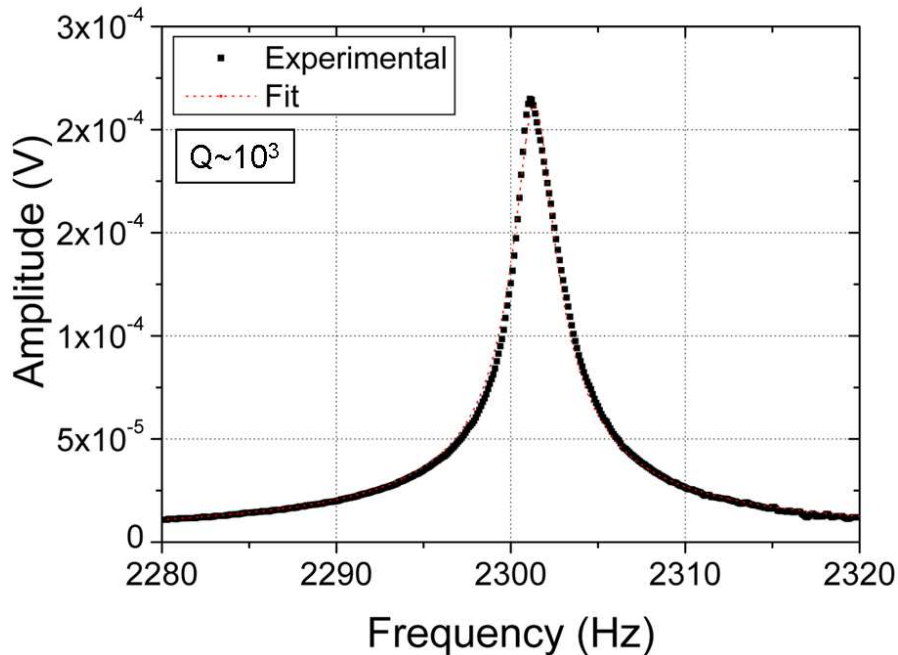


Figure 82: Resonant mechanical frequency response in vacuum

This measurement allows a good evaluation of the resonance frequency of the sensor. Since the FEM simulation and the experimental measurement gives the same resonance frequency. The analytical model is considered as validated.

## 4.2 Pressure sensor

### 4.2.1 Pressure sensor as an altimeter in MEMS inertial platforms

The objective of MEMS inertial platforms is to provide the customer with a position in space. A Z-axis accelerometers measure acceleration. Therefore their output signal has to be integrated twice before obtaining a position. From these successive integrations, large errors arise that degrade the altitude signal. Since the sensitivity and resolution of our Z-accelerometers is lower than in-plane accelerometer, Z-axis accelerometer cannot be used to extract altitude. In order to keep track of the position along the z-axis on earth, pressure is another parameter can be easily measured. Figure 83 shows the pressure variation along altitude.

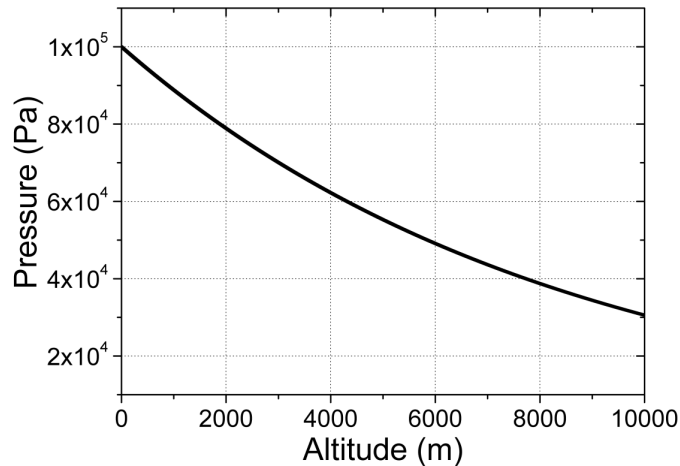


Figure 83: Relationship from pressure to altitude on earth

If we consider that we stay around the sea level, the equivalent pressure variation for 1 m is 11 Pa. Considering an absolute pressure sensor with a full-scale of 1 Bar, the specification in terms of dynamic range are around  $10^4$ - $10^5$ .

Pressure has the advantage that no integration is required to get information about altitude. However, weather variation can disturb pressure based altimeter. In order to cost effectively replace Z-accelerator in IMU, pressure sensors should possess a footprint comparable with those of accelerometers ( $< 1\text{mm}^2$ ) and possess a compatible process flow. A membrane-based pressure sensor that has been integrated along with in-plane accelerometers and gyroscopes is described below.

#### 4.2.2 Mechanical model

##### 4.2.2.a Concept

The transducer discussed here is a proof-of-concept of the integration of the M&NEMS concept onto a membrane-based pressure sensor [Dei13]. Figure 84 shows a side view of the final step of a process flow that would allow the creation of ultra-compact absolute pressure sensor based on mechanical amplification.

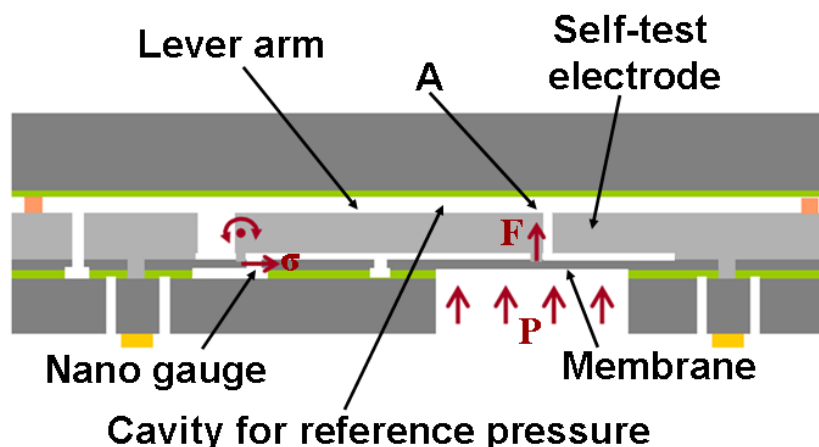


Figure 84: Side view of a piezoresistive pressure sensor with mechanical amplification

The pressure sensor is based on a membrane which deforms when submitted to a differential pressure. This deformation induces a force on point A (See figure 84). From here, the rest of the transduction chain is identical to the one of a Z-accelerator (i.e stress amplification through a pivot/gauge assembly and readout through a half-Wheatstone bridge).

The presented transducer has been fabricated and tested. Figure 85 is a colored SEM image of the fabricated transducer. The mechanical footprint of the pressure sensor is about 0.04 mm<sup>2</sup> (200μm\*200μm), much below the footprint of state-of-the-art for membrane based pressure sensors.

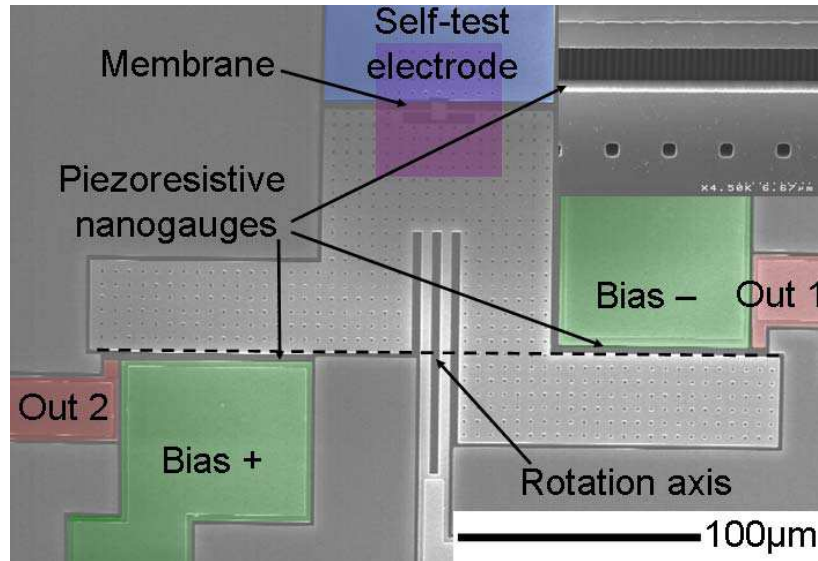


Figure 85: Top view of the fabricated transducer

Pressure forces are huge with respect to electrostatic or acceleration forces at MEMS scale (See Eqn (70)). Therefore some different design choices have been made:

- High forces require stiffer springs. The nanogauge dimension has been increased in order to reduce the 1/f noise, with the objective of an increased dynamic range.
- Stiffer flexural beam replace the torsion beam of the Z-accelerometers.

#### 4.2.2.b Membrane model

The membrane created through the NEMS layer has been modeled through figure 86. A vertical force  $F_e$  and an external pressure  $\Delta P$  are considered as two ways of deforming the membrane.

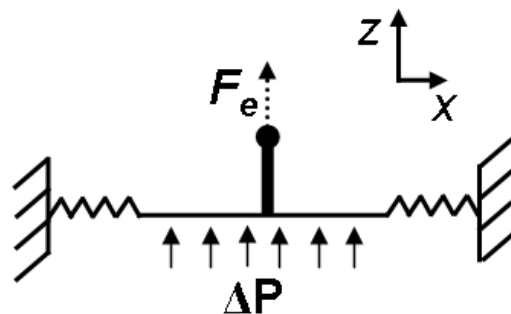


Figure 86: Kinematic scheme of the fabricated transducer

Considering no external force and a square membrane, the displacement-pressure relationship can be expressed as:

$$\Delta z_1 = \frac{\alpha}{k_m} S_m \Delta P \quad (63)$$

With  $\alpha$  is a constant evaluated from the Roark's textbook around 0.0138 [Roark12] and  $S_m$  the membrane surface. Considering no differential pressure and an external force  $F_e$  the transfer function becomes:

$$\Delta z_2 = \frac{\beta}{k_m} F_e \quad (64)$$

With  $\beta$  a constant evaluated at 0.0611 from [Roark12].

#### 4.2.2.c Detection arm model

Figure 87 shows the kinematic model of the pressure sensor from a cross-section view. The out-of-plane pivot/gauge assembly is identical to the one already described for the Z-accelerometer.

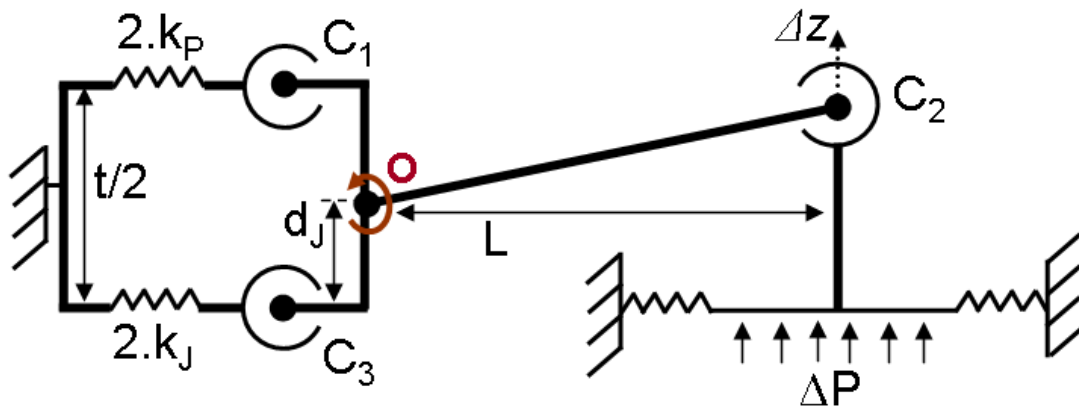


Figure 87: Kinematic scheme of the fabricated transducer

The membrane is linked to the out-of-plane pivot/gauge assembly through a transmitting pivot of stiffness  $C_2$ . All the influence of the detection arm can be considered mechanically in terms of stiffness and reported at the center of the membrane. Equation (65) shows the expression of the detection arm stiffness  $k_{arm}$  reported at the center of the membrane.

$$k_{arm} = \frac{2.k_J.d_J^2 + 2.k_P.\left(\frac{t}{2} - d_J\right)^2 + C_1 + C_2 + C_3}{L^2} \quad (65)$$

Figure 88 shows the behavior of the detection arm when submitted to a compressive stress.

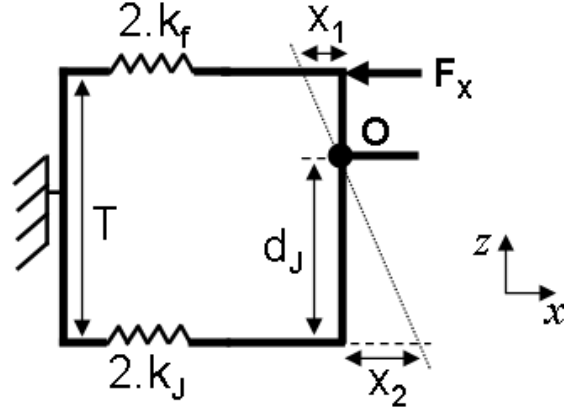


Figure 88: Kinematic scheme of the detection arm submitted to a compressive force

Using equations (39) and (40) the gauge to center of rotation distance  $d_J$  has been estimated to  $1.9 \mu\text{m}$ .

#### 4.2.2.d Transfer function

The force exerted by the detection arm onto the membrane can be expressed through the force-displacement law of an elastic spring.

$$F_{arm} = k_{arm} \cdot \Delta z \quad (66)$$

The vertical displacement of the membrane corresponds to the addition of the displacement due to an additional pressure and to a deformation occurring because of an external force. Using equations (63), (64) and (66) we can deduce the pressure-displacement relationship of the transducer.

$$z = z_1 + z_2 = \frac{\alpha}{k_m + \beta \cdot k_{arm}} S_m \Delta P \quad (67)$$

In order to obtain the complete transfer function of the sensor, the displacement-resistance change relationship was evaluated in equation (68).

$$\frac{\Delta R}{R} = E \pi_l \frac{d_J}{L} \cdot \frac{\Delta z}{l_J} \quad (68)$$

With  $l_J$  is the gauge length,  $\pi_l$  the longitudinal piezoresistive coefficient and  $L$  the lever arm (i.e distance from the pivot to the center of the membrane). Using equation (67) and (68) the complete transfer function of the pressure sensor is shown in equation (69).

$$\frac{\Delta R}{R} = \frac{E \cdot \pi_l}{l_J} \cdot \frac{\alpha}{k_m + \beta \cdot k_{arm}} \cdot \frac{d_J}{L} \cdot S_m \Delta P \quad (69)$$

The optimal sensitivity is obtained when the term  $2 \cdot k_j \cdot d_J^2 / L^2$  in the term  $k_{arm}$  is the predominant stiffness. This case corresponds to the case when most of the constraints are transferred to the gauge.

### 4.2.3 Simulations and model validation

#### 4.2.3.a Model validation

The analytical model described in the previous section has been validated both experimentally and through simulations. Figure 89 shows the simulated vertical displacement of the membrane for various differential pressures.

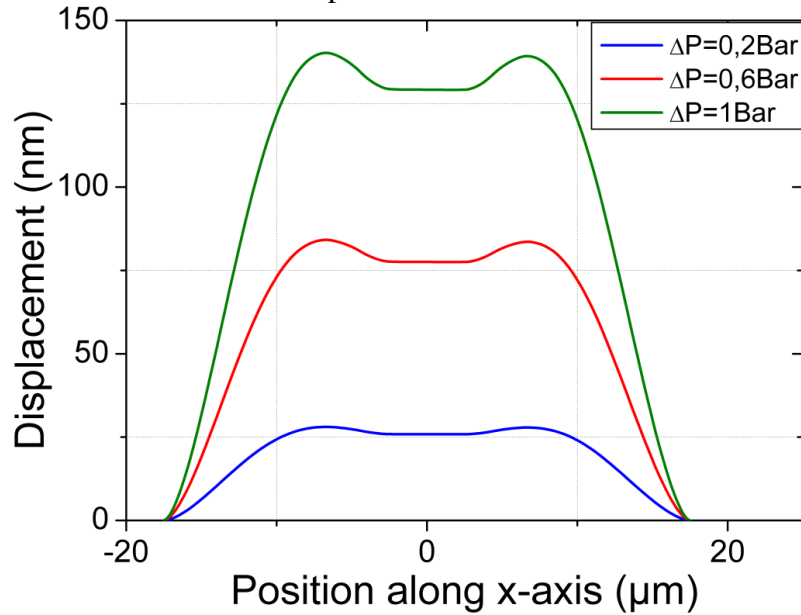


Figure 89: Simulated shape of the membrane deformation for various pressures

The Finite Element Model simulations shown in figure 89 confirm that the dominant stiffness is the stiffness  $k_{arm}$  of the detection mean reported at the center of the membrane. A quantitative comparison between the analytical model, the FEM simulation and the measured deformations yields 68 nm/Bar, 129 nm/Bar and 110 nm/Bar respectively. This basic analytical model, which allows an evaluation of the sensor sensitivity within 50 % discrepancy, appears to be convenient for a rough description of the sensor operation.

#### 4.2.3.b Cross-axis sensitivity (Crosstalk)

Like the other MEMS inertial sensors described in this thesis, the pressure sensor is based on a pivot/gauge assembly. To increase sensitivity, the center of rotation is far from the center of mass. From a theoretical point of view, the sensor will exhibit sensitivity to inertial force, (i.e acceleration along  $Z$  and rotation along  $Y$ ). The analytical model along with FEM simulations shows that the sensitivity to acceleration is around  $1 g$  for  $1 Pa$ . The extremely small mass of the sensor is the main argument to explain this very low sensitivity to inertial force. If for a given application, this cross-axis sensitivity has to be reduced, implementation of a counter weight is easily done. Figure 90 shows a possible implementation of such counter weight.



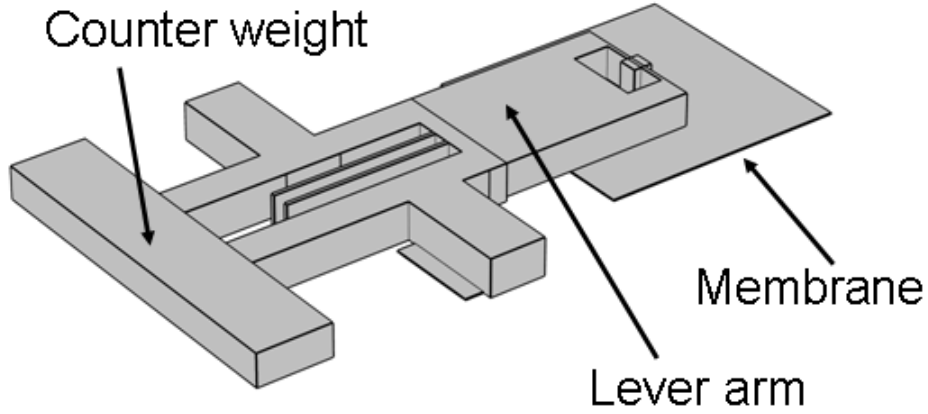


Figure 90: View of a pressure sensor with parasitic acceleration compensation

#### 4.2.4 Characterization and performances

##### 4.2.4.a Functional validation

One of the advantages of the proposed sensor is that self-test electrodes can be easily implanted onto the membrane. Additionally to testing purposes, they can be used for quasi-static compensation of the atmospheric pressure. Using this self-test electrode, the transfer function of the sensor has been validated. Equation (70) gives the parameters that control the applied electrostatic pressure.

$$P_{el} = \frac{F_{el}}{S_m} = \frac{S_{el}}{S_m} \frac{\epsilon_0 V_{DC}^2}{g^2} \quad (70)$$

Here  $S_{el}$  is the electrode surface,  $S_m$  is the membrane surface,  $g$  is the gap between the electrode and the membrane.  $P_{el}$  is the electrostatic pressure, and  $F_{el}$  the electrostatic force.  $V_{DC}$  is the voltage difference between the electrode and the membrane. The self-test electrode gives a conversion parameter around 3.4 Pa/V<sup>2</sup>.

Figure 91 shows the measured characteristic of the relative resistance change recorded for different electrostatic pressure levels. The sensor exhibits a sensitivity of about 450  $\mu$ V/V/Bar.

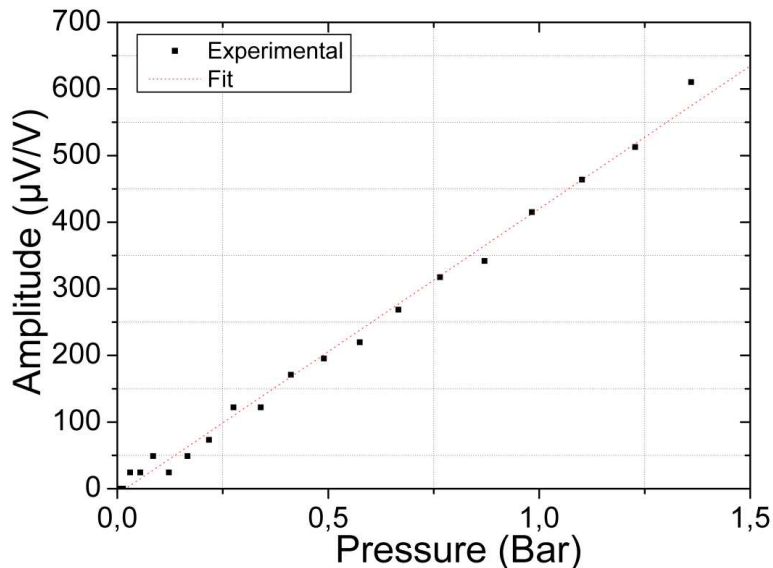


Figure 91: Measured output of the piezoresistive nanogauge

#### 4.2.4.b Dynamic characterization

Like the other transducers, the transfer function of the pressure sensor has been measured. Figure 92 depicts the transfer function of the sensor in air (red curve) and in vacuum (blue curve).

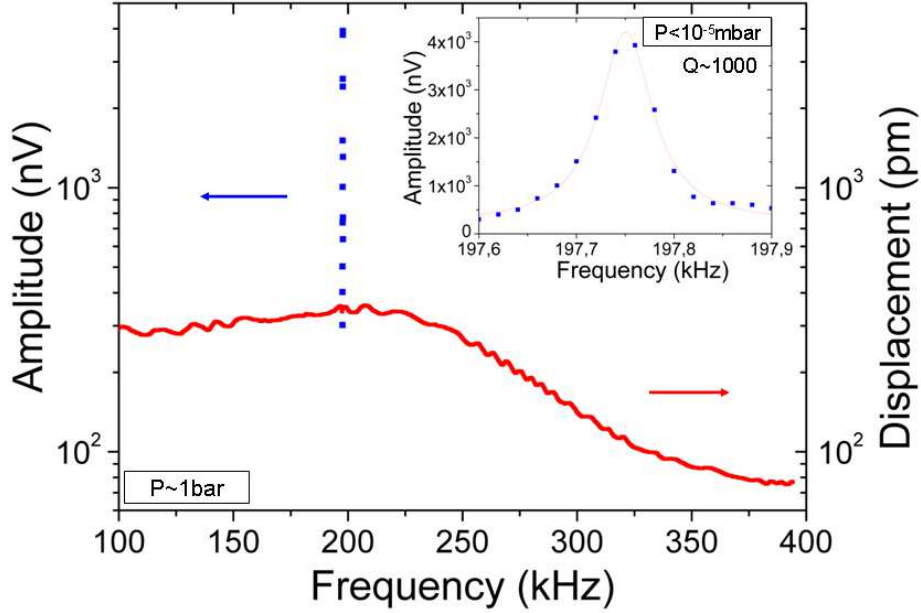


Figure 92: Frequency response extracted using vibrometer and electric measurement

If the reference pressure is atmospheric pressure, then the sensor will be over-damped. If the reference cavity is under vacuum, it will have a quality factor around  $10^3$ . In both cases, the resonant frequency of the sensor is high enough (i.e.  $\sim 200$  kHz) to prevent implication on the bandwidth of the sensor.

#### 4.2.4.c Dynamic range evaluation

Using the noise measurement presented in chapter 2. It is possible to evaluate the dynamic range of the sensor. Considering a bandwidth of  $[10^{-8}, 10^2$  Hz] the major noise contribution is expected to be the Flicker noise. The power spectral density of the  $1/f$  noise is given in equation (71) from [Hoo78]:

$$S_{1/f} = \frac{\alpha \cdot V_{POL}^2}{N \cdot f} \quad (71)$$

Here  $N$  is the number of carrier,  $f$  is the frequency and  $V_{POL}$  is the voltage drop across the gauge. From the measurements, a Hooge factor of  $4 \cdot 10^{-6}$  has been extracted. To guarantee the linearity of the piezoresistive transduction, a safe limitation of 100 MPa has been taken as the maximum gauge stress. Considering the  $1/f$  noise, an electronic noise of  $20$  nV/ $\sqrt{Hz}$  and a polarization voltage  $V_{POL}$  of 1 V, the dynamic range of the sensor can then be evaluated to  $8 \cdot 10^4$ . Such dynamic range translates into a resolution of about 80 Pa for a full scale around 60 Bars. This result confirms the feasibility of an altimeter using the proposed fabrication principle and transduction means.

### 4.3 Two-axis accelerometers

Considering that the main objective is the fabrication of a MEMS inertial platform with the capability to give the user true position, accelerometers should be implanted in the three directions in order to provide position.

One can ask whether a structure able to measure accelerations along several axes at the same time is more efficient than several single axis structures. In this section, we will describe a two-axis accelerometer that has been fabricated. Comparison of single axis solution with respect to multi-axes accelerometer in terms of footprint is then proposed in the last part of the chapter.

#### 4.3.1 Principle of operation

The objective of multi-axes sensor is to reuse mechanical parts in order to improve either performance or footprint. Considering that in the M&NEMS concept the detection arm consists of a pivot/gauge assembly, each axis has to be read on a dedicated half Wheatstone bridge. The inertial mass however can be shared between the different axes. Considering these constraints, figure 93 shows a kinematic scheme of the proposed two-axis accelerometer.

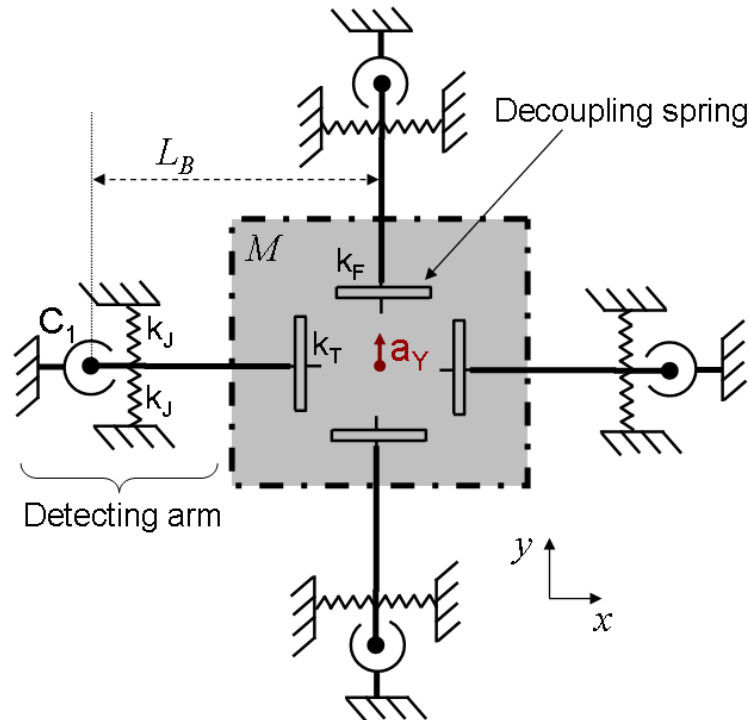


Figure 93: Kinematic scheme of the two-axis accelerometer

The two-axis accelerometer is made of 3 different parts. The inertial mass  $M$  moves when submitted to inertial force, the set of four decoupling springs transmit the movement in the corresponding transmitting direction and deform in the decoupling direction. The four corresponding detecting arms see displacements only when it compress/tense the piezoresistive gauges.  $k_F$  stands for the flexion spring; it is the spring that will deform in case of  $y$ -acceleration.  $k_T$  stands for transmission spring. In case of  $y$ -acceleration, it will transmit the effort to the detection arm.

The structure is symmetrical in order to keep the inertial mass displacement in the direction of the acceleration. Also, a full Wheatstone bridge readout is provided for each direction.

### 4.3.2 Design

Figure 94 is an optical image of the fabricated two-axis accelerometer. The measurement of a full Wheatstone bridge for each axis induces a large number of electrical connections, which induce a rather large footprint. To obtain a functional two-axis accelerometer, only 11 electrical connections are needed (but the measurement will be based on a half-Wheatstone bridge only).

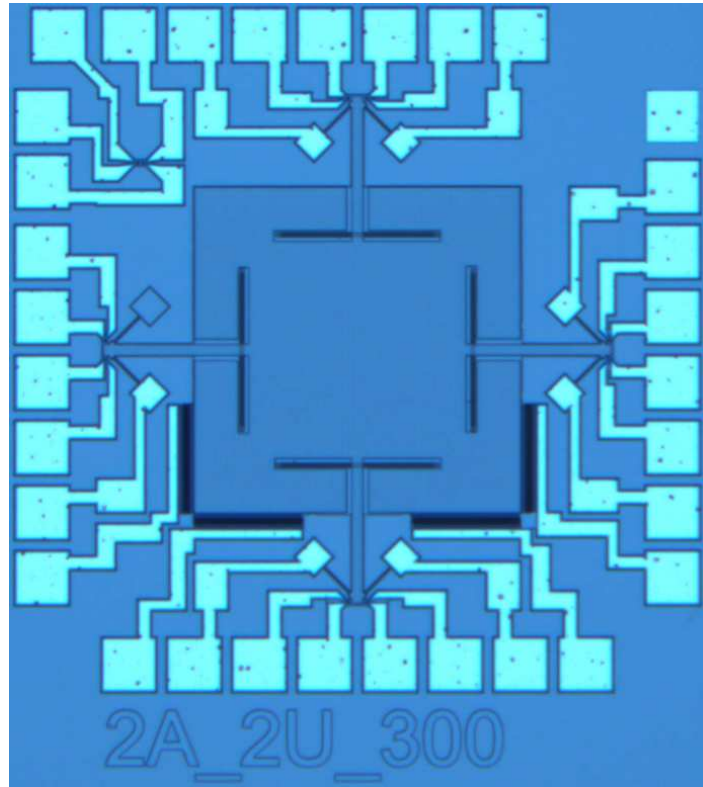


Figure 94: SEM image of the fabricated two-axis accelerometer

The equation of movement occurring on the inertial mass is given in equation (72) considering a unidirectional acceleration along the y-direction:

$$M \ddot{y} + \gamma \dot{y} + y \left[ 2.k_F + 2. \left( \frac{k_T.(C_1 + 2.k_J.d_J^2)}{k_T.L_B^2 + C_1 + 2.k_J.d_J^2} \right) \right] = 0 \quad (72)$$

The decoupling spring will have an influence on sensitivity as shown in equation (72) and on the inertial mass displacement. Their dimension will have to comply with the following constraints:

- In terms of shocks, the inertial mass should hit the stoppers situated at 1  $\mu\text{m}$  of the inertial mass before the nanogauges are submitted to a stress higher than 1 GPa (which correspond to the maximum constraint allowed before irreversible deformation. Here we are out of the linear range of the piezoresistive effect  $\sim 100\text{MPa}$ ).
- The objective is to obtain a full scale of 20 g.

In the sensing direction, the decoupling spring should transmit as much effort as possible to the detecting arm. In the decoupling direction, the spring should be as compliant as possible.

In the proposed design, the spring deforms in **compression** in the **sensing direction**. The decoupling spring deforms in bending in the decoupling direction. Bending and compression stiffness of a given spring are linked. Equation (73) gives the ratio between flexural (bending) and compression stiffness:

$$\frac{k_T}{k_F} = \frac{E.W.t/L}{E.W^3.t/L^3} = \frac{L^2}{W^2} \quad (73)$$

Since there are no stoppers at the bottom and top parts of the sensor, the mechanical suspension part should be stiff enough along the  $z$ -axis, in order to prevent sticking issues. To comply with this requirement, the decoupling spring length has been fixed to  $250 \mu\text{m}$  for  $1 \mu\text{m}$  width forming a double U-shape geometry (the thickness of the spring is around  $10 \mu\text{m}$ ).

The cross-axis sensitivity should not be a problem considering that, if any displacements are not absorbed by the decoupling spring, then the detecting arm displacement will induce bending that will be identical on both gauges. Therefore the piezoresistive signal extracted from cross-axis acceleration should remain low. Figure 95 and 96 show the detection mode of the sensor when acceleration along the  $x$ -axis and  $y$ -axis occurs, respectively.

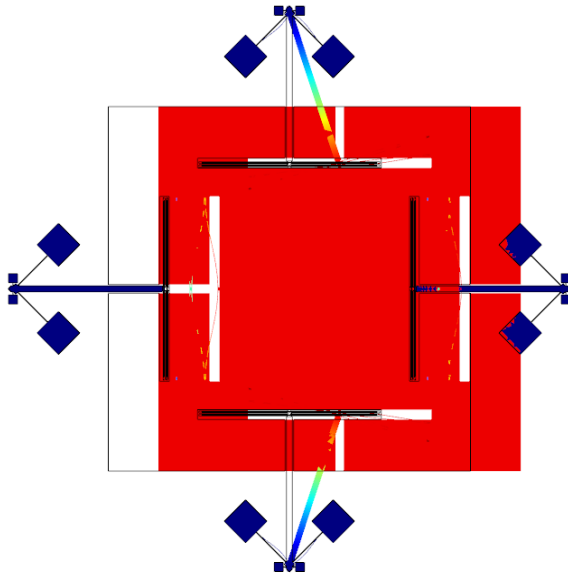


Figure 95: Simulated deformation of the sensor for  $x$ -axis acceleration

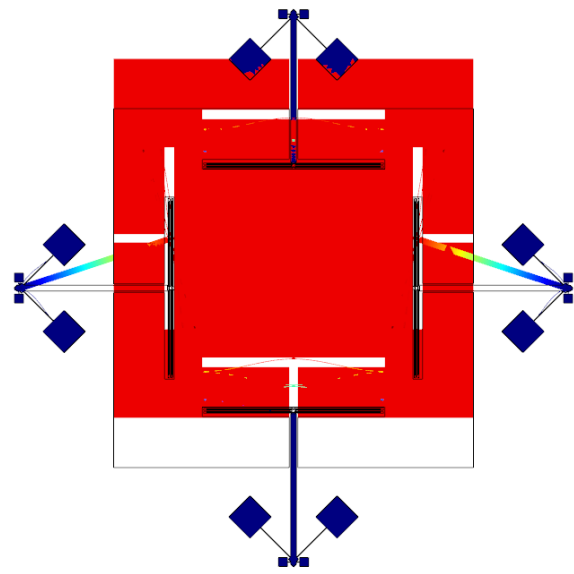


Figure 96: Simulated deformation of the sensor for  $y$ -axis acceleration

Table 14 sums up the most important properties of the sensor. The gauge maximum stress is around  $350 \text{ MPa}$  assuming stoppers at  $1 \mu\text{m}$  along the detection axes. With a gap of  $1 \mu\text{m}$ , shocks in the  $z$ -direction of at least  $60 \text{ g}$  are needed to produce sticking problems. From simulation point of view, the designed two-axis accelerometer complies with specifications. Table 14 shows the simulated performance of the two-axis accelerometer.

Sensitivity / Full Scale	6.2MPa/g or FS=16g
Relative Cross-axis sensitivity	3 ppm
Displacement of the inertial mass for 1g in the :	
• In-plane direction	32 nm
• Out-of-plane direction	15 nm
Mechanical Footprint	1 mm <sup>2</sup>
<i>Table 14 : Simulated performance of the two-axis sensor</i>	

#### 4.3.2.a Dynamic behavior

Even if accelerometers are quasi-static sensors, eigen frequencies simulations have been carried-out seeking for possible weakness in the design. The relatively small stiffness of the decoupling springs reduces the resonant frequency of the parasitic mode shown in figure 97. This parasitic mode has been observed experimentally. Attention should be paid to always actuate the sensor symmetrically in order to simulate a truly directional acceleration when conducting quasi-static experiments. Additionally if the two half-bridges are measured on a given sensing axis, they should compensate each other so that the sensitivity to this parasitic mode is efficiently reduced.

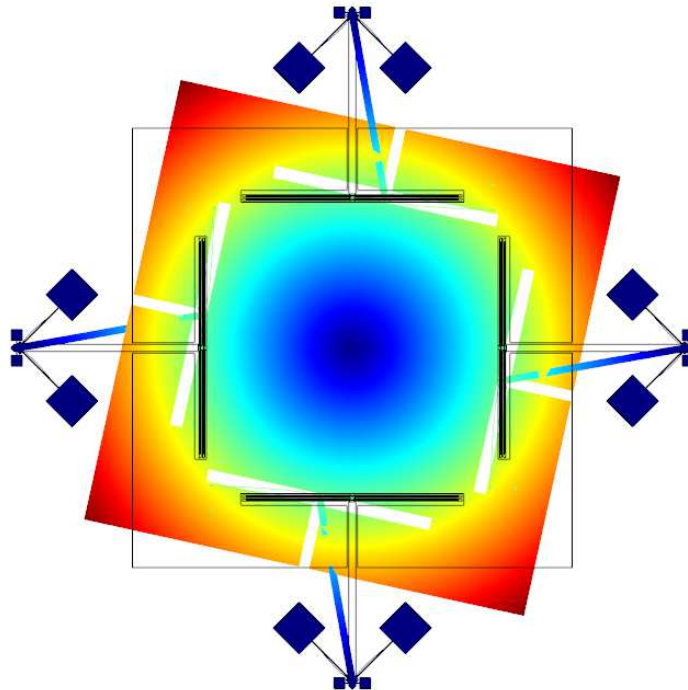


Figure 97: 1<sup>st</sup> parasitic in-plane mode of the two-axis accelerometer ( $f \sim 3050\text{Hz}$ )

### 4.3.3 Characterization

#### 4.3.3.a Quasi-static validation

Validation of the two-axis accelerometer has been performed, using the setup described in the noise measurement section (in chapter 2) and implementing the above-mentioned electrostatic actuation embedded for testing purposes. Using the AC voltage probed on the gauges and demodulation through the use of a Lock-in amplifier, the differential resistance change has been recorded across time. DC actuation voltage has been produced on different electrodes to emulate in-plane acceleration. Figure 98 shows the measured output voltage at the middle of the half bridge after demodulation for different

actuation voltages. Figure 99 shows both actuation voltages applied as well as the output voltage measured across time.

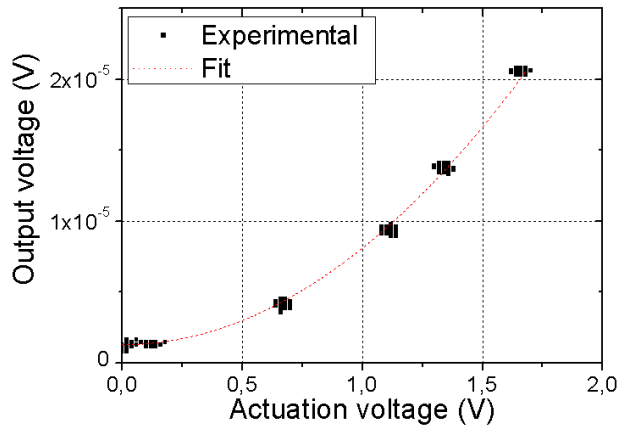


Figure 98: Experimental testing of the two-axis accelerometer using embedded electrostatic actuation

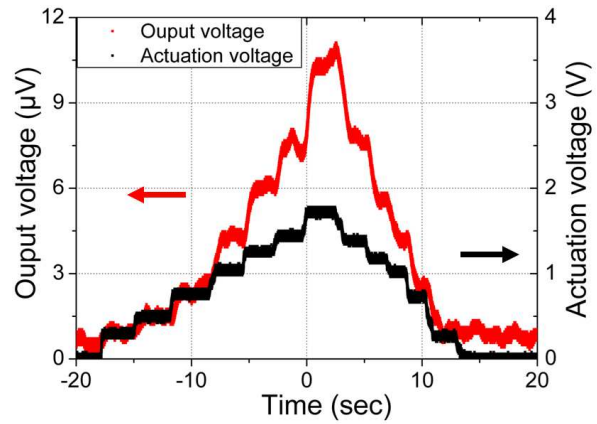


Figure 99: Raw Actuation voltage (in black) and corresponding output voltage (in red) during measurement

The actuation voltage has been moved manually up to  $\sim 1.7V$ . The transient response was measured *in situ*. Several identical measurements were done on different actuation electrodes. The electrostatic force created is proportional to the square of the actuation voltage. Polynomial fit with only a constant and a quadratic component were carried out. These measurements give fits with identical fitting parameters. From these different fits, an average sensitivity of  $900 \mu V/V/g$  on one half bridge could be extracted. This leads potentially to a full scale of 30 g, which is extrapolated from this measurement.

An improved analytical model of the decoupling spring should be built in order to provide a better analytical model along with an understanding of the parasitic rotation mode.

## 4.4 Prospects of three-axis accelerometers

### 4.4.1 Footprint comparison of multi-axes accelerometers with respect to single axis accelerometers

In the previous sections of this chapter, in-plane and out-of-plane accelerometer were proposed and characterized along with two-axis accelerometers. At first glance, multiple axis accelerometers with only one inertial mass lead to smaller sensor footprint than several single-axis accelerometers with several inertial mass. Table 15 shows the measured performances along with the footprint of the different sensors. We define the efficiency/axis (used in table 15) as the ratio between the sensors sensitivity and its total footprint (by axis). The highest efficiency defines the sensor with the best performances given identical design rules. At this stage, it is worth mentioning that the cross-axis sensitivity is not taken into account.

Sensor type	Sensitivity	Mechanical footprint	Total footprint	Efficiency/axis
In-plane accelerometer	2 mV/V/g	300x400 $\mu m^2$ $\sim 0.12 \text{ mm}^2$	$\sim 0.36 \text{ mm}^2$	5.5 mV/V/g/ $\text{mm}^2$
Out-of-plane accelerometer	1.8 mV/V/g	340x600 $\mu m^2$ $\sim 0.2 \text{ mm}^2$	$\sim 0.6 \text{ mm}^2$	3 mV/V/g/ $\text{mm}^2$
Two-axis accelerometer	3.6 mV/V/g	950x950 $\mu m^2$ $\sim 0.9 \text{ mm}^2$	$\sim 1.6 \text{ mm}^2$	4.5 mV/V/g/ $\text{mm}^2$ (2 axes)



Pressure sensor	450 $\mu\text{V/V/bar}$	200x200 $\mu\text{m}^2$ ~0.04 $\text{mm}^2$	~0.17 $\text{mm}^2$	2.6 $\text{mV/V/bar/mm}^2$
<i>Table 15: Performances of the different sensors proposed</i>				

From the upper table, we can say that the out-of-plane accelerometer possess lower performances than in-plane accelerometers. This can be explained by the low performances of the out-of-plane pivot.

A comparison of the in-plane accelerometer with respect to the two-axis accelerometer shows that the single axis-accelerometer is much smaller than its two-axis counterparts. The footprint gains expected from multi-axis sensing did not show up. This table should be taken with care given that none of the designs are perfectly optimized and that the increased footprints due to the sealing ring and the sawing are not taken into account (which will enlarge all footprints).

The intrinsic difference of multiple-axis accelerometers with respect to their single-axis counterpart is the use of decoupling springs. The intrinsic performance of several sensing axes can be reduced to a decoupling ratio. Let's consider a two-axis accelerometer with an inertial mass twice as large as its single-axis accelerometer counterpart. The detecting arms are considered identical on both sensors. The amount of inertial force transmitted to a detecting arm corresponds to the inertial mass multiplied by the decoupling ratio. For a two-axis accelerometer, if the decoupling ratio is higher than  $\frac{1}{2}$ , the performances will be higher than its single axis counterpart. It will have the same footprint but higher sensitivity.

The most critical part when designing a multi-axis accelerometer is the design of the decoupling spring through the obtained decoupling ratio. It will determine the effectiveness of the multi-axis solution with respect to the single-axis solution.

#### *4.4.2 Footprint repartition of piezoresistive accelerometers based on M&NEMS concept*

In this section, we will conclude on analyzing the footprint repartition of the three-axis accelerometer formed by the solutions described in this section 4.4.1. Figure 100 shows the footprint repartition of the different parts of the sensor considering that a 3-axis accelerometer has been fabricated out of two single axis in-plane accelerometer (and one out-of-plane accelerometer). Figure 101 shows the same footprint repartition but considering that a two-axis accelerometer is used instead of the single-axis accelerometers.

This analysis has been performed using the following design rules.

- Electrical pads are fixed to 100x100  $\mu\text{m}^2$ .
- The sealing ring width is assumed to be 100  $\mu\text{m}$ .
- The saw width is supposed to be 70  $\mu\text{m}$ .



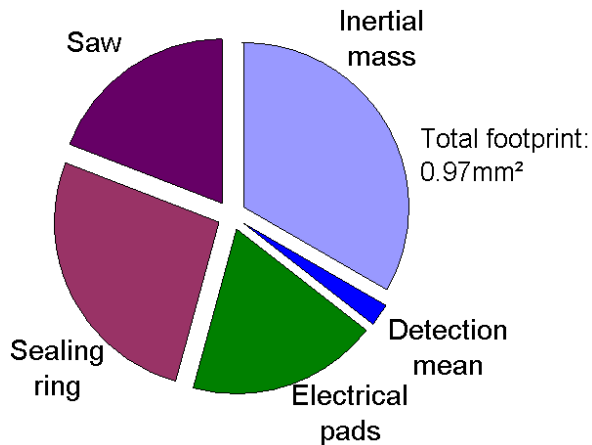


Figure 100: Footprint repartition view of a 3-axis accelerometer based on single-axis accelerometer

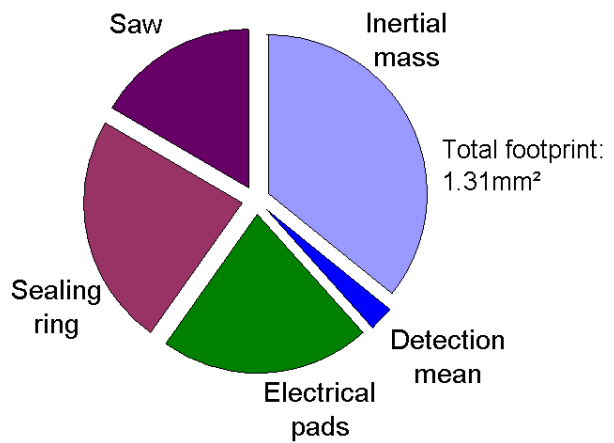


Figure 101: Footprint repartition view of a 3-axis accelerometer based on two-axis accelerometer

From figure 100 and 101 the effective mechanical footprint of the sensor (light blue) takes about a third of the whole footprint. The objective of the M&NEMS concept to reduce the mechanical footprint of sensors is achieved. In order to reduce again the footprint of the accelerometer, gains will have to be obtained in the environment of the sensor. For instance large gain can be expected from the introduction of TSV (Through Silicon Vias) technology which would allow drastic reduction of the electrical pads area.

#### 4.5 Conclusion

In this chapter, different inertial sensors have been designed: (i) single-axis, (ii) dual axis for in-plane accelerations and (iii) out-of-plane accelerometer. The analytical models of these inertial sensors are given and validated through both FEM and experimental measurements, mainly based on electrical testing through emulation of the acceleration force, by means of embedded electrostatic actuation. Some measurements based on real acceleration have been conducted as well for the single-axis accelerometer, which led to the validation of the whole electromechanical chain of the nanogauge-based accelerometer sensor and the corresponding modeling methodology. Beside the stoppers, whose function is to ensure a limit for the maximum displacement, a new strategy for shock protection based on decoupling spring has been validated. Furthermore, an original, ultra-compact membrane-based pressure sensor with mechanical amplification is reported as a candidate for retrieving the altitude within an IMU platform. Based on the proposed figure of merit towards mass production of inertial sensors, the in-plane single axis accelerometers exhibit the best sensitivity-footprint tradeoff. Finally, a compact out-of-plane accelerometer has been validated, completing the whole set of sensors for retrieving the linear degrees of freedom X, Y and Z of an IMU.

# Chapter 5: Resonant structures

In order to easily understand the structures I worked on, the dual-mass gyroscope is described in the first section of this chapter, as a background to what will follow. The additional value of this chapter lies mostly in the sections 5.2 to 5.4.

## 5.1 Dual-mass gyroscopes with piezoresistive detection

In this section, the working principle of a dual-mass gyroscope is described and divided into different mechanical and electrostatic parts.

As described in chapter 1, the aim of dual-mass configuration is to:

1°) provide a differential measurement by forcing an opposite displacement of the two inertial masses.

2°) introduce differential measurement in order to improve the common mode rejection in order to suppress the sensitivity to acceleration.

Additionally the use of symmetric decoupling springs reduces the influence of the drive part on the sense part. It also contributes in reducing energy loss and hence reaching high values for the quality factor of the resonators.

On figure 102 is depicted a schematic view of a dual-mass gyroscope with improved mode ordering. The drive part of the device (in green) will be actuated along the x-direction. The drive part is mechanically coupled to the inertial mass (in red) by decoupling springs that are stiff in the drive direction and compliant in the sense direction. The movement of the inertial mass along the sense direction is monitored by the detection part (in blue) here with piezoresistive detection.

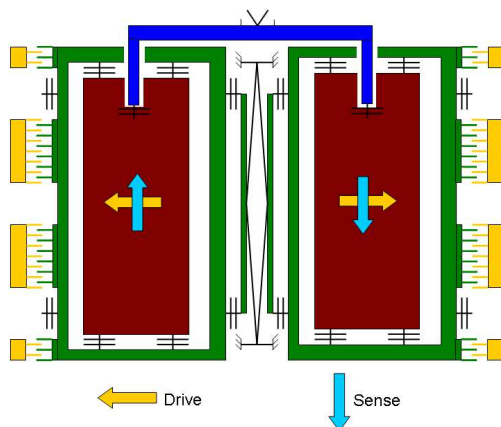


Figure 102: Cinematic scheme of an improved mode ordering piezoresistive dual-mass gyroscope [Wal12]

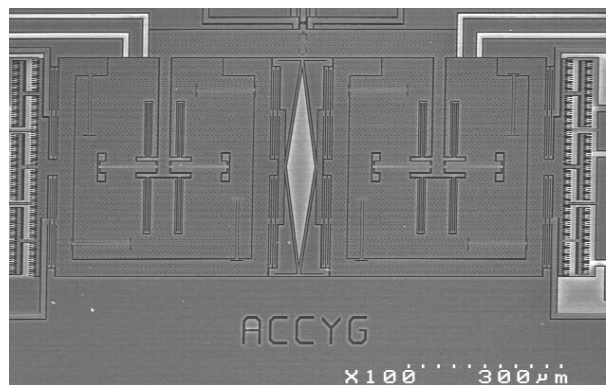


Figure 103: SEM picture of the fabricated gyroscope [Wal12]

Figure 103 shows a SEM picture of the fabricated gyroscope. The following sections describe in detail the governing equations and the transfer function of this mechanical sensor.

### 5.1.1 Drive mechanical part

The drive part of the dual-mass gyroscope can be modeled by a spring-mass system of 2 masses as shown in figure 104.

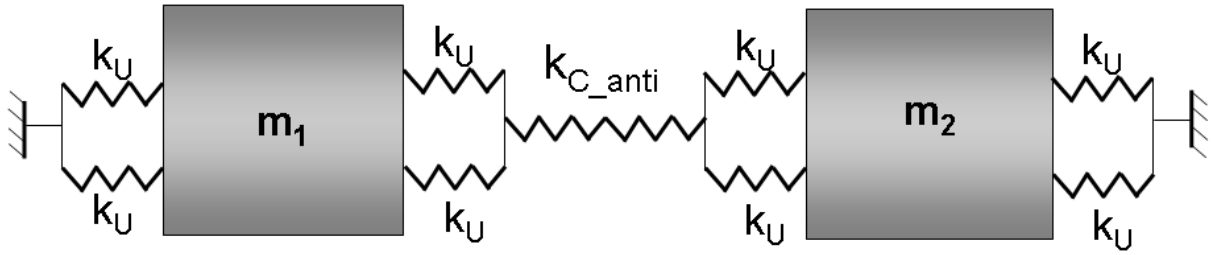


Figure 104: Mechanical model of the drive part of the dual-mass gyroscope

$m_i$  corresponds to the excitation mass.  $x_i$  corresponds to the displacement of the mass along the horizontal direction.  $F_{EXTi}$  corresponds to the external forces applied on  $m_i$ .  $\gamma_i$  is the damping factor.  $i$  can refer either to mass 1 or 2 independently. The coupling stiffness is expressed as  $k_{12}$ . In chapter 3 the coupling spring have already been studied and two different stiffness  $k_{C\_phase}$  and  $k_{C\_anti}$  have been calculated.

Using the calculation done in this section the natural in-phase and anti-phase frequencies are evaluated in equation (74) and (75).

$$\omega_{phase} = \sqrt{\frac{4.k_U}{m_i}} \quad (74)$$

$$\omega_{anti} = \sqrt{\frac{2.k_U + k_{C\_anti}}{m_i}} \quad (75)$$

### 5.1.1.a Drive mode frequencies

The drive mechanical part of the dual-mass gyroscope possesses two degrees of freedom along the x-direction and therefore two resonant frequencies in this direction (i.e one for the in-phase motion and one for the anti-phase motion).

Depending on the coupling spring, two configurations are possible. For more details about coupling springs please refer to chapter 3. Figure 105 and 106 shows the transfer function obtained for the two different configurations. In the left graph, the coupling spring forces the two inertial masses to move with an identical movement and the in-phase mode comes first. In the graph on the right, the inertial masses are forced in an opposite movement by the coupling spring and the out-of-phase mode comes first. The global force to displacement transfer function is a low pass filter of the second order.

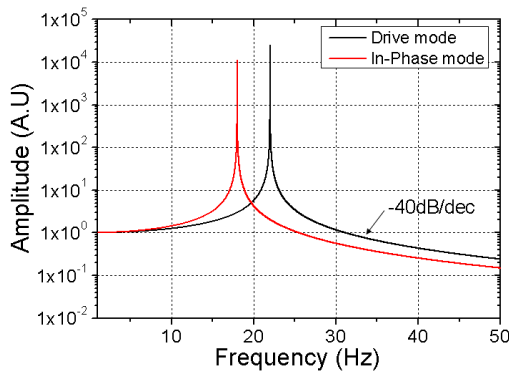


Figure 105: Deformation mode of a spring mass system with an coupling spring forcing an in-phase mode

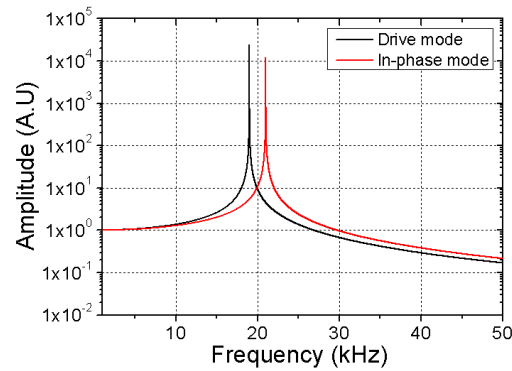


Figure 106: Deformation mode of a spring mass system with an coupling spring forcing an anti-phase mode

To obtain acceleration compensation, the excited drive mode should correspond to the anti-phase mode. In order to improve the common mode rejection of acceleration, the in-phase frequency is seen as a parasitic mode and should also be kept far from the desired anti-phase drive mode. Assuming an anti-phase movement, the drive mode transfer function is given in equation (76).

$$H(\omega) = \left\| \frac{x_1 - x_2}{F_{EXT}} \right\| = \frac{1}{k_d} \cdot \frac{1}{\sqrt{\left(1 - \frac{\omega^2}{\omega_d^2}\right)^2 + \left(\frac{\omega}{Q_d \cdot \omega_d}\right)^2}} \quad (76)$$

$Q_d$  and  $\omega_d$  corresponds respectively to the drive mode quality factor and natural pulsation.  $F_{EXT}$  corresponds to the electrostatic excitation actuation.

### 5.1.2 Sense mechanical part (with piezoresistive detection)

#### 5.1.2.a Cinematic considerations

Figure 107 shows the equivalent cinematic diagram of the dual-mass gyroscope. The drive frame is guided along the x-axis. Unidirectional Coriolis forces along Y induce a **straight displacement** of the inertial mass along Y. The decoupling spring tends to guide the inertial mass in a translation movement along Y. The detection frame is fixed by a pivot. Its only degree of freedom is a **rotation**. In order to cinematically allow movement, another pivot is needed at the intersection of the inertial mass and the detection frame.

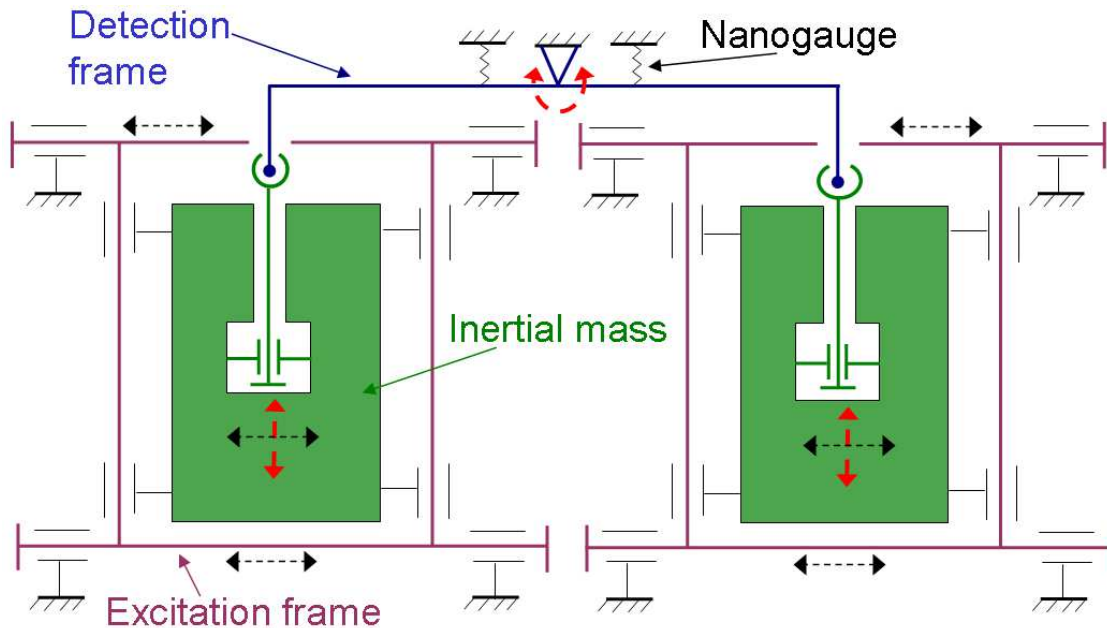


Figure 107: Cinematic scheme of the detection part of a dual-mass gyroscope

The need for a transmitting pivot at the limit between the vertical displacement of the inertial mass and the rotation of the detection frame is cinematically proven. Analytical evaluation of this additional mechanical link increases the model complexity. This fulcrum adds a very low parasitic stiffness in series with other existing stiffness (such as the decoupling spring stiffness). In the following sections the effect of this additional fulcrum on the sense mode are neglected.

### 5.1.2.b Sense transfer function

The sense part of the dual-mass gyroscope studied [Wal12] is very close to the structure of a single axis accelerometer described in chapter 4.1. Figure 108 depicts the architecture of the sense mechanical part.

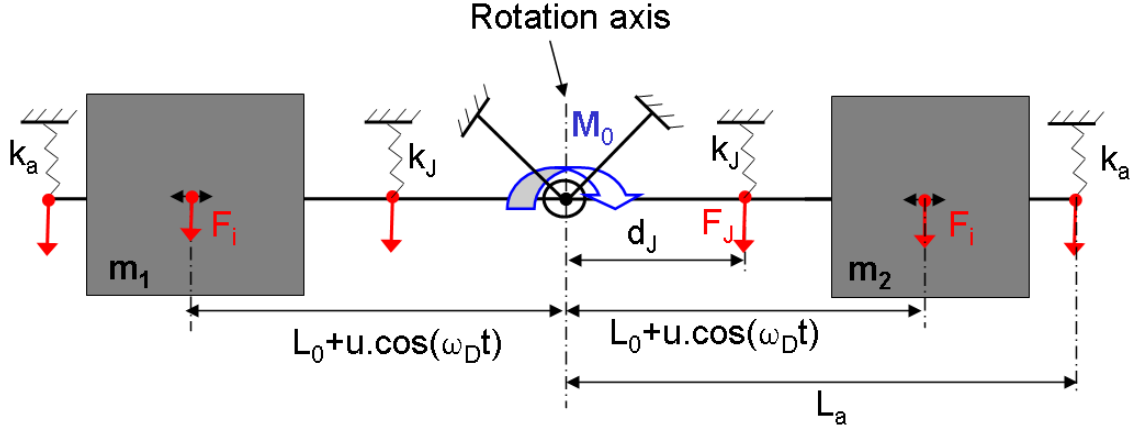


Figure 108: Model of the sense dual-mass gyroscope with piezoresistive detection

$k_J$ ,  $k_a$  and  $k_{rot}$  respectively stands for the compression gauge stiffness, the guiding spring stiffness and the fulcrum rotational stiffness. The gauge and guiding springs are respectively at a distance  $d_J$ , and  $L_a$  from the center of rotation. The Coriolis force  $F_C$  is applied at a distance  $\sim L_0$  from the center of rotation. Because the drive movement is an anti-phase movement, the Coriolis force has an opposite direction on each of the inertial mass.

Considering an external force  $F_C$  applied at a distance  $L_0$  from the center of rotation, the transfer function of the sense part can be calculated. We can reuse equation (4) of chapter 4.1.1 to express the gauge stress as a function of the Coriolis forces.

$$\frac{\Delta R/R}{F_C} = G \cdot \frac{L_0}{d_J} \cdot \frac{d_J^2}{l_J} \cdot \frac{1}{J\omega^2 + j\omega\gamma_s + k_{rot} + 2k_J \cdot d_J^2 + k_a \cdot L_a^2} \quad (77)$$

$J$  is the moment of inertia.  $\gamma_s$  is the damping factor of the sense mode and  $G$  the piezoresistive gauge factor defined in chapter 2. From equation (77) we can obtain the resonant frequency of the sense mode of a dual-mass gyroscope with piezoresistive detection. Let's define  $k_{TOT}$  as the total rotational stiffness in the sense mode and  $k_{tot}$  the total translational stiffness reported at the nanogauge position. The equivalent surface  $S_{eq}$  correspond to the surface of the nanogauge if the parasitic spring were included inside this nanogauge. Equation (79) gives the expression of  $S_{eq}$  with respect to the nanogauge cross-section  $S_J$ .

$$k_{TOT} = k_{tot} \cdot d_J^2 = k_{rot} + 2k_J \cdot d_J^2 + k_a \cdot L_a^2 \quad \text{with} \quad k_{tot} = \frac{E \cdot S_{eq}}{l_J} \quad (78)$$

$$S_{eq} = 2S_J + (k_{rot} + k_a \cdot L_a^2) \cdot \frac{l_J}{E \cdot d_J^2} \quad (79)$$

$$\omega_s = \sqrt{\frac{k_{TOT}}{J}} \quad \text{and} \quad Q_s = \frac{\sqrt{J \cdot k_{TOT}}}{\gamma_s} \quad (80)$$

Using equation (77) to (80) the transfer function of the sense part is given by equation (81). The transfer function in sense direction is stimulated at the frequency of the drive movement.

$$H(\omega) = \left\| \frac{\Delta R/R}{F_C} \right\| = \pi_l \cdot \frac{L_0}{d_J} \cdot \frac{1}{S_{eq}} \cdot \frac{1}{\sqrt{\left(1 - \frac{\omega^2}{\omega_s^2}\right)^2 + \left(\frac{\omega}{Q_s \cdot \omega_s}\right)^2}} \quad (81)$$

From equation (81), we see that the sensitivity is proportional to the longitudinal piezoresistive factor  $\pi_l$ , the lever amplification  $L_0/d_J$  and inversely proportional to the equivalent surface  $S_{eq}$ . The excitation frequency  $\omega$  given in equation (81) correspond to the frequency of the Coriolis force, which is the same frequency as the drive movement, as imposed by the electrostatic actuation.

### 5.1.3 Frequency matching, sensitivity and bandwidth

$\omega_d$  is the displacement pulsation and  $\omega_i$  is the rotation speed pulsation. The Coriolis force can be expressed as:

$$\begin{aligned} F_C &= 2 \cdot m \cdot \omega_d \cdot \|x\| \cdot \|\Omega\| \cdot \cos(\omega_d) \cdot \cos(\omega_i) \\ &= m \cdot \omega_d \cdot \|x\| \cdot \|\Omega\| \cdot [\cos(\omega_d + \omega_i) + \cos(\omega_d - \omega_i)] \end{aligned} \quad (82)$$

From equation (82), we see that the Coriolis force has two frequency components. The signal due to a rotation speed at pulsation  $\omega_i$  is therefore the sum of two components. Equation (83) gives the complete transfer function of the gyroscope.

$$\left\| \frac{\Delta R/R}{\Omega} \right\| = \pi_l \cdot \frac{1}{S_{eq}} \cdot \frac{L_0}{d_J} \cdot m \cdot \omega_d \cdot \|x\| \cdot \left( \frac{1}{\sqrt{\left(1 - \frac{(\omega_d + \omega_i)^2}{\omega_s^2}\right)^2 + \left(\frac{(\omega_d + \omega_i)}{Q_s \cdot \omega_s}\right)^2}} + \frac{1}{\sqrt{\left(1 - \frac{(\omega_d - \omega_i)^2}{\omega_s^2}\right)^2 + \left(\frac{(\omega_d - \omega_i)}{Q_s \cdot \omega_s}\right)^2}} \right) \quad (83)$$

Figure 109 shows the gyroscope sensitivity given in equation (83) (assuming a constant drive amplitude) with respect to  $f_i$  the rotation speed frequency. The drive resonant frequency has been set arbitrarily to 20 kHz. The sense resonant frequency varies with each curve (21 kHz, 20.5 kHz and 20.2 kHz). In open loop configuration, the bandwidth of the gyroscope is  $BW = \Delta\omega = \omega_s - \omega_d$ . The quality factor of the sense mode is set to  $4 \cdot 10^4$ . The bandwidth of the gyroscope will be defined by the relationship between  $\omega_s$  and  $\omega_d$ .

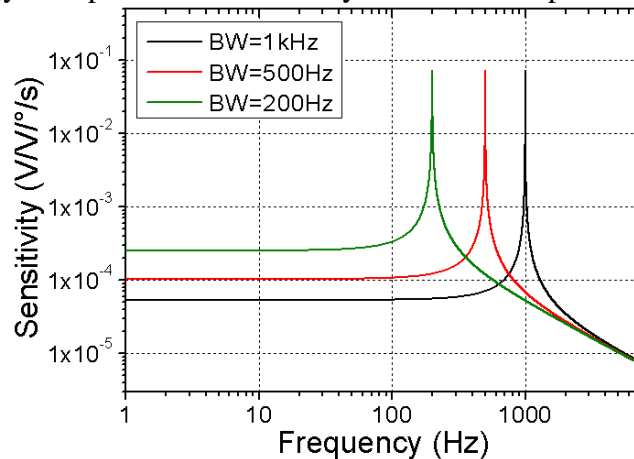


Figure 109: Sensitivity and bandwidth relationship in a gyroscope (Analytical)

Figure 109 shows that the sensitivity of the gyroscope is linked to the difference ‘ $\Delta\omega=\omega_s-\omega_d$ ’. If  $\Delta\omega$  is large, the gyroscope will show a large bandwidth and a relatively low sensitivity. If  $\Delta\omega$  is low but positive, the sensitivity of the gyroscope will be higher but its bandwidth reduced.

The sensitivity is maximized if  $\omega_d=\omega_s$ . It corresponds to the closed loop configuration. In closed loop configuration, the bandwidth is fixed by the electronics and the retroaction loop (typically in the order of  $10^2$  Hz). In practice, because of technological variation, gyroscopes are fabricated with a sense mode just a little higher than the drive mode. Trimming is applied to the sense mode. It induces a reduction of the sense resonant frequency. Through trimming, frequency matching of the sense mode and the drive mode can be achieved. More information about trimming technique is given in the following section.

### 5.1.4 Electrical Part

The electrostatic environment of a resonant sensor is complex and electrodes are numerous. In this section, we will dimension various electrodes and explain their respective place and function. Electrodes are generally designed for correcting fabrication defects or as a way to measure physical quantities for the electronics.

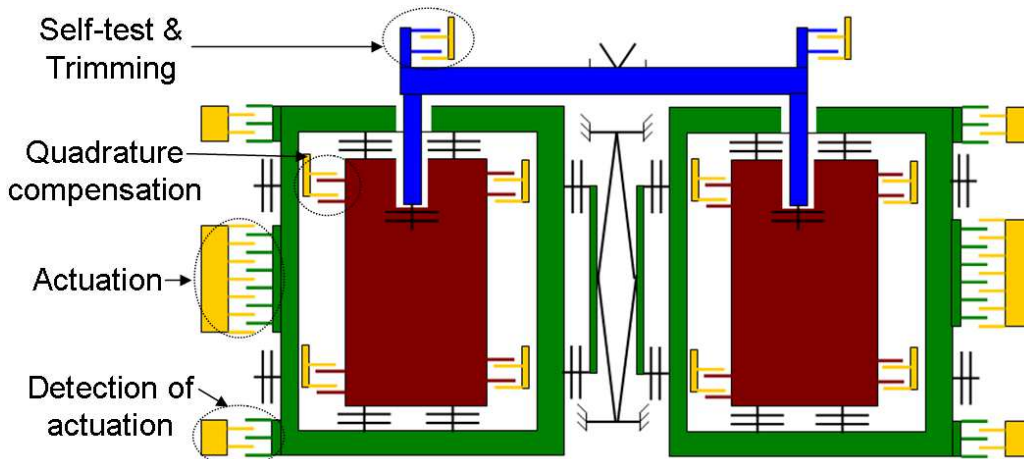


Figure 110: Design : Electrodes in a dual-mass gyroscope sensor

#### 5.1.4.a Actuation electrodes

The comb drive electrodes are designed to provide the inertial mass with a translational movement along the drive axis. They are placed on the drive frame (green) as symmetrically as possible to reduce bias. Actuation electrodes are dimensioned using the following formula:

$$x = \frac{F_x \cdot Q_x}{k_x} = \frac{Q_x}{k_x} \cdot \frac{2 \cdot N \cdot \epsilon_0 \cdot t \cdot V_{DC} \cdot V_{AC}}{g} \quad (84)$$

$N$  is the number of teeth in the comb drive.  $t$  the thickness of the comb and  $g$  the gap between each comb.  $\epsilon_0$  is the permittivity of vacuum,  $Q_x$  the quality factor of the drive mode at resonance and  $k_x$  the spring stiffness in the drive direction.  $V_{DC}$  and  $V_{AC}$  are the actuation voltages. Large amplitude of drive movement increase sensitivity. This formula is valid only if the frequency of the voltage actuation  $V_{AC}$  corresponds to the resonance frequency of the drive mode.

However the non-linear behavior of springs will limit the drive amplitude to a few microns [Kaa04]. In this section, we have considered a maximum displacement of the inertial



mass at 1.5 $\mu\text{m}$ . Additionally, we assume that the maximum voltage (no charge pump considered) in an ASIC is 3.3V. Depending on the quality factor, the comb drive number of teeth and dimensions can be provided.

#### 5.1.4.b Drive detection electrodes

In order to measure the amplitude and phase of the drive movement, detection electrodes have been placed on the excitation frame along side with the actuation electrodes. They can also be used to measure the resonance frequency. The capacitance sensitivity ( $dC/dx$ ) of these electrodes is given in equation (85).

$$\frac{\partial C}{\partial x} = \frac{2.N.\epsilon_0.t}{g} \quad (85)$$

These electrodes are used for feedback purposes. The frequency and voltage actuation are modified by the measurement on the drive detection electrodes through the feedback loop in order to obtain constant drive amplitude.

#### 5.1.4.c Quadrature bias compensation electrodes

These electrodes are placed within the inertial mass itself for movement compensation purposes. Indeed, due to fabrication non idealities, the actuation electrodes will induce both the desired horizontal displacement and a parasitic vertical displacement. The vertical displacement (i.e bias) will be seen as a signal from the sense part of the device. In order to compensate for this offset, gap-variation electrodes have been implemented. The objective is to counter-balance the parasitic vertical force induced by actuation. The induced force by gap-variation electrodes is given in equation (86).

$$F_y = \frac{N.\epsilon_0.L.t.V_{DC}.V_{AC}}{g^2} \quad (86)$$

Such electrostatic force can compensate a vertical force corresponding to a quadrature bias up to:

$$B_q = \frac{F_y}{2.\omega_s.m_{exc}} \cdot \frac{180}{2.\pi} \quad (87)$$

#### 5.1.4.d Trimming electrodes

The term ‘trimming’ refers to the use of an electrode as a spring with a negative stiffness. By decreasing the overall stiffness of the structure, the resonance frequency of the sense mode will decrease. Trimming electrodes have been placed on the detection frame (blue) as far as possible from the rotation center in order to increase their influence. In order to maximize the negative stiffness obtained, these electrodes are gap-variation electrodes. The trimming electrodes are dimensioned in order to be able to match all gyroscopes on a single wafer.  $L_T$  is the distance from the trimming electrode to the center of rotation. The negative rotational stiffness obtained with gap-variation electrode is given in equation (88).

$$k_{neg} = \frac{N.\epsilon_0.L.t.V_{DC}^2}{g^3} . L_T^2 \quad (88)$$

The change in resonance frequency is proportional to the ratio between the negative rotational stiffness  $k_{neg}$  and the total rotational stiffness  $k_{TOT}$ .



$$\Delta f \approx \frac{k_{neg}}{2.k_{TOT}} \cdot f_0 \quad (89)$$

The sense transfer function of a fabricated dual-mass gyroscope has been recorded for different trimming voltages. Figure 111 shows the resonance frequency variation of the sense mode for an increasing trimming voltage.

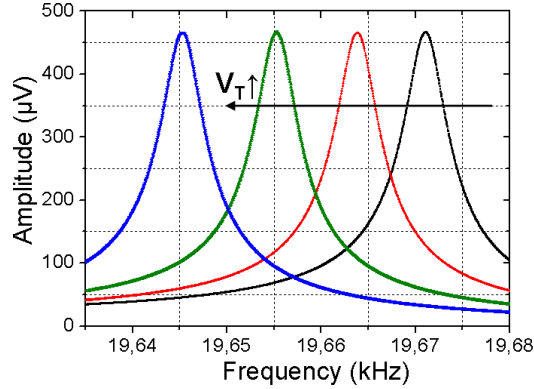


Figure 111: Experimental validation of the trimming electrode

#### 5.1.4.e Sense self-test electrodes

The same electrodes can be used as test for the sensing part of the sensor. In case of closed loop configuration, these electrodes will act as feedback actuation electrode for the sense mode since they can simulate a Coriolis force. They can also be used to evaluate the amplification factor of the detection part and more importantly the resonance frequency in the sense direction. Equation (90) gives the stress induced by the gap-variation electrodes through a quasi-static electrostatic actuation.

$$\sigma_y = \frac{N \cdot \epsilon_0 \cdot L \cdot t \cdot V_{DC} \cdot V_{AC}}{g^2} \cdot BL \cdot \frac{1}{2 \cdot S_J} \cdot H(j\omega) \quad (90)$$

$H(j\omega)$  corresponds to the transfer function in sense,  $BL$  to the lever arm amplification and  $S_J$  to the nanogauge cross-section.

#### 5.1.4.f Parasitic capacitance

The parasitic capacitances are expected to stay lower than 1 pF using thin electric lines and a gap of 1.5  $\mu\text{m}$ . Without ASIC the main parasitic capacitance will be due to external wiring. Typically a coaxial cable adds 100 pF/m.

### 5.1.4.g Summary of all electrodes behavior

A summary of the different types of electrodes described is given in table 16. The column 'Dimensions' is ordered as following: number of fingers  $N$ , length  $L$  and gap  $g$  of each finger. All electrodes have a thickness  $t$  of the MEMS level i.e  $10\ \mu\text{m}$ .

Function	Electrode type	Mass related	Ideal Influence	Dimensions N:L*g
Actuation electrode	Comb drive	drive	$1.5\ \mu\text{m}$ (Max: $15\ \mu\text{m}$ )	80:10 $\mu\text{m}$ *1 $\mu\text{m}$
Detection of actuation electrode	Comb drive	drive	$3.10^{-8}\ \text{F/m}$	160:10 $\mu\text{m}$ *1 $\mu\text{m}$
Quadrature bias compensation electrode	Gap-variation electrode	Coriolis	$1000^\circ/\text{s}$	6: 10 $\mu\text{m}$ *1 $\mu\text{m}$
Trimming electrode	Gap-variation electrode	Detection	400 Hz	8: 30 $\mu\text{m}$ *1 $\mu\text{m}$
Detection test electrode	Gap-variation electrode	Detection	100 MPa	8: 30 $\mu\text{m}$ *1 $\mu\text{m}$

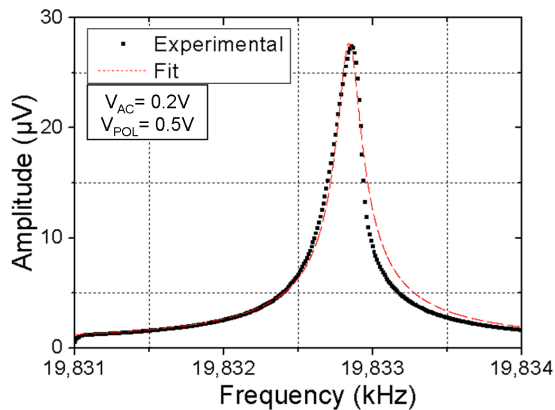
*Table 16: Summary of the electrodes present on dual-mass gyroscope*

### 5.1.5 Characterization

Mechanical characterization has been performed using the Lakeshore CPX prober. The prober allows measurement in vacuum environment ( $P^o \sim 10^{-5}\ \text{mbar}$ ). Using frequency sweep, the drive and sense mechanical functions have been validated.

#### 5.1.5.a Drive mode validation

Figure 112 shows the voltage obtained at the detection electrode of the drive mode for an actuation  $V_{AC}$  and an inertial mass polarization of  $V_{DC}$ .



*Figure 112: Drive mode of the dual-mass gyroscope (capacitive measurement)*

The drive mode is measured at a frequency of 19.83 kHz which corresponds well to the theoretical value. The quality factor of the drive mode is evaluated to  $1,2 \cdot 10^5$ . Due to the rather large deflection in the drive mode, a slight non-linear behavior is observed in this case, thanks to the deformation of the spectral response, which is typical of dynamic nonlinear behavior.

### 5.1.5.b Sense mode validation

Figure 113 shows the piezoresistive response of the sense mode of a dual-mass gyroscope.

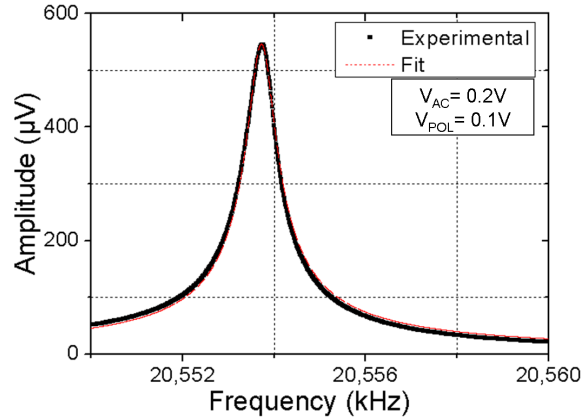


Figure 113: Sense mode of the dual-mass gyroscope (piezoresistive measurement)

The sense mode resonance frequency is measured around 20.55 kHz. The sense mode quality factor is evaluated to  $3.3 \cdot 10^4$ . It is close to the quality factor obtained for an accelerometer under vacuum. Typically using this technology and a non-compensated structure under vacuum the quality factor will saturate below  $5 \cdot 10^4$ .

### 5.1.6 Bias: theory and experimental evaluation

#### 5.1.6.a In-phase bias and quadrature bias

Bias or offset is a defect and can be compensated in some cases. Bias can be evaluated using equation (91):

$$\Omega_0 = B = \frac{F}{2 \cdot m_i \cdot \omega_d \cdot \|x\|} \quad (91)$$

$m_i$  is the inertial mass of the sensor. It is submitted to both  $x$  and  $y$  displacements. There are several sources of bias in a resonant sensor. Bias sources can be put in one of the 2 following categories:

A bias can be either an in-phase bias ( $B_i$ ) or a quadrature bias ( $B_q$ ). These biases are named after their position with respect to the output signal (i.e in a gyroscope an in-phase bias will be in-phase with the Coriolis signal). Considering a two-dimensional spring-mass system, the complete equation of motion is given in equation (92).

$$\begin{bmatrix} m_x & 0 \\ 0 & m_y \end{bmatrix} \begin{bmatrix} \ddot{x} \\ \ddot{y} \end{bmatrix} + \begin{bmatrix} c_x & c_{yx} \\ c_{xy} & c_y \end{bmatrix} \begin{bmatrix} \dot{x} \\ \dot{y} \end{bmatrix} + \begin{bmatrix} k_x & k_{yx} \\ k_{xy} & k_y \end{bmatrix} \begin{bmatrix} x \\ y \end{bmatrix} = \begin{bmatrix} F_{exc}^x \\ F_{exc}^y \end{bmatrix} + \begin{bmatrix} 0 & 2\Omega m_x \\ -2\Omega m_y & 0 \end{bmatrix} \begin{bmatrix} \dot{x} \\ \dot{y} \end{bmatrix} \quad (92)$$

$m_x$  and  $m_y$  correspond to the mass submitted to an  $x$  respectively  $y$  displacement.  $c_x$  and  $c_y$  correspond to the damping factor in the  $x$  and  $y$  directions. Identically  $k_x$  and  $k_y$  correspond to the stiffness in the  $x$  and  $y$  directions.  $c_{xy}$  and  $k_{xy}$  correspond to cross-influence terms of damping and stiffness, respectively (i.e a displacement in the  $x$  direction will induce a force  $k_{xy} \cdot x$  in the  $y$  direction).

The terms in red in equation (25) will generate bias. For each of these terms ( $c_{xy}$ ,  $k_{xy}$  and  $F_{ext}^y$ ) the corresponding bias has been derived based on the results developed in [Wal13] and [Wei06].

$c_{xy}$  is a term that corresponds to cross-induced damping. It is linked to velocities effect and generates an in-phase bias for a gyroscope.

$$B_i = \frac{c_{xy}}{2.m_i} \quad (93)$$

$k_{xy}$  corresponds to mechanical defects created during the DRIE step. The folded stiffness  $k_{xy}$  generates a quadrature bias proportional to the etching angle ( $\theta_{etching}$ ) for out-of-plane movement and to local variation of width ( $\delta w_{spring}$ ) for in-plane movement.

$$B_q = \frac{k_{xy}}{2.m_i.\omega_d} \propto \frac{\delta w_{spring}}{w} \text{ or } \propto \theta_{etching} \quad (94)$$

$F_{exc}^Y$  corresponds to defect in the comb drive geometry. These defects are likely created during the DRIE step. To evaluate its exact contribution to bias, the complete electrostatic force should be derived. Figure 114 shows a defect on one comb drive. The corresponding electrostatic force is calculated in equation 95.

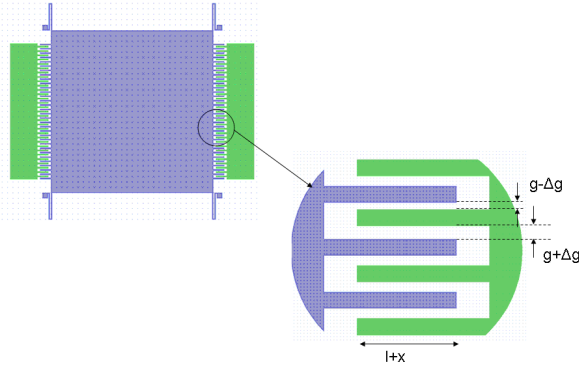


Figure 114: Defect in comb drive [Wal13]

$$F_X = \frac{\epsilon_0.t.V_{dc}.V_{ac}.Q_d}{g}$$

$$F_Y \approx \frac{2.\epsilon_0.(l+x).t.V^2}{g^3} .(\Delta g + y)$$

Equation 95: Electrostatic forces due to one comb drive

Using equation 95, the vertical electrostatic force can be divided into three different terms (The term in  $x*y$  has been neglected).

$$F_Y = \frac{2.\epsilon_0.t.V_{dc}}{g^3} .(y.l.V_{dc} + x.\Delta g.V_{dc} + 2.l.\Delta g.V_{ac}) \quad (96)$$

The first term corresponds to a negative stiffness coefficient. The second term which is proportional to the displacement along  $x$  corresponds to a quadrature bias  $B_q$  and the last term is an in-phase bias  $B_i$  due to its proportionality to  $V_{AC}$  (The AC voltage is shifted by  $90^\circ$  with respect to the displacement  $x$  at resonance). The displacement along  $x$  can be expressed as:

$$\|x\| = \frac{F_X}{m_X.\omega_d^2} = \frac{2\epsilon_0.N.t.V_{dc}.V_{ac}.Q_d}{g.m_x.\omega_d^2} \quad (97)$$

For  $N$  comb drive we can express the bias using equation (91) and (97).

$$B_q = \frac{\epsilon_0.t.V_{dc}^2 \Delta g_{rms} \sqrt{N}}{g^3.m_i.\omega_0} = \frac{V_{dc}}{V_{ac}} . \frac{\|x\|.\omega_0}{\sqrt{N}.Q_d} . \frac{\Delta g_{rms}}{g^2} \quad (98)$$

$$B_i = \frac{2.\epsilon_0.l.t.V_{dc}.V_{ac}.\Delta g_{rms} \sqrt{N}}{g^3.m_i.\omega_0.X} = \frac{l.\omega_0}{\sqrt{N}.Q_d} . \frac{\Delta g_{rms}}{g^2} \quad (99)$$

With  $\omega_0$  the resonant frequency,  $g$  the gap between the comb drive teeth,  $\Delta g$  the etching-induce error on the gap,  $t$ ,  $l$  and  $N$  the thickness, length and number of the comb drive,

$m$  the inertial mass and  $\varepsilon_0$  the permittivity of vacuum.  $Q_d$  is the quality factor in drive mode. Equations (98) and (99) show that both in-phase and quadrature bias are proportional to  $\Delta g/g^2$ . A strategy could be to increase the gap  $g$  but this is not recommended because it will also reduce the actuation electrostatic force.

Increasing the quality factor of the drive mode  $Q_d$  and the number of finger  $N$  should reduce the bias.

The objective is to obtain a very directional actuation force. In order to extract guidelines to fulfill this objective, the ratio between the electrostatic force created along  $X$  over the force along  $Y$  has been evaluated for both in-phase and quadrature bias.

$$\frac{F_{Y-Bi}}{F_X} = 4.l.K \quad \text{and} \quad \frac{F_{Y-Bq}}{F_X} = \frac{V_{dc}}{V_{ac}} \cdot 2 \cdot \|x\| \cdot K \quad (100)$$

$$\text{with } K = \frac{1}{\sqrt{N} \cdot Q_d} \cdot \frac{\Delta g_{rms}}{g^2}$$

The expression of the ‘bias factor’  $K$  is present in both of the bias terms coming from electrostatic defect. In order to minimize the bias coming from the electrostatic actuation,  $K$  should be minimized. Table 17 gives a summary of the different sources of bias that have been identified in equation (92).

Source	Analytical expression	Phase
Non diagonal stiffness	$\frac{k_{xy}}{2 \cdot m_i \cdot \omega_d}$	Quadrature
Non diagonal damping	$\frac{c_{xy}}{2 \cdot m_i}$	In-phase
Electrostatic actuation	$\frac{V_{dc}}{V_{ac}} \cdot \frac{\Delta g_{rms}}{g^2} \cdot \frac{\ x\  \cdot \omega_d}{\sqrt{N} \cdot Q_d} \cdot \frac{k_{xy}}{k_y}$	Quadrature
Electrostatic actuation	$\frac{\Delta g_{rms}}{g^2} \cdot \frac{l \cdot \omega_d}{\sqrt{N} \cdot Q_d} \cdot \frac{k_{xy}}{k_y}$	In-phase

*Table 17 : Summary of Bias sources and analytical expressions [Wal13]*

### 5.1.6.b Experimental evaluation of bias

The bias corresponds to the influence of the actuation on the detection part of the system. The vertical displacement due to bias has been measured through the piezoresistive readout. A polarization  $V_{AC}$  is applied to the actuation electrode of the gyroscope. The nanogauges are polarized by  $V_{POL}$ . Figure 115 shows the measured voltage on the nanogauge bridge for a frequency sweep on  $V_{AC}$ .

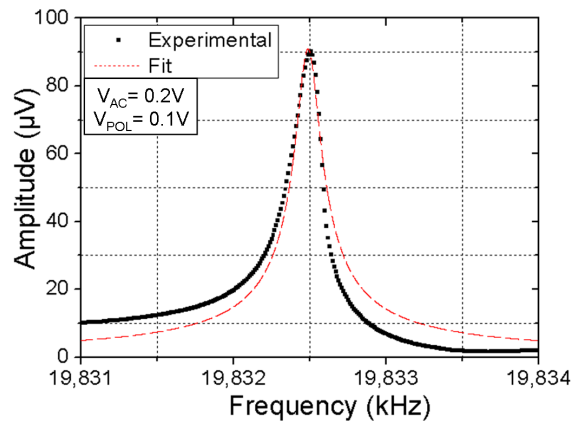


Figure 115: Bias observed on the dual-mass gyroscope (piezoresistive measurement)

The resonance frequency found in the bias measurement is identical to the drive resonance frequency. The quality factors of both bias and drive measurements are identical. Using previous measurements, the amplitude of the displacement obtained in the drive direction and in the sense direction have been extracted. The ratio between those displacements gives the directionality of the decoupling spring. For the dual-mass gyroscopes, the ratio of the displacement obtained under an identical actuation gives the value of  $5 \cdot 10^{-5}$ . It corresponds to an offset equivalent to  $600 \text{ }^\circ/\text{s}$  at the sensing stage (knowing that the full scale is  $5000 \text{ }^\circ/\text{s}$ ).

## 5.2 Design of a two-axis gyroscope

### 5.2.1 Advantage of a two-axis gyroscope architecture

The electronic control loop of the gyroscope drive mode is one of the electronics parts which **consume most of the power in a standard ASIC**. If three mechanical structures are used in order to provide the user with a complete IMU (Inertial Measurement Unit), three control loops will be required. They represent significantly large power consumption.

Structures which provide actuation in different directions using only one control loop allow a large reduction in power consumption. Figure 116 shows the SEM image of a fabricated two-axis gyroscope based on a circular approach.

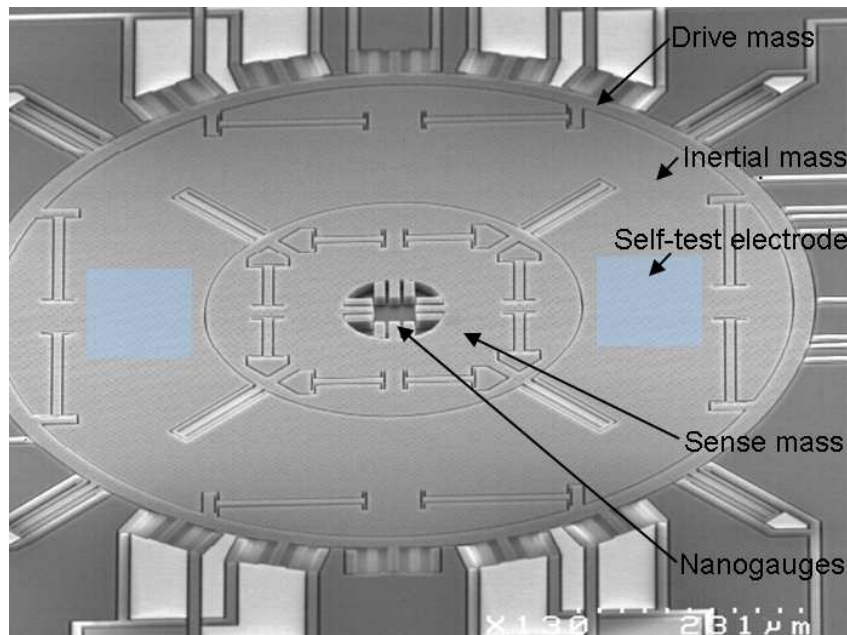


Figure 116: SEM top view of the two-axis gyroscope

The two-axis gyroscope follows similar architecture as the dual-mass gyroscope described in the previous section. The drive part corresponds to the external ring. Decoupling springs are used to transfer the actuation to the inertial mass (middle ring). The inner ring corresponds to the sensing mass. The piezoresistive gauges are placed at the middle of the sensor (see figure 119). Electrical connections below the MEMS allow for gauge polarization and readout along with actuation and self-test of the sense mode.

### 5.2.2 Drive part

The external ring is actuated in rotation along the  $z$  axis. The drive mass revolves around the center of the MEMS. The circular motion of the driving mass is mainly a motion along  $y$  on the right and left parts of the device, whereas the motion is mainly along  $x$  on the top and bottom parts of the device. These ‘mainly horizontal’ movement and ‘mainly vertical’ movement can be considered as two different driving movements. Since this design uses one inertial mass only, there is no coupling spring. The guiding springs are dimensioned to obtain a drive resonance frequency around 20 kHz. Figure 117 shows the simulated deformation of the sensor for a drive mode at 18.4 kHz.



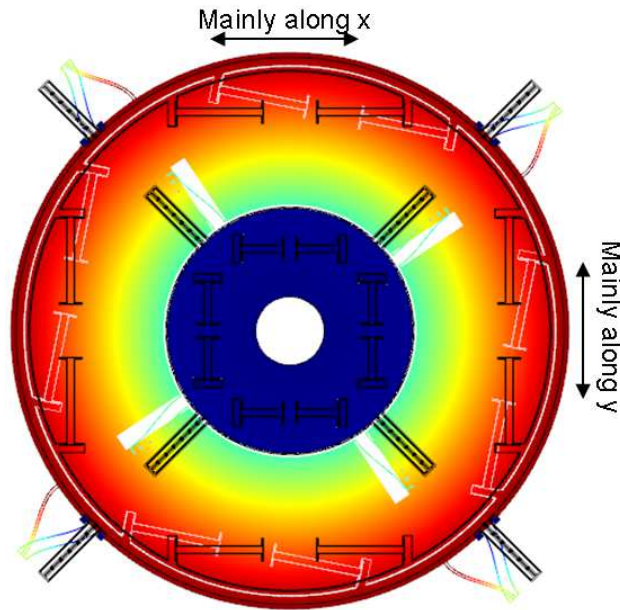


Figure 117: Drive mode of the two-axis gyroscope ( $f=18.4\text{kHz}$ )

### 5.2.3 Sense part

Due to a rotation speed  $\Omega_x$ , the inertial mass excited by a movement ‘mainly along  $Y$ ’ will be submitted to an out-of-plane Coriolis force (along  $Z$ ). Symmetrically the parts excited by a movement along  $X$  will exhibit a Coriolis force also along  $Z$  due to a rotation speed along  $\Omega_y$ . The net effects of those  $Z$  motions will be rotational motions around  $X$  axis and  $Y$ -axis, respectively.

The sensing mass possesses two degree of freedom in rotation around the  $X$  and  $Y$  axis respectively. Figure 118 shows the two sense modes of the gyroscope at 20.09 kHz and 20.03 kHz respectively. The two sensing modes correspond to the Coriolis forces created by rotation speed along  $X$  and  $Y$  respectively.

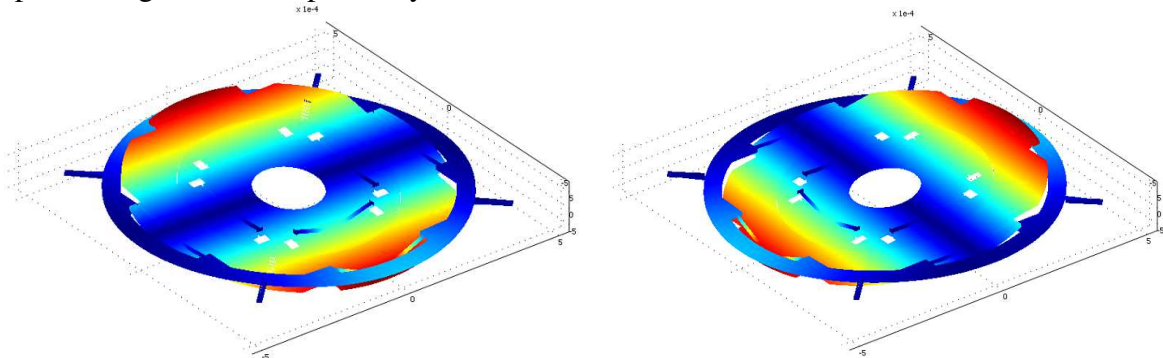


Figure 118: Sense modes of the two-axis gyroscope

These rotations around the center of the MEMS are monitored through 8 piezoresistive nanogauges. The two sensing modes are rotational movements revolving around the piezoresistive nanogauges. Because the nanogauges are not at the same height as the axis of rotation, they will be compressed / stretched by the sense modes displacements. Figure 119 shows the mechanical and electrical architecture of the detecting part.



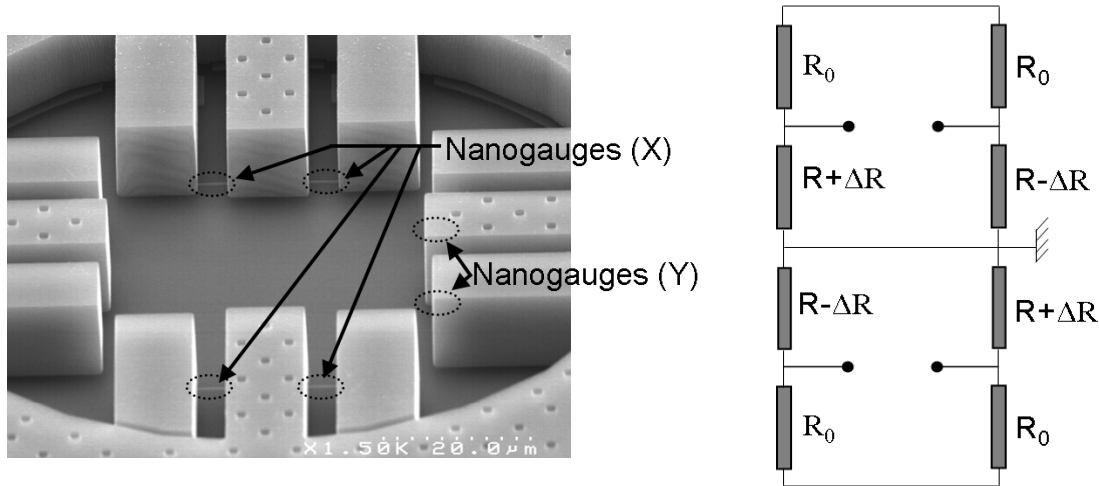


Figure 119: Detection scheme of the two-axis gyroscope

For each axis, 4 piezoresistive nanogauges are mechanically organized in two identical Wheatstone bridge. Both bridges measure an identical stress due to rotation. Concerning the crosstalk, the nanogauges detecting  $\Omega_X$  are deformed in bending when a rotation speed  $\Omega_Y$  occurs. Moreover, the piezoresistive signal due to bending is small with respect to the piezoresistive signal obtained for a compressive / tensile behavior.

The middle point of the all half-bridge is electrically linked by the detection mass doped at  $5 \cdot 10^{19} \text{ cm}^{-3}$ . To reduce sticking issue the inertial mass and the substrate are set to the electrical ground. The reading output of the sensor is then reduced to 4 independent two-point resistance measurements.

## 5.2.4 Mechanical characterization

### 5.1.4.a Drive mode validation

Using frequency sweep, the drive and sense mechanical functions has been validated. Figure 120 shows the transfer function obtained for an actuation  $V_{AC}$  and an inertial mass polarization of  $V_{DC}$ .

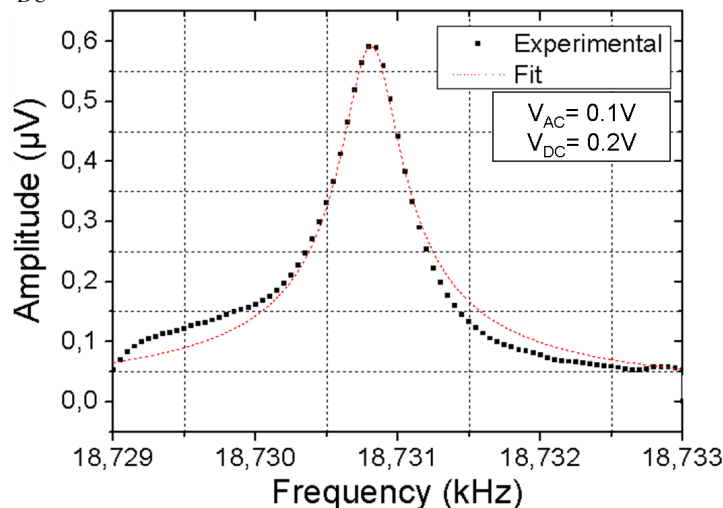


Figure 120: Drive mode of the two-axis gyroscope (capacitive measurement)

The measured drive mode resonance frequency corresponds well with the simulated value. The extracted quality factor of the drive mode is around  $4,7 \cdot 10^4$ . It corresponds to the values already obtained for non compensated structures.

### 5.1.4.a Sense mode validation

The sense mode of the gyroscope has been measured. One half-bridge measuring the X axis has been polarized by  $V_{POL}$ . One self-test electrode actuates the sensing mass through an AC voltage  $V_{AC}$ . Figure 121 shows the piezoresistive signal obtained for different actuation frequencies.

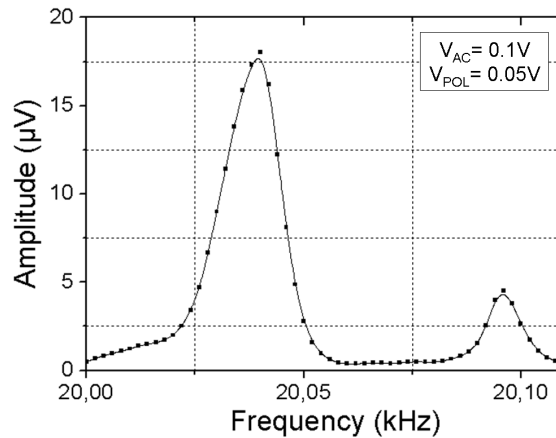


Figure 121: Sense mode of the two-axis gyroscope (piezoresistive measurement)

The piezoresistive measurement shows a double peak. The frequency difference between the two peaks is about 70 Hz. From the previous simulations we have seen that the two sensing modes possess the same difference in terms of frequency (20.09 and 20.03 kHz). A possible explanation is that the sensing modes are not perfectly aligned with the nanogauge directions. Due to over etching of springs for instance, the sensing mode can rotate. If it is the case, the piezoresistive signal will be sensitive to both sense modes which can explain the presence of two peaks on the piezoresistive signal.

### 5.1.4.a Bias measurement

The actuation of the drive mode can be measured on the piezoresistive readout. Using previous measurements of the drive and sense responses, bias measurement has been performed. The ratio between the in-plane displacement (the actuation) and the out-of-plane displacement (corresponding to the bias) has been measured around 5%. Such large bias may come from a direct transmission of the drive movement. If the anchored springs are not stiff enough in the drive direction, the sensing mass will rotate along the Z-axis. The nanogauge will be compressed by this rotation and exhibit a large piezoresistive signal.

### 5.2.5 Improvement

A parasitic out-of-plane piston-like translation mode exists and possesses a resonance frequency close to the sense modes. Figure 122 shows the simulated deformation due to this parasitic mode.

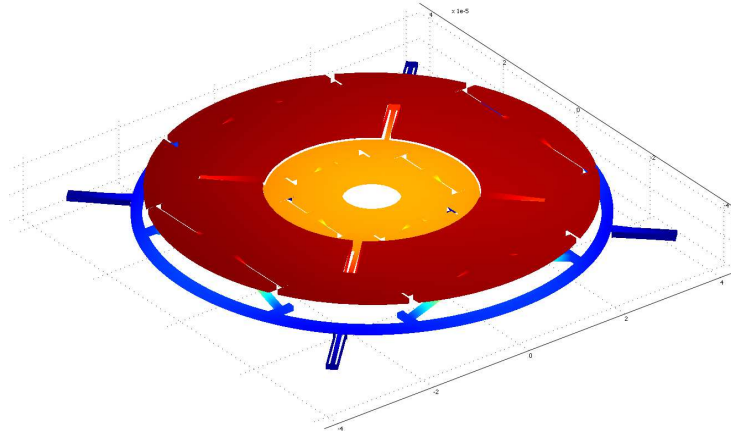


Figure 122: Parasitic sense mode of the two-axis gyroscope ( $f=24.5\text{kHz}$ )

The parasitic mode is an out-of-plane translation of the inertial mass and the detection mass. In order to increase the resonance frequency of the parasitic mode, a geometrical modification of the sensor is needed. A coupling spring has been added on the sensing mass. Figure 123 shows the architecture of the proposed coupling spring.

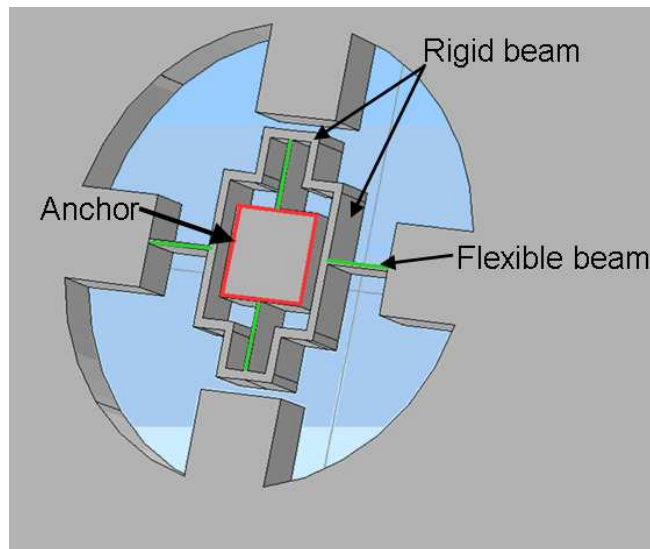


Figure 123: Proposed coupling spring for the two-axis gyroscope

To postpone the resonance frequency of the parasitic mode, an additional spring should be added. The resonance frequency of the two sense modes (rotation along  $X$  and  $Y$  axis) should not be modified. The center of the MEMS is the only place where the out-of-plane translation mode induces movement whereas the sensing mode does not. The coupling spring is designed to exhibit a small stiffness to rotation along  $X$  and  $Y$  axes (sense mode). On the other hand it exhibits a large stiffness to translation in the  $Z$  direction (parasitic mode). Additionally the anchored spring should be strengthened in order to reduce the bias.

## 5.3 Dynamic accelerometer

### 5.3.1 From static to dynamic accelerometers

We have seen in chapter 4, that a major issue of accelerometer and gyroscope co-integration concerns the pressure level (vacuum) of a possibly unique cavity. Gyroscope needs vacuum in order to obtain large excitation amplitude. Quasi-static accelerometers need atmospheric pressure to avoid very long relaxation time.

A possible solution to co-integrate a gyroscope and an accelerometer can be to design two resonant sensors (i.e that should function in vacuum). There are multiple differences between quasi-static sensors and resonant ones. Accelerometers deliver a low frequency signal whereas resonant sensors deliver a modulated signal. The dominant noise is different i.e 1/f for accelerometers and Johnson/Brownian noise for gyroscopes. The control loop of the drive mode of the gyroscope does not exist in accelerometers.

In the next section we will describe a resonant accelerometer whose architecture is very close from the one of a gyroscope. The use of such sensors to build an IMU allows a single pressure requirement for the packaging, vacuum but one additional electronics control loop.

### 5.3.2 Principle of operation

The accelerometers described in chapter 4 are based on the amplification of the inertial force by a lever arm and a fulcrum. The momentum induces large stress levels inside the piezoresistive nanogauge.

The stresses inside the nanogauge are proportional to the momentum. The momentum  $M$  is proportional to the inertial force  $F_i$  and the distance of the center of mass to the center of rotation  $L$  as expressed in equation (101).

$$M = F_i \cdot L = m_i \cdot L \cdot \vec{a} \quad (101)$$

$m_i$  is the inertial mass and 'a' the acceleration in the sensing direction.

The main idea of the dynamic accelerometer is to modulate the distance  $L$  by an actuation. As shown in equation (102), the distance  $L$  will oscillate around a mean value  $L_0$  with a pulsation  $\omega_d$ .

$$L = L_0 + u \cdot \cos(\omega_d \cdot t) \quad (102)$$

Here  $u$  is the amplitude of the oscillation. The created momentum will have two components, one DC component of quasi-static inertial force and one component at  $\omega_d$ . Quasi-static accelerometers are limited by the 1/f noise of the nanogauge resistance. If the stress is modulated at high frequency the 1/f noise can be greatly reduced. Using this concept, low noise accelerometer has been fabricated. Figure 124 shows a top view of the fabricated dynamic accelerometer.

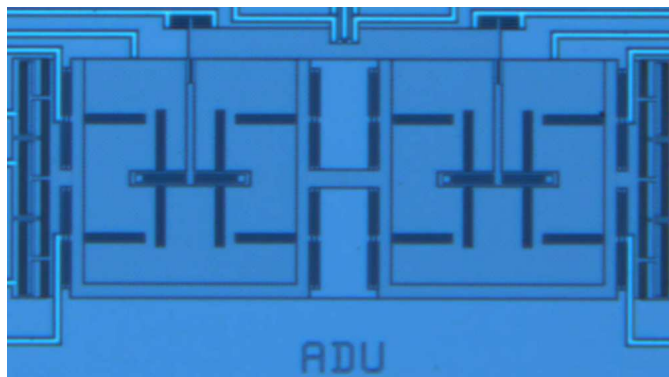


Figure 124: Top view of a dynamic accelerometer

#### 5.3.2.a Drive mode

The drive mode of the dynamic accelerometer is almost identical to the drive mode of the dual-mass gyroscope. The only difference is the coupling spring. Here the coupling spring

forces an **in-phase movement** (as configuration of 105). The mechanical system is reduced to a simple spring mass-system with one mass.

In order to be compatible with the electronics developed for the dual-mass gyroscope, the drive frequency is kept around 20 kHz. Figure 125 shows the deformation expected from the drive mode.

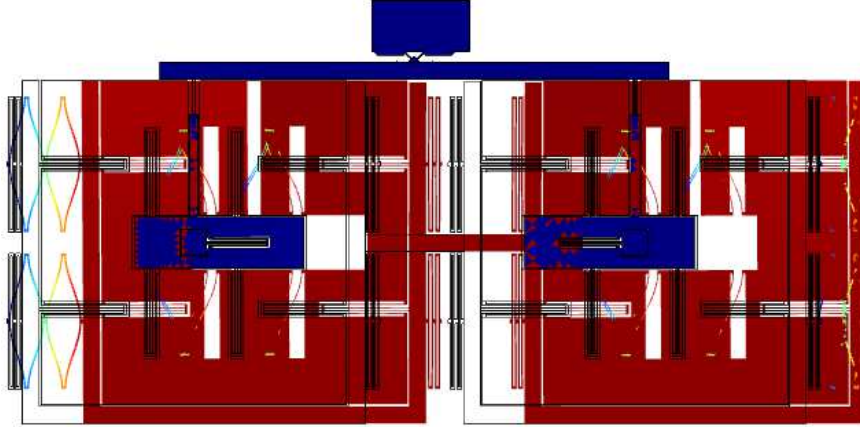


Figure 125: Simulated view of the drive mode of the dynamic accelerometer

### 5.3.2.b Sense mode

The sensing mode of the device is also close to the one of a dual-mass gyroscope. A schematic view of a fabricated dynamic accelerometer is given in figure 126.

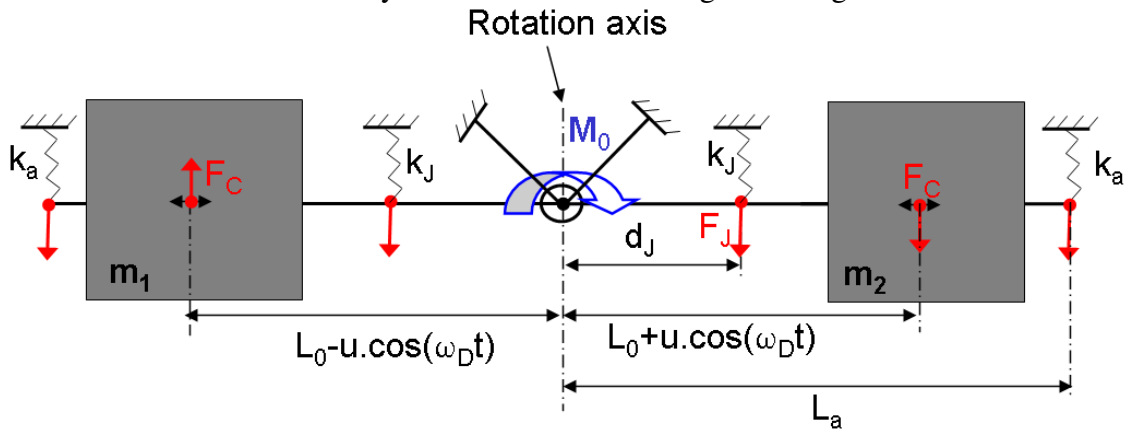


Figure 126: Schematic view of a dynamic accelerometer

The drive mode is used to modulate the lever arm distance in order for the gauge to see a modulated inertial force. Quasi-static acceleration is compensated through dual-mass geometry. The gauge sees a modulated stress at the drive frequency. Using the definitions already used in section 5.1.2, equation (103) gives the transfer function of the sense mode.

$$\left\| \frac{\Delta R/R}{a} \right\| = \pi_l \cdot m_i \cdot \frac{u}{d_J} \cdot \frac{1}{S_{eq}} \cdot \frac{1}{\sqrt{\left(1 - \frac{\omega_d^2}{\omega_s^2}\right)^2 + \left(\frac{\omega_d}{Q_s \cdot \omega_s}\right)^2}} \quad (103)$$

$S_{eq}$  correspond to the equivalent surface of the total stiffness considered as a single nanogauge of length  $l_j$ . The mechanical system behaves as a resonating low pass filter. The same issues of frequency matching techniques already developed in the dual-mass gyroscopes will impact the bandwidth and sensitivity of the dynamic accelerometer. A strong difference

with the gyroscope transfer function is the lever effect which is reduced to  $u/d_J$ . Expression of the sense mode pulsation and quality factor is given in equation (104).

$$\omega_s = \sqrt{\frac{k_{rot} + k_J \cdot d_J^2 + k_a \cdot L_a^2}{J}} \quad \text{and} \quad Q_s = \sqrt{\frac{J \cdot (k_{rot} + k_J \cdot d_J^2 + k_a \cdot L_a^2)}{\gamma}} \quad (104)$$

### 5.3.3 Characterization and Limitation

#### 5.3.3.a Drive and Sense modes

After fabrication the device was characterized in order to validate the mechanical function of the sensor. The drive mode was measured at 19.4 kHz and the sense mode at 19.5 kHz for a dimensioning aiming 20 kHz. The quality factors of the respective modes are  $2 \cdot 10^4$  and  $4 \cdot 10^4$ .

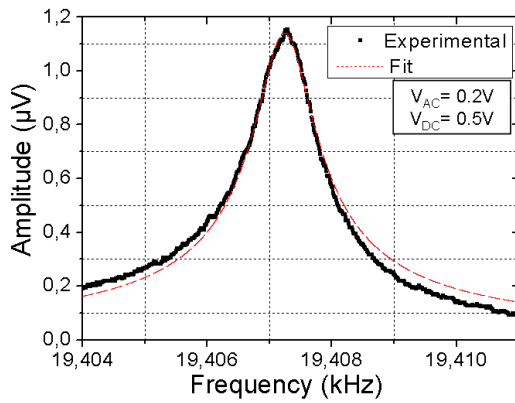


Figure 127: Drive mode of the dynamic accelerometer

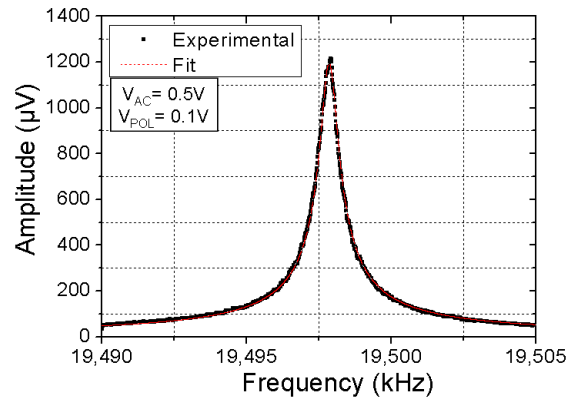


Figure 128: Sense mode of the dynamic accelerometer

The quality factor of the dynamic accelerometer drive mode is almost one order of magnitude smaller than the quality factor of the dual-mass gyroscope drive mode. Such reduction can be explained by the change from anti-phase mode to in-phase mode. Because of the **non balanced** in-phase movement, the inertia mass exchange a larger amount of energy with the substrate, this energy exchange leads to energy losses and hence a lower quality factor.

#### 5.3.3.b Bias measurement

Using the same protocol described in 5.1.5.c the bias also called the Zero Output Rate has been measured. The evaluation of the offset of the dynamic accelerometer (expressed as a ratio) gives  $6 \cdot 10^{-5}$ . Table 18 gives a summary of the different bias measured for the resonant sensor characterized in the chapter.

Type of sensor	Ratio of displacement $u_Y / u_X$	Zero Output Rate
Z gyroscopes	$5 \cdot 10^{-5}$	600 °/s
Two-axis gyroscopes	5%	$10^5$ °/s
Dynamic accelerometers	$6 \cdot 10^{-5}$	100g

Table 18 : Summary of the bias obtained for the different resonant sensors



The bias of the dynamic accelerometer is very high when compared to the acceleration that will be measured. This offset is due to the large distance between the sense center of rotation and the drive axis of translation.

The drive mode is an in-phase mode. From the sense point of view, the drive displacement of the inertial mass acts as a pendulum. This pendulum displacement is detected by the sensing part of the sensor and causes the large measured bias.

### 5.3.4 2<sup>nd</sup> generation Design

The main limitation of the dynamic accelerometer is the in-phase bias, measured because of the pendulum geometry. In order to reduce this bias source, the center of rotation of the sense part is placed on the displacement axis of the drive part. Additionally new technological change offers new opportunities for the design. The introduction of TSV (Through Silicon Vias) allows the presence of contact pad in the middle of the mechanical system. The increase of the MEMS thickness to 20  $\mu\text{m}$ , has also a direct impact on the sensitivity. However due to a limited aspect ratio (evaluated at 1:20), the dimension of some springs had to be modified. Figure 129, respectively 130 show the simulated deformation of the drive mode, respectively sense mode of the dynamic accelerometer of 2<sup>nd</sup> generation.

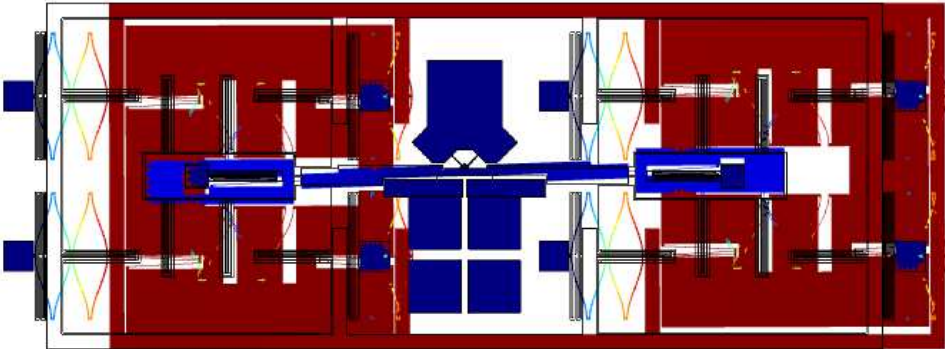


Figure 129: Drive mode of the coupled accelerometer-gyroscope (20.2kHz)

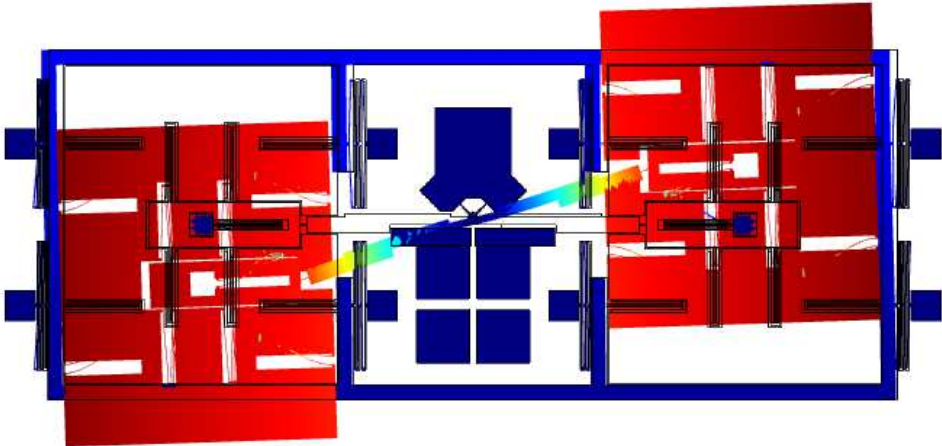


Figure 130: Sense mode of the coupled accelerometer-gyroscope (20.5kHz)

The closest parasitic mode is shown in figure 131. Given its large simulated resonance frequency it should not interact with the sense mode.

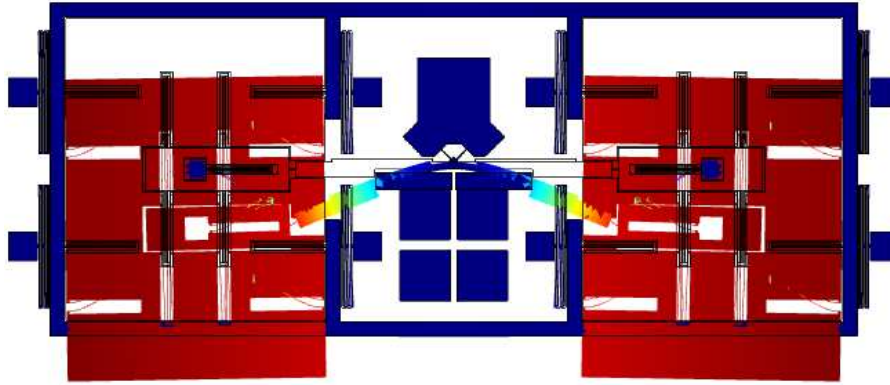


Figure 131: 1<sup>st</sup> Parasitic mode of the coupled accelerometer-gyroscope (28.2kHz)

### 5.3.5 Dynamic range comparison

Aside from the advantage on the co-integration with gyroscope, the main advantage of the dynamic accelerometer lies in its high dynamic range. In order to evaluate the sensor dynamic range, a noise evaluation is proposed. The Flicker noise, Johnson noise, Brownian noise and electronic noise are evaluated. A comparison with respect to the quasi-static accelerometer is done. Table 19 shows the various noise components assuming a bandwidth of 100 Hz and a polarization voltage of 0.1 V. The electronics noise is set to  $10^{-16} \text{ V}^2/\text{Hz}$ .

Type of accelerometer	Johnson Noise	Flicker Noise	Brownian Noise	Electronic Noise	Total Noise
Quasi-static accelerometer	78.1 nV	343.4 nV	$6 \cdot 10^{-4}$ nV	100 nV	366 nV
Dynamic accelerometer	50 nV	7 nV	27 nV	100 nV	115 nV

Table 19: Noise comparison between the fabricated quasi-static and dynamic accelerometers

Considering that a stress of 100 MPa corresponds to a detection signal evaluated to 3% of the polarization voltage (i.e 3 mV). The dynamic range ( $a_{\max}/a_{\min}$ ) of the quasi-static sensor is  $8 \cdot 10^3$  whereas the dynamic accelerometer shows a dynamic range of  $26 \cdot 10^3$ . The dynamic range of the dynamic accelerometer depends largely on the frequency mismatch  $\Delta\omega$ . In order to optimize the noise performances of the sensor, the electronics noise should be reduced further.

## 5.4 Design of a coupled accelerometer-gyroscope

The dynamic accelerometer has been proposed in order to find a solution for co-integration of accelerometer and gyroscopes. The dynamic accelerometer shows a lot of common points with the dual-mass gyroscope. In order to push further the co-integration of these two types of inertial sensors, a mechanical structure integrating both functions is proposed in this section. Such structure would require only one electronics control loop and would lead to a smaller footprint than a dynamic accelerometer added to a dual-mass gyroscope.

### 5.4.1 Mechanical organization of the in-plane structure

The aim of a coupled in-plane accelerometer-gyroscope structure is to provide a single sensor able to measure both acceleration and rotation speed. The sensor is based on the concepts of dynamic accelerometer and dual-mass gyroscope. The sensing parts of the system



are placed at the left and right sides of the structure. The driving part of the system functions in **anti-phase mode**. Figure 132 shows the architecture of the mechanical structure.

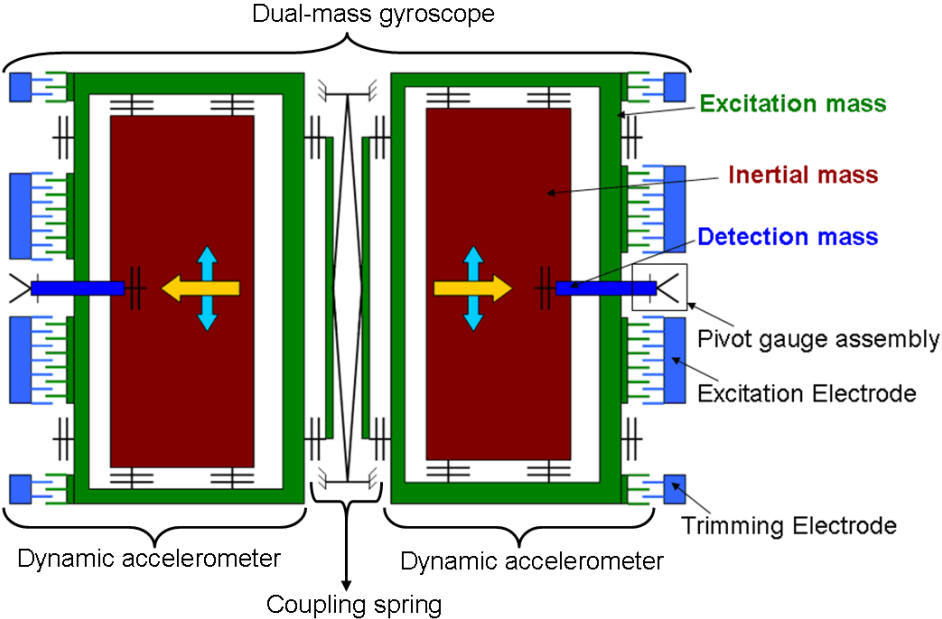


Figure 132: Architecture of the in-plane coupled accelerometer-gyroscope

The structure is symmetric and possesses two sensing parts. The actuation is provided through electrostatic comb drive (light blue). The actuation induces a periodic movement of the excitation mass (green) in the horizontal direction. The driving movement is transmitted to the inertial mass (red) through decoupling springs. The detection part (dark blue) amplifies the inertial force along Y and the piezoresistive nanogauges allow the extraction of an electrical signal.

5.4.2 Drive mechanical part

The drive part of the coupled accelerometer-gyroscope is identical to the drive part of the dual-mass gyroscope described in section 5.1.1.

5.4.3 Sense mechanical part

In this section, we will focus on the detection part of the coupled accelerometer-gyroscope. The sensing part of the system is symmetric on both sides of the system. We can focus on one part of the system. The behavior of the symmetric part can be deduced from this section. The architecture of the sensing part is identical to the sensing part of a dynamic accelerometer with only one inertial mass. Figure 133 shows a schematic of the sense part of the coupled accelerometer-gyroscope.

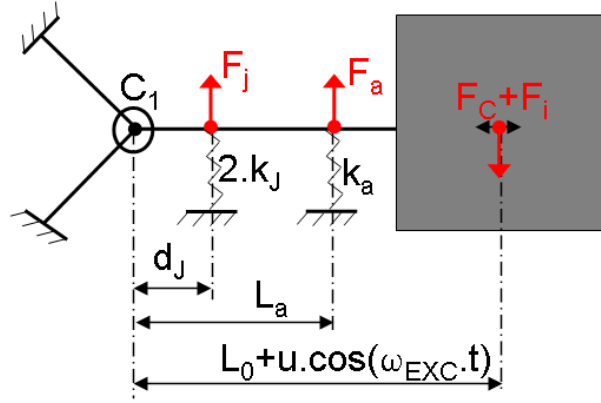


Figure 133: Architecture of the sense part of an coupled accelerometer-gyroscope

Here  $k_J$ ,  $l_J$  and  $d_J$  corresponds respectively to the gauge stiffness, length and distance to the centre of rotation.  $k_a$  and  $L_a$  corresponds respectively to the parasitic spring stiffness and distance to the centrer of rotation.  $L_0$  and  $u$  corresponds to the static and dynamic distance from the center of mass to the center of rotation. As in the dynamic accelerometer section, the torque of a force applied on the center of mass can be expressed as:

$$M_i = L.F_i = (L_0 + u.\cos(\omega_D.t)).F_{EXT} \quad (105)$$

The equation of motion assuming an external force  $F_{EXT}$  is given in equation (106).

$$J \ddot{\theta} + \gamma \dot{\theta} + \theta(k_{rot} + 2.k_J.d_J^2 + k_a.L_a^2) = F_{EXT}.(L_0 + u.\cos(\omega_D.t)) \quad (106)$$

$k_{rot}$  is the rotational spring stiffness of the fulcrum. The expressions of the total rotational stiffness in sense  $k_{TOT}$ , the sense quality factor  $Q_S$  and the sense pulsation  $\omega_S$  are given in equation (107).

$$k_{TOT} = k_{rot} + 2.k_J.d_J^2 + k_a.L_a^2 \quad \text{with} \quad k_{TOT} = \frac{E.S_{TOT}}{l_J}.d_J^2 \quad (107)$$

$$\omega_S = \sqrt{\frac{k_{rot} + k_J.d_J^2 + k_a.L_a^2}{J}} \quad \text{and} \quad Q_S = \frac{\sqrt{J.\omega_S}}{\gamma}$$

$S_{TOT}$  corresponds to the equivalent nanogauge cross-section if all stiffness contributions where included in this theoretical nanogauge. The transfer function of the sense mode for a piezoresistive readout is:

$$\left\| \frac{\Delta R/R}{M_i} \right\| = \pi_l \cdot \frac{1}{S_{TOT}} \cdot \frac{1}{d_J} \cdot \frac{1}{\sqrt{\left(1 - \frac{\omega_D^2}{\omega_S^2}\right)^2 + \left(\frac{\omega_D}{\omega_S.Q_S}\right)^2}} \quad (108)$$

External forces applied to the sense part are inertial forces (from acceleration along Y) and Coriolis force (from rotation speed along Z). They are expressed in equation (109).

$$F_Y = m_i.a_Y \quad \text{and} \quad F_C = 2.m_i.u.\omega_D.\Omega_Z.\cos(\omega_D.t) \quad (109)$$

$\Omega_Z$  is the rotation speed along Z,  $a_Y$  the acceleration along Y,  $m_i$  the inertial mass,  $\omega_D$  the drive resonant frequency and  $u$  the amplitude of the displacement in the drive direction. We consider the amplitude of displacement in drive as constant. The different frequency components of the torque applied are given in equation (110).

$$\begin{aligned}
M &= (F_C + F_Y).(L_0 + u.\cos(\omega_D.t)) = \\
&= m_i.a_Y.L_0 \\
&+ m_i.u.a_Y.\cos(\omega_D.t) \\
&+ 2.m_i.u.\omega_D.\Omega_Z.L_0.\cos(\omega_D.t) \\
&+ m_i.u^2.\omega_D.\Omega_Z.\cos(2.\omega_D.t) \\
&+ m_i.u^2.\omega_D.\Omega_Z
\end{aligned} \tag{110}$$

Equation (110) possess several terms:

- A quasi-static force with two components.
- A force at pulsation  $\omega_D$  with two components, one proportional to acceleration and one proportional to rotation speed.
- A force at pulsation  $2.\omega_D$  proportional to rotation speed only.

The terms in  $u^2$  are likely to be negligible with respect to the other terms. An analytical model has been built in order to evaluate the different stresses present in the gauges. Table 20 gives some of the numerical values used in the analytical model.

Frequency component	Dimension	Constant
$f_d = 20$ kHz	$u = 1.5$ $\mu\text{m}$	$\pi_l = 23.10^{-11}$ Pa <sup>-1</sup>
$f_s = 20.5$ kHz	$d_J = 15$ $\mu\text{m}$	$l_J = 2$ $\mu\text{m}$
$Q_S = 4.10^4$	$L_0 = 50$ $\mu\text{m}$	$S_{EQ} \sim 700*700\text{nm}^2$
$Q_D = 1.10^5$	$m_i = 4.7$ ng	

*Table 20: Geometrical dimension and sensor characteristics used in the analytical model*

Table 21 gives the order of magnitude of the signal levels generated at each frequency. It gives an overview of the main sources of stress and which terms can be neglected.

Detection Frequency component	Acceleration signal	Coriolis signal
@ DC	$\sim 70$ $\mu\text{V/V/g}$	$\sim 8.10^{-5}$ $\mu\text{V/V/}^\circ/\text{s}$
@ $\omega_D$	$\sim 45$ $\mu\text{V/V/g}$	$\sim 1$ $\mu\text{V/V/}^\circ/\text{s}$
@ $2.\omega_D$	-	$\sim 3.10^{-5}$ $\mu\text{V/V/}^\circ/\text{s}$

*Table 21: Order of magnitude of the constraints generated at each frequency*

There are 3 components large enough to be measured. The main component is the **quasi-static acceleration**. The **dynamic accelerometer signal** is also present at  $\omega_D$ . The **Coriolis signal** of the gyroscope function is also present at a frequency  $\omega_D$ .

### 5.4.3.a Accelerometer and gyroscope signal

We have seen in the previous section that the half-bridge are submitted to both the acceleration signal and the Coriolis signal. In order to extract the acceleration and rotation speed signal, a small post processing is needed. Table 22 shows the variation of the two half-bridge when the sensor is submitted to: 1°) acceleration  $a_Y$  and 2°) rotation speed  $\Omega_Z$ .

Detection Signal	Half-bridge 1	Half-bridge 2
Acceleration $a_Y$	↑	↑
Rotation speed $\Omega_Z$	↓	↑

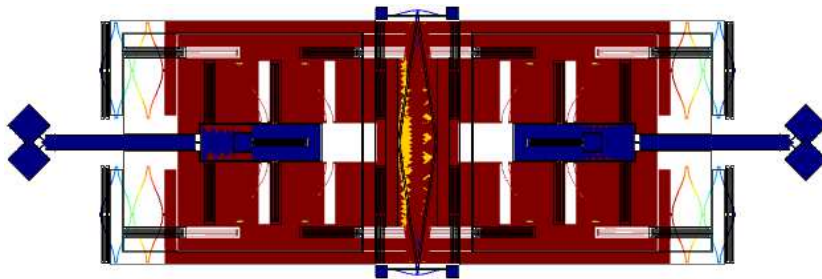
*Table 22: Behavior of each half-bridge depending on the input signal*

From table 22, the acceleration signal can be extracted by adding the output signals of both half-bridges. On the other hand the **rotation speed** signal can be obtained by **subtracting** the output signals of both half-bridges.

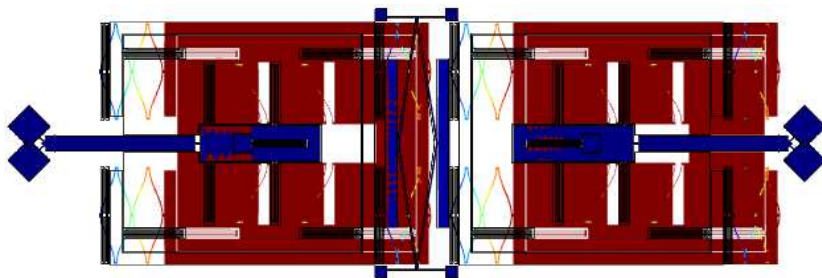
Additionally the dynamic acceleration signal (proportional to  $u$ ) is shifted by  $90^\circ$  from the Coriolis signal (proportional to  $j.u.\omega_D$ ). Specific phase filtering can be done in order to separate both signals.

### 5.4.3.b Simulated frequency matching

Figure 134 and 135 shows the drive and 1<sup>st</sup> parasitic mode of the in-plane coupled accelerometer-gyroscope.

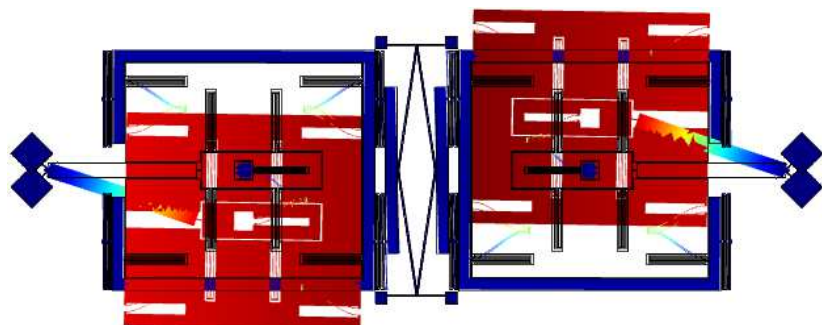


*Figure 134: Drive mode obtained by FEM for a coupled accelerometer-gyroscope structure (19.2 kHz)*



*Figure 135: In-phase parasitic mode obtained by FEM for a coupled accelerometer-gyroscope structure (22.8 kHz)*

The simulated frequency difference between the drive mode and its 1<sup>st</sup> parasitic is around 3.5 kHz according to FEM simulation results. It corresponds well with the value extracted from the analytical model. The sense geometry doesn't have an impact on the drive modes. Figure 136 and 137 shows the two sense modes of the in-plane coupled accelerometer-gyroscope.



*Figure 136: Sense mode (Coriolis force) obtained by FEM for a coupled accelerometer-gyroscope structure (19.4 kHz)*

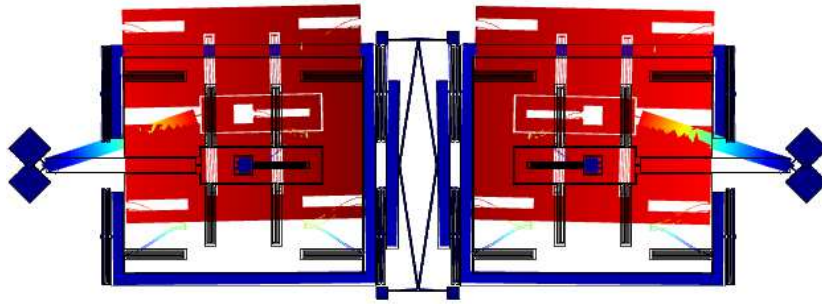


Figure 137: Sense mode (Dynamic acceleration) obtained by FEM for a coupled accelerometer-gyroscope structure (19.35 kHz)

Thanks to the good directionality of the decoupling spring, the two sense parts are almost uncorrelated. It allows a good frequency matching ( $\sim 100$  Hz) of the Coriolis sense mode, the dynamic accelerometer sense mode and the drive mode.

### 5.4.3.c Link between accelerometer and gyroscope Full scale

The maximum gauge stress has been defined as 100 MPa. The total gauge stress is the sum of the terms described in Table 21. The quasi-static and  $2.\omega_D$  Coriolis terms can be neglected. The quasi-static acceleration signal is responsible for most of the stress. Since the dynamic acceleration signal is shifted by  $90^\circ$  from the Coriolis signal, adding both signals creates a stress with amplitude of  $\sqrt{2}$ . Figure 138 shows the full scale of gyroscope depending on the acceleration measured.

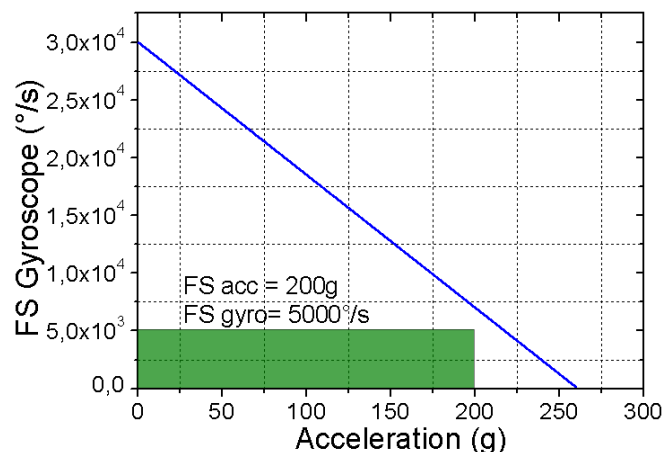


Figure 138: Full scale of accelerometer with respect to gyroscope

The blue line in Figure 36 corresponds to the 100 MPa limitation. The green square corresponds to a full scale of 200 g for the accelerometer and 5000 °/s for the gyroscope.

### 5.4.3.c Bias

Since the dynamic acceleration signal is shifted by  $90^\circ$  from the Coriolis signal, both in-phase bias and quadrature bias will act as an offset on the acceleration signal and the gyroscope signal, respectively.

### 5.4.4 Quasi-static acceleration compensation

The quasi-static acceleration is the largest stress contribution present in the gauge. However it is not the component of main interest. It only reduces the full scale of the sensor. The sensing part of a structure with compensated quasi-static acceleration is proposed in figure 139. This structure provides a larger dynamic range. Using a compensating mass part

of the detection frame, the effect of quasi-static acceleration can be compensated mechanically.

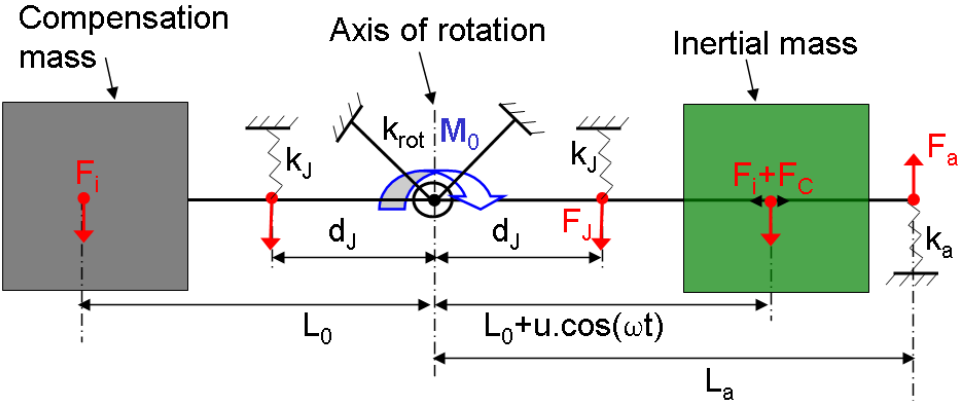


Figure 139: Scheme of the gauge/fulcrum assembly with compensated mass

In practice the compensation mass is smaller than the inertial mass because the guiding spring generates losses. Figure 140 gives a possible implementation for the acceleration compensation.

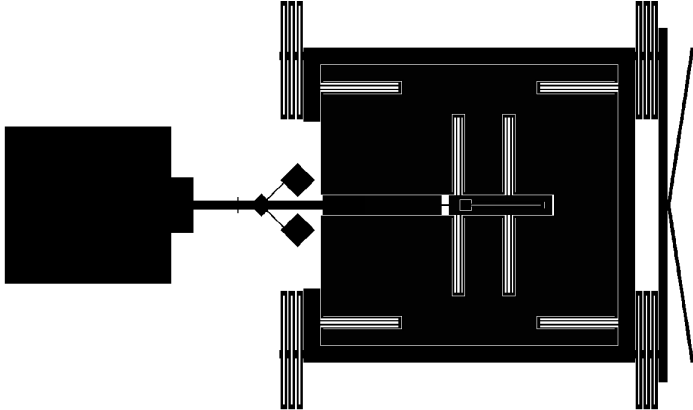


Figure 140: Possible implementation of the coupled accelerometer gyroscope with an additional compensation mass

Figure 141 gives the amount of quasi-static stress obtained in the nanogauge for an increasing compensation mass. Quasi-static acceleration is simulated by an acceleration of  $1\text{ g}$  applied to the whole mechanical structure. The dynamic modulated acceleration is created by applying the  $1\text{ g}$  acceleration to the inertial mass only.

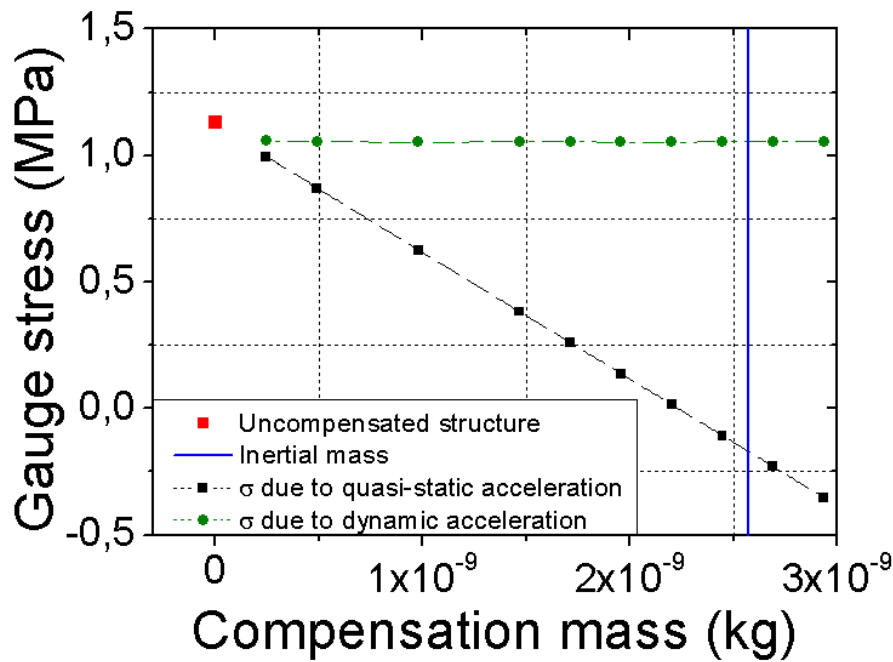


Figure 141: Simulated gauge stress due to mass compensation

In order to obtain a good compensation, the simulation gives a compensation mass equal to 85 % of the inertial mass. This compensation is made at design level. A perfect compensation cannot be obtained by this method, but a significant reduction of the quasi-static acceleration influence by two orders of magnitude can be expected. If a better compensation is needed, implementation of **active compensation through an electrostatic force** can be an efficient solution in term of footprint. In closed loop configuration, we can imagine an electrostatic compensation where the electrostatic force is set equal to inertial acceleration in order to compensate the quasi-static acceleration. This solution would have several advantages such as perfect compensation and small footprint. However an additional closed loop configuration is required.

#### 5.4.5 Towards IMU integration

In the previous section, a structure allowing mechanical co-integration of  $Y$  accelerometer and  $Z$  gyroscope has been described. In order to propose a complete '6-axis' IMU (6 degrees-of-freedom), an out-of-plane structure based on the same principle should be described.

##### 5.4.5.a Out-of-plane coupled accelerometer-gyroscope

The out-of-plane coupled accelerometer-gyroscope possesses the same architecture than the in-plane coupled accelerometer-gyroscope. Figures 142 and 143 show the drive mode and 1<sup>st</sup> parasitic mode of the out-of-plane structure.

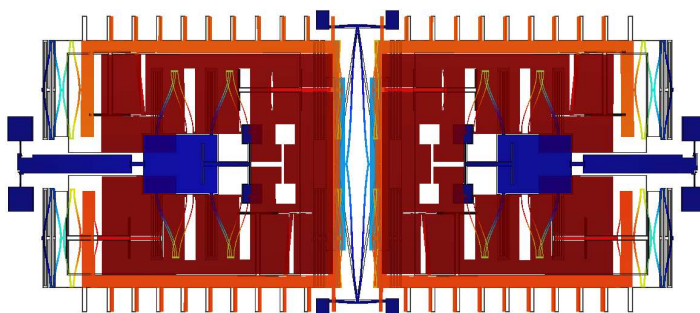


Figure 142: Drive mode obtained by FEM for a coupled accelerometer-gyroscope structure (19.8 kHz)



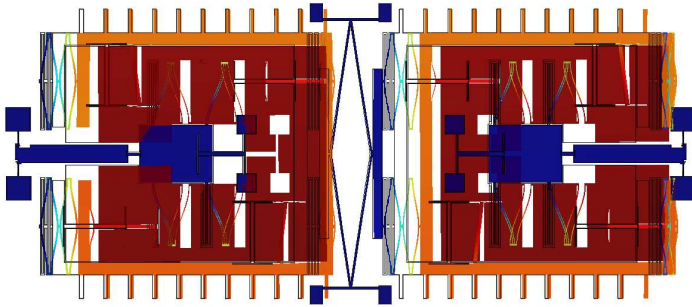


Figure 143: In-phase parasitic mode obtained by FEM for a coupled accelerometer-gyroscope structure (21.2 kHz)

The drive mode of the out-of-plane coupled accelerometer-gyroscope is identical to the drive mode described in the in-plane structure. Figure 144 corresponds to the mode excited by a rotation speed along Y (if we consider a drive mode along X). Figure 145 shows the sense mode excited by the dynamic acceleration along Z.



Figure 144: Sense mode (Coriolis force) obtained by FEM for a coupled accelerometer-gyroscope structure (20.5 kHz)



Figure 145: Sense mode (Dynamic acceleration) obtained by FEM for a coupled accelerometer-gyroscope structure (20.0 kHz)

One of the limitations of the out-of-plane coupled accelerometer-gyroscope is the influence of the coupling spring in the out-of-plane direction. The coupling spring is designed specifically to provide a large stiffness difference between the in-phase mode and the anti-phase mode in the drive direction. However, it applies the same effect in the out-of-plane direction. The resonance frequency difference between the two sense modes comes from the coupling spring. An improvement of the decoupling spring will limit the effect of the coupling spring on the sense modes.

#### 5.4.5.b Opening to 2A2G ('4-axis' sensor)

An in-plane structure with accelerometer and gyroscope functions has been described along with its out-of-plane counterpart. In order to push for low electronics power consumption, a large mechanical structure merging the in-plane and the out-of-plane coupled accelerometer-gyroscope is proposed. The objective is to reduce the number of control loops needed for a complete IMU.

The architecture of the 4-axis sensor is given in figure 146. The in-plane coupled accelerometer-gyroscope (in green) and the out-of-plane coupled accelerometer-gyroscope (in red) can be found in this architecture.

Here the drive mode is based on the rhomb-shape coupling spring. The driving mode is axially symmetric. The spring possesses two main positions of deformation. In these positions, two opposite mass come near the center of the sensor whereas the two other masses go away. The coupling spring forces an **anti-phase mode**. Figure 147 shows the simulated deformation obtained for the proposed drive mode.



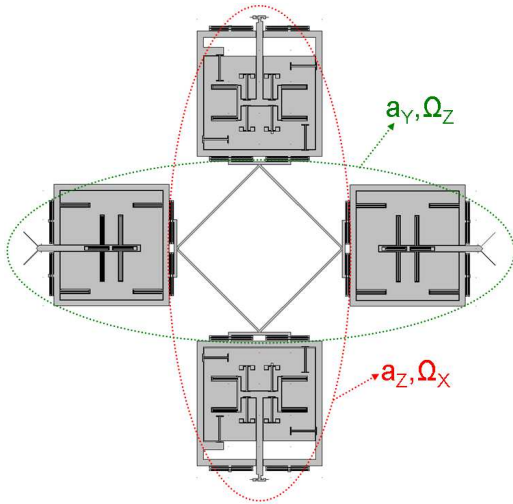


Figure 146: Architecture of the proposed 4-axis sensor

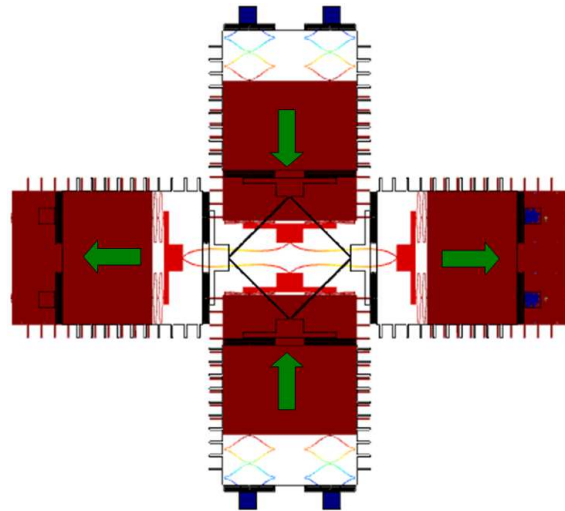


Figure 147: Drive mode of the proposed 4-axis resonant structure ( $a_x$ ,  $a_y$  and  $\Omega_z$ ,  $\Omega_x$ )

## 5.5 Conclusion

Introduction of the dynamic accelerometer proved that co-integration of different types of sensors can be achieved under the same pressure environment. The coupled accelerometer-gyroscope architecture shows the possibility to merge acceleration and gyroscopes functions at mechanical level. The four-axis sensor proposed in this section is an opening to further work on co-integration of sensors with reduced power consumption, smaller footprint and larger dynamic range.

However these sensors are still resonant sensors. In order to use quasi-static sensor in low pressure environment, a controllable source of damping is proposed in the next chapter. This additional source of losses can theoretically enable the direct co-integration of quasi-static sensors together with resonant gyroscopes in a unique low pressure cavity.

# Chapter 6: Electromechanical damping

## 6.1 Motivation towards co-integration of gyroscopes with non resonant accelerometers.

In the previous chapter, resonant accelerometers were described. They allow an easy co-integration with gyroscopes because both kinds are resonant sensors, which are compatible with vacuum packaging technologies. However these structures have two major drawbacks, their large footprint and the complexity of their electronics control circuit. A factor 2 can be expected from the footprint of a dynamic accelerometer with respect to the footprint of quasi-static accelerometer sensor. Moreover the feedback loop required by these structures induces a complex control electronics which increases the power consumption. In order to provide the consumer with cost-effective solutions, the footprint and the power consumption should be reduced. To achieve these goals, the straightforward co-integration of quasi-static accelerometer with resonant gyroscopes is still the best trade off solution. However, as quasi-static accelerometers require quite large damping, they are not compatible with vacuum packaging, and hence, their co-integration with a resonant gyroscope is not straightforward.

In this section, we will describe a controllable damping source that can decrease the quality factor of a specific sensor (here a quasi-static accelerometer) by at least two orders of magnitude with respect to an identical sensor in the same cavity without this damping source. This additional damping source is expected to provide enough damping to comply with the constraints on quality factor described in the end of chapter 1 i.e to allow co-integration of quasi-static accelerometer and resonant gyroscope in the same cavity.

## 6.2 Theory of RC coupling

In order to selectively increase the damping of mechanical sensors, we propose to couple the quasi-static mechanical sensor with an electric dissipative circuit. The idea is to use the self-test electrode of our sensor as a variable capacitance,  $C(x)=C_0+C'x$ .  $C_0$  is the constant part of the capacitance which includes all parasitic capacitance.  $C'$  corresponds to the variation of capacitance induced by a movement of the inertial mass. This capacitance should then be coupled to a dissipative resistance  $R$  (See Figure 148). This electromechanical coupling has already been described in [Jou07] and [Bar12]. Figure 148 shows the electrical circuit considered in this section. The mechanical system considered in this section is given in figure 149.

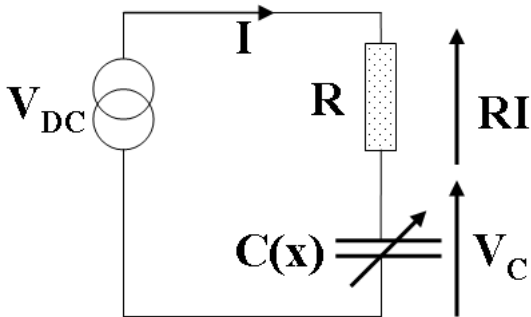


Figure 148: Equivalent electrical scheme

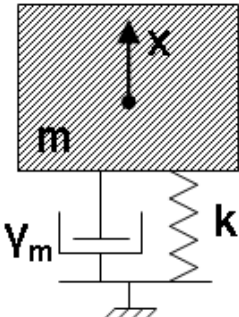


Figure 149: Equivalent mechanical scheme of a quasi-static sensor

By coupling a mechanical degree of freedom with an electrical degree of freedom, the energy oscillates between the electrical and mechanical domains. The energy transferred from the mechanical system to the electrical system is partly dissipated through Joule effect. Figure 150 shows the dissipation loop and the link between the electrical and mechanical domains.

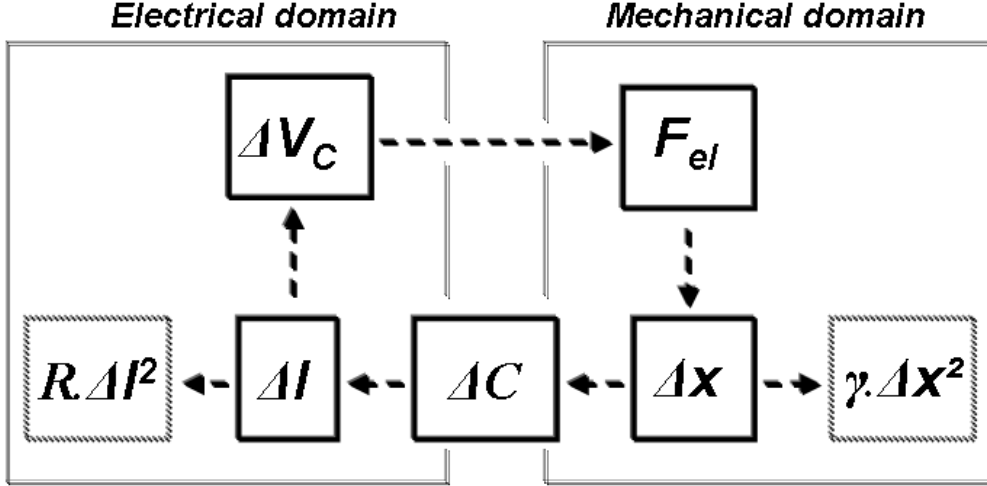


Figure 150: Dissipation loop through back action

In this case, the electro-mechanical coupling allows energy to pass from mechanical form to electrical form. A displacement  $\Delta x$  induces a variation of the capacitance  $\Delta C$  in the electrical circuit. A capacitance variation in an RC circuit is followed by a current variation  $\Delta I$  in the circuit. Part of this current is being dissipated in the resistance through the Joule effect. The polarisation voltage being constant, the voltage  $V_C$  across the capacitance varies. This induces a different electrostatic force  $F_{el}$ , which induces a different mechanical response  $\Delta x$ .

### 6.2.1- Energetic considerations

The system possesses both electrical and mechanical energy. The variation of the mechanical energy across time is proportional to the damping coefficient of the system and any external work provided. Equation (111) gives the elastic and kinetic energy variation of the system across time.

$$\frac{d}{dt} \left( \frac{1}{2} m \dot{x}^2 + \frac{1}{2} kx^2 \right) = -\gamma_m \dot{x}^2 + F_{EXT} \dot{x} \quad (111)$$

$F_{EXT}$  is an hypothetical external force. In the electrical system only the capacitor stockpiles energy. In the electrical domain the resistance dissipates energy. The electromechanical coupling term is expressed as the work of the electrostatic force as shown in equation (112).

$$\frac{d}{dt} \left( \frac{1}{2} C(x) V_C^2 \right) - V_{DC} \cdot I = -RI^2 - F_{el} \dot{x} \quad (112)$$

$V_C$  is the voltage across the capacitance. Additionally, like the displacement, the current is an AC current at frequency  $\omega$  that has theoretically no DC component. The power extracted from the DC source ' $V_{DC}I$ ' over a period is therefore equal to zero. The total energy present in the system is expressed in equation (113).

$$\frac{d}{dt} \left( \frac{1}{2} C(x) V_C^2 + \frac{1}{2} m \dot{x}^2 + \frac{1}{2} k x^2 \right) = -\gamma_m \dot{x}^2 - R I^2 + F_{el} \dot{x} + V_{DC} I + F_{EXT} \dot{x} \quad (113)$$

$F_{EXT} \cdot x'$  and  $V_{DC} \cdot I$  do not dissipate energy. Three dissipative terms can be identified, the viscous term, the Joule effect and the coupling term.

### 6.2.2- Transfer function

Jourdan et al. [Jou07] described the charge  $Q$  on the capacitance of figure 148 at the 1<sup>st</sup> order as:

$$Q = C \cdot V_C = C_0 \cdot V_{DC} + C' \cdot x \cdot V_{DC} - R \cdot C \cdot I \quad (114)$$

From equation (55) we see that the electrical circuit depends on the mechanical displacement  $x$ . In this chapter we will focus on the case where the electrical circuit is the 'slave' of the mechanical circuit. If we derive it with respect to time, equation (55) becomes:

$$I = C' \dot{x} V_{DC} - R C \dot{I} \quad (115)$$

In the frequency domain, the current  $I$  can be expressed as:

$$I = \frac{C' V_{DC} \dot{x}}{1 + R C j \omega} \quad (116)$$

Equation (116) shows the expression of the current generated by the displacement of the electrode.  $\omega$  corresponds to the pulsation of the inertial mass. At low  $\omega$ , the stiffness will dominate the mechanical system, whereas at high  $\omega$  any displacement will be cut by the transfer function of the mechanical system. Hence the frequency range where large displacement can occur is close to the resonant frequency. This current exhibits a cut-off frequency. This cut-off frequency is directly related to the electrical circuit i.e our RC series circuit corresponds to a low pass filter for the damping factor.

The mechanical system described in figure 149 is a 1-D spring mass system. Any force applied on the inertial mass of the quasi-static sensor will induce a displacement  $x$  of this mass following the displacement equation of the mass-spring system:

$$m \ddot{x} + \gamma_m \dot{x} + kx = F_{el} + F_{ext} \quad (117)$$

With  $m$  the inertial mass of the system,  $k$  the stiffness and  $\gamma_m$  the mechanical damping coefficient.

From figure 148, the electrostatic force applied on the MEMS by the electrical system is expressed in equation (118). The constant terms have been neglected. Assuming small amplitude of oscillation, the expression is considered at the first order. The negative spring stiffness is not considered in this equation.

$$F_{el} = \frac{1}{2} \cdot C' \cdot V_C^2 = C' \cdot V_{DC} \cdot R \cdot I \quad (118)$$

By inserting the electrostatic force of equation (118) in the spring-mass system described by equation (7), we can extract the complete transfer function of the electro-mechanical system:

$$\frac{X}{F_{ext}} = \frac{1}{k - \omega^2 \left( m - \frac{C'^2 R^2 V_{DC}^2 C}{1 + R^2 C^2 \omega^2} \right) + j\omega \left( \gamma_m + \frac{C'^2 R V_{DC}^2}{1 + R^2 C^2 \omega^2} \right)} \quad (119)$$

From equation (119), the influence of the electrical circuit can be found in two main characteristics of the system, **the natural frequency** and **the damping coefficient**. The resonance frequency of the system can be extracted from the transfer function as:

$$\omega_0 = \sqrt{\frac{k}{m - \frac{C'^2 R^2 V_{DC}^2 C}{1 + R^2 C^2 \omega^2}}} \quad (120)$$

Given the order of magnitude of C and C' in a typical MEMS, the additional inertial term is likely to be negligible with respect to the inertial mass of the system. Numerical estimation gives a relative variation of the inertial term around  $10^{-16}$ . Additionally this resonance frequency modification will be hidden by the negative stiffness effect due to the geometry of the capacitance which applies the electrostatic force. Experimental observation reports resonance frequency variation up to 3% due to **negative stiffness** effect.

The damping of the electromechanical system will be increased by a coupling term. The total damping can be expressed as:

$$\gamma = \gamma_m + \gamma_C = \gamma_m + \frac{(V_{DC} C')^2 R}{1 + R^2 C^2 \omega^2} \quad (121)$$

Using equation (116) and (119), we can demonstrate as shown in equation (122) that the electrical energy dissipation in the electrical system corresponds entirely to the energy drained from the mechanical system through the increased damping.

$$\gamma_C \dot{x}^2 = \frac{(V_{DC} C')^2 R}{1 + R^2 C^2 \omega^2} \cdot \frac{\|I^2\| (1 + R^2 C^2 \omega^2)}{(C' V_{DC})^2} = R I^2 \quad (122)$$

### 6.3 Experimental results

The following experiments have been carried out using the MEMS structure of the in-plane accelerometer described in section 4.1.1. We have modified the polarisation circuit of the sensor to include an electromechanical damping. Proceeding this way, a controllable damping mechanism with no pressure dependency should increase the damping factor on the accelerometer only.

#### 6.3.1- Measurement protocol and experimental setup

As already described in chapter 4, the accelerometer studied possess a rotational displacement. It can be modelled as a pendulum. The displacement of the inertial mass will be a rotation. The model defined in section 6.2 can be reused through the use of table 23.

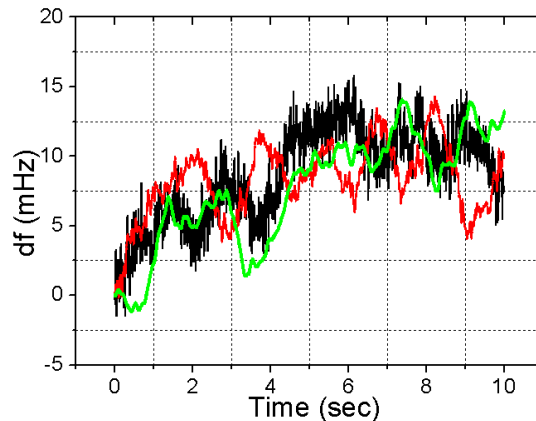
	Translation	Rotation	Correspondence formula
Inertia	m [kg]	J [kg.m <sup>2</sup> ]	$J = m.L^2$
Linear / Angular Displacement	x [m]	$\theta$ [rad]	$\theta = x / L$
Linear / Rotational Stiffness	k [N/m]	C [N.m]	$C = k.L^2$
Damping	$\gamma$ [s <sup>-1</sup> ]	$\gamma_\theta$ [m.s <sup>-1</sup> ]	$\gamma_\theta = \gamma.L$
Electrostatic force /torque	$F_{el} = \frac{1}{2} \frac{\partial C}{\partial x} V^2$	$M_{el} = \frac{1}{2} \frac{\partial C}{\partial \theta} V^2$	

*Table 23: Translation to rotation correspondence formula*

Here  $L$  is the distance of the considered object to the center of rotation. The governing equation that should be considered during the next experimental section is the equation (123) below:

$$J \ddot{\vartheta} + (\gamma_m + \gamma_{el}) \dot{\vartheta} + C\theta = M_{EXT} \quad (123)$$

The measured natural resonance frequency has been followed overtime. The accelerometer has been excited at a frequency close to the resonant frequency. The phase difference with respect to the reference signal allows an evaluation of the stability of the resonance frequency. Figure 151 shows several measurements of the resonance frequency variation over a short period of time.



*Figure 151: Resonance frequency variation of accelerometer in vacuum during 10sec*

The natural resonance frequency variation has been followed overtime and exhibit variations larger than 10 mHz during a typical measurement time (i.e 10 sec). Resonance frequency variations can be due to temperature variation or thermo-mechanical noise.

In vacuum, the response time of a resonator is several seconds. Given the characteristic of our sensor in vacuum environment ( $Q \sim 4.10^4$  and  $f_0 \sim 3.5$  kHz), the accelerometer will exhibit a frequency full width  $\Delta f$  at half maximum (FWHM: Full Width at Half Maximum) below 100 mHz.

In order to properly measure a sweep frequency curve, the sensor should be stabilized. The stabilization time of our sensor is several seconds. During this stabilization time the resonance frequency varies by at least 10 mHz as shown in figure 151. Measuring correctly a Lorentzian curve with a FWHM below 100 mHz is therefore very difficult. Sweep frequency measurements techniques cannot be used. In order to measure properly the damping coefficient, another measurement method already implemented in [Gia08] has been used.

Figure 152 depicts the different electrical potential at which the MEMS is submitted. The mechanical sensor is excited with a very low frequency square voltage  $V_{AC}$ . The MEMS response is real-time monitored through the half-bridge formed by the piezoresistive gauges polarized by  $V_{POL}$ . A ceramic resistance  $R$  has been inserted after the self-test electrode and submitted to a polarisation  $V_{DC}$ . The voltage  $V_m$  is then filtered and recorded by a 24 bits Analog to Digital Converter for post processing.

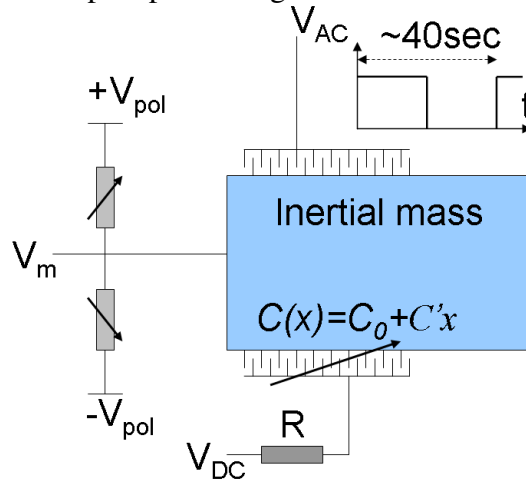


Figure 152: Electrical scheme of the experimental setup

The measurement being done in vacuum, the transient response of the MEMS is a sinusoidal exponential with negative growth. Band-pass filtering around the natural frequency of the sensor is done directly after the measurement. Fitting the measured transient response allowed a precise evaluation of the relaxation time along with the natural frequency of the accelerometer. Post-processing aims at extracting the following 4 parameters  $A_0$ ,  $\tau$ ,  $\omega$  and  $\varphi$  by fitting the experimental data with the theoretical equation described in equation (124). A precise assessment of the natural frequency is obtained through the FFT of the signal measured.

$$V_m(t) = A_0 \cdot e^{-t/\tau} \cdot \cos(\omega \cdot t + \varphi) \quad (124)$$

The quality factor  $Q$  of the system is given in equation (125) with respect to  $\tau$  and  $\gamma$ .  $\tau$  is the relaxation time and  $m$  the inertial mass. The damping factor  $\gamma$  will be the reference parameters during the following sections.

$$Q = \frac{\tau \cdot \omega}{2} = \frac{\omega}{\gamma} \quad (125)$$

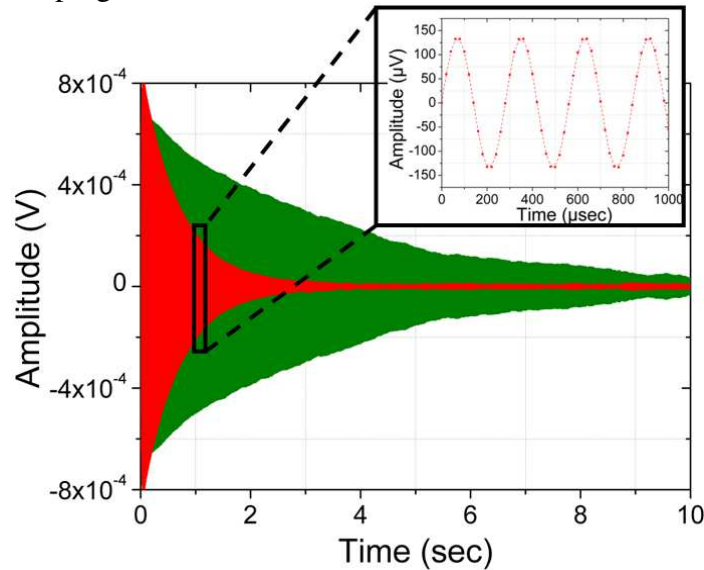
In order to give the reader an idea of the order of magnitude involved in this chapter, table 24 provides some numerical estimation of several of the parameters used in the theoretical section.

$\gamma_m$	$V_{DC \text{ MAX}}$	$V_{POL \text{ MAX}}$	$i_{MAX}$	$f_{RES}$	$C'_{THEO}$	$J$
$0.53 \text{ s}^{-1}$	10 V	0.3 V	70 pA	3.5 kHz	$7.4 \cdot 10^{-13} \text{ F/rad}$	$1.10^{-16} \text{ kg.m}^4$

*Table 24: Typical numerical values for the studied accelerometer*

$\gamma_m$  is the mechanical damping factor obtained in vacuum ( $10^{-5}$  mbar).  $V_{DC \text{ MAX}}$  is the maximum voltage applied to the damping loop.  $V_{POL \text{ MAX}}$  is the maximum polarisation voltage.  $i_{MAX}$  is the peak current given by the DC source of the damping loop.  $f_{RES}$  gives the resonant frequency of the accelerometer measured in this chapter and  $C'_{THEO}$  gives an analytical value of the circular comb drive capacitance variation.  $J$  corresponds to the moment of inertia of the accelerometer.

Figure 153 shows two measurement results of the transient response of the sensor. The green curve depicts the natural behaviour of the mechanical sensor. The red curve is done under the same conditions except for a  $V_{DC}$  voltage of about 10V that creates an observable electromechanical damping.



*Figure 153: Typical transient response of the mechanical sensor ( $V_{DC} = 0$  &  $10V$ )*

The period  $T$  of  $V_{AC}$  excitation has been set to ensure that no residual signal is left at the end of half period. The linearity of the response has been validated by the use of various amplitude voltages  $V_{AC}$ . Additionally using a polarization voltage of 0.1 V, the linear range of the readout signal is 3 mV. The repeatability of the measurements has been evaluated. The standard deviation extracted on the fitting parameters after post processing is below 1 % for 10 repetitive measurements.



### 6.3.2- Behavior with respect to DC voltage

Using the measurement protocol described in the previous section, the evolution of the sensor damping coefficient has been recorded for different configurations. Figure 154 shows the evolution of the damping coefficient  $\gamma$  for different values of the polarization voltage  $V_{DC}$ . Experimental data fits well with the theoretical values. The square proportionality of the damping factor with the polarisation voltage is thereby ensured.

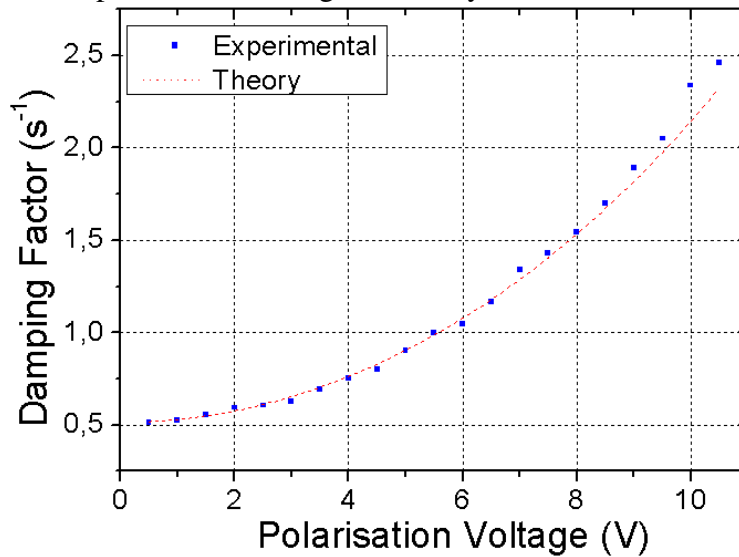


Figure 154: Damping factor reduction due to electromechanical coupling ( $V_{POL}=0.1V$ ;  $V_{AC}=3V$ )

The red dashed line represents the best fit line using an expression for the damping factor described in equation (121) with two fitting parameters. The damping obtained for  $V_{DC} = 0$  is the mechanical damping rate of the MEMS. The free parameter  $\gamma_m$  can be evaluated to  $0.53 \text{ s}^{-1}$  from figure 154. The best fit line gives a value for the second free parameter of  $0.017 \text{ V}^{-2}$ .

### 6.3.3- Behavior with respect to the detection circuit

The measurement protocol imposes the use of an excitation voltage of amplitude  $V_{AC}$  along with a gauge polarisation voltage  $V_{POL}$ . Figure 155 depicts the damping factor variation for various excitation and detection condition.

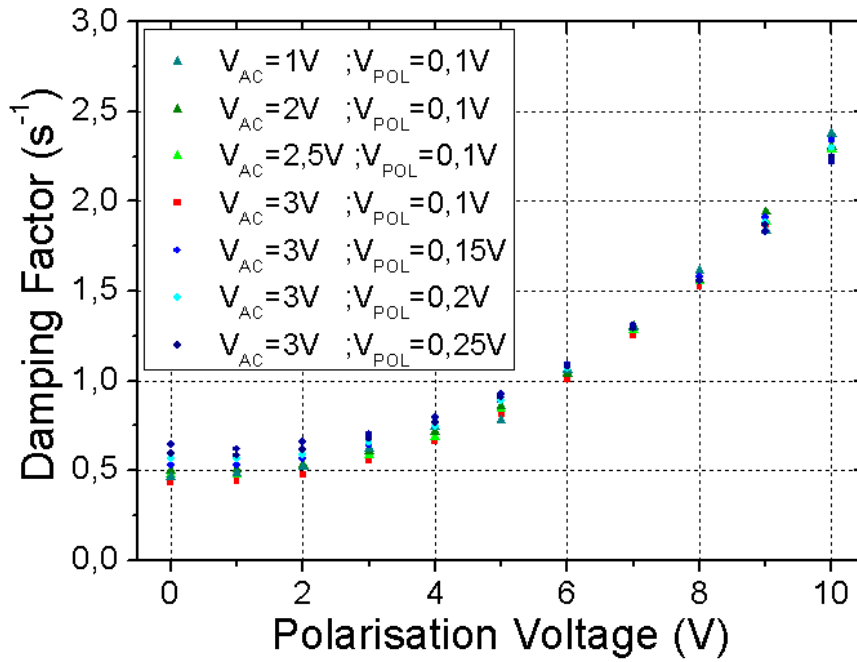


Figure 155: Influence of the detection circuit on the damping factor

The voltages  $V_{AC}$  and  $V_{POL}$  do not seem to have a large influence on the damping parameter. For low  $V_{DC}$  a small influence of the gauge polarisation voltage  $V_{POL}$  is noticed. Due to technological imperfection, the piezoresistive nanogauges do not have exactly the same electrical resistance value. When polarizing the nanogauges bridge, the inertial mass (at the middle of the bridge) is set to a voltage proportional to the nanogauge discrepancy. The voltage capacitance is then  $V_{DC}-V_m$  with  $V_m$  the inertial mass voltage.

$$V_m = \frac{R_1 - R_2}{R_1 + R_2} \cdot V_{POL} \quad (126)$$

However this discrepancy has been evaluated to a few percent in chapter 2. The influence of this effect on the voltage applied is too weak to explain the observed effect. Possibly self-heating effect can modify the behaviour of the nanogauge and have an impact on the damping factor. These small variations of the damping factor due to  $V_{POL}$  are not very well understood.

In order to minimize this effect, an identical polarization gauge voltage  $V_{POL}$  of 0.1 V and an actuation voltage  $V_{AC}$  of 3 V have been used in all the remaining experiments.

#### 6.3.4- Experimental evaluation of the damping cut-off frequency

Figure 156 shows the influence of the dissipative element on the damping factor. According to equation (121) the electromechanical coupling should exhibit a maximum damping when  $R=1/C \cdot \omega_{MEMS}$ . Different resistance values have been implemented and measured. Figure 156 shows the damping factor obtained after post processing for different resistance values.

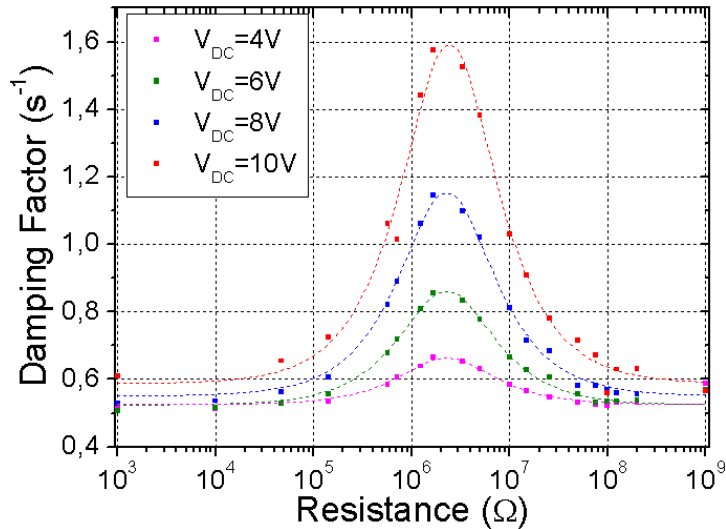


Figure 156: Damping Factor cut-off frequency (Different resistance values)

The experimental values were plotted on a semi-logarithmic scale. The dash lines represent the theoretical damping expressed in equation (121). The extracted values for  $C'$  and  $C_0$  gives respectively  $1.118 \text{ pF/rad}$  and  $20.4 \text{ pF}$ . The theoretical value of  $C'$  is  $0,74 \text{ pF/rad}$ . The complex geometry of the circular comb finger can explain the discrepancy between the experimental and the theoretical value. The extracted value for  $C_0$  is orders of magnitude higher than the theoretical values for the capacitance of the self-electrode (evaluated analytically to  $0.4 \text{ pF}$ ). This means that the dominant capacitance is the parasitic capacitance with a value around  $20 \text{ pF}$ . This makes sense since the ceramic resistance is separated from the MEMS by centimetres of coaxial wires (which are known to introduce stray capacitance of about  $100 \text{ pF/m}$ ).

### 6.3.5- Additional damping with pressure

The damping factor obtained with electromechanical damping has been measured for various pressures. Using self-test electrodes and external dissipation resistance, the dissipation due to the electromechanical damping is equivalent to the viscous effect of a pressure around  $0.1 \text{ mbar}$ . For pressure higher than  $1 \text{ mbar}$  the influence of the electromechanical damping on the tested structures is negligible.

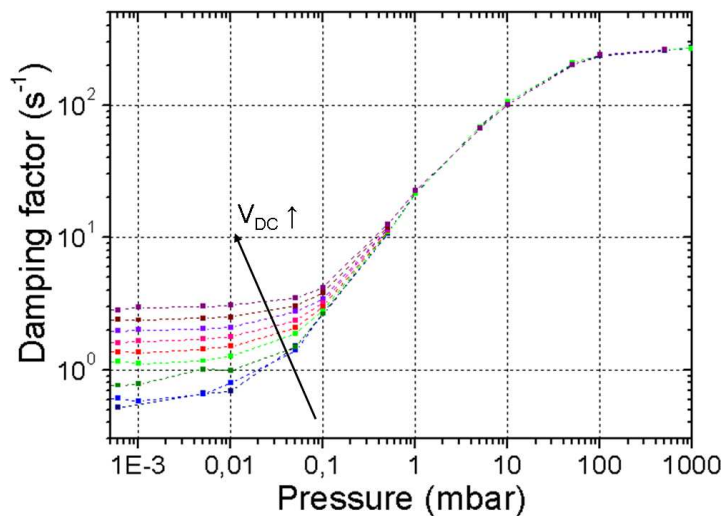


Figure 157: Pressure limitation of electromechanical coupling no quality factor

Using specific designs, this pressure limitation could be drastically increased.

## 6.4 Vacuum packaged low Q accelerometers sensors

The electromechanical damping limitation has been experimentally measured in figure 156. The couple of  $R$ ,  $C$  and  $\omega$  values define the cut-off frequency. By reducing the parasitic capacitance, values of  $C$  could be reduced by one order of magnitude. The limitation due to the cut-off frequency would be delayed. In order to validate the use of electromechanical damping as a way to efficiently co-integrate gyroscopes and accelerometers in the same cavity, the damping should be enough to comply with constraints given in section 1.6 i.e  $Q < 20$ . Complete IMU packaged in one single cavity with a low pressure (typically 0.01 mbar) could be fabricated. Specific designs with reduced parasitic capacitance are proposed in the next section.

### 6.4.1- Design proposal

The objective is to place the dissipative resistance the closest possible to the capacitance. This will allow a drastic reduction of the parasitic capacitance. In order to create large resistance values, the process flow has been modified to include a mask during the doping at  $5.10^{19} cm^{-3}$ . The masked area will exhibit the intrinsic doping.

#### 6.4.1.a- Resistance design

A resistivity of  $10 \Omega.cm$  has been assumed for the area with an intrinsic doping. Lightly doped suspended nanowires with dimensions similar to the piezoresistive naogauge i.e  $10 \times 0.25 \times 0.25 \mu m^3$  has been implemented. Each nanowire should exhibit an electrical resistance of the order of  $16 M\Omega$ . The diffusion lengths due to the thermal budget of the process are larger than  $250 nm$ . These diffusion lengths are expected to suppress the heavily/lightly doped semiconductor interface. Such large diffusion length configuration should suppress any semiconducting behavior.

#### 6.4.1.b- Capacitance design

Considering the variable capacitance, the objective is to obtain the highest  $C'/C_0$  ratio. However, if we consider very large capacitance, their negative spring stiffness will become overwhelming with respect to the mechanical stiffness. If the negative spring stiffness of the capacitance is too large the mechanical system will become unstable. Table 6 shows 2 types of variable capacitance implemented with their pros and cons.

Capacitance type	$C'/C_0$ ratio	Negative stiffness	Robustness
Circular comb drive	Medium	Low	High
Parallel plate	High	High	Medium

*Table 25 : Pros and cons of different types of variable capacitance*

$g$  is the capacitance gap. Thanks to their  $1/g^2$  relationship, the capacitance variation of the parallel plate capacitance show the highest  $C'/C_0$  ratio. However their negative stiffness increases with  $1/g^3$ .

The circular comb drives theoretically show no negative stiffness. Experimentally the effect of the negative stiffness is evaluated to 100 Hz for the studied sensor with  $V_{DC} = 10V$  i.e 3% of the resonance frequency. Assuming an identical behavior, the negative stiffness has been designed to be smaller than 1 % of the mechanical stiffness.

Analytical calculation gives a parasitic capacitance around 1 pF. The main parasitic capacitance comes from the intermediate connection pads and the mechanical anchor of the

capacitance. They are the only parts between the capacitance and the resistance. A different capacitance geometry has been implemented. Circular comb fingers shows the safest behavior hence two sensors have been implemented with this type of variable capacitance. One sensor with parallel plate capacitance has also been implemented. The objective of reducing the parasitic capacitance seems to be attainable.

### 6.4.1.c- The cut-off frequency limitation

In the previous section, the electrical circuit (Couple of resistance and capacitance) has been designed so that the electrical cut-off frequency is higher than the resonant frequency of the mechanical sensor. In order to maximize damping several electromechanical damping loops have been implemented. Figure 158 shows a scheme of the corresponding configuration.

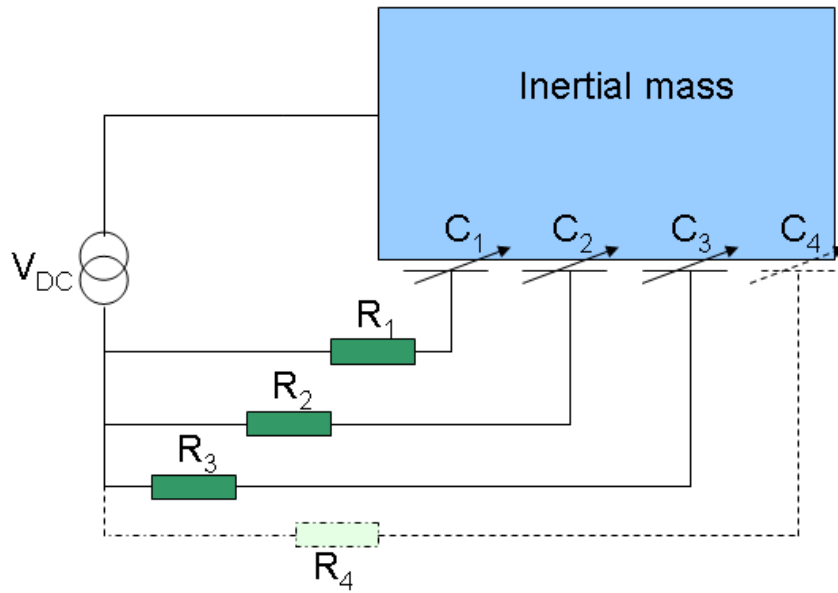


Figure 158: Scheme of an electromechanically damped sensor with several damping loop

The total damping factor using  $n$  damping loops each using a resistance  $R_i$  and a capacitor  $C_i$  can be expressed as:

$$\gamma_{TOT} = \sum_{i=1}^N \frac{R_i \cdot V_{DC}^2 \cdot C_i^2}{1 + R_i^2 C_i^2 \omega^2} \quad (127)$$

Assuming a mechanical resonant frequency of the sensor of  $\omega_{res}$ , each of the couple  $R_i$ ,  $C_i$  of figure 10 should be designed with the constraint expressed in equation (128).

$$\omega_{res} \leq \frac{1}{R_i \cdot C_i} \quad (128)$$

In order to obtain high damping, the electrical cut-off frequency should be higher than the mechanical resonance frequency. Each of the damping loops will increase the overall damping of the sensor. Using multiple loops, the cut-off frequency limitation can be circumvented. Additionally if the damping loops are placed symmetrically, the capacitive attraction on the inertial mass can be cancelled. The DC voltage could then be increased with no other limit than the maximum voltage allowed by the ASIC.

Figure 159 and 160 shows two implementations of an electromechanically damped accelerometer. Figure 159 shows a solution with circular comb drive. Figure 160 shows a solution with parallel plate capacitance and a corresponding resistance of 160 MΩ.

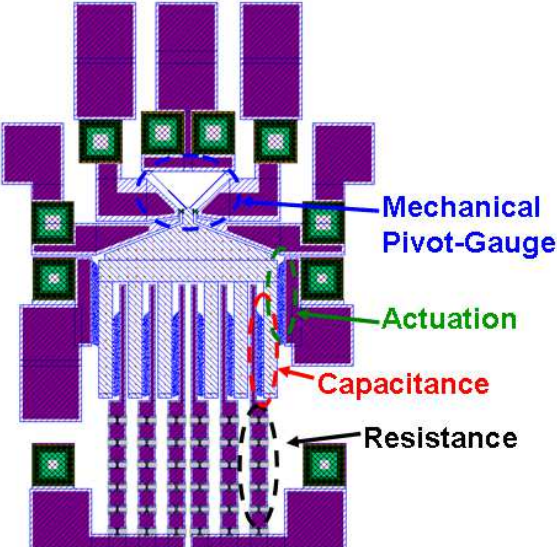


Figure 159: Top view of a damped accelerometer using parallel plate capacitance

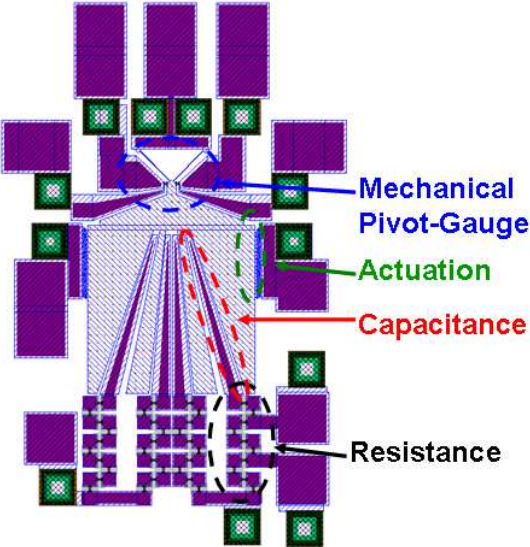


Figure 160: Top view of a damped accelerometer using circular comb drive

The mechanical design of the MEMS is identical to the precedent single-axis accelerometer design. Actuation electrodes with no embedded resistance are provided for testing purposes. 4 to 6 symmetrical damping loops are present in the designs. These designs are expected to exhibit a quality factor in vacuum around 50 for a  $V_{DC}$  of 10 V. Their fabrication is underway.

## Conclusions and prospects:

The M&NEMS technology is based on the use of nanogauge piezoresistors. It provides a platform allowing fabrication in an ultra-compact fashion, of the so-called “10-axis” inertial sensor (meaning the following set of sensors: 3 axis for acceleration, 3-axis for rotation speed, 3 axis for magnetic field as well as absolute pressure). This work highlighted and addressed some of the strongest constraints induced by the co-integration of these very different sensors, based on the same technological process flow.

Quasi-static sensors such as accelerometers in various forms as well as pressure sensors have been proposed and characterized. Decoupling springs have proven their validity as shock protection tools.

Single axis accelerometers appeared more efficient than multi-axis accelerometers, thanks to a proposed figure of merit where sensitivity is estimated with respect to the sensor footprint.

An original concept of an ultra-compact membrane-based pressure sensor with embedded mechanical amplification and self-test capabilities was proposed and validated. This approach allows a good electrical isolation, a large dynamic range (of almost 100 dB) and an extremely small footprint ( $\sim 0.04 \text{ mm}^2$ ) in the state-of-the-art, probably the smallest membrane-based pressure sensor ever reported. Pressure sensor based on this new concept can provide a very efficient solution to standard piezoresistive limitations. Following works should focus on the long-term stability of the sensor and its capacity to act as an altimeter (i.e long-term vacuum packaging and drift related issues) as well as testing its capacity for different measurement range.

Additionally, a study of the impact of the power consumption on the dynamic range and resolution of quasi-static sensors based on piezoresistive nanogauge should be conducted. An optimum current polarization is likely to exist and should be exploited in an efficient manner.

Following a previous study conducted within our research group, single-axis gyroscopes and two-axis gyroscopes have been characterized. Concerning the two-axis gyroscope, we contributed further by proposing a new design with improved mode ordering through a coupling spring in the sense direction. This mode ordering enabled to have the useful out-of-phase resonant mode in the first position, rejecting the “parasitic” in-phase mode to higher frequencies.

Resonant accelerometers are proposed in order to allow an IMU fabrication fully compatible with low pressure environment imposed by the gyroscope constraints of vacuum packaging. The dynamic accelerometer approach was explored as a potential solution to get rid of this constraint. The design of such a dynamic accelerometer was proposed and validated experimentally. This sensor exhibits a large dynamic range of  $3 \cdot 10^4$  for a footprint equivalent to the one of a gyroscope. The concept have been improved further by proposing a new mechanical design that allows both acceleration and rotation speed measurement on the same mechanical structure. This coupled accelerometer-gyroscope requires only one electronic control loop (for 2 axis measured), possess the footprint of a standard gyroscope and allow a shared electronics readout for all 6-axis.

Prospects for resonant sensors lie in the functional validation of a fully resonant IMU with its readout electronics. Future investigations might cover the development of a high performance 4DoF gyroscope. Additionally, in order to reach the ultimate objective of a low cost, ultra-compact IMU, the mutualisation of the readout electronics is going to be a critical advantage.

Targeting a trade-off between the opposite requirements for co-integration of a resonant gyroscope (low pressure for a high Q-factor) and an accelerometer working in quasi-static mode (high pressure for low Q-factor), we conducted a study on tuneable damping. To this end, an electromechanical coupling, though already known in its fundamental principle, has been used for the first time in a MEMS device, as an additional damping source. This damping source is very convenient since it is controllable through a simple DC source, consume almost no power and have a reasonably low impact on the footprint of the sensor. The physical behavior has been studied and the experimental data fits well with the theoretical model. This concept has been successfully implemented and led to large variations of the quality factor in the same pressure environment. Up to now, further increase of the damping is limited by the parasitic capacitance induced by the experimental setup. The fabrication of a dedicated structure using embedded dissipative resistance is underway. The theoretical quality factor of this structure is below  $10^2$  in vacuum environment with initial values of  $4 \cdot 10^4$ .

The characterization of this structure and its implementation in a vacuum packaged IMU can provide a good insight on the potential industrialization of this damping source, as an efficient way for co-integration of accelerometers and gyroscope into the same vacuum-sealed package.



## Appendix

### Appendix 1: 4-point measurement method

Following Ohm's Law, the electrical resistance of a device can be retrieved from the ratio between the voltage measured across its length and the current flowing through it. However, proper measurement of the resistance of microstructures can be difficult due to access limitation. Voltmeters and sourcemeters are generally tens of centimeters wide, whereas our piezoresistive nanogauge's typical dimensions are  $0.25 \times 0.25 \times 5 \mu\text{m}^3$ . This contrast in dimension creates the need to account for an appropriate bridge between the macro- and the micro- world. Figure 161 shows the main non idealities taken into consideration in such a bridge.

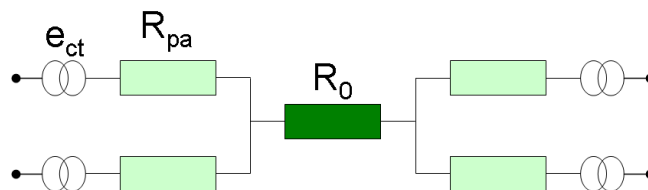


Figure 161: 1<sup>st</sup> order model of a micro-resistance linked to a macro system for measurement

Due to the long wires needed to access the micro-resistance, parasitic resistances  $R_{pa}$  can artificially increase the apparent value of the measured resistance. Additionally, if different metals are present in your electrical circuit, a built-in voltage  $e_{ct}$  will form at their interface. A voltage measurement being involved to extract the value of a resistance, this built-in voltage will add an offset to the measurement.

In order to compensate for parasitic resistances and parasitic voltages, the so-called “four-point measurement method” has been developed. The idea is to use different paths for current and voltage measurement. The only part where these paths are common defines the resistance that is actually measured and this turns to be our resistance of interest.

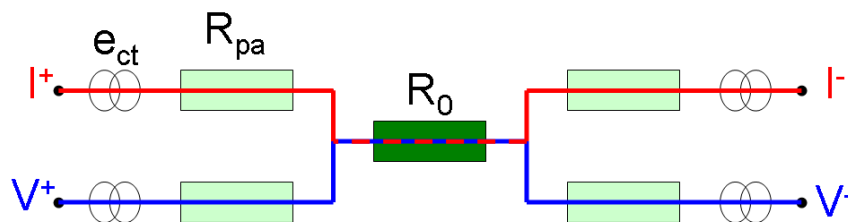


Figure 162: Four point measurement polarization scheme

Parasitic resistances vary largely with the technological process involved in the nanogauges fabrication. Concerning wires parasitic resistance, they are usually below  $10 \Omega$ . In order to compensate for the possible built-in voltages, a two step measurement is used. Figure 163 shows the typical I-V curve obtained for a resistive behavior. In order to suppress the built-in voltage  $e_{ct}$ . The offset has to be measured. By measuring the voltage induced for two different values of the current (for instance:  $I^+ = I_0$  and  $I^- = -I_0$ ), the offset due to the built-in voltage can be suppressed, assuming that it does not vary with time, as an effect of temperature variations for instance.

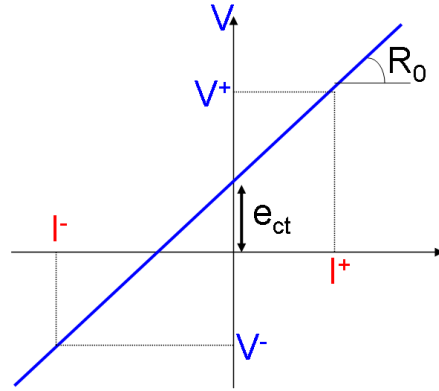


Figure 163: Typical I-V curve revealing an offset voltage  $e_{ct}$  induced by metal-metal contact

In all 4-point measurements done during this thesis, the same protocol is used. First the gauge is polarized with a current  $I^+$ . The corresponding voltage  $V^+$  is measured. Shortly after, an opposite current  $I$  is applied through the nanogauge. To finish, the corresponding voltage  $V$  is measured. The nanogauge resistance is then extracted using equation (9).

$$R_0 = \frac{V^+ - V^-}{I^+ - I^-} \quad (129)$$

## Appendix 2: TCE: Thermal Coefficient of Extension

The Thermal Coefficient of Extension (TCE) of silicon nanogauges could not be experimentally measured. Previous experiment found in literature [Lyo77] shows that the TCE increases with increasing temperature. A numerical value of  $2.6 \text{ ppm}/^\circ\text{C}$  at 300K has been considered throughout the study.

## Appendix 3: Y- $\Delta$ Transformation in case of spring stiffness

In some complex cases, springs are linked using triangle ( $\Delta$ ) or star (Y) architecture. A formula to convert springs in a triangle configuration into a star configuration is given below. Figures 165, respectively 164, show the scheme of a triangle ( $\Delta$ ) configuration, respectively a star (Y) configuration.

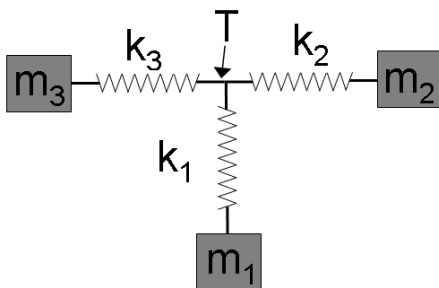


Figure 164: Scheme of springs in a Y geometry

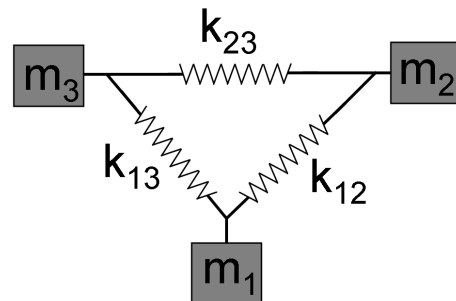


Figure 165: Scheme of springs in a  $\Delta$  geometry

$M_1$ ,  $M_2$  and  $M_3$  are the seismic mass.  $k_1$ ,  $k_2$  and  $k_3$  correspond to the stiffness of the springs in the star configuration.  $k_{12}$ ,  $k_{13}$  and  $k_{23}$  correspond to the stiffness of the springs in the triangle configuration.

### 3.2.2.a Demonstration of Y-Δ transformation for unidirectional mechanical problems

In this section, all the stiffness reported are stiffness along the same direction (here the horizontal direction). Figures 166 and 167 show the respective (Y) and (Δ) configurations considering a unidirectional problem.

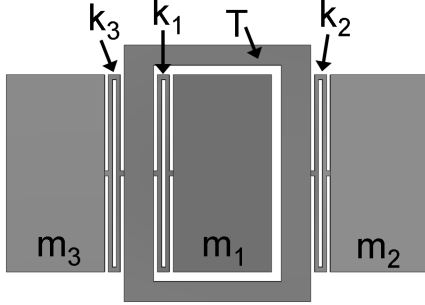


Figure 166: Scheme of a (Y) geometry for unidirectional mechanical springs

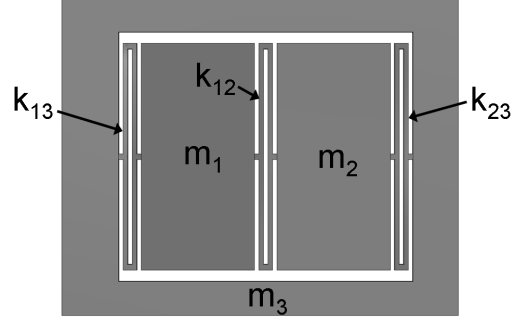


Figure 167: Scheme of a (Δ) geometry for unidirectional mechanical springs

$T$  is the fourth mass at the intersection of all springs in the star configuration.

#### Y to Δ transformation:

Let's consider the isolated assembly of figure 166. Using Hooke's Law, we can write the force-displacement relationship of each spring:

$$F_{i/0} = k_i \cdot (u_i - u_T) \quad (130)$$

Here  $F_{i/0}$  stands for the force applied on solid  $i$ . Solid  $i$  is isolated.  $i$  equals 1, 2 or 3. Using the 2<sup>nd</sup> Newton's law on  $T$ :

$$\sum F_{T/0} = F_{1/0} + F_{2/0} + F_{3/0} = 0 \quad (131)$$

Using equations (130) and (131) we can express the displacement of the mass  $T$ .

$$u_T = \frac{k_1 \cdot u_1 + k_2 \cdot u_2 + k_3 \cdot u_3}{k_1 + k_2 + k_3} \quad (132)$$

Let's consider the assembly of figure 167. The force-displacement relationship states:

$$F_{1/0} = k_{12} \cdot (u_1 - u_2) + k_{13} \cdot (u_1 - u_3) \quad (133)$$

$$F_{2/0} = k_{12} \cdot (u_2 - u_1) + k_{23} \cdot (u_2 - u_3) \quad (134)$$

$$F_{3/0} = k_{13} \cdot (u_3 - u_1) + k_{23} \cdot (u_3 - u_2) \quad (135)$$

Using equation (131) and (132) we can obtain respectively equations (136), (137) and (138) using  $i=1, 2$  and  $3$  respectively.

$$k_1 \cdot (u_1 - u_T) = u_1 \cdot (k_{12} + k_{13}) \quad (136)$$

$$k_2 \cdot u_T = k_{12} \cdot u_1 \quad (137)$$

$$k_3 \cdot u_T = k_{13} \cdot u_1 \quad (138)$$

Assuming  $u_2 = u_3 = 0$ , the expression of  $u_T$  of equation (136) is simplified in equation (139).

$$u_T = \frac{k_1 \cdot u_1}{k_1 + k_2 + k_3} \quad (139)$$

Replacing  $u_T$  in equation (137) and (138) gives:

$$k_{12} = \frac{k_1 \cdot k_2}{k_1 + k_2 + k_3} \quad \text{and} \quad k_{13} = \frac{k_1 \cdot k_3}{k_1 + k_2 + k_3} \quad (140)$$

We have fixed both the mass  $m_1$  and  $m_2$ . Hence  $k_{23}$  is still unknown. If we fix the solid  $m_1$  and  $m_3$ , then we have  $u_1 = u_3 = 0$ . Using the problem's symmetry, the expression of  $k_{23}$  can be obtained.

$$k_{23} = \frac{k_2 \cdot k_3}{k_1 + k_2 + k_3} \quad (141)$$

Expressions of  $k_{12}$ ,  $k_{13}$  and  $k_{23}$  have been expressed using  $k_1$ ,  $k_2$  and  $k_3$ . The transformation from triangle to star configuration will give the reciprocal formulas.

$\Delta$  to Y transformation:

Using equations (140) and (141) the expressions of  $k_1$ ,  $k_2$  and  $k_3$  can be obtained.

$$k_1 = \frac{k_{13} \cdot k_{12} + k_{23} \cdot k_{13} + k_{23} \cdot k_{12}}{k_{23}} = \frac{\sum_{i=1..3} k_{ij} \cdot k_{ik}}{k_{jk}} \quad (142)$$

$$k_2 = \frac{k_{13} \cdot k_{12} + k_{23} \cdot k_{13} + k_{23} \cdot k_{12}}{k_{13}} \quad (143)$$

$$k_3 = \frac{k_{13} \cdot k_{12} + k_{23} \cdot k_{13} + k_{23} \cdot k_{12}}{k_{12}} \quad (144)$$

Assuming identical springs, the problem of stiffness is equivalent to a problem of electrical admittance concerning the  $\Delta$ -Y transformation. Figure 168 gives an example of  $\Delta$ -Y transformation with springs of identical stiffness.

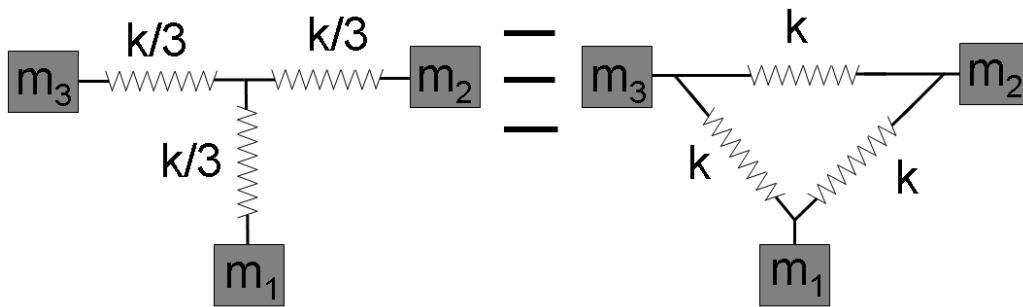


Figure 168: Example of  $\Delta$  to Y transformation

## References:

- [Acar03]: C. Acar, A. M. Shkel "Nonresonant Micromachined Gyroscopes With Structural Mode-Decoupling" IEEE Sensors J., Vol. 3 (4), pp.497-506, 2003.
- [Bosch96]: US Patent: "Method of anisotropically etching silicon", US5501893A.
- [Bar09]: A.A Barlian, W.T Park, J.R Mallon, A.J Rastegar, B.L Pruitt "Review: Semiconductor Piezoresistance for Microsystems" PROCEEDINGS OF THE IEEE, Vol.97 (3), pp.513-552, 2009.
- [Bar12]:T. Barois, A.Ayari, A. Siria, S.Perisanu, P.Vincent, P.Poncharal, S.T Purcell "Ohmic electromechanical dissipation in nanomechanical cantilevers" Physical review B Vol.85 (7), DOI: [10.1103/PhysRevB.85.075407](https://doi.org/10.1103/PhysRevB.85.075407), 2012.
- [Che09]: L. Che, B. Xiong, Y. Li, Y. Wang "A novel electrostatic-driven tuning fork micromachined gyroscope with a bar structure operating at atmospheric pressure" J. Micromech. Microeng. Vol: 20, DOI:10.1088/0960-1317/20/1/015025, 2009.
- [Dei13]:Y.Deimerly, P.Robert, G.Jourdan, P.Rey, T.Bourouina " Ultra-compact absolute pressure sensor based on mechanical amplification coupled to a suspended piezoresistive nanogage" TRANSDUCERS 2013, 17th International conference on Solid-State Sensors, Actuators and Microsystems, Barcelone, 16-22 June, pp. 1767-1770 2013.
- [Eng09] M. Engesser, A. Franke, M. Maute, D. Meisel, J. Korvink "Miniaturization limits of piezoresistive MEMS accelerometers" Microsyst Technol, Vol.15(12), pp.1835–1844, 2009.
- [Ett11]: Ettelt PhD thesis, Univeristé de Grenoble "Conception et fabrication d'un magnétomètre à jauge de contrainte", 2012.
- [Fedder94]: G. Fedder, "Simulation of Microelectromechanical Systems" PhD thesis, University of California, Berkley, 1994.
- [Gou04]: D.Goustouridis, G.Kaltsas, A.G. Nassiopoulou "A CMOS compatible thermal accelerometer without solid proof mass, based on porous silicon thermal isolation" PROCEEDINGS OF THE IEEE SENSORS, Vol. 1-3, pp.848-851 2004.
- [Gia08]: Giacomo Langfelder, Antonio Longoni, Federico Zaraga "Low-noise real-time measurement of the position of movable structures in MEMS" Sensors and Actuators A Vol.148 (2) pp.401–406, 2008.
- [Har00]: J. A. Harley, T. W. Kenny "1/f Noise Considerations for the Design and Process Optimization of Piezoresistive Cantilevers" J.Microelectromech. Systems, Vol. 9, pp.226-235, 2000.
- [Hoo81]: F. N. Hooge, T G M Kleinpenning, L K J Vandamme, "Experimental studies on 1/f noise", Rep. Prog. Phys., Vol. 44,pp. 479-532, 1981.
- [Hoo78]:F. N. Hooge, L K J Vandamme. "Lattice scattering causes 1/f noise" Physics Letters A Volume: 66 Issue: 4 (1978-01-01) pp. 315-316.
- [Jou07]: G. Jourdan, G.Torricelli, J.Chevrier, F.Comin "Tuning the effective coupling of an AFM lever to a thermal bath", Nanotechnology Vol.18 (47), DOI: [10.1088/0957-4484/18/47/475502](https://doi.org/10.1088/0957-4484/18/47/475502), 2007.
- [Kaa04]: V. Kaajakari, T. Mattila, A. Oja, H. Seppä "Nonlinear Limits for Single-Crystal Silicon Microresonators" J.Microelectromech. Systems, Vol. 13 (5), pp.715-724, 2004.
- [Kan91]: Y. Kanda "Piezoresistance effect of silicon" Sensors and Actuators A, Vol: 28 pp.83-91, 1991.
- [Kan82]: Y. Kanda "A Graphical Representation of the Piezoresistance Coefficients in Silicon" IEEE TRANSACTIONS ON ELECTRON DEVICES, VOL. ED-29, NO. 1 , 1982.

- [Kacem10]: Najib Kacem “Nonlinear dynamics of M&NEMS resonant sensors: Design strategies for performance enhancement” PhD thesis, Université de Lyon-CNRS INSA-Lyon 2010.
- [Kunz01]: K. Kunz, P. Enoksson, G. Stemme “Highly sensitive triaxial silicon accelerometer with integrated PZT thin film detectors” *SENSORS AND ACTUATORS A-PHYSICAL*, Vol. 92 (1-3) , pp.156-160, 2001.
- [Lyo77]: K. G. Lyon, G. L. Salinger, C. A. Swenson, and G. K. White “Linear thermal expansion measurements on silicon from 6 to 340 K” *J. Appl. Phys.*, Vol:48 (3), pp.865-868, 1977.
- [Lui06]: X.Liu, Z.Yang, G.Yan “Design and fabrication of a lateral axis gyroscope with asymmetric comb-fingers as sensing capacitors” 1st IEEE International Conference on Nano/Micro Engineered and Molecular Systems, pp.808 (11), 2006.
- [Lef06]: *Journal of Micromechanics and Microengineering* “Highly Decoupled Single-Crystal Silicon Resonators: an approach for the intrinsic quality factor” *J. Micromech. Microeng.* Vol.16, S45–S53, 2006.
- [Min96]: T Mineta, S Kobayashi, Y Watanabe, S Kanauchi, I Nakagawa, E Sugauma and M Esashi “Three-axis capacitive accelerometer with uniform axial sensitivities” *J. Micromech. Microeng.* Vol.6, pp.431–435, 1996.
- [Mat98] Y. Matsumoto, M. Nishimura, M. Matsuura, M. Ishida " Three-axis SOI capacitive accelerometer with PLL C-V converter” *SENSORS AND ACTUATORS A-PHYSICAL*, Vol.75, pp.77-85, 1998.
- [Moch99]: Y. Mochida, M. Tamura, K. Ohwada, "A Micro Machined Vibrating Rate Gyroscope with Independent Beams for the Drive and Detection Modes", *Proc. IEEE MEMS*, 1999, pp. 618-623.
- [Par00]: A. Partridge, J. K. Reynolds, B. W. Chui, E. M. Chow, A. M. Fitzgerald, L. Zhang, N. I. Maluf, T. W. Kenny “A High-Performance Planar Piezoresistive Accelerometer” *J. Microelectromech. Systems*, Vol.1, pp.56-66, 2000.
- [Rey10]: P. Rey, D. Ettelt, C. Coutier, M. Savoye, G. Jourdan, M. Cartier, O. Redon, Y. Zhang, , D. O’Brien, F. Dumas-Bouchiat, D. Givord, N. M. Dempsey , G. De Loubens, C. Fermon, W. Rahajandraibe, S. Meillère, E. Kussener, H. Barthélemy, Y. Caritu "CAPPUCINE" Journée Nationale en Nanoscience et Nanotechnologie, Strasbourg, France, 9 Novembre, 2010.
- [Roark7]: Roark’s Warren C. Young, “Roark’s Formulas For Stress & Strain”, Chapter 7. McGraw-Hill, USA, 1989.
- [Roark8]: Roark’s Warren C. Young, “Roark’s Formulas For Stress & Strain”, Chapter 8. McGraw-Hill, USA, 1989.
- [Roark11]: Roark’s Warren C. Young, “Roark’s Formulas For Stress & Strain”, Chapter 11. McGraw-Hill, USA, 1989.
- [Roarks12]: Roark’s Warren C. Young, “Roark’s Formulas Stresses Strain”, Chapter 12. McGraw-Hill, USA, 1989.
- [Rob09]: Ph. Robert, V. Nguyen, S. Hentz, L. Duraffourg, G. Jourdan, J. Arcamone and S. Harrisson. “M&NEMS : A new approach for ultra-low cost 3D inertial sensor” *IEEE Sensor Conference*, Christchurch pp.963-966, 2009.
- [Ste11]: P. G Steeneken, K. Le Phan, M. J. Goossens, G. E. J. Kooops "Piezoresistive heat engine and refrigerator” *Nature Physics*, Vol:7 -4 pp.354-359, 2011.
- [Sim13]: B.R Simon, A.A Trusov, A.M Shkel "Anti-Phase Mode Isolation in Tuning-Fork MEMS using a Lever Coupling Design" 11th IEEE Sensors Conference, TAIWAN, *IEEE Sensors* pp. 295-298, 2012.
- [Ter12]: T. Terasawa, T. Watanabe, T. Murakoshi “Electrostatically Levitated Ring-Shaped Rotational-Gyro/Accelerometer Using All-Digital OFDM Detection With TAD” 11th IEEE Sensors Conference, Taipei, TAIWAN, OCT 28-31, 2012.

- [Tru09]: A.A. Trusov, A.R Schofield, A.M Shkel., "Micromachined rate gyroscope architecture with ultra-high quality factor and improved mode ordering", Sens. Actuators A: Phys. Vol.165, pp.26-34, 2011.
- [Tru11]: A. A. Trusov, I. P. Prikhodko, S. A. Zotov, A. M. Shkel "Low Dissipation Silicon Tuning Fork Gyroscopes for Rate and Whole Angle Measurements" IEEE Sensors J. Vol.11 (11), pp.2763-2770, 2011.
- [Tsai06]: Deng-Horng Tsai, Weileun Fang "Design and simulation of a dual-axis sensing decoupled vibratory wheel gyroscope" Sens. Actuators A: Phys. Vol.136 pp.33-40, 2006.
- [Van86]: L. Vandamme, "Annealing of ion-implanted resistors reduces the 1/f noise," Journal of Applied Physics, Vol. 59 (9), pp.3169-3174, 1986.
- [Wal12]: A. Walther, M. Savoye, G. Jourdan, P. Renaux, F. Souchon, P. Robert, C. Le Blanc, N. Delorme, O. Gigan, C. Lejuste "3-axis gyroscope with Si nanogage piezo-resistive detection" 25th IEEE International Conference on MEMS ,29 Jan-02 Feb 2012 pp.480-483.
- [Wal13]: A. Walther, C. Le Blanc, N. Delorme, Y. Deimerly, R. Anciant, and J. Willemin "Bias contributions in a MEMS tuning fork gyroscope" Journal of Microelectromechanical Systems, Vol.22 (2), pp.303-8. 2013.
- [Wang12]: W. Wang, X. Lv, F. Sun "Design of Micromachined Vibratory Gyroscope With Two Degree-of-Freedom Drive-Mode and Sense-Mode" " IEEE Sensors J. Vol.12 (7), pp.2460-2464, 2012.
- [Wei01]: J. W. Weigold, K. Najafi, S. W. Pang" Design and Fabrication of Submicrometer, Single Crystal Si Accelerometer" J.Microelectromech. Systems, Vol. 10 (4), pp.518-524, 2001.
- [Wei06]: MS .Weinberg, A. Kourepenis "Error sources in in-plane silicon tuning-fork MEMS gyroscopes" JOURNAL OF MICROELECTROMECHANICAL SYSTEMS, Vol.15 (3), pp.479-491, 2006.
- [Yole11]: Yole Technology. "Trends for Inertial MEMS Volume 1: Analysis" December 2011. Commercial benchmark report from Yole Development.
- [Zeng11]: HS. Zeng,Y. Zhao "Review: Sensing Movement: Microsensors for Body Motion Measurement" Sensors 2011, 11, pp.638-660, 2011.
- [Zha07]: Z. Zhang, K. Li "Design, Simulation and Multi-Dimension Coupling Research of Monolithic MEMS Three-Axis High-G Accelerometer" Proceedings of the 2007 International Conference on Information Acquisition, Jeju City, Korea, 2007.

# Vers les centrales inertielles ultra-compactes basées sur des nanojauges piezoresistives: Problématiques de co-intégration

## 1- Contexte de la thèse

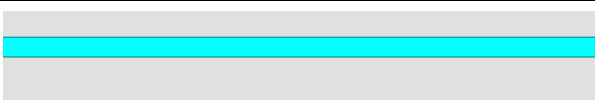
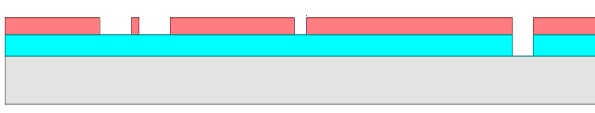
### 1.1- Une co-intégration poussée: vers le capteur inertiel « 10-axes »

Cette thèse a été effectuée dans un contexte industriel de forte concurrence en lien avec des capteurs miniatures en silicium. Des marchés jusqu'à présent bien différents, tel que celui des magnétomètres ou des capteurs de pression, ont évolué pour former un gigantesque marché appelé marché 'consumer' dont l'application phare est le 'smartphone'. Rapidement le capteur inertiel 10-axes (accéléromètre 3-axes, magnétomètre 3-axes, gyromètre 3-axes et capteur de pression) a été identifié comme étant la centrale inertielle correspondant aux attentes du marché [Yole11]. Dans ce contexte, les entreprises ayant un cœur de métier axé sur un seul type de capteur essayent de s'adapter à ce marché en élargissant leur gamme de capteurs.


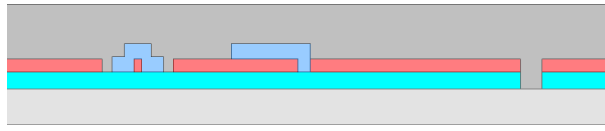
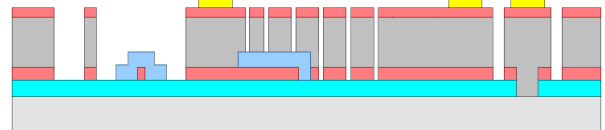
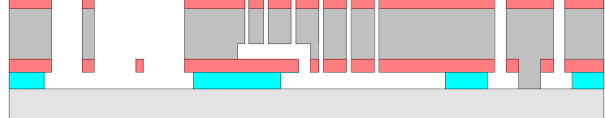
### 1.2- La technologie M&NEMS

La technologie M&NEMS a été développée pour répondre à cette attente. L'objectif est de fournir un procédé de fabrication bas coût commun à tous les capteurs de la centrale inertielle « 10-axes » et permettant de fabriquer cette centrale inertielle tant recherchée. Le procédé de fabrication en question est basé sur l'utilisation de deux couches de silicium monocristallin d'épaisseur très différentes. L'une fine (sub-micronique, ~250 nm) appelée NEMS, qui définit l'élément sensible (i.e une nano-jauge suspendue piézorésistive dont le modèle multi-physique est décrit dans le chapitre 2). L'autre, épaisse (~10 μm), définit la masse d'inertie des capteurs. L'utilisation de nanojauges suspendues permet plusieurs améliorations par rapport aux jauges de contraintes piézorésistive classiques.

Tout d'abord, outre le gain en compacité, la dimension nano se traduit également par une forte concentration des contraintes induite sur la faible section de la nano-jauge. Ensuite, le fait d'obtenir une jauge suspendue permet d'obtenir une très bonne isolation électrique. Pour finir, un ensemble mécanique pivot/jauge organisé en bras de levier permet d'amplifier davantage la contrainte appliquée à la jauge. Un procédé de fabrication simplifié est décrit dans la table ci-dessous:

Départ sur un substrat SOI: (Si Top d'une épaisseur typique de : 250nm, BOX:1μm)	
Étape de dopage, recuit et lithographie de la couche NEMS. Définition des nanojauges.	



<p>Une couche de protection (<math>\text{SiO}_2</math>) est déposée sur les parties critiques du NEMS (i.e nanojauges, électrodes).</p>	
<p>Épitaxie de silicium monocristallin afin de former l'épaisseur MEMS. Planarisation de la couche à une épaisseur autour de 10 <math>\mu\text{m}</math>.</p>	
<p>Gravure profonde. Définition de la structure MEMS (i.e masse d'inertie, suspensions élastiques, peignes électrostatiques)</p>	
<p>Libération des structures par gravure HF en phase vapeur de la couche d'oxyde</p>	
<p><i>Table 26 : Description des principales étapes du procédé de fabrication 'M&amp;NEMS'</i></p>	

Au début de la thèse, chacun des capteurs pris individuellement (accéléromètre, magnétomètre et gyromètre) avait été développé, et leur fonctionnement respectif validé [Rob09], [Ett11], [Wal12]. Les travaux présentés ici sont donc axés sur la problématique de co-intégration de ces capteurs sur une même plaque et dans un même environnement de packaging collectif sous vide, afin de valider la compatibilité de l'ensemble du procédé de fabrication, dans la perspective d'une plateforme inertielle « 10 axes ».

## 2- Motivation de la thèse

### 2.1- Accéléromètre quasi-statique

Un accéléromètre piézorésistif fonctionne sur un principe similaire à celui du pendule, basé sur un système masse-ressort constituant le corps d'épreuve du capteur. Lorsqu'une accélération est appliquée, la masse se déplace et par effet bras de levier induit une contrainte sur les nanojauges piézorésistives, qui assurent la transduction entre les domaines mécanique et électrique. Cette contrainte est ensuite lue et transformée en signal électrique grâce à un demi-pont de Wheatstone et un circuit électronique dédié. La figure 169 montre une image MEB d'un tel accéléromètre fabriqué.

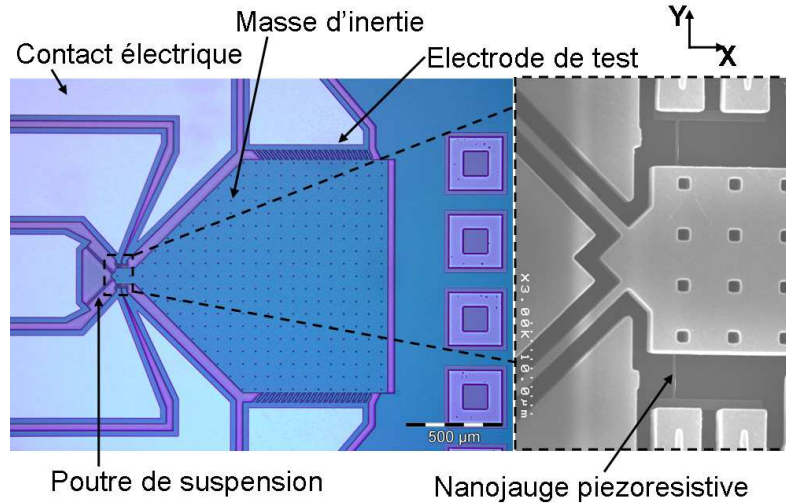


Figure 169 : Vue de dessus d'un accéléromètre un axe à détection piezoresistive à base de nano-jauge de contrainte

La sensibilité  $S_{DC}$  quasi-statique de ce capteur est donnée par l'équation (145) :

$$S_{DC} = \frac{\Delta R}{R} = m_i \cdot \pi_l \cdot \frac{L_0}{d_J} \cdot \frac{1}{S_{EQ}} \quad (145)$$

Ici  $m_i$  correspond à la masse d'inertie du capteur,  $\pi_l$  au coefficient piezoresistif,  $L_0/d_J$  à la valeur du rapport d'amplification mécanique du bras de levier et  $1/S_{EQ}$  à une indication du gain prodigué par la concentration des contraintes, obtenue grâce à la faible section  $S_{EQ}$  de la nano-jauge. Le temps de réponse  $\tau$  d'un tel capteur est donné par l'équation (146).

$$\tau = \frac{Q}{\pi \cdot f} = \frac{2}{\gamma} \quad (146)$$

$Q$  est le facteur de qualité du résonateur mécanique obtenu par l'association masse-ressort amorti,  $f$  la fréquence de résonance et  $\gamma$  le facteur d'amortissement. On estime généralement le régime permanent atteint au bout de  $5\tau$ . C'est donc le temps d'attente nécessaire entre deux mesures d'accélération. En considérant des valeurs typiques de 100 Hz pour la bande passante et de 3.5 kHz pour la fréquence de résonance, on peut déduire l'existence d'un facteur de qualité maximum tolérable  $Q_{MAX} = 20$ . Les accéléromètres quasi-statiques développés durant cette thèse sont décrits plus en détail dans le chapitre 4.

## 2.2- Gyromètre à effet Coriolis

Un gyromètre mesurant la force de Coriolis fournit une évaluation de la vitesse de rotation. L'expression de la force de Coriolis  $F_Y$  est donnée par l'équation (147).

$$\vec{F}_Y = -2 \cdot m_i \cdot \vec{v}_X \wedge \vec{\Omega}_Z \quad (147)$$

$m_i$  représente la masse d'inertie du capteur,  $v_X$  la vitesse d'excitation selon l'axe  $X$  et  $\Omega_Z$  la vitesse de rotation (mesurande) selon l'axe  $Z$ . La force obtenue est perpendiculaire à la fois à la vitesse d'excitation et à la vitesse de rotation.

Les gyromètres MEMS à force de Coriolis sont basés sur un système masse-ressort selon deux directions, la direction d'excitation (*drive*) et la direction de détection (*sense*). La figure 170 montre le schéma cinématique d'un tel capteur.

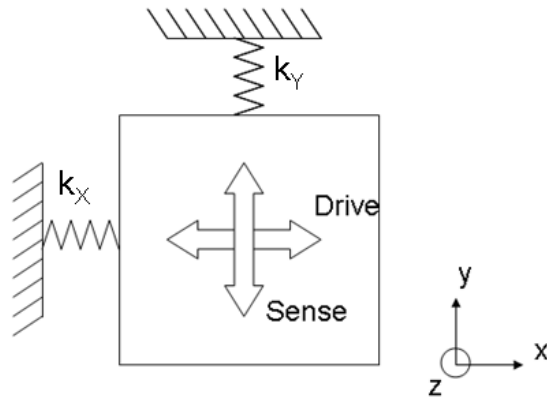


Figure 170: Schéma cinématique d'un gyromètre à force de Coriolis

La partie *drive* est excitée à amplitude et fréquence contrôlées par l'électronique d'asservissement. Le but est de continuellement exciter le système à sa fréquence de résonance selon l'axe  $x$  (celle du *drive*) afin de conserver une vitesse d'excitation constante.

Afin d'obtenir une force de Coriolis de grande amplitude, il est nécessaire de maximiser la vitesse d'excitation  $v_x$  à travers l'amplitude d'excitation  $u_x$  de la partie *drive*. Obtenir des amplitudes d'excitation supérieures à  $1 \mu\text{m}$  sans amplification par le facteur de qualité est extrêmement difficile. C'est pour cela que dans la majorité des cas, le gyromètre à force de Coriolis est un **capteur résonant à haut facteur de qualité**. En tenant compte des différentes contraintes d'encombrement et de tension, on peut fixer une amplification minimum tolérable ( $Q_{MIN} = 2.10^3$ ) nécessaire pour obtenir une amplitude d'excitation de  $2 \mu\text{m}$ .

La figure 171 montre un schéma du gyromètre conçu (et fabriqué). Sur cette figure le cadre vert correspond à la partie excitation (*drive*) du capteur. La masse rouge correspond elle à la masse d'inertie. La partie bleue correspond à la partie détection (pivot + élément de détection).

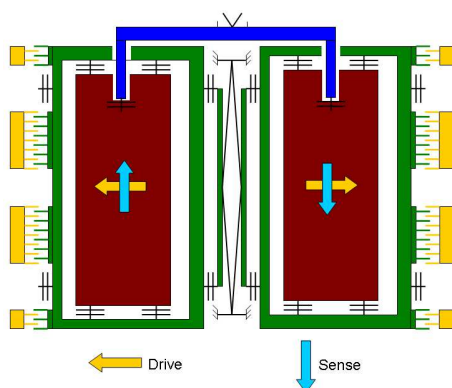


Figure 171: Schéma d'un gyromètre double masse complètement découplé

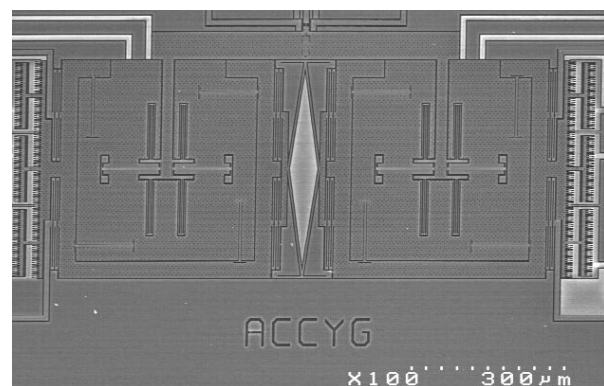


Figure 172: Image MEB d'un gyromètre double masse fabriqué [Wal12]

### 2.3- Problématique de la thèse

La figure 173 montre des résultats de mesure du facteur de qualité des accéléromètres ainsi que celui de la partie excitation des gyromètres, en fonction de la pression environnante.

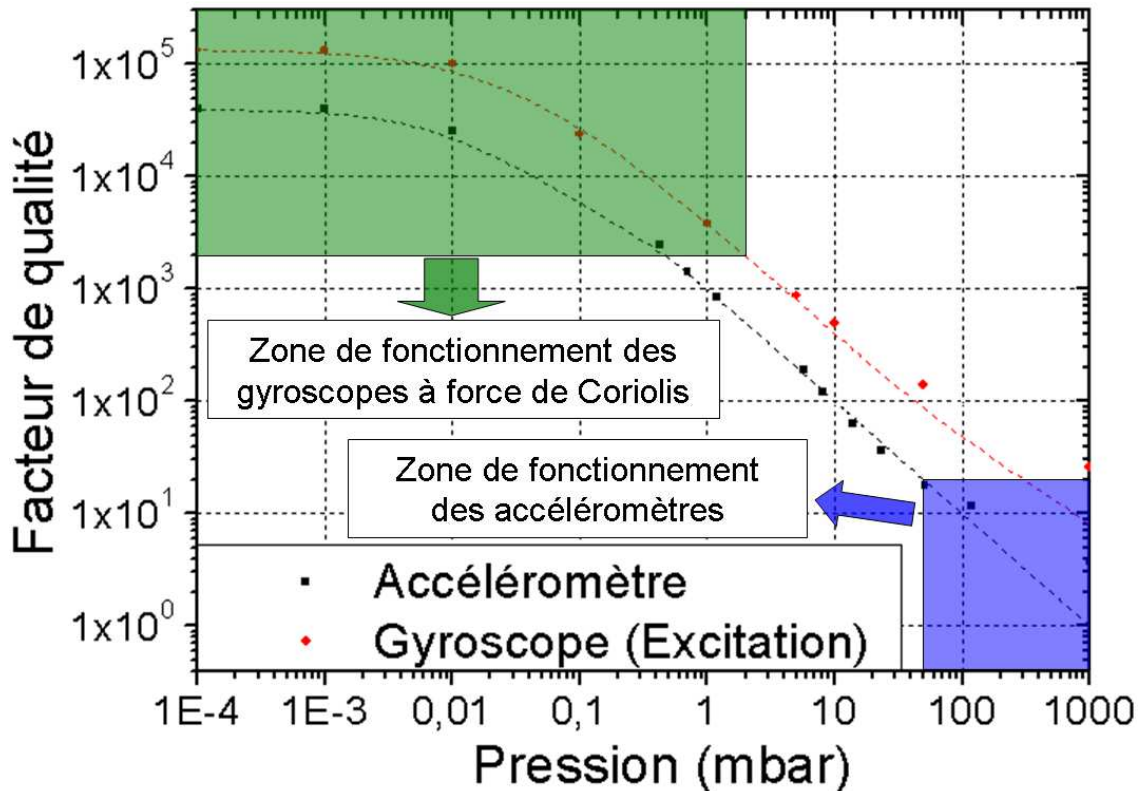


Figure 173: Zones de fonctionnement respectives des accéléromètres pendulaires (zone bleue) et des gyromètres à force de Coriolis (zone verte), illustrant une des difficultés de co-intégration de ces 2 types de capteurs, dans ce cas lie à la nécessité d'avoir un même environnement de pression.

Les deux courbes sont très largement corrélées. Les cadres vert et bleu correspondent respectivement aux zones de fonctionnement des gyromètres et des accéléromètres, telles que définies par les facteurs de qualité maximum et minimum décrits précédemment.

La figure 173 montre qu'il n'existe pas, *a priori*, de plage de pression commune permettant de co-intégrer les deux capteurs. Partant de ce constat, nous avons exploré et développé au cours de cette thèse, des solutions permettant de faire fonctionner accéléromètres et gyromètres à force de Coriolis sous une même pression.

Ces solutions ont été développées en gardant en tête l'objectif de la technologie M&NEMS qui est d'obtenir des capteurs à bas coût (en plus de la co-intégration). Cette problématique de co-intégration, s'étend au-delà du couple accéléromètre-gyromètre ; elle concerne également les magnétomètres et les capteurs de pression, dans la perspective ultime d'intégration d'une plateforme inertielle complète, dite « 10 axes ». Des problématiques inhérentes au capteur de pression ainsi qu'aux 3 axes de mesure d'un accéléromètre, sont également traitées dans cette thèse.

### 3- Solutions basées sur des structures résonantes

#### 3.1- Accéléromètre dynamique

Une solution permettant de co-intégrer accéléromètre et gyromètre, est d'utiliser un accéléromètre résonant (i.e fonctionnant sous vide). On obtient ainsi deux capteurs fonctionnant sous vide. Un tel capteur est décrit dans la figure 174.

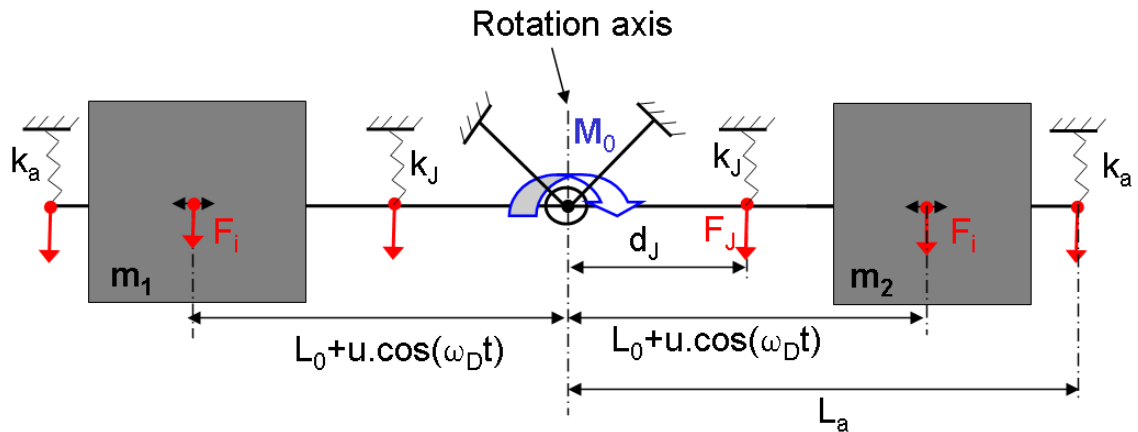


Figure 174: Schéma de principe de l'accéléromètre dynamique proposé

L'idée à la base de l'accéléromètre dynamique réside dans le fait que la contrainte mesurée dans les nanojauges suspendues est proportionnelle au **moment** induit par l'accélération. Si la valeur du bras de levier est modulée, alors la contrainte dans la jauge est également modulée. L'équation (148) montre l'expression du moment  $M$  induit par une accélération  $a_Y$ .

$$M = a_Y \cdot m_i \cdot (L_0 + u \cdot \cos(\omega_d \cdot t)) \quad (148)$$

$a_Y$  est l'accélération selon l'axe sensible.  $m_i$  correspond à la masse d'inertie.  $L_0$  correspond à la longueur du bras de levier au repos et  $u$  à l'amplitude du déplacement de la masse d'inertie à la résonance.  $\omega_d$  correspond à la pulsation de ce mouvement. L'utilisation de deux masses d'inertie permet de compenser le terme d'accélération quasi-statique proportionnelle à  $L_0$ .

L'architecture de ce capteur est très proche d'un gyromètre à force de Coriolis. Tout comme le gyromètre, ce capteur comprend deux directions distinctes, excitation (*drive*) et détection (*sense*). De plus, son fonctionnement requiert une boucle de contrôle de la partie excitation.

En termes de sensibilité à l'accélération, l'accéléromètre dynamique possède un bras de levier plus faible, mais du fait que c'est un capteur résonant, on peut espérer une grande amplification due au facteur de qualité. En sus, la gamme dynamique du capteur est élargie car le bruit prédominant aux fréquences (relativement) élevées (au-delà de la zone DC) n'est plus le bruit de Flicker ( $1/f$ ) mais le bruit brownien (nettement plus faible).

Les caractérisations modales de ce capteur donnent des performances très proches de celles d'un gyromètre ( $f_d=19.4$  kHz,  $f_s=19.5$  kHz,  $Q_d=2 \cdot 10^4$  et  $Q_s=4 \cdot 10^4$ ). Un biais important a été mesuré sur ce dispositif. Ce biais a été expliqué et une seconde version de l'accéléromètre dynamique a été proposée pour le réduire. Les figures 175 et 176 montrent les principaux modes de déformation de cette seconde implémentation.

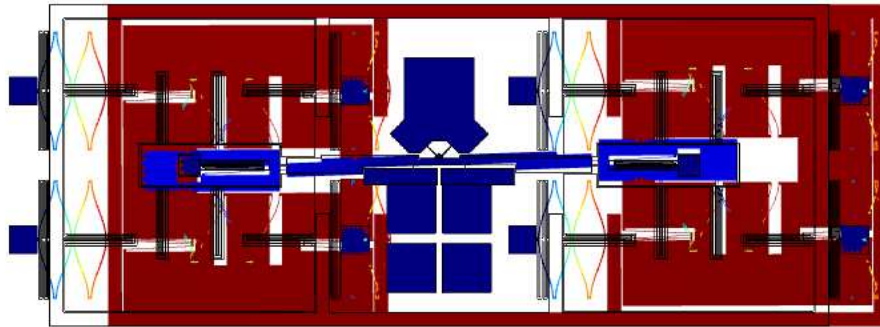


Figure 175: Mode d'excitation de l'accéléromètre dynamique (20.2 kHz)

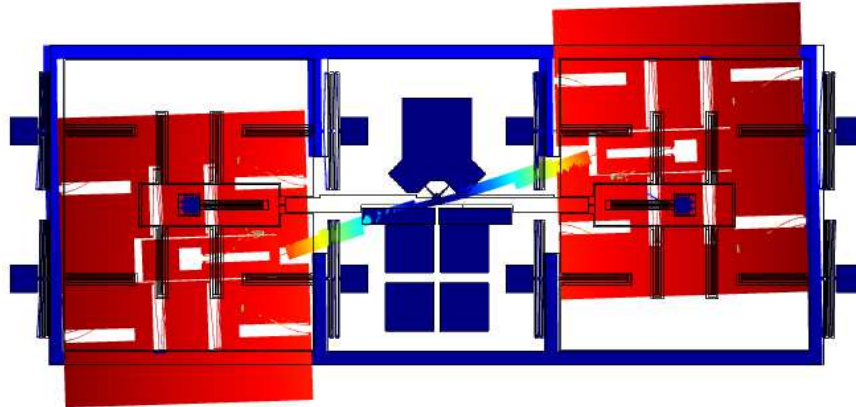


Figure 176: Mode de détection de l'accéléromètre dynamique (20.5 kHz)

Une solution de co-intégration à été proposée à travers l'accéléromètre dynamique. Cette solution intègre un capteur résonant mesurant l'accélération et résout ainsi la problématique de pression environnante. Cependant, ce capteur résonant nécessite une électronique de contrôle complexe (tout comme le gyromètre) et possède un encombrement et une consommation électrique largement supérieure à ceux d'un accéléromètre quasi-statique standard. La structure décrite en 3.2 ci-après est destinée à limiter ces inconvénients afin de rendre cette solution de co-intégration plus viable.

### 3.2- Accéléromètre-Gyromètre couplé

Afin de réduire les inconvénients inhérents aux capteurs résonants, une solution possible consiste à mutualiser les parties excitation entre elles afin de réduire par exemple le nombre de boucles de rétroaction nécessaires. Dans cette optique, un capteur intégrant intrinsèquement une mesure d'accélération et de vitesse de rotation est présenté dans la figure 177.



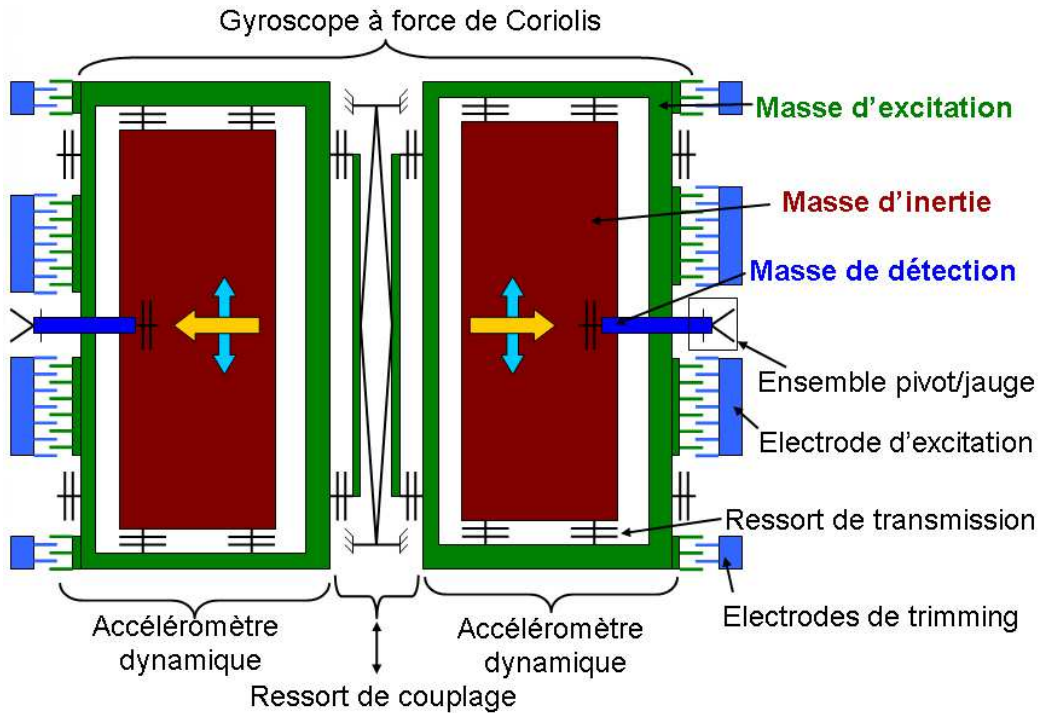


Figure 177: Schéma fonctionnelle de l'accéléromètre-gyromètre couplé

Afin d'être sensible à la fois au signal d'accélération et de vitesse de rotation, le bras de détection a été éloigné du centre des masses. La partie excitation du système (en vert) est identique à celle d'un gyromètre double masse à force de Coriolis. Concernant la partie détection (en bleu), chacune des parties symétriques du système correspond à un accéléromètre dynamique non compensé (Voir figure 178).

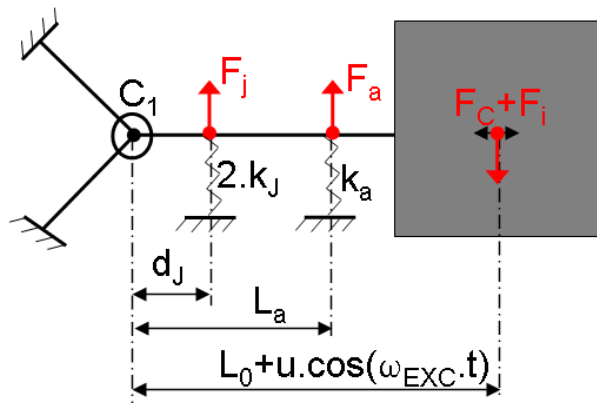


Figure 178: Schéma mécanique de la partie détection d'un système accéléromètre-gyromètre couplés

$k_J$  et  $k_a$  correspondent respectivement aux raideurs des jauges et des ressorts de transmission.  $C_1$  correspond à la raideur en rotation du pivot.  $d_J$  et  $L_a$  correspondent à la distance pivot-jauge et à la distance du ressort de transmission au pivot. Lorsqu'un tel système est soumis à une accélération  $a_Y$  et à une vitesse de rotation  $\Omega_Z$ , on obtient un moment possédant plusieurs termes. L'équation (149) décrit ces différents termes.

$$\begin{aligned}
M &= (2.m_i.u.\omega_D.\Omega_Z + m_i.a_Y).(L_0 + u.\cos(\omega_D.t)) = \\
&= m_i.a_Y.L_0 \\
&+ m_i.u.a_Y.\cos(\omega_D.t) \\
&+ 2.m_i.u.\omega_D.\Omega_Z.L_0.\cos(\omega_D.t) \\
&+ m_i.u^2.\omega_D.\Omega_Z.\cos(2.\omega_D.t) \\
&+ m_i.u^2.\omega_D.\Omega_Z
\end{aligned} \tag{149}$$

On peut extraire les différents termes obtenus en fonction de leurs fréquences et de leurs origines inertielles. La table 27 donne les contraintes théoriques générées sur chacun des bras de détection par un signal d'accélération et/ou un signal de vitesse de rotation.

Fréquence de détection	Signal d'accélération	Signal de Coriolis
@ DC	<b>70 <math>\mu\text{V/V/g}</math></b>	$\sim 8.10^{-5} \mu\text{V/V}^\circ/\text{s}$
@ $\omega_D$	<b>45 <math>\mu\text{V/V/g}</math></b>	<b>1 <math>\mu\text{V/V}^\circ/\text{s}</math></b>
@ $2.\omega_D$	-	$\sim 3.10^{-5} \mu\text{V/V}^\circ/\text{s}$

*Table 27: Ordres de grandeur des sensibilités théoriques obtenues à chaque fréquence.*

Les deux signaux modulés à  $\omega_D$  présentent une amplitude suffisante pour être utilisés. Cependant il faut encore pouvoir décorréler les signaux provenant d'une accélération de ceux provenant d'une vitesse de rotation. Le mouvement d'excitation des deux masses d'inertie est en opposition de phase grâce au ressort de couplage en forme de losange (Cette forme particulière est décrite en détail dans le chapitre 2 ainsi que d'autres fonctions mécaniques). Ainsi que le montre la table 28, un tel mouvement d'excitation permet d'obtenir des signaux de détection opposés pour chacun des bras de détection.

Signal de détection	Bras de détection 1	Bras de détection 2
Accélération $a_Y$	↑	↑
Vitesse de rotation $\Omega_Z$	↓	↑

*Table 28: Comportement de chacun des bras de détection en fonction du signal inertiel*

D'après la table 28, le signal d'accélération peut être obtenu en additionnant les signaux extraits des deux bras de détection. A l'inverse la **vitesse de rotation** peut être obtenue en **soustrayant** ces deux signaux.

De plus l'accélération dynamique (proportionnelle à  $u$ ) est déphasée de  $90^\circ$  par rapport à la contrainte due à une force de Coriolis (proportionnelle à  $j.u.\omega_D$ ). Un filtrage en phase (de type détection synchrone) pourrait donc permettre de décorréler les deux types de signaux.

Un capteur résonant intégrant les fonctionnalités d'accéléromètre (dynamique) et de gyromètre a été présenté. Son fonctionnement ne nécessite qu'une boucle de rétroaction et l'encombrement du capteur est équivalent à celui d'un gyromètre standard. L'ensemble des capteurs résonants étudiés dans cette thèse sont décrits plus en détail dans le chapitre 5.



## 4- Amortissement par couplage électromécanique

Dans cette section on décrit une source d'amortissement électromécanique contrôlable pouvant permettre la réalisation d'un accéléromètre sur-amorti conditionné sous vide. Ce type d'amortissement à déjà été décrit dans [Jou07] et [Bar12].

Afin d'augmenter sélectivement l'amortissement d'un capteur mécanique, nous proposons de coupler la partie mécanique du capteur à un circuit dissipatif électrique. L'idée est d'utiliser l'électrode de test du capteur comme capacité variable  $C(x)=C_0+C'x$ .  $C_0$  représente la partie constante de la capacité.  $C'x$  correspond aux variations de capacité induite par un mouvement de la masse d'inertie. Les charges successives de la capacité (dues au mouvement mécanique) sont déchargées ensuite dans une résistance  $R$  par effet Joule. Les figures 179 et 180 montrent respectivement le schéma équivalent électrique et le schéma équivalent mécanique du système.

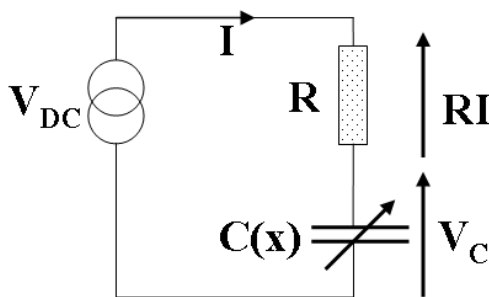


Figure 179: Schéma électrique équivalent

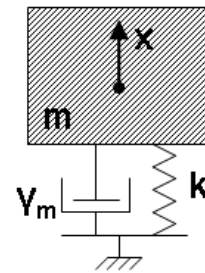


Figure 180: Schéma mécanique équivalent

La mise en équation des systèmes représentés dans les figures 179 et 180 induit la fonction de transfert de l'équation (150).

$$\frac{X}{F_{ext}} = \frac{1}{k - \omega^2 \left( m - \frac{C'^2 R^2 V_{DC}^2 C}{1 + R^2 C^2 \omega^2} \right) + j\omega \left( \gamma_m + \frac{C'^2 R V_{DC}^2}{1 + R^2 C^2 \omega^2} \right)} \quad (150)$$

Les termes d'origine électrique se traduisent principalement par un terme d'amortissement de couplage  $\gamma_C$  exprimé dans l'équation (151).

$$\gamma = \gamma_m + \gamma_C = \gamma_m + \frac{(V_{DC} \cdot C')^2 \cdot R}{1 + R^2 \cdot C^2 \cdot \omega^2} \quad (151)$$

Cet amortissement a été mesuré expérimentalement en utilisant l'accéléromètre de la figure 169. Les données expérimentales sont en accord avec la théorie (cf figure 181).

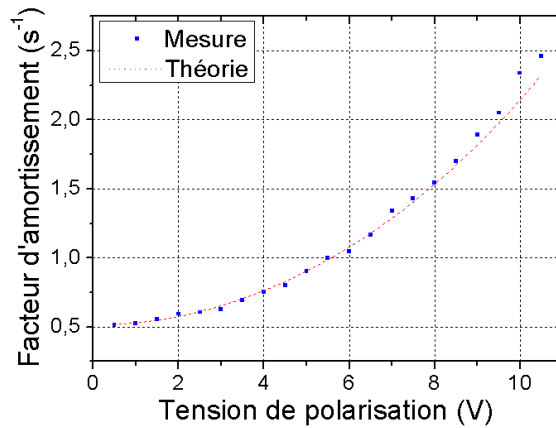


Figure 181: Facteur d'amortissement dû à un couplage électromécanique

D'après l'équation (151), un optimum d'amortissement existe pour  $C=1/\omega_{RES}R$ . Avec  $\omega_{RES}$  la pulsation propre du capteur. En utilisant plusieurs valeurs de résistance, la valeur de la capacité  $C$  (formé ici principalement par des capacités parasites) a été extraite, et l'existence d'un optimum d'amortissement a été démontrée (Voir figure 182).

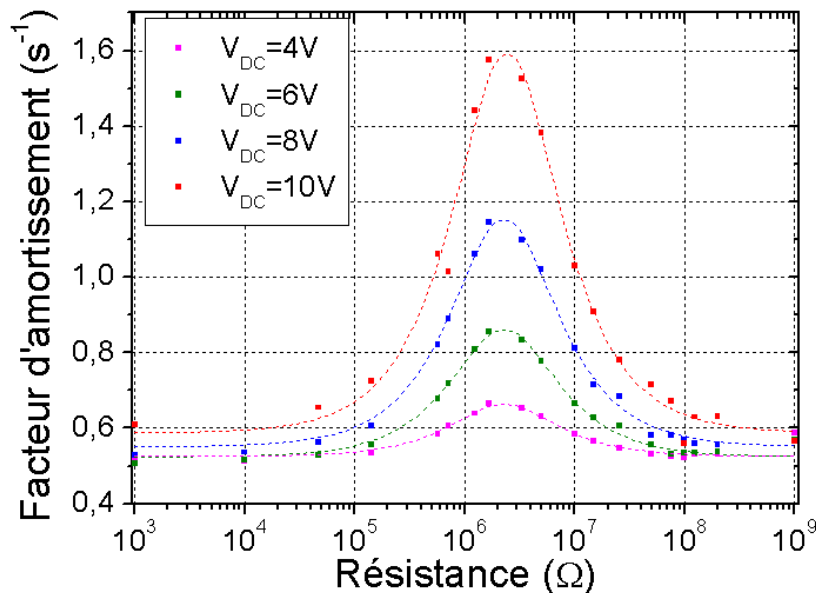


Figure 182: Mise en évidence d'une fréquence de coupure principalement due à des capacités parasites

Un amortissement électromécanique contrôlable par une simple tension DC a été utilisé pour réduire le facteur de qualité d'un accéléromètre MEMS. Les mesures expérimentales effectuées correspondent très bien à la théorie. Un design optimisé permettant théoriquement d'atteindre un facteur de qualité de 50 pour un  $V_{DC}$  de 10 V sous vide a été proposé. De prochains tests permettront d'évaluer les performances de cet amortissement. Le chapitre 6 décrit plus en détail les principaux résultats présentés ici.

L'utilisation d'un tel amortissement à des fins de co-intégration permettrait de contourner totalement la problématique de pression environnante. Ainsi, grâce à la possibilité d'introduire un amortissement supplémentaire par voie électrique dans le système mécanique résonant, il serait alors possible d'utiliser un accéléromètre quasi-statique (de faible encombrement, et sans électronique de contrôle) dans un

environnement compatible avec l'utilisation de gyromètres à force de Coriolis, nécessitant un environnement de vide relativement poussé.

Au cours de cette thèse, plusieurs types de capteur inertiels (accéléromètre, gyromètre, capteur de pression) ont été fabriqués en utilisant un unique procédé de fabrication centré sur l'utilisation de nano-jauges piézorésistives. Ces capteurs ont été caractérisés et des contraintes de co-intégration ont été extraites de ces caractérisations. Plusieurs solutions à la problématique de pression environnante ont été proposées. Deux solutions portant sur une centrale inertielle basée sur des capteurs résonants à été proposé. Une solution alternative permettant d'intégrer des accéléromètres quasi-statiques sous faible pression a également été validée.

L'intégration de différents types de capteurs dans un procédé de fabrication commun ouvre la voie vers une prise en compte plus globale de la problématique 'capteur'. En effet l'importance de l'électronique dans les performances d'un capteur résonant et/ou piézorésistif est prépondérante. Afin d'obtenir une centrale inertielle bas-coût, il est également nécessaire de mutualiser et d'optimiser la partie électronique.

## Références:

- [Bar12]: T. Barois et al "Ohmic electromechanical dissipation in nanomechanical cantilevers" Physical review B Vol.85 (7), (075407), 201
- [Ett11]: Dirk Ettelt, Guillaume Dodane, Marcel Audoin, Arnaud Walther, Guillaume Jourdan, Patrice Rey and Philippe Robert, Jerome Delamare "A Novel Microfabricated High Precision Vector Magnetometer" Sensors IEEE, pp .2010-2013, 2011.
- [Jou07]: G. Jourdan et al "Tuning the effective coupling of an AFM lever to a thermal bath", Nanotechnology Vol.18 (47), (475502) 2007.
- [Rob09]: Ph. Robert, V. Nguyen, S. Hentz, L. Duraffourg, G. Jourdan, J. Arcamone and S. Harrison. "M&NEMS : A new approach for ultra-low cost 3D inertial sensor" IEEE Sensor Conference, Christchurch pp.963-966, 2009.
- [Yole11]: Yole Technology. "Trends for Inertial MEMS Volume 1: Analysis" December 2011.
- [Wal12]: A. Walther, M. Savoye, G. Jourdan, P. Renaux, F. Souchon, P. Robert, C. Le Blanc, N. Delorme, O. Gigan, C. Lejuste "3-axis gyroscope with Si nanogage piezo-resistive detection" 25th IEEE International Conference on MEMS ,29 Jan-02 Feb 2012 pp.480-3.

## Résumé

Cette thèse a été effectuée dans un contexte industriel de forte concurrence en lien avec les capteurs miniatures en silicium, destinés au gigantesque marché dit 'consumer', dont l'application phare est le 'Smartphone', pour laquelle les fonctionnalités accrues engendrent un besoin en matière de multi-capteurs inertiels dits 10-axes (accéléromètre 3-axes, magnétomètre 3-axes, gyromètre 3-axes et capteur de pression). Tout comme les circuits intégrés, les contraintes de coût de tels capteurs se traduisent par une exigence en termes de densité d'intégration. La technologie M&NEMS (*Micro- & Nano- Electro Mechanical Systems*) a été développée pour répondre à cette attente. Elle repose sur l'intégration de jauges de contraintes de dimensions nanométriques (~250 nm) avec des structures électromécaniques micrométriques, ce qui prodigue une compacité hors-pair des capteurs, ouvrant la voie à la co-intégration de multi-capteurs sur la même puce de silicium. Toutefois, la nature différente des grandeurs physiques à mesurer impose des contraintes supplémentaires, parfois opposées, ce qui rend leur co-intégration difficile. Partant de ce constat, nous avons exploré et développé, des solutions devant permettre le fonctionnement sous une même pression environnante, d'accéléromètres et de gyromètres à force de Coriolis. Cette problématique de co-intégration, s'étend au-delà du couple accéléromètre-gyromètre. Des questions inhérentes au capteur de pression ainsi qu'aux 3 axes de mesure d'un accéléromètre, sont également traitées dans cette thèse.

**Mots-clés:** MEMS, NEMS, Senseurs inertiels, Co-intégration, Piézorésistivité, Accéléromètre, Gyromètre, Capteur de pression, Couplage électromécanique, Amortissement.

## Abstract

This thesis was carried out in an industrial context of strong competition in connection with miniature silicon sensors for the huge so-called 'consumer' market, where the 'Smartphone' is the killer application; its increasing functionality creates a need for the so-called '10-axis' inertial multi-sensors (3-axis accelerometer, 3-axis magnetometer, 3-axis gyro sensor and pressure). Similarly to integrated circuits, cost constraints on such sensors translate into a requirement in terms of integration density. The M & NEMS (Micro- & Nano- Electro-Mechanical-Systems) technology has been developed to meet this expectation. It is based on the integration of nanoscale (~ 250 nm) strain gauges together with micrometric electromechanical structures, which ensure unrivaled compactness, paving the way for the co-integration of multiple inertial sensors on the same silicon chip. However, the different nature of the physical quantities to be measured imposes additional constraints, sometimes conflicting, which leads to a difficult co-integration. Based on this observation, we have explored and developed solutions to allow operation under the same ambient pressure, of accelerometers together with Coriolis force based gyroscopes. This issue of co-integration extends beyond the accelerometer-gyroscope couple. Issues inherent to the pressure sensor and to the 3-axis accelerometer measurements, are also addressed in this thesis.

**Keywords:** MEMS, NEMS, Inertial sensors, Co-integration, Piezoresistivity, Accelerometer, Gyroscope, Pressure sensor, Electromechanical coupling, Damping.